Soleil et microphysique des plasmas naturels

Carine Briand

Observatoire de Paris, LESIA, CNRS
UPMC Univ. Paris 06, Université Denis Diderot Paris 07

Soleil et Microphysique des plasmas naturels

Carine BRIAND

Habilitation à Diriger des Recherches
de l'Université Pierre et Marie Curie
Soutenue le 29 Octobre 2010

Composition du Jury

Philippe Savoini : Président
Bernard Gelly : Rapporteur
Ioannis Dandouras : Rapporteur
Jean-Louis Pinçon : Rapporteur
Bertrand Lembège : Examinateur

Table des matières

Chapitre 1

Présentation Générale

La première partie de ma carrière d'astronome adjoint (1996-2003) s'est déroulée en tant qu'astronome de support pour le télescope solaire franco-italien THEMIS, à Tenerife (Iles Canaries, Espagne). Une grande partie de ces sept années a été consacrée aux tâches de service (accueil des chercheurs venant observer, suivi instrumental, promotion du télescope au niveau international, participation aux Conseils – administration et scientifique – ponctuant tous les 3 mois la vie du télescope). En parallèle, j'ai maintenu une activité de recherche concernant le magnétisme solaire au niveau de la photosphère et de la chromosphère. Je me suis en particulier attachée à l'évolution temporelle des régions actives. Le but étant d'apporter des données observationnelles pouvant être confrontées aux théories d'émergence et d'évolution du champ magnétique.

De retour en France en Mars 2004, j'ai intégré le groupe de physique des plasmas du LESIA (Observatoire de Paris) afin de donner une nouvelle orientation à ma carrière. Je souhaitais en effet revenir à mes bases (DEA de physique des plasmas et stage au CETP sur les ondes basses fréquences dans la magnétosphère de la Terre) afin de les appliquer aux plasmas spatiaux, au vent solaire en particulier. J'ai donc quitté le domaine optique pour m'intéresser au domaine radio basses fréquences (quelques Hz à une centaine de kHz, c'est-à-dire au domaine des ondes principalement électrostatique dans le milieu interplanétaire) et dans une moindre mesure au domaine des plus hautes fréquences (10-30MHz) pour une étude sur la couronne solaire. L'objectif de ce travail est de comprendre les liens entre les processus cinétiques à petites échelles et les structures à grande échelle du milieu interplanétaire. Seule l'alliance de l'observation (spatial et sol) et des simulations numériques cinétiques (de type Vlasov) permet d'aborder cette question.

Le travail d'un membre du CNAP comprend également de larges volets de "tâches de service", d'enseignement et de vulgarisation scientifique.
Depuis 2006, mes nouvelles tâches de service sont en rapport avec ma nouvelle activité scientifique. En dépit de la richesse exceptionnelle des mesures de forme d'onde pour la compréhension de la physique de base des plasmas astrophysiques, la plupart de ces données sont difficilement accessibles pour les non initiés et très rarement disponibles en ligne. J'ai donc proposé un archivage et une valorisation de ces données au CDPP (Centre de Données de la Physique des Plasmas). Ce projet est actuellement en cours de développement.

L'enseignement et la vulgarisation grand public ont toujours joué un grand rôle dans ma carrière. Si je n'ai pas pu enseigner – au niveau universitaire – lors de mon séjour en Espagne, j'ai participé à la formation pour les enseignants du secondaire et surtout assuré de

nombreuses visites du télescope. Depuis mon retour, j'ai repris l'enseignement à l'université tant en France qu'en Italie et j'ai assuré des soutiens aux professeurs des collèges à travers des parrainages de classes. Enfin, mon activité vers le grand public s'est accrue à travers de nombreuses conférences (en France et à l'étranger), des émissions radiophoniques et télévisées et la rédaction d'un livre de vulgarisation. J'ai également assuré la vice-présidence de la coordination européenne de l'Année Héliophysique Internationale (entre 2006 et 2009). Enfin, depuis la dernière Assemblée Générale de l'IAU, je suis chargée au sein de la division II d'un groupe sur "Communiquer l'héliophysique avec le public". Ceci représente une partie des tâches que j'assume au quotidien.

Ce manuscrit est divisé en deux chapitres : le chapitre 2 retrace les principaux travaux réalisés pendant ma mise à disposition au télescope THEMIS. Il aborde des aspects scientifiques mais également les développement instrumentaux auxquels j'ai pris part. Le chapitre 3 aborde une description des études sur la physique des plasmas du milieu interplanétaire, avec les aspects observationnels et la partie simulation numérique. Chacun de ces chapitres commence par une introduction permettant de replacer les articles, présentés en fin de chaque partie, dans le contexte général de l'étude menée.

Chapitre 2

Champ magnétique solaire : photosphère et chromosphère

2.1 Introduction

Pourquoi s'intéresser encore au Soleil ? C'est une question qui revient souvent, tant chez certains scientifiques que dans le grand public. Différentes réponses peuvent être apportées : (a) dans un cadre scientifique classique (b) dans le cadre environnemental des relations Soleil-Terre.

Des livres chinois du commerce datant de 800 avant J.C. mentionnent la présence de tache à la surface du Soleil mais l'observation systématique du Soleil n'a réellement commencé qu'avec l'apparition des premières lunettes au XVIIème siècle. Ces observations ont permis de développer, ce que l'on appellerait dans notre langage moderne, une base de données exceptionnelle, mais les réels progrès en terme de physique solaire sont beaucoup plus récents. Sans le développement de la spectroscopie (fin XIXème) et l'observation dans les domaines des hautes énergies ainsi que dans le domaine radio (qui datent toutes deux de la seconde moitié du XXème siècle) aucune avancée majeure dans la compréhension des mécanismes physiques gouvernant la dynamique solaire n'était possible. Autrement dit, en dépit des apparences, la physique solaire est jeune !
Seule étoile permettant des observations à très haute résolution spatiale ou temporelle, le Soleil se révèle un laboratoire de premier plan pour de nombreux domaines de physique (soit pour bâtir des théories nouvelles soit pour les tester). Cet avantage conduit aussi rapidement à de hauts degrés de sophistication rendant ce domaine de recherche souvent abscons pour les non spécialistes. Et pourtant, transfert d'énergie, reconnection magnétique, physique nucléaire, magnétohydrodynamique, turbulence, ondes etc... sont des sujets abordés non seulement dans d'autres domaines de l'astrophysique mais également par d'autres physiciens en laboratoire.

Dernièrement, un regain d'intérêt pour la physique solaire est venue du cadre environnemental pour comprendre les relations entre le Soleil et la Terre.
Le Soleil a un impact non seulement sur le climat de la Terre [1] mais également sur le géomagnétisme terrestre et l'activité technologique humaine. Depuis la fameuse panne électrique de Mars 1989 au Canada ou la perte de satellite de communication en 1994, de nombreux industriels

1. et l'activité humaine encore plus ...

s'intéressent de près à ces questions d'impact de l'activité solaire. Si leurs motivations sont uniquement opérationnelles, des études plus fondamentales en amont sont indispensables pour permettre la mise en place de modèles de prévision fiables et exploitables.
Perturbations de l'ionosphère (scintillation, variation de la fréquence plasma) et conséquences sur la réception des signaux des réseaux de positionnement (GPS, Galileo) avec des impacts sur des très nombreux utilisateurs (navigation marine ou aérienne, recherche pétrolière, agriculture), perturbations de l'atmosphère terrestre par échauffement dû au rayonnement UV solaire (ayant des conséquences sur l'altitude et l'attitude des satellites, le positionnement des débris spatiaux), génération de courants induits dans les structures métalliques de grandes dimensions (pipelines, lignes à haute tension), black-out de communication aérienne, irradiation des équipages d'avion et irradiation des spationautes (en station autour de la Terre ou sur la Lune) sont quelques exemples des conséquences des phénomènes éruptifs d'origine solaire (voir aussi la Figure 2.1).

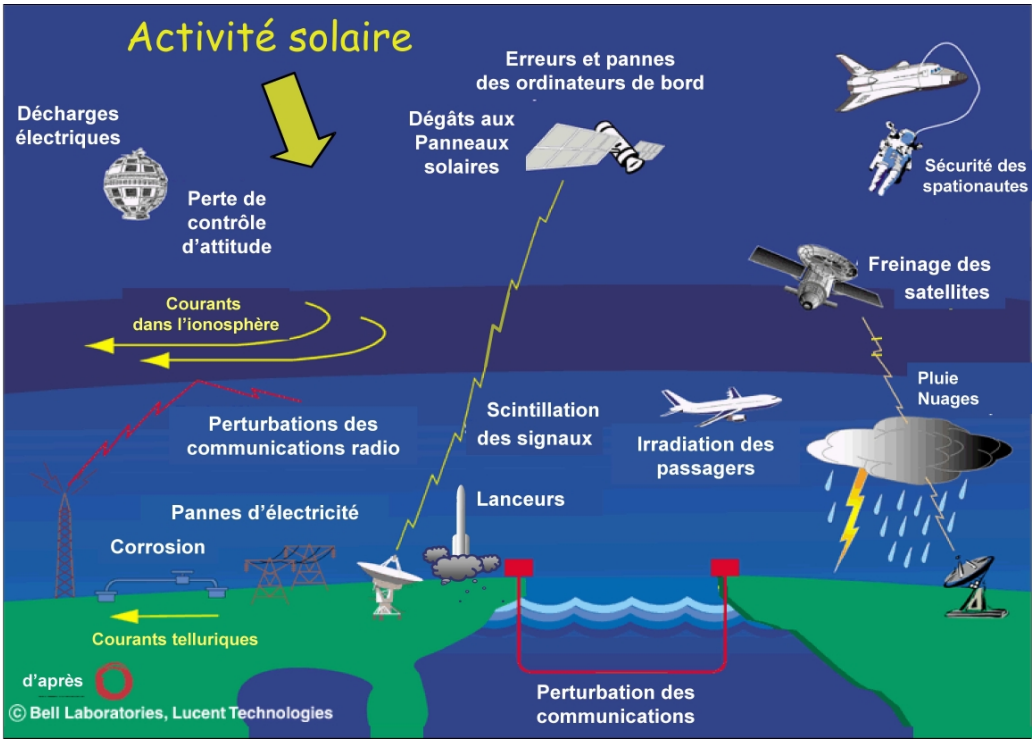

FIGURE 2.1 – Une vue schématique – souvent utilisée dans mes conférence grand public – des principaux domaines technologiques pouvant être affecté par des éruptions solaires. Figure adaptée de Bell Laboratories - Lanzerotti

La compréhension des mécanismes régissant le cycle solaire, ainsi que ceux conduisant aux éruptions est donc un enjeu essentiel afin de prévenir les effets néfastes des sursauts du Soleil sur l'activité technologique humaine. Les programmes de météorologie de l'espace, qu'ils soient américains, européens ou d'autres pays (comme le Japon et la Chine), ont pour objectif d'établir un dialogue opérationnel entre les scientifiques et les "consommateurs" (opérateurs satellites, compagnies aéronautiques, opérateurs des réseaux de distribution d'énergie, etc ...).

Que savons nous actuellement sur l'activité solaire ? Sommes-nous prêts pour des prévisions à quelques jours ou quelques heures comme requis par de nombreux opérateurs ? Je vais tâcher d'apporter quelques éléments de réponse, en me restreignant toutefois aux aspects proches de

mes sujets d'études.

2.1.1 Relations Soleil-Terre

Les relations entre le Soleil et la Terre passent par trois vecteurs : (1) le rayonnement, (2) le vent solaire et les perturbations du champ magnétique interplanétaire, (3) les particules énergétiques. Voyons comment et pourquoi ces paramètres peuvent varier.

Le soleil rayonne comme un corps noir à 5700K. A 1UA, le flux solaire (intégré sur toutes les longueurs d'onde) est de 1363 watt/m^2. De récentes études de ce flux montrent deux phénomènes : (1) une relative constance du flux solaire, intégré sur toutes les longueurs d'onde, en fonction du temps (des variations ne dépassant pas 0.1% sont enregistrées au cours du cycle solaire), (2) des variations beaucoup plus importantes de flux UV (et dans une moindre mesure IR [2]) en fonction du cycle et de la présence de phénomènes éruptifs sur le soleil. Ces variations du flux UV solaires entraînent des modifications : (a) du taux de photodissociation de l'ozone (processus jouant un rôle fondamental dans le bilan thermique de l'atmosphère terrestre), (b) de la densité atmosphérique terrestre à haute altitude dû à l'échauffement des couches supérieures de l'atmosphère terrestre (avec des répercussions sur le contrôle d'altitude et d'attitude des satellites en orbite basse).

Les planètes du système solaire reçoivent un flux continu de rayonnement mais également de particules d'origine solaire. Ce flux d'électrons, protons et ions constitue le *vent solaire*. L'existence d'un vent solaire s'est imposée pour expliquer la présence de la queue plasma des comètes. Les premiers modèles de vent solaire ont été fournis par Parker (1958) en abandonnant l'idée d'une atmosphère solaire en équilibre hydrostatique. Un flux continu de particules chargées est donc émis par le soleil. Le modèle de Parker montre également qu'au-delà d'une certaine distance au Soleil, le vent solaire devient supersonique et super-Alfvénique. Les mesures *in situ* ont montré que le modèle de Parker était vérifié au premier ordre. Elles ont aussi mis en évidence la présence de deux composantes : un vent lent relativement stable dans le temps (i.e. présentant peu de fluctuations en fonction du cycle solaire) et restreint à des latitudes héliographiques faibles ($< 30°$) et un vent rapide présentant des fluctuations temporelles beaucoup plus importantes et situé plutôt à hautes latitudes. Le modèle de Parker ne permet pas de rendre compte de ces deux vents puisqu'il est basé essentiellement sur une description hydrodynamique, alors qu'une description cinétique est nécessaire pour expliquer les valeurs observées de vent solaire rapide (Chamberlain 1960; Lemaire and Scherer 1971; Lemaire and Pierrard 2001; Zouganelis et al. 2004).
Par ailleurs, la conductivité électrique du plasma interplanétaire est très grande. La diffusion des lignes de champ magnétique est faible. Le champ est alors dit gelé dans le plasma. De plus, le rapport β de la pression cinétique à la pression magnétique est très supérieur à 1 dans le vent solaire : le plasma entraîne le champ magnétique solaire. Le milieu interplanétaire est ainsi constitué de particules chargées se déplaçant à des vitesses supersoniques et super-Alfvéniques, entraînant avec elles le champ magnétique solaire.

La première conséquence de la présence d'un vent solaire est de comprimer la magnétosphère des planètes du côté jour et de l'étirer du côté nuit. La position de la magnétopause (région où la pression cinétique du vent solaire est égale à la pression magnétique de la magnétosphère) varie

2. Plus de 60% des variations du flux intégré sont produits par des longueur d'onde en dessous de 400nm

FIGURE 2.2 – Premier orage magnétique produit par le nouveau cycle solaire (minimum du cycle 23 atteint en Décembre 2008). Aurore observée le 20 Janvier 2010 au niveau du cercle arctique. Credit : A.D. Skjervold

donc en fonction de la vitesse d'écoulement du vent solaire. Les satellites (naturels ou artificiels) peuvent ainsi être alternativement dans et hors magnétosphère en quelques minutes. La seconde conséquence est d'approvisionner ces mêmes magnétosphères en particules énergétiques. Des réservoirs d'électrons, ions et particules α sont ainsi créés dans la queue de la magnétosphère ("plasma sheet") ou dans le "ring current" autour de l'équateur terrestre par exemple. La déstabilisation de ces réservoirs donnent lieu aux aurores polaires (Fig. 2.2) ainsi qu'à des perturbations des courants électriques circulant autour de la Terre (qui eux-mêmes modifient le champ magnétique terrestre induisant ainsi des courants dans les structures métalliques au niveau de la Terre).

Les flux radiatifs et particulaires sont étroitement liés à l'activité de notre étoile. Cette activité prend plusieurs aspects tant sur le plan temporel que spatial. C'est ce que nous allons décrire dans ce qui suit.

2.1.2 Activité solaire

L'activité solaire se manifeste à différentes échelles spatiales et temporelles. La plus grande échelle spatiale implique le soleil dans son ensemble. C'est tout d'abord le cycle solaire qui voit l'inversion des pôles magnétiques du soleil selon une périodicité d'environ 22 ans. Ce changement de polarité implique aussi des variations cycliques de l'organisation des vents solaires lent et rapide (qui vont couvrir des latitudes plus ou moins grandes en fonction de la phase d'activité).
La manifestation la plus visible du cycle solaire réside dans l'apparition d'un nombre de plus en plus grand de taches à la surface du soleil. Elles apparaissent d'abord à hautes latitudes en

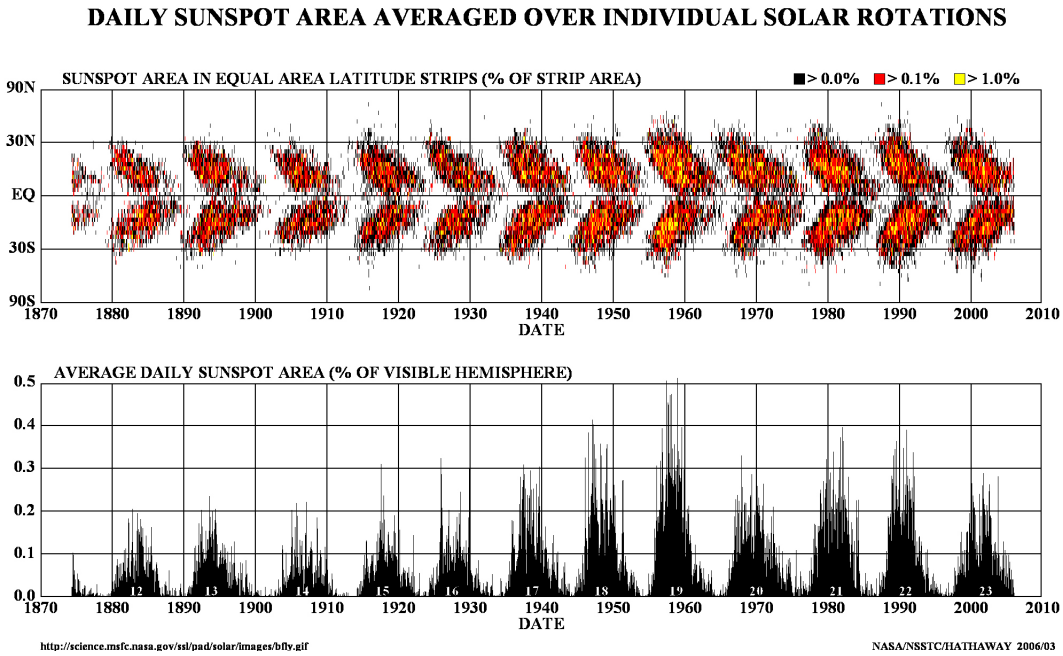

FIGURE 2.3 – Graphe supérieur : localisation de l'apparition des taches solaires en fonction de la latitude et du temps. Graphe inférieur : nombre de taches solaires observées en fonction du temps @NASA

début de cycle puis de plus en plus proche de l'équateur solaire, donnant lieu au "diagramme papillon" (Fig. 2.3), aussi appelé loi de Spörer.

Les taches solaires correspondent à l'émergence dans la photosphère de tubes de flux magnétique de plusieurs milliers de Gauss générés au niveau de la tachocline. Le cisaillement engendré par la variation de la vitesse du haut de la zone de radiation et du bas de la zone de convection ainsi que la rotation différentielle de la vitesse du soleil en fonction de la latitude rendent en effet possible le mécanisme de dynamo, convertissant ainsi l'énergie mécanique en énergie magnétique (pour une récente revue sur la dynamo solaire, voir Weiss and Thompson 2009).

Les taches solaires, d'une taille variant de quelques secondes à quelques minutes d'arc [3], ont une durée de vie variant de quelques heures à quelques semaines. Elles sont entraînées par la rotation du Soleil mais possèdent également une vie propre. La compréhension des mécanismes d'évolution de ces structures constitue l'un des enjeux majeurs de la physique solaire.

Souvent regroupées pour former des régions étendues (plusieurs minutes d'arc) et de fort gradient horizontaux de $\mathbf{B}$, elles sont à l'origine de phénomènes éruptifs brusques que nous appellerons – selon la terminologie anglaise – *flares*. Ces éruptions engendrent la libération dans l'atmosphère solaire de quelques 10^{25}J en quelques minutes. Ces flares produisent (i) des particules énergétiques, (ii) d'intenses rayonnements dans une très large gamme de longueur d'onde (notamment X, EUV et radio). Les particules sont accélérées jusqu'à atteindre des énergies de plusieurs centaines de MeV et se propagent dans le milieu interplanétaire à des vitesses allant de 0.1c à 0.6c. Elles parcourent donc 1UA en quelques heures.

Le second phénomène éruptif majeur (en termes d'énergie libérée) est appelé Ejection Coronale de Masse (ou CME pour l'acronyme anglais [4]). La découverte des CME est relativement

3. 1 seconde d'arc vue de la Terre représente environ 700 km sur la surface solaire
4. la terminologie anglaise est aussi souvent critiquée car la masse éjectée n'est pas uniquement d'origine

récente puisque la première observation date de 1971. Contrairement aux flares dont l'origine est relativement localisée, les CME s'étendent dès la basse couronne sur des distances excédant largement la taille d'une seule région active. Il est maintenant admis que la déstabilisation des filaments, qui s'étendent le long des lignes neutres entre deux régions de polarité opposée, joue un rôle fondamental dans le déclenchement des CME. L'onde de choc engendrée en amont des CMEs est à l'origine de l'accélération graduelle des particules (produisant des SEP pour *Solar Energetic Particles*) vers des énergies allant au-delà de 10MeV (et des densités pouvant atteindre 10^{10}particules/cm^2 pour les plus intenses). Se déplaçant à des vitesses allant de 20 à 2000km.s^{-1}, les CME mettent entre 1 et 3 jours pour parvenir dans l'environnement de la Terre.

Les prévisions de l'activité solaire sont requises sur plusieurs échelles de temps :
- Sur l'échelle d'un cycle (missions d'observation solaires ou missions d'exploration interplanétaire – habitées ou non) ;
- Sur des échelles de quelques jours (lancement de satellites, prévisions de maintenance, surveillance des satellites etc) ;
- Sur des échelles de quelques heures (sorties extra-véhiculaires, lancement de satellites etc) ;

Sur l'échelle d'un cycle, les questions qui se posent concernent la prévision de son amplitude, de la surface couverte par les taches (force du cycle) et de sa longueur. Les mécanismes détaillés conduisant à la régulation de ce cycle solaire sont loin d'être connus et les simulations numériques ne permettent pas encore de reproduire simultanément les différentes échelles spatiales concernées (depuis l'intérieur du Soleil jusqu'à l'émergence des taches au niveau de la photosphère). Les prévisions se basent donc sur des indicateurs dont la pertinence est une âpre source de débat. La figure 2.4 montre l'évolution des prévisions pour le prochain cycle. Il est clair que nous sommes encore loin de prévoir l'évolution des cycles ...

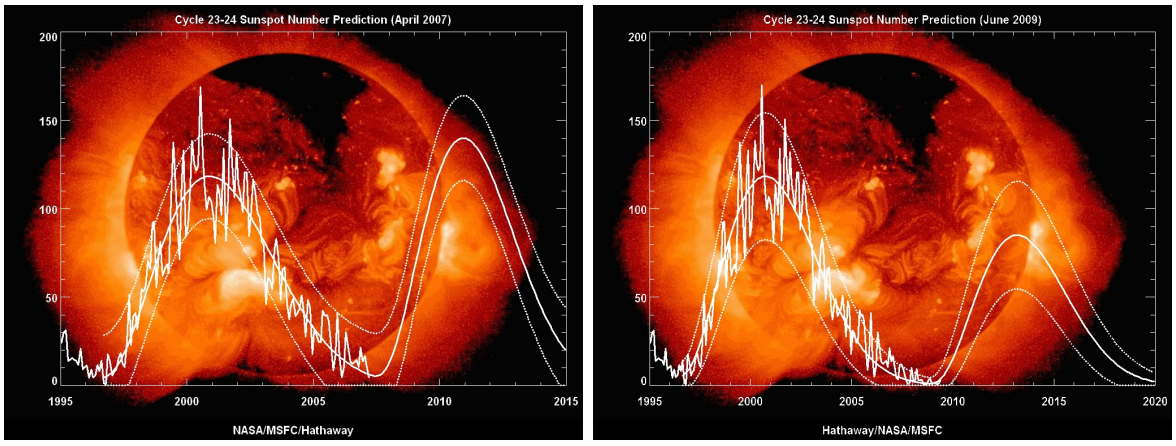

FIGURE 2.4 – La figure de gauche montre les prévisions réalisées en Avril 2007 et celle des gauche en Juin 2009. Crédit : Hathaway - NASA

A un niveau plus local, la prévision de l'évolution d'une région active n'est guère plus aisée et requière une compréhension complète des mécanismes d'émergence et d'évolution des structures magnétiques. Les questions qui se posent concernent alors l'heure de déclenchement d'une éruption, son intensité (en terme de rayonnement et de flux de particules) et la direction de propagation des particules. Une question sous jacente concerne la réponse de la magnétosphère

coronale

et des différentes couches atmosphériques terrestres à ces flux. Encore une fois, des simulations détaillées de chaque région active observée ne permettent pas des prévisions. On cherche encore une fois à utiliser des indicateurs (des *proxys*) plus faciles et surtout rapides à mesurer (et à fournir). Le choix du jeu d'indicateurs **pertinents** requièrent cependant une compréhension complète (i) des mécanismes d'accumulation de l'énergie ; (ii) des causes de déclenchement ; et (iii) les processus de transport de l'énergie et d'accélération des particules.

Dans la photosphère et la chromosphère, le rapport de l'énergie cinétique à l'énergie magnétique ($\beta \ll 1$) est tel que le champ magnétique joue un rôle fondamental dans la dynamique de la large majorité des structures solaires (voir les papiers de revue Briand 2003a,b). Le champ magnétique, généré au niveau de la tachocline, émerge en permanence au niveau photosphérique. Il apparait soit sous forme de petits tubes de flux magnétiques (sujet traité pendant ma thèse, ainsi que Briand and Solanki 1998) soit sous forme de taches solaires et de régions actives. L'émergence de nouveau flux magnétique dans une région avec un champ pré-existant engendre des déformations et des tensions des lignes de champ. De plus, le mouvement permanent des pieds des tubes de flux accroissent encore les cisaillements. Les régions actives sont ainsi des zones de forts déchirement des lignes de champ magnétique et de circulation d'importants courants électriques. Toutes ces conditions sont favorables au processus de reconnexion magnétique et permettent l'accumulation d'énergie magnétique pouvant être libérée lors des éruptions.

Un *flare* résulte en effet d'une réorganisation localisée de la topologie du champ magnétique s'accompagnant d'une libération d'énergie sous forme de chauffage du plasma et d'accélération de particules. Ceci se traduit par un accroissement de radiation dans le domaine γ, X, EUV-UV et également radio. Cette réorganisation est liée à la reconnexion des lignes de champ magnétique. A la base, pour que la reconnexion magnétique puisse avoir lieu il faut briser la condition de champ gelé et donc accroître localement la résistivité du milieu. La microphysique joue un rôle fondamental dans la modification de la résistivité (même si le détail des processus est loin d'être connu).
L'énergie libérée lors des éruptions est d'origine magnétique et provient de la composante non potentielle du champ. Celle-ci correspond à l'écoulement de courants électriques dans la couronne solaire. Il est donc fondamental de pouvoir quantifier l'écart d'une région active à une configuration potentielle. Pour cela, il faut être capable de mesurer les variations temporelles des composantes du vecteur champ magnétique ainsi que du vecteur vitesse pour en déduire les courants électriques et l'hélicité de courant. L'une des question fondamentale est de savoir comment cette énergie s'accumule. Deux directions sont suivies : (i) les tubes de flux émergent avec déjà des écoulements importants de courant électrique ; (ii) l'énergie est engendrée localement par cisaillement et torsion des tubes de flux engendrés par des mouvements sub-photosphériques *après* leur émergence à la surface du soleil.

Des modèles numériques montrent que les tubes de flux magnétiques constituant les régions actives doivent présenter un certain enroulement et cisaillement. Ainsi, des études basées sur des simulations 2D et 3D (Moreno-Insertis et al. 1994; Emonet and Moreno-Insertis 1998; Dorch et al. 1999) montrent que l'enroulement des lignes de champ autour de l'axe principal du tube permet de maintenir sa cohésion lors de la traversée de la zone de convection jusqu'à la photosphère. Ces modèles donnent ainsi des limites sur les orientations du champ émergeant au niveau photosphérique, valeurs qui peuvent être confrontées aux observations, aidant ainsi à la validation – ou non – de ces modèles de déstabilisation des tubes de flux. La mesure des composantes du champ magnétique dès son émergence au niveau photosphérique impose des contraintes sur les modèles de dynamo d'une part et de transport dans les couches solaires internes d'autre part. Elle est aussi essentiel pour mesurer le degré de tension des lignes de champ magnétique

et comprendre le rôle des couches supérieures de l'atmosphère solaire dans le processus d'accumulation d'énergie. Les résultats de ma contribution sur le sujet sont présentés en section 2.2.2.

La mesure du vecteur champ magnétique est relativement aisée dans les régions actives au niveau de la photosphère : l'hypothèse d'un équilibre thermodynamique local est souvent justifiée (simplifiant ainsi énormément l'interprétation des raies et les codes d'inversion), le champ est suffisamment fort (la levée de dégénérescence des niveaux d'énergie est suffisante pour bien mesurer la polarisation des raies par effet Zeeman), le flux radiatif est encore suffisant pour que le rapport signal/bruit soit élevé (les trois composantes du champ magnétique peuvent ainsi être déduits). Mais pour modéliser les éruptions, l'idéal serait de connaître le champ magnétique au niveau coronal. Cependant, la déduction de ce champ [5] est beaucoup plus compliquée (milieu Hors-ETL, champ magnétique faible, flux radiatif faible). Seule la norme du champ est disponible via des mesures radio (effet cyclotron). Or les modèles ont besoin du **vecteur** champ magnétique. La plupart des études sur les éruptions coronales reposent donc sur des extrapolations de champ magnétique. Les hypothèses sur lesquelles reposent ces extrapolations ne sont toutefois pas toujours justifiées, surtout dans les régions éruptives (par exemple l'hypothèse de champ potentiel).
A défaut de mesures coronales, les tentatives de déduction du champ magnétique chromosphérique se multiplient. La tâche n'est pas simple : tout comme dans le couronne, la formation des raies concernées est souvent plus compliquée (hors ETL, redistribution partielle etc), les flux magnétiques et radiatifs sont relativement faibles. Les résultats sur la détermination du champ magnétique chromosphérique sont présentés en section 2.2.3.

Une façon de mesurer l'enroulement du champ magnétique est de déduire l'hélicité de courant des mesures du vecteur $\mathbf{B}$:

$$H_c = B \cdot (\nabla \times \mathbf{B}) \tag{2.1}$$
$$\nabla \times \mathbf{B} = \mu_0 \mathbf{j} \tag{2.2}$$

Très peu de travaux existent sur le sujet du point de vue observationnel. Cela tient à plusieurs difficultés de nature différentes :

1. déterminer les composantes du champ magnétique, et notamment résoudre l'ambiguité de 180° de la composante transverse du champ ;
2. calculer le courant électrique dans des régions à fort gradient magnétique ;
3. Observationnelle : les changements de seeing (résolution spatiale) induisent des variations de détection des structures magnétiques pouvant conduire à des conclusions erronnées sur les variations temporelles des courants (ou leur neutralité)

Le dernier point est cependant maintenant en partie résolu grâce aux observations d'Hinode (Solar B) dont l'instrument *Solar Optical Telescope* (SOT) offre la possibilité de mesures de polarisation avec une résolution spatiale constante sur de longues périodes temporelles. Je présente en section 2.2.4 les résultats obtenus sur la détermination de l'hélicité magnétique dans des régions actives.

5. aucune mesure *in situ* n'est encore possible

2.1.3 Observations : requis et contraintes

Les échelles spatiales et temporelles caractéristiques des structures solaires varient souvent de plusieurs ordres de grandeur (voir table 2.1).

Pour aborder les questions de dynamique et d'évolution des taches solaires, régions actives ou filaments, il faut des instruments capables d'offrir :

a - de la haute résolution spatiale (≤ 0.5") pour voir des détails des régions (mais pas uniquement – voir remarque complémentaire ci-dessous) ;

b - de la haute résolution spectrale (R$\geq 5.10^5$) afin de contraindre de nombreux paramètres thermodynamiques (température, densité, vitesse) ;

c - de la haute résolution temporelle (les valeurs sont ici très variables et dépendent de nombreux facteurs liés d'une part à la durée de vie de la structure observée mais également à la technique d'observation) ;

d - une couverture spatiale étendue : soit pour observer la région active dans son intégralité, soit pour donner le contexte d'une observation à très haute résolution spatiale ;

e - de la haute précision polarimétrique (S/I $\leq 10^{-3}$) afin de mesurer toutes les composantes du champ magnétique et abaisser le seuil de détection de $\mathbf{B}$;

f - de la spectroscopie multi-raies afin de mesurer à différentes hauteurs dans l'atmosphère solaire et/ou apporter des contraintes différentes sur certains paramètres thermodynamiques ;

g - un domaine spectral le plus étendu possible du bleu (mesure du champ magnétique turbulent par effet Hanle) vers l'infra-rouge (mesure du champ magnétique chromosphérique par effet Zeeman).

La recherche d'une bonne résolution spatiale correspond à deux impératifs complémentaires : (a) voir le détail des structures le plus précisément possible ; (b) augmenter la sensibilité polarimétrique. Si le premier point est assez naturel, le second l'est moins.
Un instrument disposant d'une fonction d'étalement (*Point-Spread Function* ou PSF) piquée permet de dépasser le seuil de détection en concentrant le signal sur le pic central (voir Fig. 2.5). Autrement dit, des signaux de faible intensité pourront être détectés (Lee et al. 1997). Par ailleurs, si l'étalement des signaux est trop important, les profils des paramètres de Stokes sont artificiellement mélangés conduisant par exemple à la détection de polarité mixte alors qu'il ne s'agit que d'un effet instrumental (voir Fig. 2.6 extrait de Sigwarth 2001). Donc, l'apport d'une optique adaptative dans le cas d'un télescope dédié à des mesures polarimétriques ne se limite

TABLE 2.1 – Durée de vie et échelle caractéristique de quelques structures solaires (photosphère et chromosphère uniquement). La dernière colonne indique si des structures d'échelle spatiale plus petite que l'échelle caractéristique sont susceptibles d'apparaître

Structure	Durée de Vie	Echelle spatiale	Structure fine
Tube de flux	5 min	≤ 0.1"	?
Granulation	5 min	1"	oui
Pores	Heures	qq×10"	oui ($\leq$ 1" ?)
Tache solaire	qq heures à qq jours	qq ×100"	oui ($\leq$ 1")
Filament	qq heures à qq jours	qq ×100"	oui ($\leq$ 1")

pas uniquement à voir des détails des structures mais aussi (et surtout !) permet d'accroître la sensibilité polarimétrique et évite des interprétations erronées des profils de Stokes comme illustré Figure 2.6.

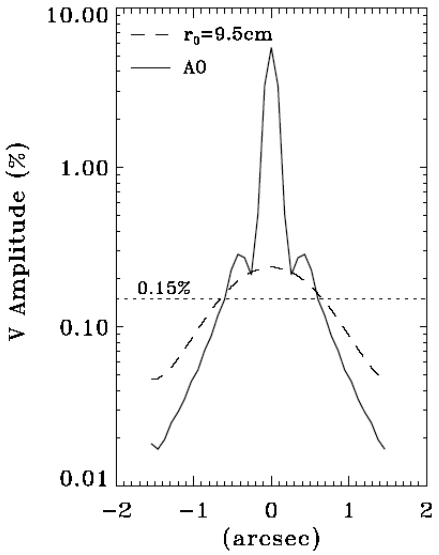

FIGURE 2.5 – Illustration du gain en rapport signal/bruit d'une mesure de polarisation pour deux PSF de largeur différente. Le seuil de détection des signaux polarimétriques (ligne horizontale pointillée) est à peine dépasser pour un instrument de PSF large (courbe en tiret, correspondant à un instrument limité par un seeing de 1") alors que l'intensité du signal est concentré avec un instrument profitant d'une optique adaptative. From Sigwarth (2001)

Il est clair que l'ensemble des contraintes observationnelles (a–g) ne peuvent être levées par un seul instrument. Des mesures simultanées par plusieurs instruments post-focaux peuvent cependant permettre de s'approcher de mesures idéales.
L'instrument idéal ? un télescope avec une optique adaptative alimentant des instruments post-focaux travaillant en parallèle. Ces instruments doivent être :
– un spectrographe permettant l'observation simultanée de 2 à 4 domaines spectraux : on acquiert une haute résolution spectrale, et en limitant l'extension spatiale du champ observé on peut gagner sur la résolution temporelle (qui n'est pas le point fort de la spectroscopie) ;
– une à deux caméras grand champ avec filtre à bande étroite : pour obtenir le contexte photosphère-chromosphère. La très haute résolution spatiale peut être obtenue par des techniques de post-processing telles que speckle ou phase diversity ;
– un Fabry-Perot : utile pour des mesures de vitesse sur des grands champs ainsi que des cartes de champ magnétique sur des zones étendues ;
A cela, on doit ajouter une à deux lignes de lumière libre pour recevoir des instruments invités et permettre des développements instrumentaux nouveaux. Comme on le voit, tous les instruments bénéficie de la correction d'image de l'optique adaptative. L'ajout d'un polarimètre en instrument pré-focal permet d'alimenter tout ou partie des instruments post-focaux pour des mesures de polarisation.

La multiplication des surfaces optiques, la séparation de faisceaux et leur dispersion, engendrent des pertes importantes en terme de photons. D'où la nécessité aussi pour les observations solaires de se diriger vers des télescopes de grand diamètre. Le projet *European Solar Telescope*

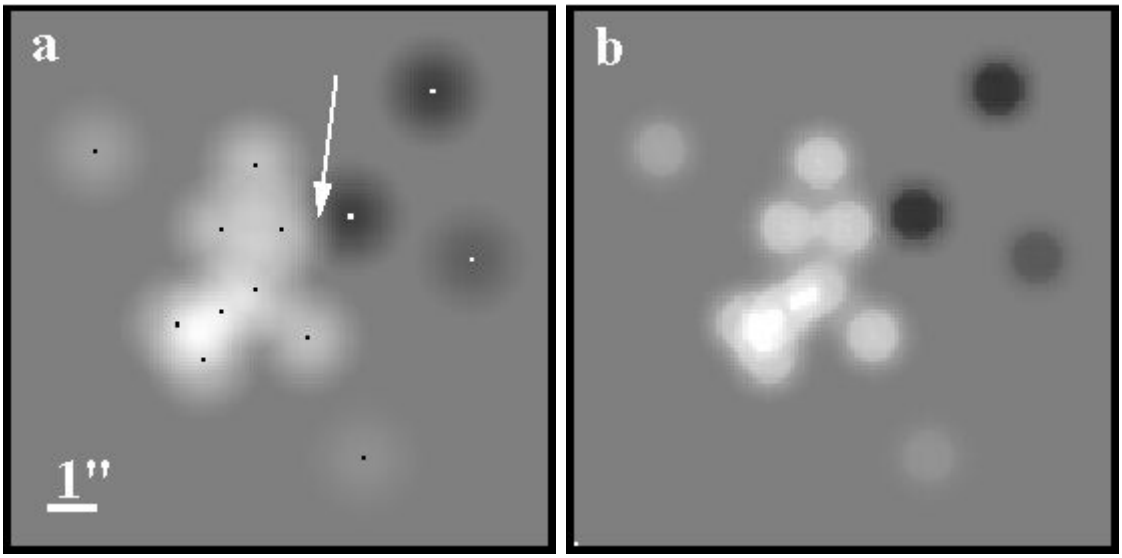

FIGURE 2.6 – Apparence de tubes de flux magnétiques depuis une PSF correspondant à un seeing de 1" (à gauche) et à un système d'optique adaptative de bas ordre (15 premiers termes de correction), à droite. Dans le premier cas, les signaux sont artificiellement mélangés – au niveau de la flèche – conduisant à des profils de Stokes asymétriques. Extrait de Sigwarth (2001)

(EST) s'inscrit parfaitement dans cette ligne. Il est à souhaiter que ce projet aboutisse rapidement de façon à maintenir la communauté solaire européenne à la tête de la recherche dans ce domaine.

2.2 Résultats

2.2.1 Traitement des données

La mesure de la polarisation des raies spectrales permet de déduire les caractéristiques du champ magnétique ainsi que certains paramètres thermodynamiques du milieu. Différents exemples sont présentés dans les sous-sections suivantes. Toutefois, la déduction des paramètres de Stokes d'une raie est délicate. Je détaille maintenant les mesures spectro-polarimétriques qui ont servi pour mes études. Cette introduction met notamment en avant les difficultés que l'on peut rencontrer lors de telles mesures et permet de comprendre leurs limitations.

Avant cela, rappelons brièvement la terminologie utilisée pour décrire la polarisation d'une onde électromagnétique. La polarisation d'une onde est décrite à partir d'observables connues sous le nom de paramètres de Stokes (du nom du chercheur anglais George Gabriel Stokes qui les introduisit en 1852). Il s'agit d'un vecteur à quatre composantes, traditionnellement écrit I, Q, U et V. La composante I donne l'intensité totale (quelque soit le degré de polarisation) du faisceau. Les composantes Q et U donnent la polarisation linéaire à $\pm 45°$. La composante V décrit la polarisation circulaire. Pour une onde partiellement polarisée, nous avons la relation :

$$\sqrt{U^2 + Q^2 + V^2} \quad < \quad I \tag{2.3}$$

L'égalité entre les deux termes traduit une onde totalement polarisée. Une description détaillée de la polarisation des ondes électromagnétiques est donnée dans Collett (1992) .

Soit $S = (I, Q, U, V)$ le vecteur de polarisation solaire et $S' = (I_1, I_2, I_3, I_4)$ le vecteur de polarisation observé. S et S' sont reliés par la matrice de modulation M de l'ensemble optique (télescope, optique de transfert, polariseur) avant la mesure de polarisation. Cette matrice décrit les relations linéaires entre les paramètres de Stokes du rayonnement solaire :

$$S' \quad = \quad MS \tag{2.4}$$

Connaissant M, il est possible d'inverser la matrice pour obtenir S, la polarisation d'origine recherchée.
La matrice M doit inclure la modulation introduite par toutes les surfaces optiques situées en amont de la mesure de polarisation (miroirs et polarimètre). Dans le cas d'un coelostat, la connaissance de M est une tâche délicate qui requiert notamment de nombreux étalonnages instrumentaux pendant les observations et des modélisations du télescope (voir par exemple Skumanich et al. 1997). Dans le cas du télescope THEMIS, la mesure de polarisation est effectuée au niveau du foyer primaire du télescope, avant tout miroir incliné. La modulation provient alors essentiellement du polarimètre [6]. Les mesures de polarisation sont effectuées par rotation successive de deux lames $\lambda/4$. L'équation 2.4 montre qu'il suffit de 4 mesures de polarisation (donc 4 positions de lame) pour inverser la matrice. Afin d'optimiser à la fois le temps de mise en place des lames et réduire les franges d'interférence, la séquence optimum d'observation s'est avérée être la suivante : +Q (0,0), -Q (45,45), +U (22.5,22.5) et +V (-45,0), où les chiffres entre parenthèses indiquent l'angle des lames quart d'onde avec l'axe du polariseur. A titre d'illustration, l'équation 2.4 pour la raie λ6302Fe I et la séquence de mesure décrite précédemment devient :

6. La polarisation introduite par la lame d'entrée du télescope n'a, à ma connaissance, jamais été une limitation aux mesures

$$\begin{pmatrix} I+Q \\ I-Q \\ I+U \\ I+V \end{pmatrix} = \begin{pmatrix} 1 & 1 & 0 & 0 \\ 1 & -0.994 & 0 & 0.0348 \\ 1 & 0.0003 & 0.9997 & 0.0247 \\ 1 & 0.0175 & 0 & -0.9998 \end{pmatrix} \cdot \begin{pmatrix} I \\ Q \\ U \\ V \end{pmatrix} \tag{2.5}$$

ce qui conduit aux paramètres de Stokes suivants :

$$\begin{pmatrix} I \\ Q \\ U \\ V \end{pmatrix} = \begin{pmatrix} 0.4912 & 0.4917 & 0 & 0.0172 \\ 0.5089 & -0.4917 & 0 & -0.0172 \\ -0.0377 & -0.5036 & 1.003 & 0.0071 \\ 0.5001 & 0.4832 & 0 & -0.9833 \end{pmatrix} \cdot \begin{pmatrix} I+Q \\ I-Q \\ I+U \\ I+V \end{pmatrix} \tag{2.6}$$

Cette équation montre clairement que :
- le cross-talk entre paramètres de Stokes peut-être important même dans le cas du Stokes I (par exemple dans certaines zones de régions actives où V peut être important) ;
- 4 mesures sont nécessaires et suffisantes pour une détermination précise des paramètres de Stokes ;
- la matrice de modulation dépend fortement des raies. Même dans le cas le plus optimisé (ce qui est le cas pour la raie du Fer considérée ici), le cross-talk entre paramètre de Stokes est non négligeable. Donc, avoir un polarimètre avec des positions fixes successives ou un modulateur tournant en continu sont des configurations équivalentes [7]. L'essentiel est de bien connaître la matrice de modulation

Quelque soit la configuration du polarimètre, 4 mesures sont nécessaires. Le seeing introduit des fluctuations du front d'onde pendant et entre deux observations successives. Ceci implique qu'un pixel peut recevoir des mesures provenant de sources solaires différentes. Donc, quand on applique la démodulation sur les quatre mesures successives on ne combine pas des informations provenant de la même source. C'est ce que l'on appelle le *seeing induced cross-talk*. Pour s'affranchir de cet effet, nous utilisons le fait que deux faisceaux de polarité opposée sont enregistrés simultanément sur une même caméra. Chaque faisceau est constitué par le même champ solaire (voir commentaire sur ce point un peu plus loin), et est enregistré sur deux parties distincts de la caméra. Autrement dit, si nous avions mesuré la séquence I+Q, I-Q, I+U, I+V sur la partie 'haute' de la caméra, nous enregistrons la séquence I-Q, I+Q, I-U, I-V sur la partie 'basse'. Après démodulation, les deux spectres sont donc les négatifs l'un de l'autre pour tous les signaux de polarisation *réels* mais sont identiques pour toutes les régions où la diaphonie induite par le seeing intervient. En soustrayant encore les deux spectres, il est possible de retirer cette fausse polarisation et de ne garder que le vrai signal (voir Fig.2.7).

Pour que la démodulation et la correction de seeing induced cross-talk aient un sens, il faut que les images soustraites proviennent du même champ solaire. Cette condition n'est cependant pas complètement garantie compte tenu de la configuration du spectrographe. Les deux faisceaux sont séparés à l'entrée du spectrographe, les deux polarisations empruntant dès lors des chemins optiques différents et sont interceptés par deux fentes indépendantes. Des erreurs de l'ordre de 2% sur le champ sélectionné sont possibles et varient au cours du temps (dû à la dilatation relative des pièces mécaniques et optiques dans les bras de renvoi vers le spectrographe). Seule

7. du point de vue de la précision de la mesure. L'un ou l'autre des deux système peut s'avérer cependant plus rapide

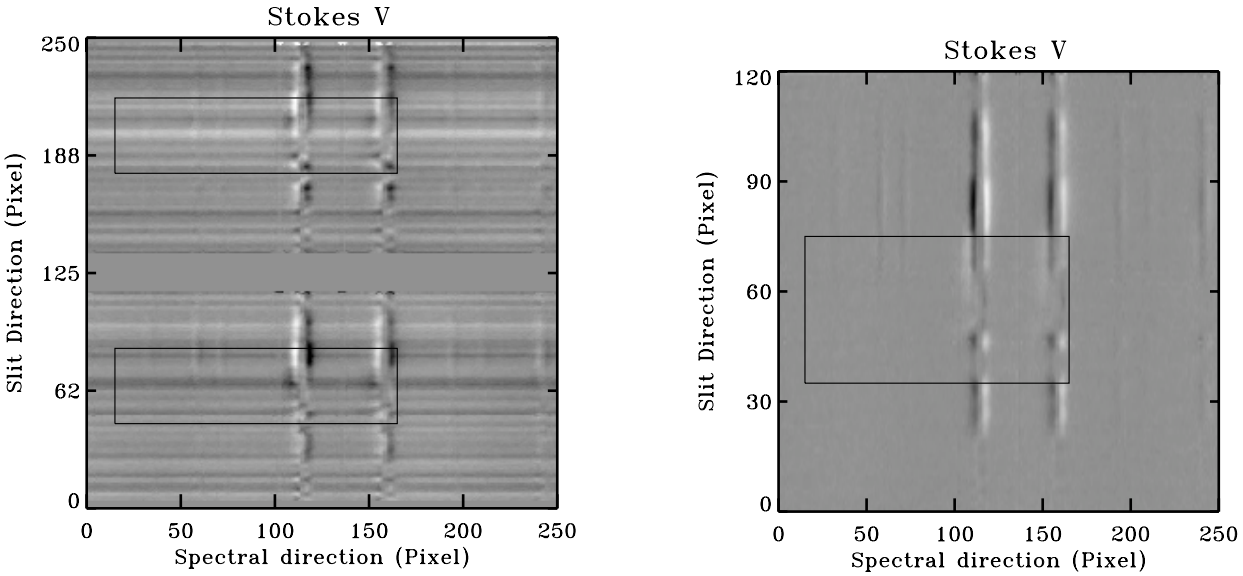

FIGURE 2.7 – Seeing induced cross-talk. Figure de gauche : une même région solaire observée sur une même caméra après démodulation. Les deux polarités sont opposées. On note la présence de signal dans le continu de la raie et des signaux de polarisation dans la raie même (à l'intérieur du cadre rectangulaire par exemple). Figure de droite (agrandie pour bien voir le résultat) : après soustraction des deux images on s'aperçoit que tous ces signaux ont disparu. Il s'agissait de seeing-induced cross-talk.

la configuration avec une grille au niveau du polariseur (pour sélectionner la région observée) et une fente unique à l'entrée du spectrographe permet de s'affranchir de ce défaut. Si ce mode semble idéal, la dérive d'image observée au niveau du foyer secondaire (voir aussi 2.3.2) en réduit l'efficacité pour des régions actives étendues. Le spectrographe et le polarimétre de THEMIS ont été décrits dans de nombreux articles et exposés à la communauté lors de congrès (voir par exemple Arnaud et al. 1996; Ceppatelli and Briand 2001, 2002; Briand and Ceppatelli 2002; Ceppatelli and Briand 2003).

Comme nous venons de le voir, la mesure de polarisation peut être polluée par beaucoup de facteurs. La réduction de données spectro-polarimétriques est donc une tâche délicate.
La réduction peut se décrire par la succession de trois étapes :

1. Suppression des défauts de l'image (poussières, franges) et correction de la courbure des raies spectrales ;
2. Calibration des caméras (gain de chaque pixel) ;
3. Démodulation des observations
4. Correction du seeing induced cross-talk

Les détails de corrections successives sont présentés dans Briand and Aboudarham (2002); Briand and Vecchio (2003).
Le code de réduction que j'ai développé est adapté pour deux des trois modes d'observation polarimétrique offerts par THEMIS : le mode dit "2x1' " et le mode grille. La réduction des données en temps (quasi) réel pendant les campagnes d'observation (ce que le code de réduction permet) est un avantage énorme afin d'optimiser les observations en fonction de la structure magnétique d'une région ou de vérifier le pointage lors de campagnes coordonnées.

Les observations ont été principalement réalisées au télescope franco-italien THEMIS mais également au Vacuum Tower Telescope (VTT, construit et exploité par des équipes allemandes) et au Dutch Open Telescope (opéré par les collègues Hollandais) pour obtenir des images grand champ en lumière blanche et en bande G des régions observées.
J'ai utilisé dans la plupart des observations les raies 630.1nm et 630.2nm du FeI, les plus sensibles à l'effet Zeeman dans le spectre visible. Elles étaient complétées par des raies chromosphériques (typiquement Hα ou CaII à 854.2nm).

2.2.2 Emergence de flux magnétique

Article de référence : Mein et al. (2000)

Les systèmes de filaments en forme d'arches (Arch Filament Systems) apparaissent dans les premiers moments de l'évolution d'une région active. lls relient généralement des taches de polarité opposée. Ils sont la signature de l'émergence de flux magnétique depuis la photosphère. Si la durée des filaments individuels n'est que de quelques dizaines de minutes, le système d'arches se maintient pendant toute la durée d'émergence de flux magnétique, c'est-à-dire jusqu'à plusieurs jours. Les pieds de ces filaments sont souvent brillants, laissant à penser qu'un important dépôt d'énergie s'y produit. Les modélisations basées sur des observations en Hα permettent de montrer que des écoulements vers la photosphère se produisent pendant toute la phase d'émergence des lignes de champ (qui, elles, se déplacent donc vers la chromosphère). Toutefois, les paramètres thermodynamiques tels que température et densité ne peuvent pas être déduits à partir de la raie de l'hydrogène seule. Nous avons montré que l'observation simultanée de la raie chromosphérique du CaII λ8542 permettait de contraindre efficacement les modèles, cette raies étant très sensible à ces deux paramètres.

Article de référence : Briand et al. (2002)

La région NOAA 9716 a été observée simultanément avec THEMIS (mode spectro-polarimétrique) et le Dutch Open Telescope (DOT). Il s'agit d'une région β en phase de décroissance. Au sein de cette région, nous nous sommes particulièrement intéressés à une zone d'émergence éphémère de champ magnétique.
L'exemple présenté en Figure 2.8 montre les cartes de flux magnétique (en couleur) obtenues à trois instants différents. Elles mettent en évidence l'émergence d'une région magnétique de fort champ magnétique (1500G), de courte durée (1h) associée à une augmentation importante de la température (8000K contre 6000 dans les régions avoisinantes). Il est important de noter qu'aucune signature de l'émergence de ce champ n'est observable sur les images obtenues en bande G par le DOT (observations coordonnées – images de droite). Ces zones sont souvent estimées à partir d'images en lumière blanche. L'exemple précédent montre que nous pouvons manquer les premières phases de l'émergence du champ.

2.2.3 Champ magnétique photosphérique et chromosphérique

Articles de référence : Briand and Martínez Pillet (2001); Briand and Vecchio (2003)

Le cas des raies formées hors-ETL (typiquement les raies chromosphériques) ou présentant des phénomènes de redistribution partielle de l'énergie au sein de la raie (Uitenbroek and Briand 1995) sont plus complexes à traiter. Afin de déduire *l'intensité* du champ magnétique

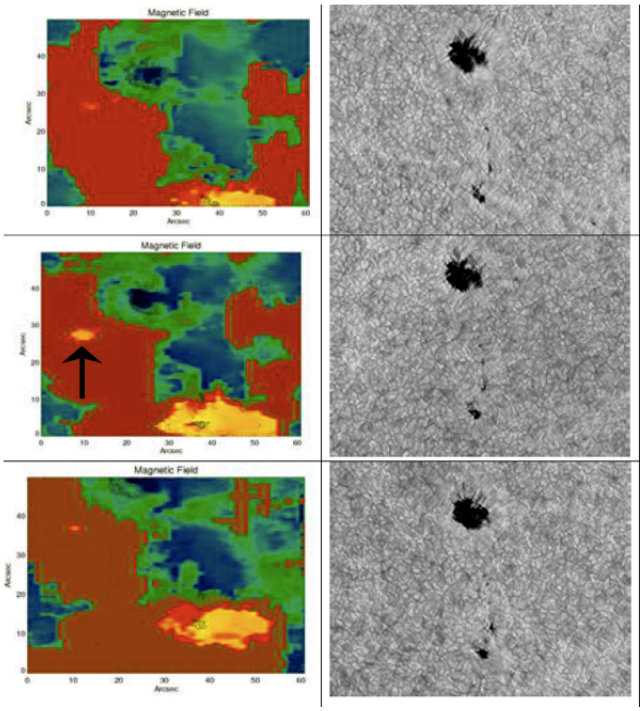

FIGURE 2.8 – A gauche : carte de champ magnétique autour d'un pore ; A droite : Image en bande G de la région observée. Sur le panneau de gauche, la flèche indique l'apparition d'une zone de champ magnétique vertical sans contrepartie visible sur les images de droite

nous utilisons alors l'approximation du champ faible (Solanki 2003) qui exprime l'intensité du paramètre de Stokes V à partir de l'intensité observée :

$$V = 4.10^{-13}.g_{eff} \times B.cos(\theta)\frac{\partial I^M}{\partial \lambda} \tag{2.7}$$

avec g_{eff} le facteur de Landé, θ l'inclinaison du champ magnétique sur la ligne de visée ($\theta = 0$ si le champ est le long de la ligne de visée et dirigé vers l'observateur), λ la longueur d'onde et I^M l'intensité observée provenant d'une région magnétique. Il est en effet important de noter que seule la région magnétique contribue à V. Or, l'intensité observée est une combinaison linéaire de l'intensité provenant de la région avec champ magnétique et de celle de la région non magnétique :

$$I = \alpha I^M + (1-\alpha)I^{NM} \tag{2.8}$$

Le facteur α appelé facteur de remplissage (filling factor en anglais) donne le pourcentage de la région magnétique dans la zone observée. La différence entre un spectre V observé et un spectre synthétisé via l'équation 2.7 permet de déduire que la région n'est pas purement magnétique (voir par exemple Briand and Martínez Pillet 2001). Le champ magnétique s'ouvrant avec l'altitude [8], le facteur de remplissage est proche de 1 pour les raies formées dans la chromosphère. Cette méthode donne accès à l'intensité du champ le long de la ligne de visée (par définition

8. conséquence de la conservation de la pression :

$$P_{int} + B^2/8\pi = P_{ext}$$

la pression gazeuse extérieure diminuant avec l'altitude ainsi que l'intensité du champ magnétique, la pression intérieure au tube de flux augmente produisant un évasement du tube avec l'altitude

du paramètre de Stokes V) mais pas aux composantes du champ. C'est une limitation. Si des mesures des quatre paramètres de Stokes peuvent être menées sur les raies chromosphériques, peu de codes permettent de les exploiter pleinement.

Dans leur article Martinez Pillet et al. (1994) ont montré la présence d'un flot supersonique dirigé *vers* la photosphère dans l'environnement d'une tache solaire isolée. Il était donc intéressant de comprendre l'origine de ce flot en comparant à des raies formées plus haut dans l'atmosphère solaire. Les observations menées à partir de l'Advanced Stokes Polarimeter installé au Vaccum Tower Telescope de Sacramento Peak (Elmore et al. 1992) comprenaient des raies du Fer mais également les raies Mgb_1 et Mgb_2. Ces deux raies sont formées dans la région du minimum de température. Les vitesses ont été déduites des paramètres de Stokes I et V via le déplacement du centre de la raie et du "zero-crossing". Les cartes de vitesse de la région du minimum de température ainsi déduites ne montrent pas la présence de flot supersonique : les valeurs restent dans la gamme $\pm 2 \mathrm{km.s}^{-1}$. Ce flot est ainsi principalement limité à la zone photosphérique. L'asymétrie des profils de Stokes V confirment la présence de structures fines, éventuellement confinées dans la partie *non magnétique* (voir aussi Briand and Solanki 1998).

La présence d'inversion de polarité du champ magnétique entre la photosphère et la chromosphère a été citée dans certains articles (Wang and Shi 1992; Li et al. 1994). Sanchez Almeida (1997) a toutefois montré de façon théorique que cette inversion pouvait simplement résulter du passage en émission du coeur de la raie chromosphérique. Nous avons voulu tester cette hypothèse à partir d'observations de deux raies photosphériques (raies du fer $\lambda 6301, 6302$) et de deux raies chromosphériques dont la réponse à une échauffement local de l'atmosphère est différent : la raie Hα et la raie du calcium $\lambda 8542$. Le paramètre de Stokes V de la raie du calcium semble indiquer une polarité opposée entre la photosphérique et la chromosphérique. Une telle inversion de polarité n'est cependant pas réelle et résulte effectivement du passage en émission du coeur de la raie chromosphérique : la raie Hα ne présente pas d'inversion de polarité. Il est important de noter que même une émission très faible de la raie du calcium peut conduire à une inversion 'apparente'. Il est donc fortement recommandé d'utiliser une deuxième raie chromosphérique pour confirmer (ou non) une inversion de polarité observée.

2.2.4 Courant électrique, non potentialité et hélicité

Résultats non publiés

Des codes de transfert de rayonnement ou d'inversion existent pour les raies formées à l'Equilibre Thermodynamique Local (ETL) – cela concerne de nombreuses raies photosphériques.
Pour déduire la stratification des paramètres thermodynamiques (température, vitesse, pression) et magnétiques (intensité et orientation du champ, facteur de remplissage) du milieu à partir des données spectro-polarimétriques, j'ai utilisé le code d'inversion « SIR » ("Stokes Inversion based on Response functions" Ruiz Cobo 1998). Ce code adapte les paramètres du milieu (à partir d'un modèle donné) pour ajuster au mieux les quatre paramètres de Stokes d'une raie à partir des fonctions réponses des raies aux différents paramètres. Cette technique permet d'optimiser l'ajustement des paramètres thermodynamiques à certaines hauteur dans l'atmosphère. La restriction du code utilisé est de travailler en plan parallèle et à l'équilibre thermodynamique local, ce qui n'est pas une contrainte pour les raies que nous avons considérées (voir section 2.1.3). Les paramètres de Stokes Q et U sont souvent plus bruités que I et V. Ce sont eux qui vont limiter l'intensité minimale du champ magnétique déduit. Typiquement, les inversions ont été effectuées pour les spectres pour lesquels le maximum de Q/I ou U/I ou V/I

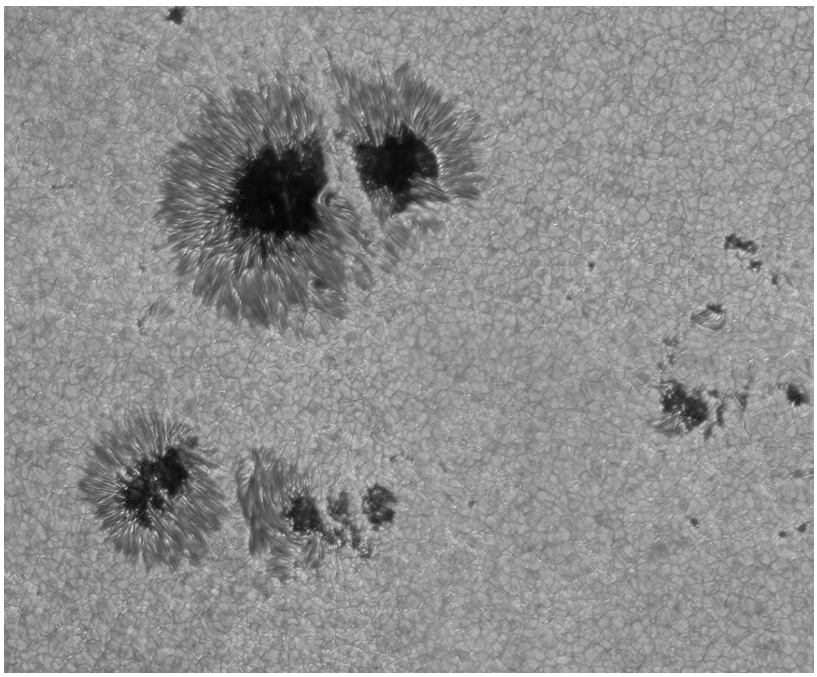

FIGURE 2.9 – Observation en lumière blanche de la région NOAA10019 suivie entre le 3 et le 6 Juillet 2002 lors d'une observation conjointe entre le DOT et THEMIS. Des observations de TRACE sont venues apportées de informations complémentaires sur l'évolution coronale de la région

est supérieur à 8.10^{-3}, ce qui correspond à un champ d'environ 400 Gauss.

Le calcul de l'hélicité d'une région active est une tâche particulièrement délicate puisqu'elle implique la détermination des composantes du champ magnétique (notamment horizontales) dans le repère local du Soleil (les observations donnent des résultats dans le repère de l'observateur).

La difficulté est aussi intrinsèque à la région : configuration magnétique compliquée (gradient horizontaux de champ magnétique) voire complexe (impliquant des relations étroites avec les couches atmosphériques supérieures). Suivre l'évolution temporelle suppose en plus d'avoir les mêmes conditions de résolution spatiale d'une observation à l'autre. L'atmosphère terrestre perturbe les observations sur des périodes très inférieures à celle de l'évolution intrinsèque de la région.

J'ai développé un code pour déterminer l'hélicité à partir de l'inversion des données spectro-polarimétriques sur les raies photosphériques. Les premiers résultats sont encourageants (voir Fig. 2.10). Les résultats n'ont pas été publiés car les variations de courant déduits peuvent aussi être imputées à des variations des conditions atmosphériques terrestres. THEMIS ne possédant pas d'Optique Adaptative ni même de tip-tilt au moment des observations, les doutes subsistent quant à la réalité des résultats. Ces travaux montrent toutefois qu'avec une meilleure stabilisation de l'image des résultats importants pourraient être obtenus.

L'étude de l'évolution temporelle des régions actives est une tâche délicate qui bénéficiera grandement du développement de l'imagerie polarimétrique (des instruments comme POLIS ou IBIS) permettant d'observer de grandes zones en des temps courts par rapport au temps d'évolution propre des structures (dans le cas d'un flare, quelques minutes). La résolution spectrale peut en effet être en partie sacrifiée pour des études exploratoires au profit du champ et

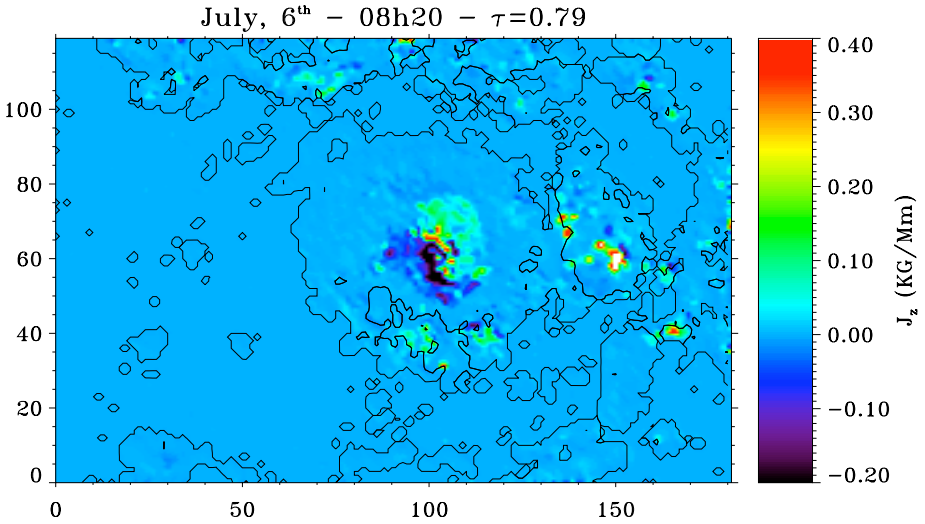

FIGURE 2.10 – Courant électrique J_z autour de la tache principale, le 6 Juillet 2002 à 08 :20. Les axes sont en secondes d'arc. Les contours des taches et zones magnétiques – telles que déduites de l'inversion des données – sont représentées en noir

de la résolution temporelle.
La spectro-polarimétrie (donnant une résolution spectrale beaucoup plus importante) doit venir en complément pour explorer des régions d'extension spatiale limitée dans des zones particulièrement critiques comme les régions de changement de polarité, toujours propices à des reconnexions et des échanges d'énergie entre la photosphère et la chromosphère.

2.3 Dévelopements instrumentaux

En tant qu'astronome de support à THEMIS, une très forte partie de mon travail a consisté en un suivi instrumental du télescope : caractérisation de certains modes de fonctionnement du télescope et proposition de développement nouveau. Je présente ici quatre domaines pour lesquels mes travaux ont conduit à des améliorations techniques de l'instrument ou/et à une meilleure connaissance de son fonctionnement. Ils ne représentent cependant pas – loin s'en faut – l'intégralité des thèmes sur lesquels j'ai travaillé.

2.3.1 Caméras CCD

Articles de référence : deux rapports internes (**Briand C.** Ziegler D., 1998, 33 pages, 32 figures ; **Briand C.**, Aumar F., Ziegler D., Lemen C., 1999, 19 pages, 15 figures)

Le mode « spectro-polarimétrie » de THEMIS était équipé de 16 caméras CCD. Elles ont

été montées avant même d'être complètement qualifiées. En 1998 et 1999, deux campagnes spécifiques ont été menées avec D. Ziegler (concepteur de l'électronique) pour caractériser leur fonctionnement en interface avec le reste de l'instrument (et notamment le système d'acquisition et de refroidissement). Ces travaux ont permis de :

- Mettre en évidence des défauts dans le système de refroidissement des caméras elles même et de celui du télescope. Des solutions correctives ont par la suite été apportées aux deux systèmes ;
- Mettre en évidence des problèmes de stabilité du courant d'obscurité. Ces travaux ont été par la suite repris par les ingénieurs pour apporter des corrections sur les alimentations des caméras ;
- Ajuster les gains de chaque caméra ;
- Détecter et corriger les défauts d'acquisition provenant des caméras elles même ou de la gestion par les cartes de la baie d'électronique ou du VME.

Une demande pour des nouvelles caméras CCD a été déposée durant le FP6 par un consortium formé par tous les opérateurs des télescopes solaires installés aux Canaries. L'idée était d'équiper tous les télescopes avec des caméras similaires de façon à en faciliter les dépannages, l'échanges et la maintenance (THEMIS est le seul télescope avec du personnel permanent sur site). Par ailleurs, nous souhaitions harmoniser le formatage des données de façon à faciliter les échanges de code de traitement et d'analyse. Cette demande, très bien perçue, a malheureusement été rejetée à la sélection finale.

2.3.2 Dérive d'image

Articles de référence : Mainella and Briand (2002); Mainella et al. (2003) – voir article en fin de chapitre

Les dérives temporelles du champ solaire sélectionné occasionnent de nombreux problèmes pendant la phase d'observation et d'exploitation des données (surtout quand les cibles ne sont pas des structures clairement identifiables – un champ granulaire par exemple). La qualité des tables de « mapping » (table de correction de pointage des axes du télescope pour compenser des erreurs systématiques dues à la mécanique de l'instrument), ainsi que la qualité des tables de calculs de positions du Soleil ont souvent été mises en question par de nombreux observateurs. Avec G. Mainella (autre astronome de support à THEMIS) nous avons donc entrepris un travail de fond pour comprendre les causes de cette dérive, fort préjudiciable à tous les modes d'observation. Nous avons ainsi mis en évidence :

1. La bonne qualité de pointage au foyer primaire du télescope (tant sur des pointages stellaires que solaires) ;
2. La bonne qualité de pointage au foyer secondaire ;
3. La bonne qualité du suivi (tant stellaire que solaire) au foyer primaire ;
4. Un défaut de suivi au foyer F2.

Les trois premiers point mettent hors de cause les tables de mapping et de calculs des positions. La dérive de l'image est due un léger défaut d'alignement des axes optiques et mécanique dans l'optique transfert, amplifié avant l'entrée au foyer secondaire par la présence d'un dérotateur de champ. Les solutions pour résoudre le problème ont ainsi pu être discutées lors des réunions du Conseil Scientifique (puisqu'elles impliquaient du temps, des risques et des dépenses). Les résultats de ces travaux ont été exposés lors d'un colloque réunissant la communauté autour du projet solaire allemand GREGOR. Ce télescope a en effet deux points communs avec THEMIS :

monture alt-azimutale et une optique de transfert. Il faut souligner que l'usage de monture alt-azimutale est récent pour des télescopes solaires (THEMIS était le premier) : cette évolution est liée à l'augmentation du diamètre des télescopes.

2.3.3 Lumière diffusée

Article de référence : Briand et al. (2006) – voir l'article en fin de chapitre

Les structures à faible contraste telle que la granulation solaire, les protubérances, ou les structures de petites dimensions dans les taches solaires peuvent être à peine visible si le taux de lumière diffusée à l'intérieur de l'instrument est trop élevé. Les mesures de vitesse Doppler, l'intensité des taches ainsi que les mesures de polarisation peuvent aussi être erronées. Une technique classique pour déterminer la lumière diffusée d'un instrument est de profiter du transit d'une planète sur le disque solaire : toute déviation de zéro de l'intensité du disque planétaire donne des indications sur le taux de lumière diffusée à l'intérieur du télescope. De telles mesures ont été possible lors du transit de Mercure le 7 mai 2003.

Nous avons notamment déduit le taux de lumière diffusé au sein de l'instrument (télescope + IPM) mais également démontré les limites de cette méthode, pourtant fort utilisée. En particulier, nous avons montré que les résultats sont sous-estimés dans le cas où les surfaces diffusantes sont situées **après** une obstruction centrale.

2.3.4 Qualité d'image

Plusieurs méthodes existent pour accroître la résolution spatiale (affiner la PSF) selon la procédure d'observation envisagée : (a) l'imagerie 2D permet d'utiliser des techniques de post-processing (correction de PSF, speckle, phase diversity), (b) les mesures spectroscopiques (polarimétriques ou non) requièrent des corrections en temps réel du front d'onde.

2.3.4.1 Reconstruction via une fonction de transfert

Le mode imageur de THEMIS était principalement constitué par Fabry-Pérot (*Italian Panoramic Monochromator*, IPM). La technique la plus simple pour accroître la résolution spatiale est d'appliquer une déconvolution de la PSF théorique de l'instrument. Ceci ne prend donc pas en compte les conditions de seeing mais permet, quand celui-ci est correct, d'améliorer la qualité des images. Une illustration d'une telle correction est donnée en Fig. 2.11.

2.3.4.2 Phase diversity

Article de référence : Del Moro et al. (2003a,b) – voir fin de chapitre

L'un des premiers objectifs de THEMIS était de fournir des images à haute résolution spatiale. Le remplacement du premier miroir primaire en 1999 a grandement amélioré la situation. Cependant, des estimations précises des limites de l'instrument n'étaient pas connues. Après avoir suivi une formation à l'Instituto de Astrofísica de Canarias en matière de qualité d'image, j'ai mis en place un groupe de travail pour étudier celle de THEMIS par la technique de « phase

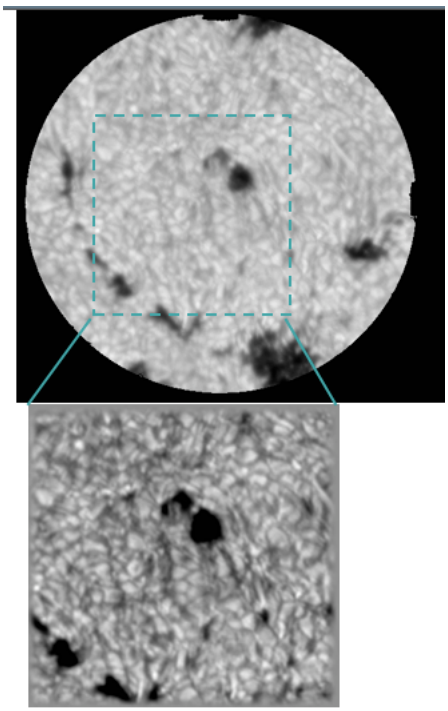

FIGURE 2.11 – Illustration du gain obtenu sur la qualité d'une image par application d'une fonction de transfert simple. En haut l'image brute ; En bas : une partie du champ reconstruit

diversity ». Je me suis adressée à deux spécialistes pour mener à bien cette étude : J.A. Bonet Navarro (IAC) et D. Del Moro (Università Tor Vergata, Roma, Italie).
Les résultats de cette première étude ont été exposés lors de congrès. Il est à remarquer que cette technique de « phase diversity » a de nouveau été utilisée dernièrement pour quantifier les résidus de défaut optiques après l'implantation d'un tip-tilt sur le télescope (je ne connais malheureusement pas les résultats).

2.3.4.3 Optique Adaptative

L'étape suivante pour permettre aux trois modes d'observation de bénéficier de la haute qualité d'image était l'implantation d'une optique adaptative le long du chemin optique principal du télescope. J'ai participé à toutes les réunions de travail, depuis celle en 2000 réunissant tous les spécialistes mondiaux dans le domaine [9] pour donner leur avis sur la nécessité d'une telle implantation à THEMIS, jusqu'aux dernières discussions avec l'ONERA pour définir le cahier des charges. Mon implication dans le projet n'était pas liée à une compétence particulière de ma part en matière d'optique adaptative mais plutôt à ma connaissance complète des interfaces scientifiques et techniques (les implications de modifications des schémas optiques sur le fonctionnement des sous systèmes du télescope, sur le déroulement des observations et sur les résultats scientifiques).

9. c'est-à-dire ceux ayant déjà implanté de l'OA sur des télescopes solaires

2.4 Conclusions

L'importance croissante de la technologie dans nos vies quotidiennes, le développement des programmes spatiaux habités, et le débat sur le rôle du Soleil dans les dérèglements climatiques actuels ont engendré un regain d'intérêt pour l'étude des relations soleil-terre. L'un des grand enjeux de la physique solaire pour les décennies à venir est de prévoir de façon fiable les éruptions (flares ou CME) et leur impact dans le milieu interplanétaire et en particulier dans l'environnement terrestre. De même que la météorologie terrestre avise de tempêtes en termes d'heure de passage sur certaines zones et d'intensité des vents associés, la météorologie de l'espace (Space Weather) doit permettre d'estimer les heures de déclenchement des éruptions, d'en prévoir l'intensité radiative (tant du point de vue des rayonnements électromagnétiques que du flux particulaire) associée ainsi que les zones d'impact des particules dans l'héliosphère. L'utilisation d'indicateurs (*proxys*) permet des mesures rapides et un passage simple vers des services d'alerte. Toutefois, la mise au point d'indicateurs fiables et plus précis requiert de comprendre le détail des processus physiques de déclenchement des éruptions, d'accumulation d'énergie et d'accélération des particules.

Le Soleil est un objet fondamentalement multi-échelles (voir la récente revue de Wedemeyer-Böhm et al. 2009). Les contraintes (cisaillement, torsion, enroulement etc ...) des lignes de champ magnétique depuis la zone de formation du champ (tachocline) jusque dans la couronne solaire jouent un rôle déterminant dans la stabilité des régions magnétiques. Le transfert d'énergie entre les différentes couches atmosphériques s'effectue via le rayonnement électromagnétique, la propagation d'ondes de choc et le développement d'instabilités plasma (conduisant à l'accélération de particules ou des échauffements localisés). Tout ces mécanismes sont des paramètres clés qu'il faut mesurer et modéliser tant dans leur étendu spatiale que temporelle.
Les mesures *in situ* du vecteur champ magnétique solaire sont encore impossibles même dans la basse couronne solaire. La déduction des composantes de $\mathbf{B}$ passe donc par une analyse des raies spectrales. La formation des raies photosphériques étant généralement plus simple, des cartes d'évolution des paramètres thermodynamiques (température, densité, pression, vecteur vitesse etc) et des composantes magnétiques dans la basse atmosphère solaire peuvent être obtenues avec une bonne précision. Mais la plupart des phénomènes éruptifs ont lieu dans la couronne, voire dans la chromosphère où les mesures spectrales et l'interprétation des raies est beaucoup plus délicate, notamment quand on cherche à obtenir les composantes du champ. Les besoins scientifiques lancent des défis instrumentaux importants dans de nombreux domaines (extension des domaines spectraux, haute résolution spatiale, précision polarimétrique etc ...).

Les enjeux scientifiques de la physique solaire moderne requièrent des télescopes offrant de multiples possibilités de combinaison d'instrumentations focales. La polarimétrie est nécessaire puisque la très large majorité des phénomènes solaires résultent de modifications des propriétés du champ magnétique. Enfin, la haute résolution spatiale est indispensable à tout instrument moderne non seulement pour voir les détails de certaines structures (les échelles des transferts d'énergie resteront de toute façon toujours en deçà de la limite de détection) mais surtout pour augmenter le rapport signal sur bruit des mesures polarimétriques. Le projet actuel European Solar Telescope doit à mon avis être largement soutenu car il satisfait tous les critères de qualité tant du point de vue instrumental que de management de projet. La présence d'un tel télescope en Europe permettra de continuer à former des jeunes non seulement à la physique solaire mais également à l'instrumentation. Des efforts énormes ont été réalisés ses dernières années pour créer une communauté européenne de physiciens solaires de haut niveau. Il faut que cet effort

se consolide à travers une implication à ce projet de tous les pays européens.

Les mesures conjointes depuis des instruments au sol et dans l'espace sont indispensables pour essayer d'aborder le système « soleil » dans toute sa complexité. Il manque cependant encore des mesures au plus près de la couronne. Souhaitons qu'elles soient apportées par « Solar Orbiter » et une sonde d'exploration de la couronne solaire dans les prochaines années.

2.5 Articles

Solar Physics (2006) 234: 187–201
DOI: 10.1007/s11207-006-0033-5

MERCURY TRANSIT FOR STRAY LIGHT EVALUATION: IPM-THEMIS CASE

C. BRIAND
LESIA, Observatoire de Paris, 5 Place J. Janssen, F-92190 Meudon CEDEX Principal, France (e-mail: carine.briand@obspm.fr)

W. MATTIG
Kiepenheuer-Institut für Sonnenphysik, Schöneckstr. 6, D-79104 Freiburg, Germany

G. CEPPATELLI
IAC, C/Vía Lactéa, s/n, E-38200 La Laguna Tenerife, Spain; On Leave from INAF-Osservatorio di Arcetri, Largo E. Fermi 5,I-50125 Firenze, Italy

and

G. MAINELLA
Fundación Galileo Galilei – INAF, Calle Alvarez de Abreu 70, E-38700 Santa Cruz de La Palma, Spain

(Received 18 July 2005; accepted 3 November 2005)

Abstract. Mercury's transit on the solar disk offers ideal conditions to determine the stray light level of instruments. We present here the results on the stray light level deduced from the observation of the Mercury transit on 2003 May 7th at the secondary focus of the THEMIS telescope with the broad-band and spectral channels of the IPM instrument. The scattered light in the broad-band channel is about 17% and about 25% in the spectral channel. The spread function was deduced for the two channels taking into account the observations on the limb and on Mercury's disk.

The goal of this paper is to underline the limits of determining the spread function from limb measurements to correct disk observations. Indeed, we show that if a diaphragm is located in the optical path of scattering surfaces, then the spread function deduced from limb measurements can be underestimated compared to the one required for disk observations. The case is illustrated with the results of the IPM-THEMIS instrument. The spread function deduced from limb measurements is able to correct disk observations in the broad-band channel but not in the spectral channel, even if the two channels are illuminated through the same telescope configuration.

1. Introduction

Many low contrast solar structures like granulation (Wittmann, 1979), coronal structures (Koutchmy and Koutchmy, 1974), or small scale structures on sunspots (Zwaan, 1965; Albregtsen and Maltby, 1981) may be hardly visible if the stray light level is too high. Also, large scale Doppler velocity measurements (De Lury, 1939; Albregtsen and Andersen, 1985) or sunspot intensity (and thus temperature determination) (Zwaan, 1965; Kneer and Mattig, 1968; Maltby and Staveland, 1971;

Collados *et al*., 1994) may be erroneous if the stray light is uncorrected. However, estimation of this spurious light level is usually difficult due to the lack of reliable reference sources. The most common method of determination consists of measuring the sky aureole (Mattig, 1971; Köppen, 1975; Mattig, 1983; Barducci *et al*., 1990). Planetary transits offer another opportunity to deduce the stray light since the planet disk provides a true-zero level reference. Thus, all non-zero signals (apart from the camera noise) observed on Mercury's disk are due to scattering from the Earth's atmosphere and the instrument (Mattig, 1971; Wittmann and Wöhl, 1975).

In order to determine the scattered light at the secondary focus of the THEMIS telescope[1], the transit of Mercury was observed on 2003 May 7th. This is the first time such an estimation has been performed for this instrument.

The Section 2 details the observing configuration. The Section 3 explains the data reduction and analysis: the stray light levels deduced for each spectral domain and channel (broad-band and spectral) are detailed there. Section 4 explains the computation of the spread function and shows a comparison with the observations.

2. Observations

2.1. Instrumental configuration

The observations were performed with the Italian Panoramic Monochromator, IPM, (Cavallini, 1998) located at the secondary focus of the telescope (Molodij *et al*., 1996). Two spectral ranges were sequentially observed: Fe I at 5194.95 Å and Ca I at 6439.08Å. The first range was sampled with twelve points: seven equally spaced in wavelength around the line core ($\Delta\lambda = 0.05$Å) and five in the blue wing of the line (between 0.55Å and 0.75Å). The second spectral domain was sampled with sixteen points equally spaced around the line core ($\Delta\lambda = 0.05$Å). Simultaneously broad-band images (50Å wide in the respective spectral range) were recorded for each spectral point. The IPM field of view is $51''$ and the sampling on the cameras is $0.1''$/pixel. Exposure time is 0.4s in the spectral domain (for both lines) and 0.1 s for the two broad-band domains. A complete sequence of measurement ($12 + 16$ spectral points) took 78 s.

The observations started at 6:50 (U.T.) when Mercury was already on the solar disk but one hour before its closest position to the Sun center. Third contact was at 10:28:58 UT ($\pm$4 s) and fourth contact at 10:33:11 UT ($\pm$ 4 s). Uncertainties on the time contact come from the temporal sampling of the observation, the uncorrected black-drop effect (Schneider, Pasachoff and Golub, 2004) and the variable seeing conditions.

[1]THEMIS is operated on the island of Tenerife by INSU-CNRS/INAF in the Spanish Observatorio del Teide of the Instituto de Astrofísica de Canarias.

A sunspot located very close to the disk center ($\mu = 0.9$, where μ is the cosine of the heliographic angle with respect to the observer) was observed from time to time. Limb measurements were also performed several times during the transit.

Seeing conditions were suboptimal at the beginning of the observation (the Sun elevation was still low) however, improved somewhat with the increase of solar elevation. African desert dust was almost absent during the observation.

3. Data Reduction and Analysis

The data were corrected for dark current and flat-field using the relation:

$$I_{\text{obs}} = \frac{I_{\text{raw}} - < Dark >}{< Flat > - < Dark >} , \tag{1}$$

where I_{obs} represents the corrected image intensity, I_{raw} the raw image intensity, $< Dark >$ the time average of the dark current images and $< Flat >$ the time average of the flat-field images. Dark current images were obtained by closing the entrance of the IPM instrument. Flat-field images were obtained while moving the telescope around the solar disk center.

Two normalizations of stray light are used:

(1) When deduced from Mercury's disk, it is defined as the ratio of observed Mercury's disk intensity I_{M} to the Quiet Sun intensity *close to Mercury* $I_{\text{QS}}(\mu)$ (Maltby, 1971; Maltby and Staveland, 1971). This choice avoids correction of intensity variation due to the time dependent Earth atmospheric extinction (increase of Sun elevation);
(2) When dealing with the aureole, it is defined as the intensity of the aureole I_{aur} to the Quiet Sun intensity *at disk center* $I_{\text{QS}}(\mu = 1)$ (Staveland, 1970; Mattig, 1983).

The way these intensities are deduced is discussed in detail in the following sections.

3.1. Mercury intensity: I_{M}

Mercury's disk intensity is deduced from an average of the intensity inside a circle of half the planet radius (5.8″), centered on Mercury disk. The choice of this value avoids the contamination due to seeing which makes the edges of Mercury unsharp (Figures 1 and 7). Inside this circle the intensity of Mercury disk is almost constant. The exact Mercury position is deduced from the coordinates, extracted from the file headers, corrected for the position of Mercury center in the successive images.

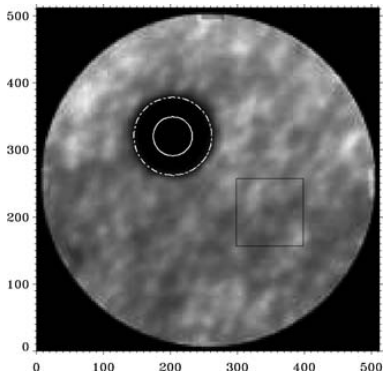

Figure 1. Typical field-of-view with Mercury on the solar disk. Both axes are expressed in pixels (1 pixel = 0.1″). Observed wavelength: 6439.08Å. The *outermost circle* around Mercury symbolizes the limits of the planet. The *innermost circle* symbolizes the area over which Mercury intensity is averaged. The *square* in the Quiet Sun represents an example of area selected to deduce the Quiet Sun intensity close to Mercury.

The coordinates recorded in the headers are deduced from the real time measured position of the telescope (Mainella, Briand and Maréchal, 2003).[2]

3.2. AUREOLE INTENSITY: I_{aur}

The intensity outside the solar disk is obtained by averaging the intensity over 5″ parallel to the limb (cf. Figure 2). The $\mu = 0$ position is defined as the location of the inflection point of the limb intensity profile. In the following, the intensities are considered for all the locations up to 19″ outside the limb (the largest common field-of-view extension of limb measurements).

3.3. QUIET SUN INTENSITY CLOSE TO MERCURY: $I_{\text{QS}}(\mu)$

The Quiet Sun intensity is determined from the average over a box of $10'' \times 10''$ close to Mercury (cf. Figure 1).

3.4. QUIET SUN INTENSITY AT DISK CENTER: $I_{\text{QS}}(\mu = 1)$

The Quiet Sun intensity at disk center has been deduced from the intensity close to Mercury (cf. subsect. 3.3) corrected for the center-to-limb variation. The fifth degree polynomial description presented by Pierce and Slaughter (1977, their

[2]For more details on the procedure to convert telescope positions into heliographic coordinates, see the internal documentation of THEMIS.

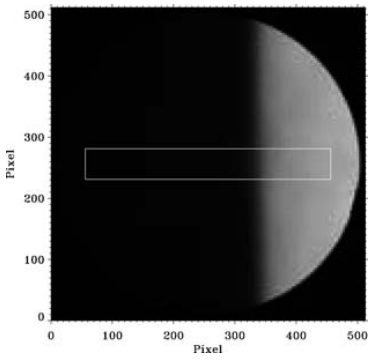

Figure 2. Typical field-of-view at the solar limb. Both axes are expressed in pixels (1 pixel = 0.1″). Observed wavelength: 6439.08Å. The *rectangular box* symbolizes the area over which the intensity is measured.

Equation (11)) is used to correct for the center-to-limb intensity variation. The coefficients are taken from their Table IV. However, since these parameters were deduced from the continuum of several spectral ranges, we had to adjust them in the spectral domain. The deduced coefficients are presented on Table I. For each intensity measurement, the attributed μ value is the one of the corresponding position of Mercury.

In order to test the accuracy of the center-to-limb correction and adjust the center-to-limb coefficients in the spectral domain, the deduced intensities are compared with the Quiet Sun values measured close to the sunspot (and also corrected for the center-to-limb intensity variation, even if the applied correction was very low since the sunspot was located at $\mu = 0.97$). For example, Figure 3 shows the Quiet Sun intensity at disk center deduced from values close to Mercury or close to the sunspot, for the Ca I domain. Clearly the correction applied to the Quiet Sun close to Mercury allows a good representation of the Quiet Sun intensity at disk center (the same happens for the other spectral range). The remaining time evolution corresponds to the variation of the Earth atmospheric extinction with Sun

TABLE I

Coefficients used to correct for the center-to-limb intensity variation (Pierce notation).

Line	Channel	A(5)	B(5)	C(5)	D(5)	E(5)	F(5)
Ca I	Broad-Band	0.33	1.38	−1.94	2.52	−1.80	0.52
	Spectral	0.41	1.46	−2.74	4.12	−3.30	1.03
Fe I	Broad-band	0.24	1.18	−0.66	−0.01	0.54	−0.30
	Spectral	0.36	1.20	−0.85	−0.01	0.59	−0.30

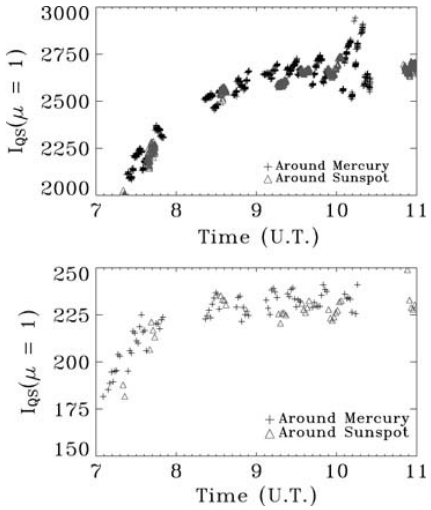

Figure 3. Comparison between the Quiet Sun intensity (Ca I line) at disk center deduced from the intensities close to Mercury after correction of the center-to-limb variation (*crosses*) and from the intensity close to the sunspot (*diamonds*). *Top*: broad-band channel: Bottom: spectral channel. Intensities are given in Analog-Digit Units (A.D.U.).

elevation. However, this variation is uncorrected since we are interested in relative intensities.

The Quiet Sun intensity at disk center corresponding to the limb observations can thus be obtained from the observing time.

3.5. STRAY LIGHT

The results of the stray light obtained from Mercury's intensity measurements are displayed in Figure 4. As expected from the wavelength dependence of the scattering process, the stray light is more prominent for the Fe I line than for the Ca I. The stray light in the broad-band channel is lower than the one in the spectral channel. The difference between the two channels is due to an increase of the number of optical surfaces along the spectral optical path (Figure 5). Indeed, this last includes a Lyot filter and a Fabry-Pérot interferometer (Cavallini, 1998). The internal stray light of the spectral channel is of the same level than other similar instruments like TESOS at the German Vacuum Tower Telescope of the Teide Observatory (Schleicher, private communication).

The small decrease of intensity ratio with decreasing μ values (when smaller than 0.3) reflects the fact that the illumination is no longer axis-symmetrical due to the proximity of the limb.

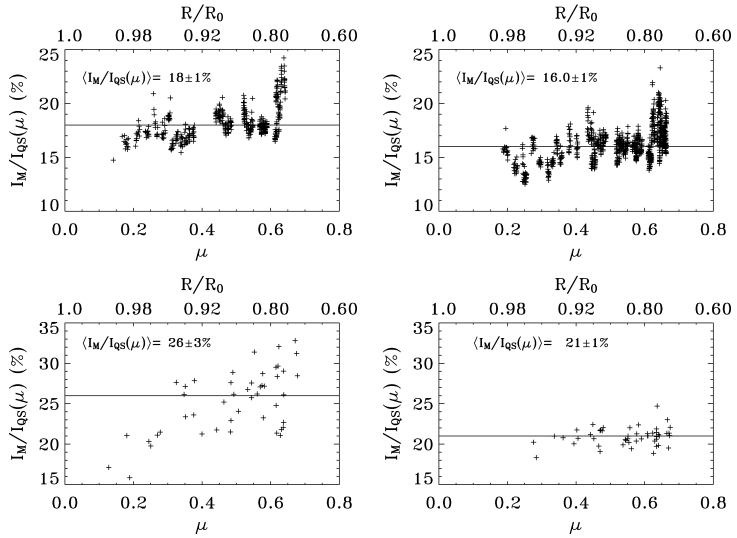

Figure 4. Stray light from Mercury intensity vs. the heliographic position expressed in term of μ (lower scale) or ratio of the radial distance R to the solar radius $R_\odot$ (upper scale). *Upper panels*: broad-band channel (Fe I: *left*; Ca I: *right*); *lower* panels: spectral channel (Fe I line core: *left*; Ca I line core: *right*). The average stray light for $0.3 < \mu < 0.6$ is expressed (in percentage) on each figure and is represented by the straight line.

Figure 4 also shows the stray light time evolution: the largest μ values ($\mu > 0.6$) correspond to earlier observing time (and also larger air mass). The constant value of stray light for $0.3 < \mu < 0.6$ strongly suggests an instrumental origin (Martinez Pillet, Ruiz Cobo and Vázquez, 1990; Barducci *et al.*, 1990): otherwise, in the case of atmospheric origin, stray light values would vary with changing air mass (thus with μ values). This is for example the case for $\mu > 0.6$ which corresponds to larger zenithal distance.

Figure 6 shows the stray light of the aureole up to a distance of 19″ outside the limb. The dependence on wavelength and channel is the same as the results from Mercury observations but less pronounced. Another interesting phenomenon appears on the spectral channel: the stray light level is higher when the solar disk covers about 50% of the field-of-view (diamond curve) than when it covers only 20% (crosses curves). When it is of instrumental origin, the stray light level depends on the amount of light reflected on the optical surfaces. In the case of the spectral channel, part of the observed stray light comes from its own optical surfaces (as seen before from Mercury observations). By reducing the light entering the IPM-channel, we also reduce the stray light. This is barely noticeable for the broad-band channel suggesting that all the optical surfaces responsible for the stray light are equivalently illuminated during disk and limb observations. Thus, they must be

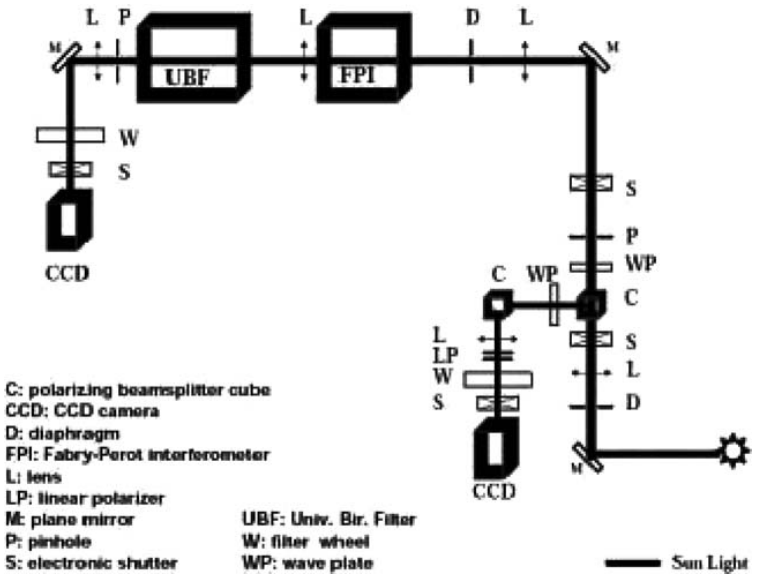

Figure 5. Scheme of the IPM optical path. The first deviation leads to the broad-band channel (*lower* optical path). The optical path with the FPI and UBF filters is the spectral channel (*upper part* of the drawing). Only optical elements of interest for the present study are included (that is, optics for calibration and control have been removed). From Cavallini (1998).

located before the entrance of the IPM instrument. We revisit on this point later in Subsection 4.2.

4. Spread Function

4.1. Equations and procedures

The observed intensity I_{obs} is the convolution of the true intensity I_{obs} with a spread function $\phi(r, \theta)$ so that:

$$I_{\text{obs}}(r, \theta) = \int_0^{2\pi} \int_0^{\infty} I_{\odot}(r', \theta')\phi(r - r', \theta - \theta')r'dr'd\theta' \tag{2}$$

with the following normalization:

$$2\pi \int_0^{\infty} \phi(r)r\,dr = 1. \tag{3}$$

As previously discussed by several authors (Staveland, 1970; Wittmann and Wöhl, 1975 and references therein), the spread function can be represented by a

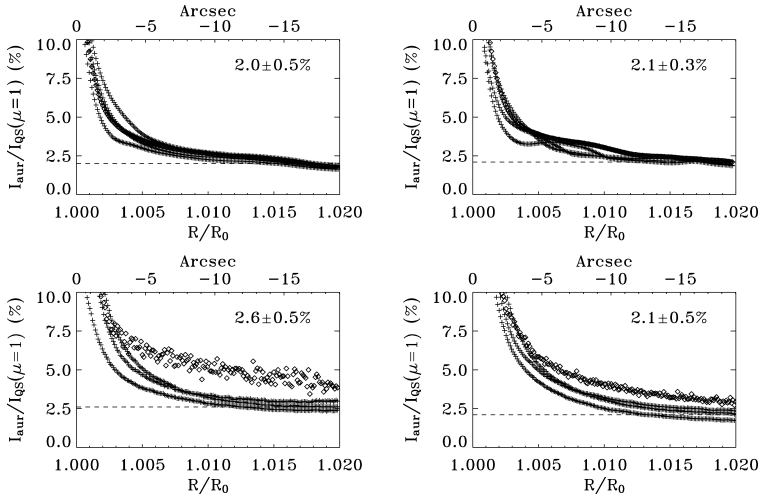

Figure 6. Aureole stray light vs. the distance to the solar limb expressed in terms of the ratio of the radial distance R to the solar radius $R_\odot$ (lower scale) or arcsec (upper scale). *Upper panels*: broad-band channel (Fe I: *left*; Ca I: *right*); *lower panels*: spectral channel (Fe I line core: *left*; Ca I line core: *right*). The stray light value of the outermost observing region is given in each panel (the horizontal dashed line sets the level). The *diamond* curves correspond to points when the solar disk still covers 50% of the field-of-view. The other curves (*crosses*) correspond to points when the solar disk covers only 20% of the field-of-view.

linear combination of one (or more) Gaussian function (for the rapid and strong fluctuations – typical for example of seeing) and a Lorentzian function (for the long term variations – e.g. scattering). Thus, following these previous works we write the function as:

$$\phi(r) = \varepsilon \frac{A_1}{A_2^2 + r^2} + (1 - \varepsilon) A_0 \exp\left(-\frac{r^2}{\sigma^2}\right), \tag{4}$$

with ε being a free parameter weighting the contribution of the Gaussian and Lorentzian function to the spread function, σ and A_2 two other free parameters setting the width of the Gaussian and the Lorentzian part of the function and finally A_0 and A_1 two normalization factors.

The normalization of the Lorentzian part of the function ϕ is a problem if we integrate over the all space. However, taking into account the spherical geometry of the solar illumination, an integration from zero to a finite distance from the disk center is required. We decided to limit the integration to half the celestial hemisphere

(that is from 0 to $\frac{\pi}{2}$) for both the Gaussian and the Lorentzian. This sets the values of A_0 and A_1 as:

$$A_0 = \frac{1}{\pi\sigma^2\left(1 - exp\left(-\left(\frac{\pi}{2\sigma}\right)^2\right)\right)}\ , \tag{5}$$

$$A_1 = \frac{1}{\pi \mathrm{In}\left[1 + A_2^2 + \left(\frac{\pi}{2}\right)^2\right]}\ . \tag{6}$$

Now, the free parameters of the spread function are deduced from a comparison between the observations and simulations of the scattering effect on the solar intensity distribution.

To do this, a 2D intensity distribution of the Sun with aureole extension up to $6'$ is created. The Pierce model is once again used to account for the center-to-limb intensity variation. Initially, the aureole has a strictly zero intensity. Also, a perfectly zero intensity disk of Mercury's diameter is superimposed on the solar disk at several locations corresponding to observational positions. The edges of Mercury are thus initially equivalent to a step function. A 2D axis-symmetric spread function is then created following the Equation 4 and the normalization given by Equations (5) and (6). Finally, the Sun intensity distribution and spread function are convolved according to Equation (2).

4.2. Results in the spectral channel

The spread function was first determined for the two spectral domains of the spectral channel. An example of Mercury's intensity profile fit is shown in Figure 7. The coefficients employed for this fit are given in Table II. Figure 8 shows the fit of the solar limb and aureole for two different observing conditions: when the solar disk fills around 50% and 20% of the instrument field of view (respectively case A and B). Figures 7 and 8 refer to the Ca I line core but similar results are obtained with the Fe I line core. The best fit parameters of the curves of both Figures are reported in Table II. Those parameters are not unique for a given profile: A_2 and ε play a similar role and several combinations of them can lead to a correct fit. In the examples of this subsection and the following one, A_2 was set to $1.5''$ in order to compare the contribution of the Lorentzian to the total spread function in all cases. This is an arbitrary choice which is justified by the fact that we do not try to give any interpretation to the A_2 parameter, which, in any case, would be impossible from these observations. Only σ is unique for, a given profile but must be adjusted from one observation to the other, supporting the notion that the Gaussian function recovers mainly the seeing fluctuations.

The parameters shown in Table II were obtained from several observations of Mercury ($\mu = 0.28, 0.34, 0.54, 0.63$) and several observations at limb. For comparison, Mercury's intensity profiles that are obtained from the limb parameters are

TABLE II

Parameters used to fit Mercury's profile (second column), aureole profile when around 50% of the field of view is covered with solar disk (third column) and aureole profile when around 20% of the field of view is covered with solar disk (fourth column), for the two spectral wavelengths (in their respective line core).

	Mercury		Aureole (Disk 50%)		Aureole (Disk 20%)	
Parameters	Fe I	Ca I	Fe I	Ca I	Fe I	Ca I
$\sigma(''')$	1.10 ± 0.05	1.10 ± 0.05	1.8 ± 0.1	1.8 ± 0.1	1.5 ± 0.1	1.6 ± 0.1
ε	0.16 ± 0.05	0.14 ± 0.05	0.15 ± 0.01	0.10 ± 0.01	0.1 ± 0.01	0.085 ± 0.005

In each case A_2 is set to $1.5''$.

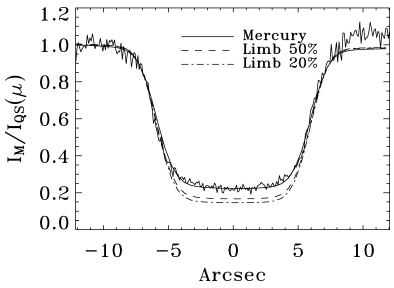

Figure 7. Comparison between observed (*solid thin line*) and the simulated Mercury profile (Ca I line core). *Solid thick line*: fit of Mercury's profile with the best parameters for Mercury (*solid line*); *Dashed line*: fit with the best parameters of case A (see text); *Dot-dashed line*: fit with the best parameters of case B.

also plotted on Figure 7. Clearly, the correction of stray light deduced from limb measurements is insufficient for the disk observations.

The calculations shows a large variation in the parameters with respect to the amount of light entering the spectral channel: the contribution of the Lorentzian function decreases when the light entering the channel is reduced. In other words, if the stray light is of instrumental origin, the spread function deduced from limb observation may be inadequate to correct stray light on the disk.

Indeed, for it to be correct the optical surfaces responsible for the stray light must receive the same amount of light during disk and limb observations. This is not the case for the spectral channel since part of the optical surfaces responsible for the stray light are located *inside* the IPM and more specifically after the IPM diaphragm. If we would apply the correction of stray light deduced from limb observations to disk observations, we would overestimate the intensities.

This may also be the reason why Maltby and Staveland (1971) observed higher intensities for Mercury than the one deduced from estimation of the stray light on the limb (see their Figure 5a). Also Wittman and Wöhl (1975) recover the amount

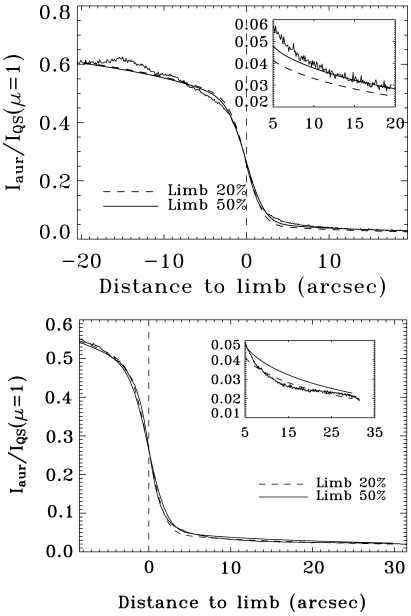

Figure 8. Comparison between observed and simulated limb and aureole profiles (Ca I line core). *Top panel*: fit when the solar disk still covers half of the field-of-view. *Bottom panel*: fit when the disk covers about 20% of the field of view. *Solid thick line*: fit with the best parameters of case A; *Dashed line*: fit with the best parameters of case B. In each Figure, the *upper right* plot shows the details of the fit in the aureole region (same units as the main plot).

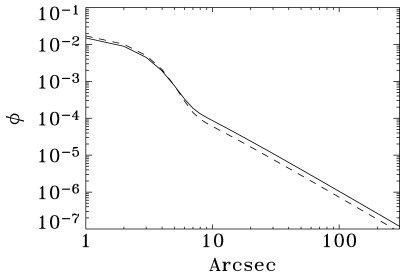

Figure 9. IPM-THEMIS spread function as deduced from Mercury (*thick line*) and limb (case B, corresponding to solar disk covering 20% of the field of view – *dashed line*) (Ca I line core).

of stray light by a factor of two. In both observations, a pinhole was used at the entrance of the main telescope.

The Figure 9 displays the spread function deduced from the fit of Mercury. Clearly the Lorentzian function is predominant for distances larger than 8″.

TABLE III
Same as Table II for the two spectral domains of the broad-band channel.

	Mercury		Aureole (Disk 50%)		Aureole (Disk 20%)	
Parameters	Fe I	Ca I	Fe I	Ca I	Fe I	Ca I
$\sigma(")$	1.10 ± 0.05	1.20 ± 0.05	1.55 ± 0.05	1.55 ± 0.05	1.85 ± 0.05	1.25 ± 0.05
ε	0.105 ± 0.005	0.105 ± 0.005	0.095 ± 0.005	0.085 ± 0.005	0.085 ± 0.005	0.075 ± 0.005

4.3. RESULTS IN THE BROAD-BAND CHANNEL

The spread function parameters deduced from the observations in the broad-band channel are given in Table III. As in the case of the spectral channel (cf. subsect. 4.2), A_2 parameter is set to 1.5". We also note here an influence of the amount of light entering in the channel on the parameter ε of the spread function even if less pronounced than in the spectral channel. This suggests that the largest part of the stray light is due to optical surfaces located before the diaphragm of the IPM but also that a small amount of stray light comes from some optical surfaces inside the broad-band channel. The wavelength dependence of ε is mainly noticeable on limb observations. It is also important to note that the ε parameter is always lower than in the spectral channel, which confirms that additional stray light is produced inside the spectral channel.

5. Conclusion

We took advantage of the Mercury transit on 2003 May 7th to deduce the stray light of the THEMIS-IPM instrument.

To explain a relatively large level of scattered light (see also Mattig (1971), Wittmann and Wöhl (1975), Mattig (1983) for other instruments), we must recall that the light encounters eleven mirrors before reaching the diaphragm of the IPM instrument. These results on the amount of stray light represent values for the IPM only. The spectropolarimetric and MSDP mode, which both benefit from the presence of a pre-slit at the primary focus of the telescope, should have a reduced amount of stray light. Other specific investigations are required for these observing modes.[3]

The main result of this work is the following. The spread function deduced from limb observations may underestimate the stray light on the disk if the optical surfaces responsible for the scattering do not receive the same amount of light

[3]For a description of the different observing modes available at THEMIS, please look at the official web page: *http://www.themis.iac.es*.

during limb and disk observation. This conclusion seems obvious but many instruments have a diaphragm in the optical path that changes the illumination condition on the optical surfaces. If the surfaces responsible for the scattering are located before the diaphragm, the procedure is correct. However, if some of the surfaces are located after it, the deduced spread function is underestimated compared to the one required for disk observations. Concerning the IPM-THEMIS instrument, the limb measurements may be safely used for the IPM broad-band channel. However, such measurements underestimate the disk spread function of the spectral channel. As an important point we note that the two channels are illuminated by the same telescope configuration.

For all instruments having a diaphragm that may change the amount of light reaching the optical surfaces responsible for the scattering (like a diaphragm or a pre-slit at the primary focus of the telescope), other specific stray light calibration procedure must be performed.

Acknowledgements

The authors want to thank Marco Pedani, Rene Rutten and Christopher D. Parkinson for their useful comments during the writing of the manuscript, and J. A. Bonet Navarro who motivated the work.

References

Albregtsen, F. and Maltby, P.: 1981, *Solar Phys.* **74**, 147.
Albregtsen, F. and Andersen, B.N.: 1985, *Solar Phys.* **95**, 239.
Barducci, A., Cavallini F., Ceppatelli, G., and Righini, A., 1990, *Astron. Astrophys.* **240**, 203.
Cavallini, F.: 1998, Astron. *Astrophysi. Suppl. Series*, **128**, 589.
Collados, M., Martínez Pillet, V., Ruiz Cobo, B., del Torn Iniesta, J. C., and Vázquez, M.: 1994, *Astron. Astrophys.* **291**, 622.
De Lury, R. E.: 1939, *J. R. Astron. Soc. Canada*, **33**(9), 345.
Kneer. F. and Mattig, W.: 1968, *Solar Phys.* **5**, 42.
Köppen, J.: 1975, *Solar Phys.* **42**, 325.
Koutchmy, O. and Koutchmy, S.: 1974, *Astron. Astrophys. Suppl. Series*, **13**, 295.
Mainella, G., Briand. C., and Maréchal, L.: 2003, *Astron. Nachr.* **324**(4), 309.
Maltby, P., 1971, *Solar Phys.* **18**, 3.
Maltby, P. and Staveland, L.: 1971, *Solar Phys.* **18**, 443.
Martínez Pillet, V., Ruiz Cobo, B., and Vázquez, M.: 1990, *Solar Phys.* **125**, 211.
Mattig, W.: 1971, *Solar Phys.* **18**, 484.
Mattig, W.: 1983, *Solar Phys.* **87**, 187.
Molodij, G., Rayrole. J., Madec. P. Y. and Colson, F.: 1996, *Astron. Astrophys. Suppl. Series*, **118**, 169.
Pierce, A. K. and Slaughter, C. D.: 1977, *Solar Phys.* **51**, 25.
Schneider, G., Pasachoff, J. M., and Golub, L.: 2004, *Icarus*, **168**, 249.

Staveland, L.: 1970, *Solar Phys.* **12**, 328.
Wittmann, A. and Wöhl, U.: 1975, *Solar Phys.* **44**, 231.
Wittman, A.: 1979, in "*Small Scale Motions on the Sun*", Kiepenheuer-Institut für Sonnenphysik, Freiburg, p. 29.
Zwaan, C.: 1965, *Rech. Inst. Astron. Utrecht*, **17**, Part 4.

A&A 403, L33–L36 (2003)
DOI: 10.1051/0004-6361:20030553

Astronomy & Astrophysics

Chromospheric polarity reversal on sunspots: New insight from spectro-polarimetric measurements

C. Briand[1,2] and A. Vecchio[3]

[1] THEMIS, C/O IAC, via Lactea, 38200 La Laguna, Tenerife, Spain
[2] LESIA, Observatoire de Meudon, 92195 Meudon Cedex principal, France
[3] Dipartimento di Fisica – Ponte P. Bucci, Cubo 31C, Universitá della Calabria, 87036 Rende (CS), Italy

Received 12 March 2003 / Accepted 13 April 2003

Abstract. We present here spectro-polarimetric observations of chromospheric and photospheric lines on an active region. We show that the presence of polarity reversal between photosphere and chromosphere cannot be detected relying on magnetograms and broad band and even narrow band filters only. We demonstrate that opposite signs in CaII magnetograms in sunspots compare to photospheric magnetograms are not due to a reversal of the magnetic field, but rather due to the presence of line core emission as suggested from theoretical arguments by Sánchez Almeida (1997).

Key words. Sun: magnetic field – Sun: photosphere – Sun: chromosphere

1. Introduction

Most of the solar magnetic field observations concern the photospheric magnetic field. The chromospheric magnetic field deserves less attention maybe due to intrinsic difficulties to measure and interpret. It is however evident that a better knowledge of the chromospheric magnetic field would be of fundamental importance, for example to study the details of the magnetic flux emergence from the low layers of the solar atmosphere to the corona, or to investigate magnetic field topology changes in active region (especially in regions giving eruptive events).

Among the few observational studies, the presence of "polarity reversal" between the photosphere and chromosphere was mentioned by Wang & Shi (1992), Li & Zhang (1994). Sánchez Almeida (1997) points out that such reversal may not be due to true magnetic field reversal but rather to the presence of emission in the line core. The arguments were based on theoretical simulation and sofar no new observations confirmed this hypothesis.

In this work we provide observational evidence supporting that the reversal is due to lie emission.

2. Observation

Observations on active region NOAA 0019 were performed between July 2nd and July 6th 2002 with the spectro-polarimetric mode of the THEMIS telescope[1]. It allows to obtain 2-dimensional maps of the solar active region. Four lines were recorded simultaneously. We report here results on the photospheric (FeI 630.2 nm) and the chomospheric (Hα 656.3 nm and CaII 854.2 nm) line profiles. The sunspot was located W39–S17 the first day of observation and reached E08–S17 the last day. The region was scanned with step of 0.5″ (the size of the spectrograph entrance slits width).

The spatial sampling along the slit is 0.5″/pixel. The spectral sampling is 35 mÅ/pixel for CaII, 27 mÅ/pixel for Hα and 22 mÅ/pixel for FeI. The exposure time for all wavelengths was 300 msec. Seeing conditions limited the spatial resolution to about 1″.

The so-called $2 \times 1'$ THEMIS spectro-polarimetric configuration was used: the two beams with orthogonal polarization exiting the analyzer are directed into a single camera. The field of view covered by the entrance slits of the spectrograph is 1′. Beam inversion was performed for the linear polarization Q: the top part of the camera received sequentially $I + Q$, $I - Q$, $I + U$ and $I - V$ while the bottom part recorded $I - Q$, $I + Q$, $I - U$, $I + V$.

This observing strategy allows to reduce the errors coming from uncertainties on the flat-field, to correct for the cross-talk between Stokes parameters (applying a known demodulation matrix) and to reduce the impact of the seeing induced cross-talk due to the time delay between to successive polarimetric measurements: 1 s (Skumanich et al. 1997).

Send offprint requests to: C. Briand,
e-mail: cbriand@themis.iac.es

[1] THEMIS is operated on the island of Tenerife by INSU-CNRS/CNR in the Spanish Observatorio del Teide of the Instituto de Astrofísica de Canarias.

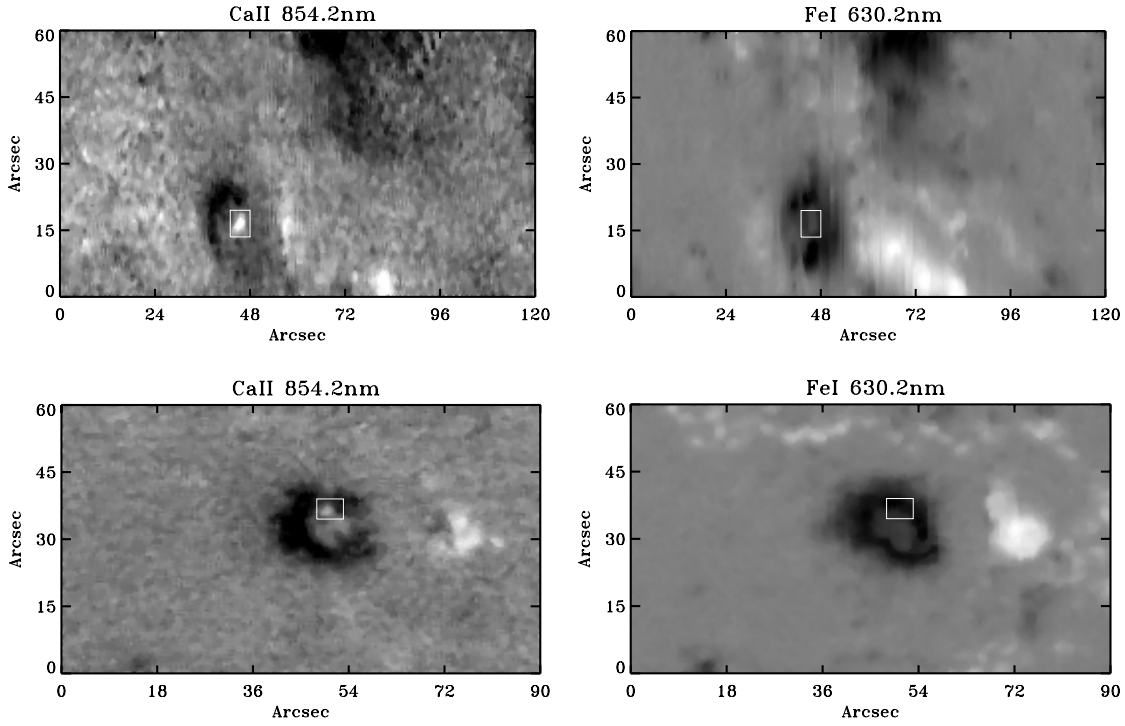

Fig. 1. Magnetograms in CaII (top) and FeI (bottom) from data obtained on June 2nd 2002 at 15h11 UT (left) and June 6th 2002 at 08h20 UT (right). The rectangles underlines the area where a "polarity reversal" seems to be present on the sunspot.

The final error of the measurements is: $S/I_c = 10^{-3}$ for FeI and 5×10^{-3} for the two chromospheric lines (S stands for one of the Q, U or V Stokes parameter and I_c stands for the intensity of the continuum in Quiet Sun region).

The Landé factor of the FeI 630.2 nm line is 2.5, of the CaII 854.2 nm line is 1.1 and of Hα is 1. All lines exhibit a normal Zeeman pattern with two lobes of opposite polarities for Stokes V.

2.1. Line of sight magnetograms reconstruction

All intensity maps were reconstructed at line center, simulating filter with a narrow bandwidth of 125 mÅ. Magnetograms presented in the following sections were drawn from a fixed pixel position corresponding to the blue peak of Stokes V of each spectral lines. Such reconstruction technique does not try to give any absolute value of the line of sight magnetic field. Rather it mimics the operation of a magnetograph and allows to show apparent reversal of the Stokes V peak.

In the weak field approximation, Stokes V is related to the magnetic field by the following formula:

$$V = 4 \times 10^{-13} g_{\rm eff} \lambda^2 \alpha B_{\rm los} \frac{{\rm d}I^{\rm m}}{{\rm d}\lambda} \quad (1)$$

where $g_{\rm eff}$ is the effective Landé factor, α the filling factor, $B_{\rm los}$ the magnetic field along the line of sight and $I^{\rm m}$ the Stokes I coming from the magnetic element. For this expression to be valid, $I^{\rm m}$ and V have the same units and wavelength and magnetic fields have to be expresssed in Angstrom and Gauss, respectively. A change of sign of V can result either from a change of $B_{\rm los}$ or from the presence of emission core in Stokes I profile that induces a change on the sign of $\frac{{\rm d}I^{\rm m}}{{\rm d}\lambda}$.

3. Data analysis

3.1. Evidences of polarity reversals?

In a first attempt, the magnetograms from CaII and FeI are compared. Two examples are presented in Fig. 1. It is clear that a small area (in the rectangles of the previously mentioned figure) shows opposite sign in the photosphere and the chromosphere. Note that the two magnetograms correspond to the same observed region (the phenomenon is thus stable over many days). However, as explained in the previous section, this phenomenon can also result from an emission in the line core. To check if the region presents activity we display its intensity maps (drawn as described in Sect. 2.1) in Fig. 2.

Such maps (even if obtained at line centre) do not exhibit a specific chromospheric activity, or at least do not strongly show if the intensity profile is or not in emission. Such kind of argument was used by Wang & Shi (1992) to prove the real nature of the polarity reversal from chromosphere to photosphere.

Another way to put in evidence the presence of a polarity reversal could be to look at the CaII Stokes V parameter. Indeed, two photospheric lines are present at about 0.3 Å on the blue wing (see also Fig. 3). Once again, we could conclude of the presence of a polarity reversal in this region.

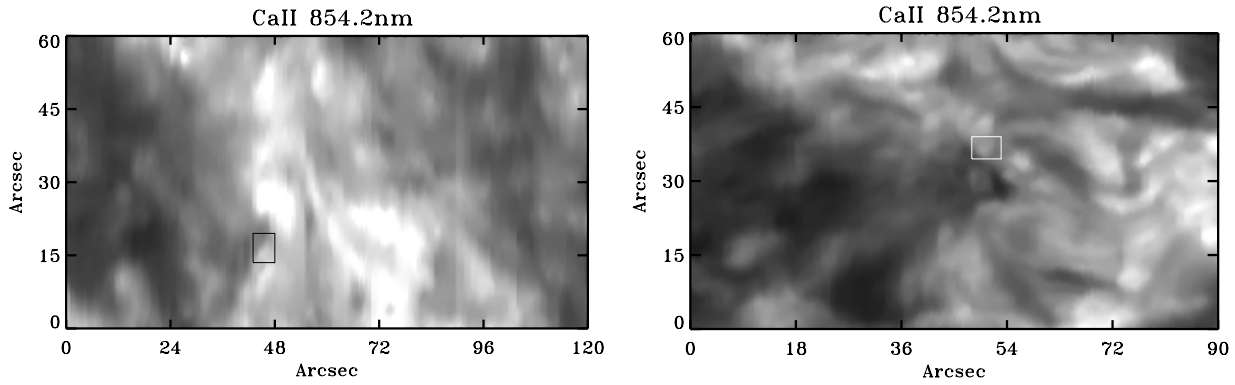

Fig. 2. Intensity reconstructed maps from the CaII IR line core corresponding to the magnetograms of Fig. 1. The rectangle underline the areas where opposite signs are detected on the magnetograms. Intensity maps are in linear scale.

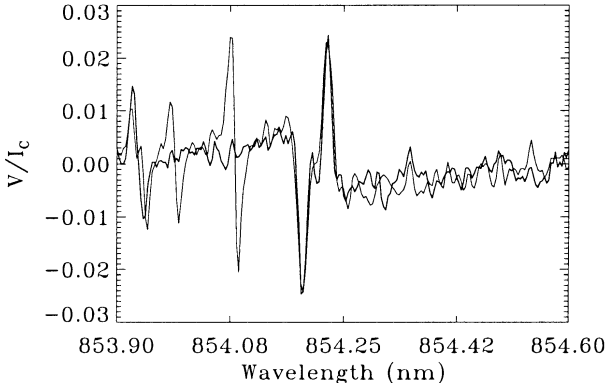

Fig. 3. Comparison between the measured Stokes *V* (thick) and Stokes *V* obtained with the weak field approximation. Both profiles are very similar for the CaII lines. The discrepancy in amplitude for the FeI line at 853.8 nm comes from the multiplicative factor that was used to adjust the CaII line (non fitted lines are telluric lines). The two lines on the blue wing of CaII are iron lines.

However, we will show in the following that this "polarity reversal" does not really exists.

3.2. Evidences for misinterpretation

To test the presence or not of a polarity reversal, we compare the observed Stokes *V* profiles with the *V* profiles coming from the weak field approximation formula. With such approach, if a polarity reversal is indeed present, the sign of the fit would be incorrect for the chromospheric lines but correct for the photospheric structures. Figure 3 shows the comparison between the Stokes *V* obtained from the weak field approximation and the observed Stokes *V*. The correct fitting of both CaII and photospheric lines shows that the reverse sign of the peak of Stokes *V* is not due to a magnetic field reversal.

As argued by Sánchez Almeida (1997), the line core emission can be undetected if it occurs in a dark structure of a sunspot. And, indeed, Fig. 4 (middle panel on right) shows the Stokes *I* profile of CaII which clearly exhibits such emission profile.

Finally, Fig. 4 presents another case of reversal of the Stokes *V* peaks for CaII together with FeI and Hα. CaII line presents an apparent reversal of the Stokes *V* peak, while Hα does not. An interpretation in terms of magnetic field reversal is hardly possible since the two lines are formed almost at the same solar height. The only way to explain this discrepancy is that the opposite sign of the Stokes *V* peaks in CaII and Hα is only due to the presence of an emission in the CaII core while Hα does not exhibit such a feature.

4. Conclusions

At first glance, chromospheric magnetic field measurement seems to show a polarity reversal of the magnetic field compared to the orientation at photospheric level. However, we have presented here several evidences from observational data that such phenomena is not real, but mainly due to the presence of core emission of an absorption line. We must quote that the results are representative of the whole set of data running from the July 2nd to July 6th 2002. We found several areas with such phenomena in CaII IR line, but we never found evidence of Stokes *V* peak reversal (compare to the photospheric lines) from Hα line except in region of flares. This difference between the two lines is easily explained by the difference of sensitivity of the two lines in respect to the temperature.

The reality of the existence of polarity reversal (or "transient events") was already discussed and rejected from observational point of view (Lotzitskaya & Lozitskiĭ 1982; Patterson 1984). However, these studies discussed the subject based on photospheric lines in case of flares. The study presented here afford new arguments from spectro-polarimetric observations of photospheric and chromospheric lines measured strictly simultaneously, in active region away from flares. It gives observational evidences for the theoretical conjecture of Sánchez Almeida (1997).

Acknowledgements. The authors thank the referee for the very pertinent remarks and J. Sánchez Almeida for the interesting discussions. A. Vecchio acknowledges the support given by THEMIS telescope.

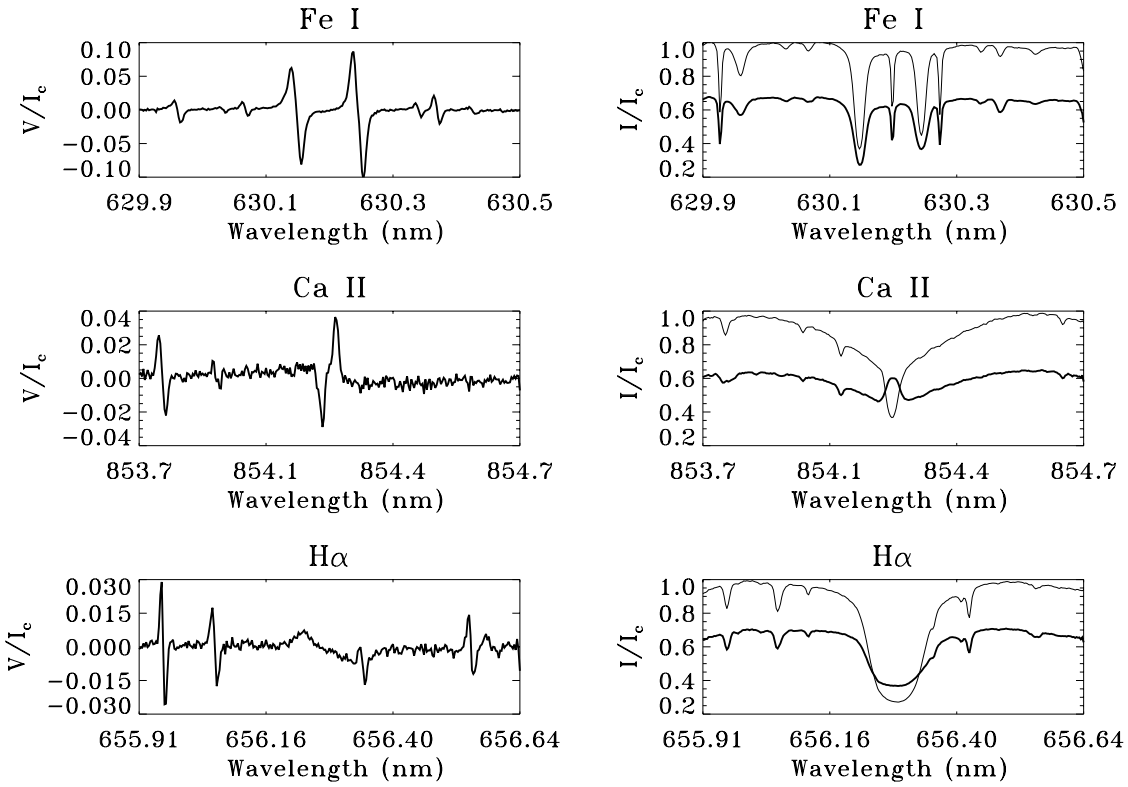

Fig. 4. Stokes *V* (left) and *I* (right) for FeI, CaII and Hα (from top to bottom), relatively to the quiet sun intensity continuum. Also superimposed on Stokes *I*, the intensity in a quiet Sun region around the "polarity reversal" area.

References

Li, W. A., & Zhang, H. 1994, Sol. Phys., 151, 1

Lotzitskaya, N. I., & Lozitskiĭ, V. G. 1982, Soviet Ast. Lett., 8(4), 270

Patterson, A. 1984, ApJ, 280, 884

Sánchez Almeida, J. 1997, A&A, 324, 763

Skumanich, A., Lites, B. W., Martínez Pillet, V., & Seagraves, P. 1997, ApJS, 110, 357

Wang, J., & Shi, Z. 1992, Sol. Phys., 140, 67

Mem. S.A.It. Vol. 74, 811

Memorie della

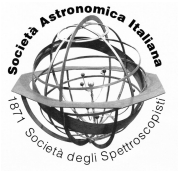

Phase diversity at THEMIS : first implementation

D. Del Moro[1,2], S. Criscuoli[3], J.A. Bonet[4], I. Márquez[4], C. Lemen[2], C. Briand[2]

[1] Dipartimento di Fisica, Università di Roma "Tor Vergata", I-00133 Roma, Italy
[2] THEMIS, E-38200 La Laguna, Tenerife, Spain
[3] INAF- Osservatorio Astronomico di Roma, I-00040 Monte Porzio Catone, Italy
[4] Instituto de Astrofísica de Canarias, E-38200 La Laguna, Tenerife, Spain

Received *date will be inserted by the editor*; accepted *date will be inserted by the editor*

Abstract. Phase diversity techniques actually provide robust post-processing methods to restore solar images degraded by seeing-optical aberrations. We present preliminary results of the application of a Partitioned Phase-Diverse Speckle (PPDS) technique at THEMIS. The images have been acquired using the IPM broad-band CCD camera and reduced using a suitable IDL code. The spectral analysis of unrestored/restored images shows a significant improvement of image quality, achieving diffraction limited resolution.

Key words. Phase diversity – Solar Convection – Numerical Techniques

1. Phase Diversity: general overview

Phase Diversity (PD) techniques are post processing procedures for correcting aberrations induced by instrument and by atmosphere in individual isoplanatic patches. These techniques do not require sophisticated observing instrumentation and are not based on theoretical models describing the atmospheric degradation, but work on simple optical principles. Their purpose is to determine the wavefront aberration expansion in terms of Zernike polynomials at the entrance pupil of the telescope, from the information contained in two simultaneously recorded images, one focused and the other affected by a known amount of defocus (Gonsalves and Chidlaw (1979)).

Send offprint requests to: delmoro@roma2.infn.it

2. Partitioned Phase-Diverse Speckle restoring

A single pair of focused/defocused images may not contain enough information to correctly estimate wavefront aberrations, as information at certain frequencies may be irretrievably lost as a consequence of the aberrations themselves. This may lead to artifacts presence in restored image. In order to correct for this effect, multiple image pairs may be used, accomplishing a more robust estimation of the real scene. As suggested by its name Partitioned Phase-Diverse Speckle (PPDS) procedure blends

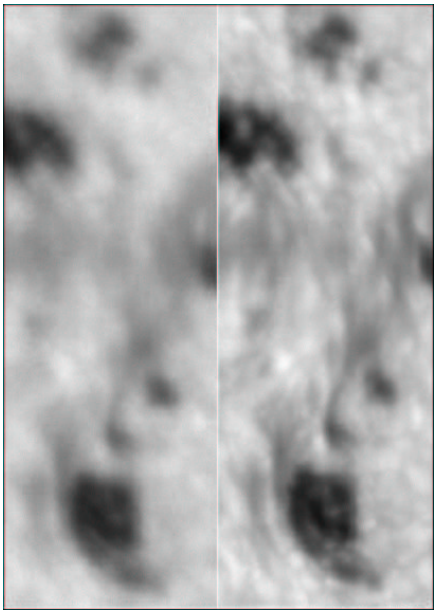

Fig. 1. Pair of focused (right) and defocused (left) images.

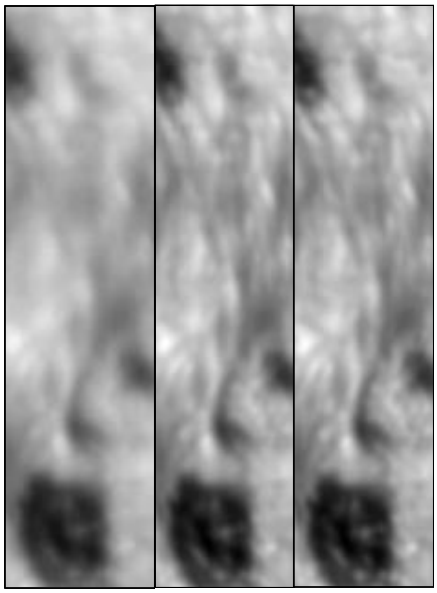

Fig. 2. Left: best of the three original images used in the PPDS process. Center: restoration without considering the central obscuration. Right: restoration taking into account the central obscuration.

the concepts of PD and Speckle imaging. It requires the collection of multiples image pairs in a relatively short time, to be sure we are imaging the same scene in all, as the goal of the PPDS is to estimate the common object and the phase aberration of each image of the pairs series (Löfdahl and Scharmer (1994); Paxman et al. (1996)).

3. Observations

Figure 1 shows a pair of near infrared (850 nm) continuum images (after dark current subtraction and flat-fielding) from the series acquired at THEMIS on May 15, 2002 between 12h05 and 12h16 in PD configuration. The PD system was implemented at the secondary focus environment of the telescope, using the white light channel of the IPM instrument. This implies that the low order aberrations we measure include the telescope and transfer optics as well as part of the optical path of the IPM system. The exposure time was of 20 ms and, due to the provisional PD set-up for testing, the field of view was reduced to 14" x 30". The pixel scale is 0.057".

Residual small aberrations were removed by implementing in the PPDS algorithm the option of considering a central obscuration in the telescope entrance pupil. Figure 2, from left to right, shows: a) the best of the three original images used in the PPDS process, b) a first attempt of restoration without considering the central obscuration of the THEMIS pupil, and c) the final result once the central obscuration is taken into account.

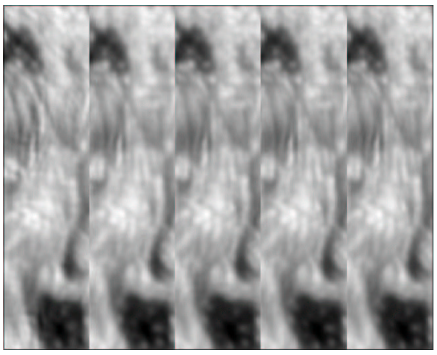

Fig. 3. From left to right: restored frames obtained by combining 1, 2, 3, 4 and 5 PD images respectively.

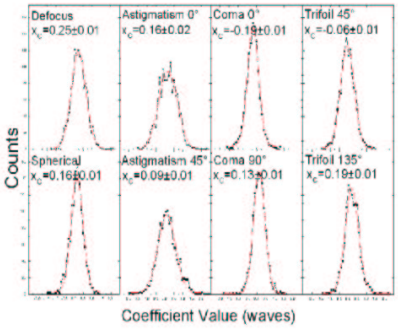

Fig. 4. Zernike coefficients histograms from 75 PPDS restorations.

In Figure 3 five restored images are shown, obtained by combining from 1 to 5 PD images respectively. In the first two cases some restoration artifacts can be distinguished. By adding more images in the speckle procedure, the artifacts disappear, leading to an optimal restoration.
The spectral analysis of the restored images revealed that all the frequencies until the cut-off due to diffraction limit of THEMIS (0.19" @850 nm) have been restored.

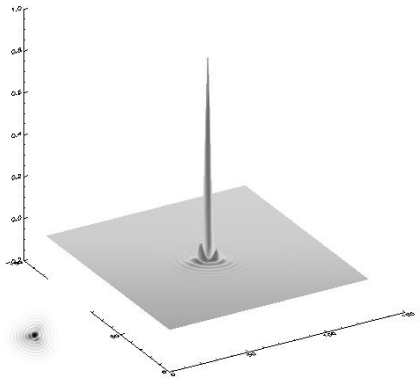

Fig. 5. 3D view and logarithmic view (lower left) of the PSF (Strehl ratio = 81%) reconstructed from the Zernike coefficient mean values from Figure 4.

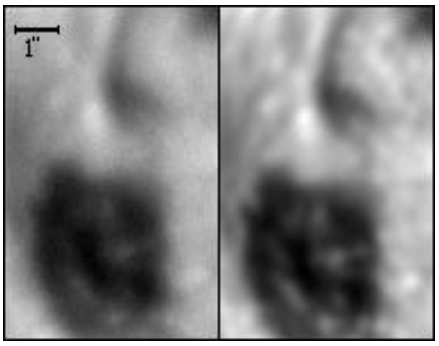

Fig. 6. Left: detail of original image used in the PPDS process. Right: same detail in restored image.

4. Estimation of the Telescope Aberration

A 1 min series of 75 images has been restored by PPDS (16 isoplanatic patches/image). From the single estimate of the wavefront error for each patch a total of 1200 sets of aberration parameters (Zernike coefficients) are obtained. For each

coefficient the correspondent histogram has been produced. A Gaussian distribution is expected for the atmospheric aberrations. The mean of such a distribution should be zero when observing with a perfect optical setup. Consequently, the mean of the histograms empirically obtained, will reveal the amount of aberration stemming from the instrument. In Figure 4 we report the histograms for the Zernike coefficients from 4 to 11 (namely: defocus, astigmatisms, comas, trefoils and spherical aberrations). A Gaussian fit is overplotted to each distribution. The coefficient values are expressed in waves @850 nm, this implies a mean defocus value (the largest aberration obtained) smaller than 3.5 mm versus a focal length of ~ 57 m. The intrinsic PSF of this optical setup has been reconstructed (see Figure 5) from the mean values of the Gaussian fits. The FWHM of this PSF is 0.19 arcsec @850 nm and the Strehl ratio is 81%.

5. Conclusions

Phase diversity techniques actually provide robust post-processing methods to restore solar images degraded by seeing-optical aberrations. We have successfully PPDS restored a series of images acquired at THEMIS. Although in this first implementation was not possible to discern between aberrations stemming from the telescope or from the transfer optics, we want to emphasize the image quality reached, which allows s ub-granular structure studies (Figure 6): the results presented show that phase-diversity techniques allow diffraction-limited imaging even with a large solar telescope.

Acknowledgements. Results based on observations made with the THEMIS telescope operated on the island of Tenerife by THEMIS/CNRS-INSU/CNR in the Spanish Observatorio del Teide of the Instituto de Astrofisica de Canarias.
J.A.B. is grateful to M.G. Lofdahl for providing his original PPDS source code in ANA and for his advice in the construction of the IDL code basis of the present work.
This project is partially financed by the Spanish MCyT project PNAYA2001-1649.

References

Gonsalves, R.A. and Chidlaw, R. 1979, Proc. SPIE, 207, 32.
Löfdahl, M.G. and Scharmer, G.B. 1994, A&A Supp. Ser., 107, 243.
Paxman, R.G., Seldin, J.H., Loefdahl, M.G., Scharmer, G.B., Keller, C.U. 1996, ApJ, 466, 1087.

Astron. Nachr./AN **324**, No. 4, 309–312 (2003) / **DOI** 10.1002/asna.200310106

Pointing and tracking analysis of alt-azimuthal multi-focus telescopes: the THEMIS case

G. MAINELLA[1,⋆], C. BRIAND[1,2], L. MARÉCHAL[1] and C. LE MEN[1]

[1] THEMIS, c/o Instituto de Astrofísica de Canarias, calle Vía Láctea s/n, E-38200 La Laguna, Canarias, Spain
[2] LESIA, Observatoire de Paris, Place J. Janssen, F-92195 Meudon CEDEX, France

Received 28 October 2002; accepted 30 January 2003; published online 20 May 2003

Abstract. We discuss the pointing and tracking configuration of THEMIS which may be considered as representative of those alt-azimuthal telescopes with an optical configuration with multiple focal planes, not all locked to both the alt-azimuthal coordinates. In the THEMIS case two focal planes are present. The primary focus F1 is locked to the alt-azimuthal mount, while the secondary focus F2 (which is used by the instruments), is only locked to the azimuth angle.
The different contributions to the final accuracy of both absolute pointing and tracking as observed at F2 are defined, and an extimation of the contribution of each component of the whole chain which affects the field position at F2 (software, mechanical and optical) is given.
The experimental data are the result of a test campaign carried on at THEMIS in February and March 2002. We can say that (a) for all the used observing configurations, the tracking accuracy is coherent at any point along the trajectory with the correspondent absolute pointing accuracy, which is an indication for the quality of the telescope dynamical performances (b) the main contribution to the residual field shift which is observed at F2 arises from the opto-mechanical alignment configuration of the optics between F1 and F2, which therefore is the crucial point for such multi-focus configuration.
More informations can be found at the official THEMIS website (`http://www.themis.iac.es`).

Key words: Sun – telescopes – techniques: miscellaneous

1. Double-focus configuration at THEMIS

The double-focus configuration of THEMIS is illustrated and described in Fig. 1. The tracking of a target at F2 can be seen as the result of two combined processes:

a) tracking the target at F1, and
b) tracking image of F1 at F2.

We will see here these two points in detail. Then, in Sect. 3, we will see how such performances are checked.

1.1. Tracking the target at F1

The guide of the alt-azimuthal mount (and thus of the telescope tube with the primary focus F1), is completely passive, that is there is no real-time correction using external references. The tracking is a sequence of re-alignments to the absolute position the target is supposed to be. Thus the tracking accuracy will never be better than the absolute pointing accuracy corresponding to the points along the trajectory.

Correspondence to: mainella@themis.iac.es
⋆ supported by CNR

At this level, the accuracy of both absolute pointing and tracking is limited by:

1) the computation of both the equatorial and the alt-azimutal coordinates of the target, including the correction for the atmospheric refraction effect;
2) the design and performance of the servo-control of the pointing axes;
3) the accuracy and stability of the encoders of the pointing axes (azimuth and elevation);
4) the dynamic performance of the telescope mount, that is its response to the driving impulses;
5) the residual misalignments of the telescope itself (mount axes, tube, mirrors M1 and M2)

The combined effect of items 1 and 2 is fully described in Mainella & Briand (2002). Items 2 and 4 only affect the coherence of the tracking accuracy with the absolute pointing accuracy corresponding to the points along the trajectory. That is, an unsatisfactory performance will move the tracking accuracy away from the absolute pointing accuracy.

Refraction correction (item 1) was introduced since observations are to be performed almost at any elevation in

 0004-6337/03/0406-0309 $ 17.50+.50/0

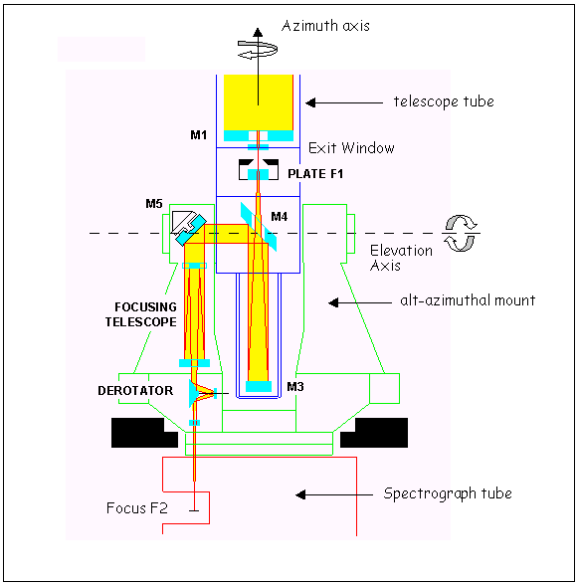

Fig. 1. The optical chain from the telescope entrance window to the spectrograph entrance presents two focal points : a primary focus F1 and a secondary focus F2. The primary focus F1 is located inside the telescope tube which is supported by the alt-azimuthal mount, thus locking F1 to both the azimuth and the elevation pointing angles. The secondary focus F2, instead, is located in the spectrograph tube which is appended at the mount bottom, and therefore is only locked to the azimuth angle. The image of F1 is transferred to the secondary focus F2 by means of a Transfer Optics (M3, M4, M5, focusing telescope and derotator): the combined effect of M4 and M5 is supposed to project all the directions in the elevation plane onto the same direction going from M5 to F2.

different environmental conditions (i.e. atmospheric temperature and pressure), while THEMIS was designed with a prismatic window for the telescope tube to correct the effect at 30 degrees of elevation, in standard conditions. Therefore the entrance window correction is treated just as an elevation offset and corrected through the alt-azimuthal correction formula which will be discussed in Sect. 2, while the Stone refraction formula (Stone 1996) is used to apply the correction to the target elevation computed so far. The temperature dependence is stronger that the pressure one. Water pressure is not taken into account.

1.2. Tracking the F1 image at F2

The transfer of the F1 image to F2 is a dynamic, not a static, process. In fact two rotations are involved:

1) the movement of the telescope tube (with F1, M3 and M4) along the elevation angle, and
2) the rotation of the derotator optics.

Because of the alt-azimuthal drive, the field observed at F1 experiences a rotation; and the image of F1 is transmitted at F2 with a further rotation due to the mutual rotation of the mirrors M4 and M5 which occurs when the telescope elevation changes.

To keep the orientation of the F1 instrumentation (i.e. a preslit) parallel to a desired axis in the sky (i.e. solar north) all such instrumentation is de-rotated around the telescope optical axis, while the further rotation at F2 is compensated by means of a derotator located just before this focal plane.

Thus, at this level, the accuracy of both absolute pointing and tracking is limited by the design, setup ad performance of the Transfer Optics (see Fig. 1), which can be seen as an open-loop system (like the telescope driving) depending only on the quality of its opto-mechanical setup.

An ideal optical alignment would imply, for any elevation angle:

– a fixed light path between M4 and M5, on-axis with the elevation rotation axis
– a fixed, vertical light path coming out from M5
– no modification in the direction of the light path passing through the derotator

Therefore a residual image displacement (drift/rotation) at F2 may be induced by :

a) the residual misalignments of the derotator optical and mechanical (rotation) axis with respect to the direction of the optical path coming from M5
b) the residual misalignments of the system M3+M4+M5, which produces a time dependent variation of the direction of the light path going from M5 to the derotator.

2. Use of an alt-azimuthal correction formula for the THEMIS open-loop driving configuration

The residual pointing errors due to mechanical flexions, opto-mechanical misalignments and any kind of offset (i.e. encoder offsets) can be minimized by introducing a correction formula in the process of coordinate computation. The parameters of such formula are established by means of a mapping procedure which consists in sampling the alt-azimuthal distribution of the pointing error using bright stars as point-like targets. The correction formula is then just an interpolation formula: it can either have an analytical form (deduced from the assumption that the error sources are well identified and their consequences can be reproduced) or can correspond to a full spherical harmonics development.

The solution adopted at THEMIS, until now, is to use a correction formula with a peculiar analytical form whose parameters are computed by observing the reference targets at F2. The formula is an adaptation of the one chosen by M. Messionier for the Laser-Lune telescope of CERGA (in France): 8 coefficients are used to describe the errors in elevation, 12 for the azimuth. This solution presents two difficulties:

1) a zenith singularity arises because of terms like $1/cos(\theta_{elevation})$; such terms are present if the true azimuth difference $\Delta(\theta_{azimuth})$ is considered instead of the true angular distance in the sky $\Delta(\theta_{azimuth}) \cdot cos(\theta_{elevation})$; in France the sun never exceeds 60 degrees of elevation while in Tenerife this can be as high as 85 degrees;

2) since the pointing error is mapped at F2, the resulting formula is supposed to handle, as best as possible, the defects of both tracking processes: target at F1 and F1 image at F2; but of course it will not be able to handle the dynamical errors arising from the opto-mechanical misalignments of the Transfer Optics. In fact, in this case, the alt-azimuthal error depends not only from the alt-azimuthal position but from one more variable: the angle between the derotator axis and the light-path coming from M5. Such variable depends on orientation of the F1 instrumentation which determines the derotator angular position, and the alt-azimuthal error is not sampled also for this variable in the mapping process.

3. Experimental results for the absolute pointing and tracking accuracy

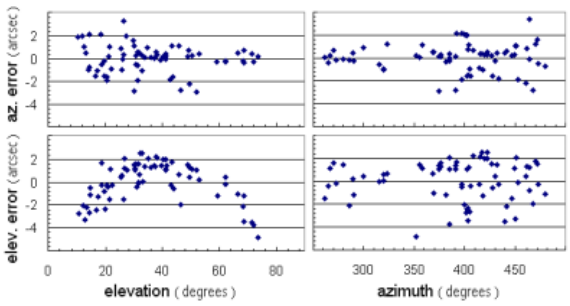

Fig. 2. Residual absolute pointing error observed at F1. A sample of some 70 bright stars (magnitude ≤ 3) was used for the mapping procedure, with $\mid \delta \mid \leq 35$ degrees, in order to improve the accuracy for solar observations. The stars were observed with a video camera mounted at F1. No field derotation was applied. The errors were measured by displacing the telescope itself and reading the correspondent, converted, encoder increment.

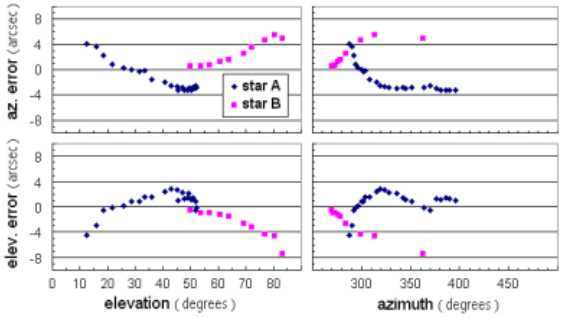

Fig. 3. Absolute tracking error observed at F1 for two stars with respectively $\mid \delta \mid = -9^\circ 23'$ (A) and $\mid \delta \mid = +21^\circ 28'$ (B). Same experimental setup as described in Fig. 2, with the displacement measured at regular intervals.

We considered three subsequent steps in order to isolate the different contributions to the final accuracy :

1) if the parameters of the alt-azimuthal correction formula are obtained by mapping the pointing errors at F1 then, when the formula is applied, the minimized residual absolute pointing errors observed at F1 will result only from the effect of the four items described at Sect. 1.1 ; an estimation of the combined effect of items 1 and 2 is reported in Mainella & Briand (2002); Figs. 2 and 3 show the observed distribution in elevation and azimuth of, respectively, the residual absolute pointing error and the tracking error;
2) if the correction formula is computed at F2 and we observe at F2, with the derotator fixed, only the effect of item a) of Sect. 1.2 will be present; no further variable is introduced besides the two alt-azimuthal coordinates and therefore the computation and the application at F2 of the correction formula is quite efficient; we can estimate, by comparison, this effect; Figs. 4 and 5 show the observed distribution in elevation and azimuth of, respectively, the residual absolute pointing error and the tracking error; Fig. 6 shows evolution of the position of a sunspot during tracking;
3) in the full standard configuration (correction formula computed at F2, arbitrary orientation of the instrumentation at F1 and detotator active) a third variable, as described in Sect. 2, is actually introduced but not taken into account when computing the formula; in this case also the effect of item b) of Sect. 1.2 will be present, and we can estimate it by comparison; Fig. 7 shows the evolution of the position of a star during tracking.

We see that in cases 1 and 2, the tracking accuracy is coherent at any point along the trajectory with the correspondent absolute pointing accuracy, and that the result does not change when the tracked target is the solar disk. Case 3 shows that the crucial point in the double-focus THEMIS configuration is the design and setup of the Transfer Optics.

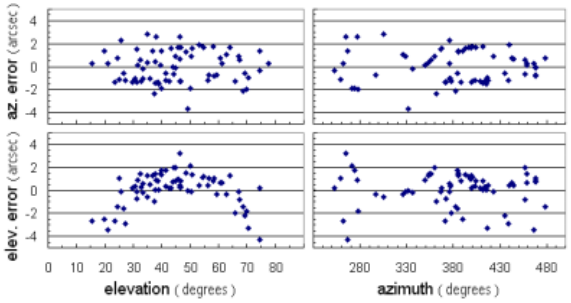

Fig. 4. Residual absolute pointing error observed at F2. A sample of some 70 bright stars (magnitude ≤ 3) was used for the mapping procedure, with $\mid \delta \mid \leq 35$ degrees, in order to improve the accuracy for solar observations. The stars were observed with a video camera mounted at F2. No field derotation was applied, either at F1 or at F2. The errors were measured by displacing the telescope itself and reading the correspondent (converted) encoder increment.

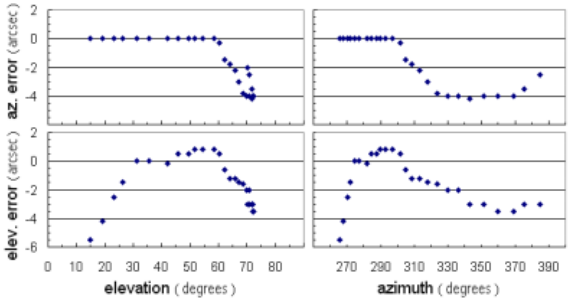

Fig. 5. Observed absolute tracking error for a star with $\mid \delta \mid = -3^\circ 42'$. Same experimental setup as described in Fig. 4, with the displacement measured at regular intervals.

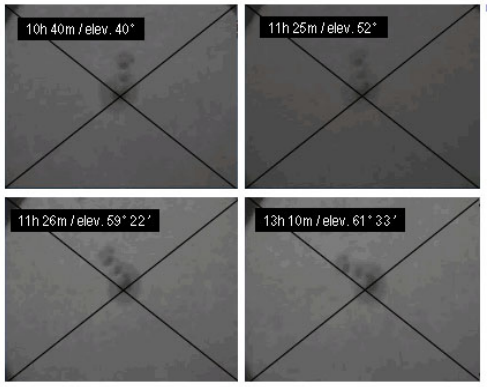

Fig. 6. A sunspot tracked during 2h30m with the same configuration as described in Fig. 4. The field rotation is due to the fact that the derotator is fixed. The residual shift is coherent with the accuracy shown in Figs. 4 and 5.

Acknowledgements. We want to thank A. Sainz Dalda for his help during the test campaign of February-March 2002 and J.L. Leroy for the useful informative notes he left at THEMIS about the pointing system.

References

Mainella, G., Briand, C.: 2002, NCimC, in press
Stone, R.C.: 1996, PASP 108, 1051

Appendix A: Pointing axes encoders and dynamical performance

The elevation and azimuth axes are equipped with both absolute and incremental encoders. The first are mounted on the motor axis and are used only for initialization and security tasks, the latter are mounted in contact with the axis wheel and are used as an independent external reference for the axis position. The incremental encoder accuracy is 0.0225 arcsec and 0.015 arcsec respectively for the elevation and the azimuth.

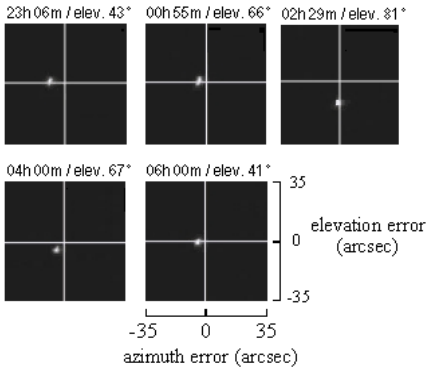

Fig. 7. A star tracked during some 9 hours with the full standard configuration (see text, item 3 of Sect. 3). The observed drift reaches more than 10 arcseconds.

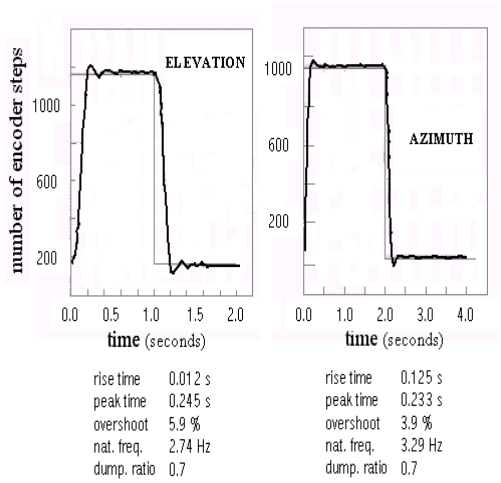

Fig. 8. Response to a step move for the elevation and azimuth axes (see Appendix A). The electronic and mechanical parameters determining the response profile are set at the level of the axis driving control software.

Due to the peculiar choice for the incremental encoder mounting in the original THEMIS design, a loss of encoder steps is possible during the telescope operation, induced by imperfect contact between the axis wheel and the encoder wheel. Such contact may also be affected by the dynamical behaviour of the telescope.

The whole system (telescope, alt-azimuthal mount, spectrograph) responds like a damped harmonic oscillator to the driving impulse. The main parameters of the dynamical behaviour (rise time, peak time, overshoot, natural frequency and damping ratio) can be estimated by monitoring the response of the system to a single, step impulse. Fig. 8 shows the test results for both the elevation and the azimuth axes.

Chapitre 3

Microphysique des plasmas naturels

3.1 Introduction

Le Soleil injecte une grande quantité d'énergie dans le milieu interplanétaire. L'énergie cinétique et magnétique, introduite aux grandes échelles (lors de CME, Flare etc), cascade par turbulence vers les échelles microscopiques où elle est convertie en énergie "thermique" (voir Fig. 3.1). Dans de nombreux plasmas spatiaux ou de laboratoire, l'échelle typique dissipative est de plusieurs ordres de grandeur inférieure aux échelles dynamiques et cinétiques. C'est par exemple le cas des plasmas de laboratoire à haute température ou du vent solaire. Dans ce dernier cas en effet, le libre parcours moyen est de l'ordre d'une unité astronomique. Ce type de plasma peut donc être considéré sans collisions. La première question qui se pose est donc de **comprendre les mécanismes de "dissipation" (redistribution) de l'énergie dans un plasma non collisionnel**. Si l'échelle exacte à laquelle se produit cette dissipation est encore une source de débat, il est clair qu'elle se situe vers ou en-dessous de l'échelle protonique.

Par ailleurs, une description fluide de ces plasmas a souvent donné de bons résultats pour décrire les structures à grande échelle [1] ainsi que leur évolution. Les mesures *in situ* ont révélées que les fonctions de distribution des particules sont beaucoup plus proches de distributions thermiques que ne le laisserait prévoir la quasi absence de collisions (voir Fig. 3.2, en haut à gauche). Ces mêmes mesures dans différents environnement spatiaux (vent solaire, foreshock des planètes) ont toutefois mis en évidence la présence de faisceaux de particules (Fig. 3.2 en bas à droite), ainsi que d'un strahl (queue d'électrons supra-thermiques) dans la fonction de distribution des électrons. Les deux questions suivantes se posent alors : **quels processus peuvent jouer le rôle des collisions pour expliquer le coeur des fonctions de distribution ? Comment expliquer la présence de particules supra-thermiques ?** Il faut s'intéresser aux processus cinétiques se déroulant aux petites échelles (de l'ordre ou en dessous d'échelles caractéristiques telles que rayon de giration des protons, épaisseur de peau et longueur de Debye) pour expliquer la présence de telles structures dans les fonctions de distribution.

Nous avons vu au chapitre précédent que des reconnexions des lignes de champ magnétique étaient possibles dans la couronne solaire ou à l'interface entre les magnétosphères planétaires et le vent solaire. La reconnexion n'est pas un problème simple. Elle suppose que la condition de "champ gelé" soit violée aux échelles magnéto-fluides, en des temps compatibles avec les observations. Dès les premiers modèles basés sur un changement de la résistivité local du

1. par rapport aux rayons de Larmor des protons

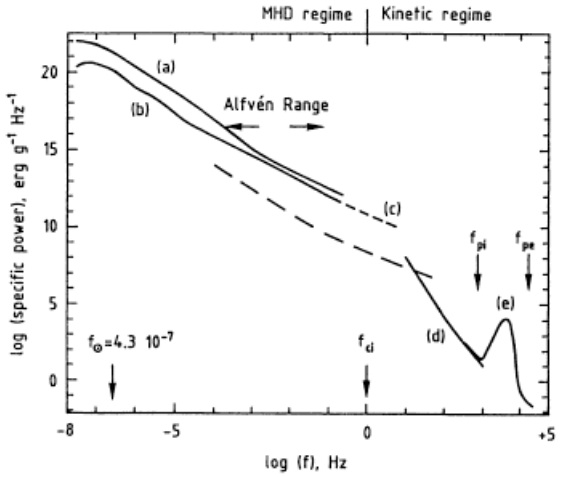

FIGURE 3.1 – Illustration de la cascade turbulente de l'énergie magnétique. Les cassures successives des pentes indiquent des changement de régime turbulent

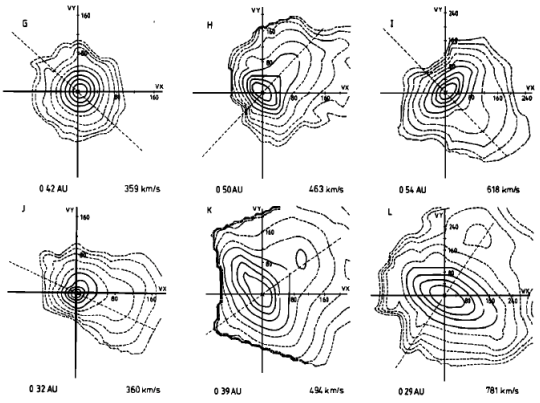

FIGURE 3.2 – Functions de distribution des protons observées dans différentes conditions de vent solaire et à différentes distances héliocentriques (extrait de Marsch et al. 1982)

plasma jusqu'aux modèles plus récents faisant intervenir l'inertie des électrons et des processus turbulents, l'approche cinétique est nécessaire pour expliquer les changements des propriétés électriques locales du plasma.
Voyons un autre exemple pour lequel les effets cinétiques sont déterminants. Il s'agit des chocs. Le vent solaire est l'écoulement d'un plasma supersonique et super-Alfvénique. Différents types de chocs peuvent donc se produire en fonction de l'obstacle rencontré : choc stationnaire (à l'avant des magnétophères), choc propagatif (CIR), ou des chocs de "blast" (dans les éruptions solaires ou l'explosion des supernovae). Les équations MHD donnent une description relativement satisfaisante (au moins au premier ordre) de l'état du plasma de part et d'autre du choc mais n'expliquent pas les processus de dissipation au sein du choc (qui apparaît alors comme une boite noire). Or pour comprendre la structure d'un choc, il faut comprendre les mécanismes de dissipation. La formation d'un état turbulent localisée dans le choc permettrait la transformation de l'énergie mécanique (écoulement d'un plasma) en énergie thermique. Le milieu étant non collisionnel, le développement d'instabilités dans le plasma est requis pour expliquer la génération d'un tel état turbulent. Ces instabilités génèrent, entre autres, des particules suprathermiques et des ondes dont les vitesses de groupe sont supérieures à la vitesse de l'écoulement incident sur le choc, et qui vont produire un précurseur en amont du choc, un

"foreshock" dans la terminologie habituelle.

Il est intéressant de noter que ces processus cinétiques se développent aux échelles caractéristiques des particules (rayon de gyration de particules, longueur de Debye) mais induisent des perturbations irréversibles aux échelles macroscopiques. La reconnexion magnétique par exemple engendre une modification de la topologie du milieu permettant la propagation de plasma dans des espaces préalablement interdits. La présence d'une onde de choc dissipe l'énergie d'un écoulement, le faisant passer de supersonique à sub-sonique. Ces deux processus participent également activement à la génération de particules de haute énergies (par exemple les protons passent de quelques keV dans le vent solaire à quelques centaines de keV dans le foreshock de la Terre). Enfin, rappelons ce que nous disions dès le premier chapitre : la présence de particules suprathermiques observées dans le vent solaire ne peut s'expliquer qu'à partir de modèles cinétiques.

La cascade "turbulente" des grandes vers les petites échelles apporte des perturbations locales de pression, de température et des assymétries des fonctions de distribution des particules, autant de sources d'énergie libre pour le développement d'instabilités de type fluide ou cinétique. La croissance d'instabilités cinétiques dans un plasma est due à des perturbations des fonctions de distribution des particules (électrons et/ou protons). Or, le temps caractéristique des protons et des électrons est très différent : les électrons ont une fréquence caractéristique autour de $f_{pe} = \sqrt{e^2 n_e/\epsilon_0 m_e}$ tandis que les ions peuvent être considérés comme immobiles à ces fréquences ($f_{pi} \approx 10^{-2} f_{pe}$). Dans la gamme $f \ll f_{pe}$ les électrons se comportent comme un fluide. Le transfert d'énergie direct entre ces deux espèces est donc quasi impossible. Les couplages ondes-ondes et ondes-particules jouent alors un rôle essentiel pour transférer de l'énergie entre les différentes espèces. De plus, les couplages ondes-ondes peuvent aussi contribuer à l'émission d'ondes électromagnétiques, autorisant ainsi le transport d'énergie sur de très grandes distances. Parmi toutes les ondes plasmas pouvant être déstabilisées, les ondes de Langmuir et les ondes acoustiques ioniques sont particulièrement intéressants pour deux raisons principales. D'une part elles permettent des transferts d'énergie sur une gamme étendue de fréquences et de nombres d'onde. D'autre part, ces ondes se rencontrent dans de nombreux environnements que ce soit dans le vent solaire ou les magnétosphères des planètes.

3.1.1 Ondes autour de f_{pe} et ondes acoustiques ioniques

Les ondes autour de la fréquence plasma sont observées dans beaucoup d'environnement : le vent solaire "libre" (dans les émissions de Type II liées aux CME, et de Type III liées aux flares, dans les trous magnétiques, dans l'environnement des ondes de choc interplanétaires), dans le foreshock de la Terre, dans la zone aurorale et les cornets polaires terrestres ainsi que dans la queue des comètes. Il s'agit pourtant de milieux très différents : si le vent solaire et le foreshock peuvent être considérés comme des milieux peu magnétisés et peu denses ($f_{pe} \leq 30$kHz), les zones aurorales et cornets polaires sont par contre très magnétisés et beaucoup plus dense (1 MHz $\leq \mathrm{f_{pe}} \leq$ 10 MHz). L'observation des ondes Langmuir permet ainsi un diagnostic du milieu.

La relation de dispersion des ondes de Langmuir dans un milieu non magnétisé s'écrit :

$$\omega_L \;=\; \omega_p \left(1 + 3k_L^2 \lambda_D^2\right)^{1/2} \tag{3.1}$$

avec $\omega_p = \sqrt{4\pi e^2 n_e/m_e}$ la fréquence (angulaire) plasma, $\lambda_D = \sqrt{\epsilon_0 k_b T_e/n_e e^2}$ la longueur de Debye, et n_e la densité électronique du milieu. Les autres variables ont leurs significations

standard (charge et masse de l'électron, permittivité du vide, constante de Boltzmann). Dans le cas d'un plasma magnétisé, un terme correctif apparaît faisant intervenir la fréquence cyclotron et les termes de propagation oblique par rapport au champ magnétique. Ce mode est appelé mode Z. Il se situe légèrement au-dessus de la fréquence plasma.

Une condition nécessaire pour générer des ondes de Langmuir est l'existence d'une dérivée positive (resp. négative) dans la partie des vitesses positives (resp. négatives) de la fonction de distribution des électrons (voir aussi Yoon et al. 2000, pour le cas de propagation oblique). L'instabilité engendre des ondes électrostatiques ayant une vitesse de phase égale à la vitesse des particules dans la partie positive de la dérivée (instabilité résonnante) et une fréquence proche de la fréquence plasma (élargie par les effets thermiques – deuxième terme de l'équation 3.1 [2]). La présence d'un excès de particules supra-thermiques produisant une telle "bosse" dans la fonction de distribution peut être expliquée par la présence d'un ou plusieurs faisceaux d'électrons. Autrement dit, les faisceaux apportent l'énergie libre nécessaire aux développements des instabilités. Les caractéristiques de ces faisceaux (densité, vitesse, homogénéité) conduisent à des instabilités résonnantes, de taux de croissance différents (de nombreux manuels traitent du sujet comme par exemple Mikhailovskii 1974, Tome 1 et 2). Dans tous les cas d'émissions d'ondes de Langmuir, l'une des questions fondamentale est donc de connaître l'origine et les caractéristiques de ces faisceaux d'électrons (voir sections 3.2.2 et 3.2.4).

Des mécanismes de saturation doivent intervenir pour limiter la croissance des ondes engendrées. Pour cela il faut annuler la condition de résonance (changement de la phase de l'onde, plateau dans la fonction de distribution) et/ou dissiper l'énergie des ondes. Dans le cadre de l'approximation quasi linéaire, la saturation de l'instabilité 'bump-on-tail' est assurée par le piégeage des électrons dans le puits de potentiel de l'onde qui engendre un plateau dans la fonction de distribution des électrons, stoppant ainsi la croissance des ondes. Quand l'amplitude des ondes est trop grande, d'autres mécanismes non linéaires viennent assurer la saturation. Il s'agit principalement de couplages onde-onde et onde-particules. L'un des mécanismes les plus étudié est celui de la décroissance paramétrique des ondes de Langmuir car elle est à l'origine des émissions de Type III (voir les travaux récents sur le sujet en section 3.2.5).

Les premières mesures obtenues avec des analyseurs de spectre dans le vent solaire calme ont révélé la présence d'une turbulence dans la gamme $f_{ci} < f < f_{pe}$. L'absence de signature magnétique et la polarisation des ondes ont montré qu'il s'agissait d'ondes électrostatiques. Ces ondes ont finalement été identifiées comme des ondes acoustiques ioniques, subissant un fort décalage Doppler de par leur advection dans le vent solaire. Les ondes acoustiques ioniques sont des ondes électrostatiques de relation de dispersion :

$$(\omega/k)^2 \quad = \quad \frac{C_s^2}{1 + k^2\lambda_d^2} + \gamma T_p/m_p \tag{3.2}$$

avec $C_s^2 = T_e/m_e$ la vitesse du son local. Dans le vent solaire, l'intensité des ondes varie entre 1 à 10μV/m en période de faible activité solaire mais peuvent atteindre quelques dizaines de mV/m dans les périodes plus actives.
Des arguments théoriques montrent que le rapport T_e/T_p est un paramètre fondamental pour la stabilité des ondes. Si $T_e/T_p \approx 1$, la vitesse de phase des ondes ($\sqrt{\mathrm{k(T_e + 3T_p)/m_p}}$) est proche de la vitesse thermique des protons. Elles sont alors fortement amorties par effet Landau. Ainsi,

2. Il est intéressant de noter que dans le cas d'un plasma chaud, la vitesse de groupe est non nulle : les ondes de Langmuir se propagent à une vitesse proportionnelle à la vitesse thermique (très supérieure à la vitesse du vent solaire)

une condition nécessaire pour que les ondes acoustiques ioniques existent est que $T_e/T_p \gg 1$. Or, de récentes observations (Mangeney et al. 1999) montrent que ces ondes existent aussi lorsque $T_e/T_p \leq 1$. Lin et al. (2001) ont aussi montré que la dépendance en température était liée au flux de chaleur électronique : plus celui-ci est fort, plus la corrélation avec le rapport de température est important. L'une des question majeure concernant les ondes acoustiques ioniques est donc de comprendre leur présence dans un milieu où elles sont largement amorties. Deux sources d'énergie libre ont été proposées : (i) flux de chaleur électronique (Forslund 1970), (ii) instabilité double faisceaux sur les ions (Gary 1978). Les observations n'ont pas encore pu départager entre les deux théories.
Les ondes acoustiques ioniques sont associées à des fluctuations de densité du milieu. Elles ont été utilisées pour étudier les couplages d'ondes dans le vent solaire, alors même que le champ électrique de l'onde ne pouvait pas être mesuré (voir section 3.2.5).

3.1.2 Simulations Vlasov

L'approche linéaire de la dynamique des plasmas permet d'expliquer certaines instabilités. Elle s'applique lorsque les perturbations du milieu sont d'amplitude faible, autorisant alors une linéarisation des équations du mouvement et de conservation de la masse. La résolution analytique des équations permet ainsi de déterminer les taux de (dé)croissance des ondes. Mais la théorie linéaire a ses limites. Elle ne prévoit en effet aucun mécanisme de saturation des instabilités (ce qui conduit à une croissance infinie des modes). La saturation de la croissance des ondes fait intervenir des processus non linéaires de couplages onde-onde et onde-particules. Par ailleurs, d'autres processus, telle que la diffusion et de génération de couches limites (ondes de choc par exemple), sont des mécanismes fondamentalement non linéaires.
Les équations de la physique non linéaire ne peuvent généralement pas être résolues analytiquement. Une approche intermédiaire a été développée au début des années 60 (voir par exemple Vedenov 1963) pour essayer de traiter des problèmes avec des instabilités non infiniment petites et tout en permettant une résolution analytique : la théorie quasi-linéaire. Dans cette approche, la fonction de distribution est écrite comme la somme d'une fonction de distribution d'un plasma non perturbée et d'une fonction de distribution moyennée sur les vecteurs d'onde et décrivant l'évolution lente du plasma sous l'impulsion d'une instabilité (le temps de corrélation du champ électrique vu par une particule résonnante est petit comparé au temps d'évolution des quantités moyennes). Cette approche quasi-linéaire est adéquate lorsque l'énergie des ondes est grande devant l'énergie thermique du bruit mais reste faible devant l'énergie thermique totale des particules. L'équation d'évolution de la fonction de distribution ainsi écrite revient alors à une équation de diffusion dans l'espace des vitesses. Toute la question est alors de traiter correctement le terme de diffusion pour prendre au mieux en compte la contribution des particules résonnantes (voir une discussion du sujet dans Adam et al. 1979; Laval and Pesme 1983a,b, 1999).
Un traitement complet de l'évolution d'un plasma non collisionnel, sans *a priori* sur l'amplitude des ondes générées, requiert donc la résolution de l'équation de Vlasov, couplée de façon auto-consistente aux équations de Maxwell-Ampère.

Une description cinétique d'un plasma permet de suivre l'évolution temporelle du système dans l'espace des phases ($\mathbf{x}$,$\mathbf{v}$), sans hypothèse *a priori* sur la distribution des particules. Dans le cas où l'on peut négliger les collisions binaires proches (hypothèse valable pour la plupart des environnements en astrophysique), des particules ayant des vitesses voisines dans un espace physique voisin ne seront pas distinguées. La description de l'évolution du système à travers

l'évolution des fonctions de distribution des particules est suffisant [3].
Si on écrit la conservation du nombre de particules, dans l'espace des phases, dans un milieu sans collisions, on obtient l'équation de Vlasov qui s'écrit en géométrie plane :

$$\frac{\partial f_i}{\partial t} + \vec{v}\frac{\partial f_i}{\partial \vec{r}} + \frac{\vec{F}}{m_i}\frac{\partial f_i}{\partial \vec{v}} = 0 \tag{3.3}$$

avec f_i et m_i la fonction de distribution et la masse d'une espèce i et F une force s'appliquant sur cette espèce. Le bouclage du système est assuré de façon auto-consistente par les équations de Maxwell (qui peuvent se restreindre à l'équation d'Ampère ou l'équation de Poisson dans l'approche électrostatique). Le système Vlasov-Poisson est un système d'équations non linéaires qui ne peut pas être résolu analytiquement, même dans les cas les plus simples.

Simuler les plasmas astrophysiques dans toute leur complexité est actuellement hors de portée. Il s'agirait en effet de tenir compte simultanément de la présence (a) d'un champ magnétique ambiant plus ou moins fort, (b) d'espèces de dynamique différente (électrons et protons au moins, et également d'ions tels que O^+ et H^+), (c) du caractère chaud des plasmas (les effets thermiques sont non négligeables), (d) de fluctuations de densité à différentes échelles, (e) d'anisotropies diverses (température, pression) (f) de faisceaux de particules. En toute rigueur, il faudrait donc être capable de simuler les trois dimensions d'espace et de vitesse, tout en suivant l'évolution temporelle du système. Autrement dit, dans sa généralité, c'est un problème à 6 dimensions (+ le temps) que l'on doit traiter. Même les ordinateurs de dernière génération n'offrent pas encore les puissances de calcul suffisantes pour considérer un tel problème dans un laps de temps raisonnable (quelques jours de calcul). Il faut donc réduire les dimensions du problème d'une façon ou d'une autre. Le choix des dimensions à conserver dépend bien sûr fortement du problème à étudier mais également des compromis acceptables.

Pour résoudre numériquement l'équation de Vlasov, on utilise le fait qu'il s'agit d'une équation aux dérivées partielles linéaire dont la solution est constante le long des caractéristiques (caractère Hamiltonien des écoulements : $d\vec{r}/dt=\vec{v}$, $d\vec{v}/dt=\vec{F}$) qui sont identiques aux équations du mouvement d'une particule. Elle peut se décomposer selon une advection dans l'espace physique et une advection dans l'espace des vitesses, ce qui donne à une dimension :

$$\frac{\partial f}{\partial t} + v\frac{\partial f}{\partial x} = 0 \tag{3.4}$$

$$\frac{\partial f}{\partial t} + \frac{F}{m}\frac{\partial f}{\partial v} = 0 \tag{3.5}$$

Deux approches ont été développées qui utilisent ses propriétés : (a) l'approche PIC (Particle-In-Cell) de nature Lagrangienne - on suit des "macroparticules" le long des trajectoires et pour calculer les moments des fonctions de distribution (les densités de courant et charge) qui interviennent dans les équations de Maxwell, (b) une résolution directe de l'équation aux dérivées partielles (approche Eulérienne), en utilisant des méthodes issues de la solution de l'advection développées en dynamique des fluides (par exemple en décomposant le mouvement selon une advection dans l'espace physique et une advection dans l'espace des vitesses).

L'approche PIC calcule la trajectoire de "macro-particules" sans recours à un maillage dans l'espace des phases. Un petit nombre de macro-particules peut être suffisant pour étudier le

3. Le recours à une description cinétique de type N-corps est nécessaire lorsque les plasmas sont modérément ou fortement couplés, comme par exemple dans le coeur du Soleil ou dans la zone convective solaire

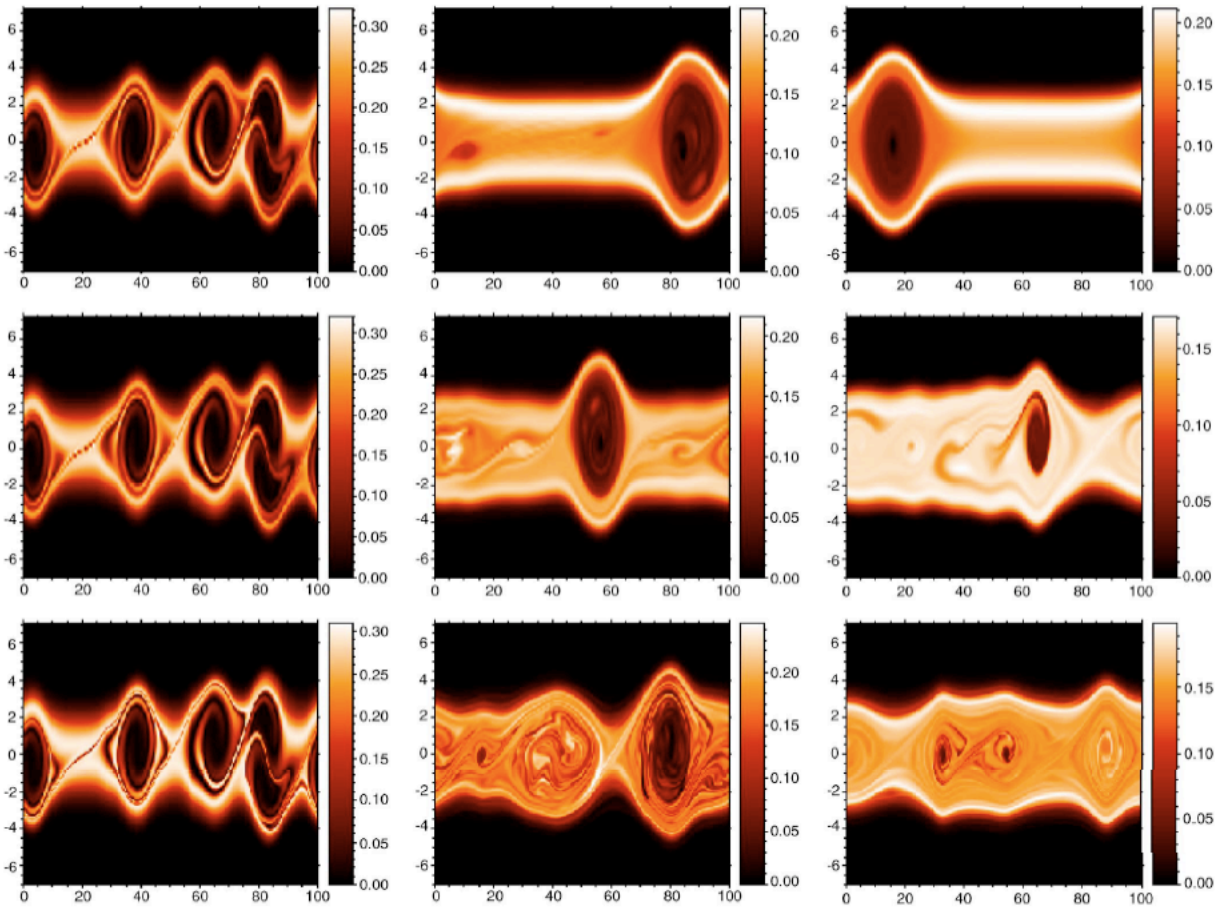

FIGURE 3.3 – Simulations avec une maille différentes pour chaque run. L'état asymptotique du plasma est modifié – nombre de trous dans l'espace des phases – même si la taille des structures générées est semblable. Extrait de Califano et al. (2007)

système. Les temps de calcul peuvent être relativement courts, les simulations sur des domaines étendus et des géométries multi-dimensionnelles abordables. C'est ce qui les a rendu très populaires. Cependant, les codes PIC présentent l'inconvénient majeur d'un bruit numérique élevé, provenant de la discrétisation en macro-particules et évoluant en $1/\sqrt{N}$ où N est le nombre de particules. Cette limite interdit la description fine de certains phénomènes à petite échelle (autour de la longueur de Debye) comme par exemple le développement des trous dans l'espace des phases.

L'approche Eulérienne est quant à elle parfaitement adaptée pour décrire le détail des processus à petite échelle grâce à un bruit numérique très faible et une discrétisation des fonctions de distribution dans l'espace des phases aussi fine que souhaitée. Aucune limitation intrinsèque n'est posée sur la géométrie des problèmes (seules des difficultés de programmation peuvent limiter certaines approches). L'une des difficultés principales de l'approche Eulérienne est cependant d'introduire des échelles de plus en plus petites en vitesses au cours du temps, même en l'absence de force appliquée sur le système. Cette filamentation en vitesse rend le code instable et provoque de la dissipation numérique. Lorsque les gradients générés dans l'espace des phases sont plus petits que l'échantillonnage de la maille, le système peut atteindre des équilibres normalement interdits (Galeotti and Califano 2005; Califano et al. 2007). L'entropie n'est plus conservée et l'état asymptotique du plasma dépend de la grille utilisée (voir Fig. 3.3). Si cette diffusion peut représenter des processus physiques, elle présente l'inconvénient majeur de ne pas

être contrôlée par l'utilisateur. Ces propriétés des "codes Vlasov" les ont rendu impopulaires pendant de nombreuses années. De multiples schémas d'intégration des équations (Fourier-Fourier, Fourrier-Hermite, schéma conservatif, semi-Lagrangienne ...) et différentes techniques de filtrage des hautes fréquences ont été développées pour limiter la génération de structures très fines. Spécifiquement, le code utilisé dans les études présentées dans la section 3.2 est basé sur une intégration par étapes ("splitting scheme") dans l'espace physique d'une part puis dans l'espace des vitesses. L'advection se calcule le long des caractéristiques et se réduit réduit à une interpolation de la fonction de distribution avec, dans le cas du code employé, une méthode de type Van Leer (les autres détails du code sont présentés dans Mangeney et al. 2002).
Les techniques de résolution de l'équation de Vlasov sont maintenant maîtrisées en 1D-1V (une dimension physique, une dimension de vitesse). L'augmentation des capacités de calcul et des mémoires des ordinateurs ont également amener à des progrès importants dans deux directions : (a) multi-dimensionnel (voir par exemple Fijalkow 1999; Eliasson 2003; Valentini et al. 2005; Eliasson 2007), (b) avec les maillages à pas adaptable (Besse and Sonnendrücker 2003; Gutnic et al. 2004; Sonnendrücker et al. 2004).

Une dernière approche pour simuler des processus à grande échelle spatiale est de considérer une espèce suivant un traitement fluide et l'autre suivant un traitement cinétique. Ces codes dits hybrides sont de plus en plus développés (Crouseilles et al. 2005; Valentini et al. 2007; Simon et al. 2009) et vont bénéficier des progrès technologiques permettant la parallélisation des codes.

3.2 Résultats

3.2.1 Ondes électrostatiques à $f \geq f_{ci}$

Un papier de revue sur les ondes électrostatiques "hautes fréquences" faisant le point sur les connaissances observationnelles sur le sujet.

Nonlin. Processes Geophys., 16, 319–329, 2009
www.nonlin-processes-geophys.net/16/319/2009/

Nonlinear Processes in Geophysics

Plasma waves above the ion cyclotron frequency in the solar wind: a review on observations

C. Briand

LESIA, Observatoire de Paris, CNRS, UPMC, Université Paris Diderot; 5 Place Jules Janssen, 92190 Meudon, France

Received: 22 December 2008 – Revised: 2 April 2009 – Accepted: 6 April 2009 – Published: 22 April 2009

Abstract. Since the very beginning of the space venture, discrepancies between hydrodynamic models and observations have raised the attention to the kinetic effects taking place in the interplanetary medium. After discussing some of these constraints, a review on the state of the art knowledge on the waves in the range $f_{ci} < f < f_{pe}$ (f_{ci} – about 10^{-1} Hz – is the ion cyclotron frequency, and f_{pe} – a few 10 kHz – the electron plasma frequency) observed in the free solar wind, i.e., not magnetically connected to the Earth's bow shock, is addressed.

1 Introduction

The solar wind is a supersonic, super Alfvénic flow of tenuously magnetized ($f_{pe} \gg f_{ce}$, where f_{pe} stands for the electron plasma frequency and f_{ce} for the electron cyclotron frequency), highly ionized and almost collisionless plasma. A first predictive, theoretical model of solar wind was given by Parker (1958) from an hydrodynamic approach (steady state expansion of a thermally driven electron-proton flow out of the hot solar corona). However, this model and the many derived from it were unable to explain the high speed solar wind observed at 1 AU without ad-hoc deposition of momentum and/or energy in the corona. Exospheric/kinetic models have provided better descriptions (Lemaire and Scherer, 1971; Maksimovic et al., 1997; Zouganelis et al., 2004). Moreover, detailed in situ measurements of the shape of the particles distribution function also support kinetic approach. Since the collision length is much larger than the typical interaction length between the waves and particles, the distribution functions are expected to deviate from a Maxwellian shape. Observations indeed reveal that the electron distribution functions consist of a core (typically below 50 eV) almost Maxwellian, but also of a halo (representing electrons of higher energy) which strongly departs from a thermal distribution function. In some specific environments (high speed solar wind, far from magnetic sector boundaries), a third component appears: called a "strahl", it represents an enhancement of particles with energies between 100 eV and 1 keV propagating away from the Sun (Pilipp et al., 1987a,b). Moreover, whereas the core of the distributions is rather isotropic, the halo part is highly anisotropic. The high energy particles of the halo present a broad pitch angle while the particles of the strahl are more focused along the magnetic field lines. However, this schematic picture varies considerably according to the solar wind conditions. The proton distribution functions also deviates from a thermal distribution. They show noticeable anisotropies between the temperatures parallel and perpendicular to the magnetic field (Montgomery et al., 1968; Marsch et al., 1981, 1982, and Fig. 1) and present a pronounced field-aligned heat flux or deformations like a bump at high energy.

In situ measurements revealed that the total temperature[1] anisotropies increase with decreasing heliocentric distances and sometimes exhibit a second proton component that moves along the magnetic field direction with high differential velocities (Marsch et al., 1981, 1982; Marsch, 1991a, and Fig. 1).

The observed deformations of the distribution functions are, however, not as strong as one would expect from the free propagation of the particles. Likely, numerous instabilities develop that limit the scope of the deformations. This means that the plasma somehow reacts to restore stability to the system. Two kinds of back reaction may occur: a

Correspondence to: C. Briand
(carine.briand@obspm.fr)

[1] It must be stressed that the use of the total temperature (i.e. third moment of the distribution function, integrated over all energy) may contradict the detailed anisotropies when an extended tail exists in one of the parallel or perpendicular component.

Published by Copernicus Publications on behalf of the European Geosciences Union and the American Geophysical Union.

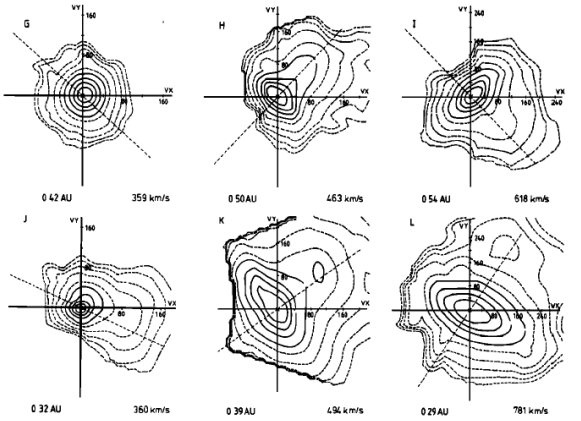

Fig. 1. Helios 2 proton distribution function as measured for low, intermediate and fast solar wind speed (from left to right) and various radial heliocentric distances. Dashed (non contour) line indicates the direction of the magnetic field. From Marsch et al. (1982).

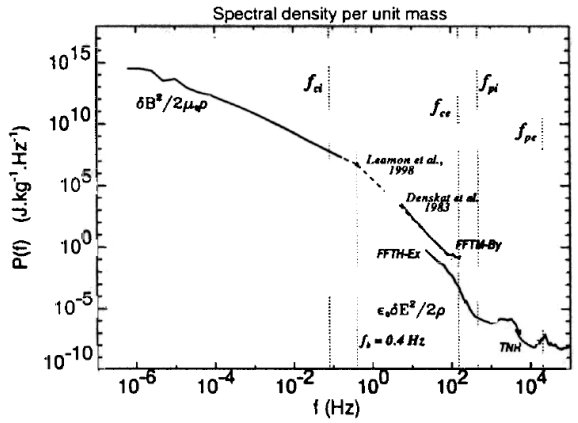

Fig. 2. Magnetic power spectrum observed in the solar wind. From Mangeney et al. (2001).

quasilinear relaxation leading to waves with random phases (turbulence) or more complex nonlinear effects which induce coherent structures.

The solar wind energy spectrum shows that the energy is distributed over a broad range of frequencies (Fig. 2). Three zones are usually distinguished following the exponent α of the power law that characterizes each of them: the very low energy regime with $\alpha \approx -1$, the inertial region (roughly $10^{-4}\,\mathrm{Hz} < f < f_{ci}$) where $\alpha \approx 5/3$ and the high frequency domain ($f > f_{ci}$) which is thought to be where the energy is finally converted into heat. The evolution of the first part of the diagram (low frequencies) is compatible with the WKB propagation of fluctuations in a spherically expanding solar wind. As the frequency gets closer to about $\approx 10^{-4}$ Hz nonlinear coupling between MHD (Alfvén) waves start to be important and allow the cascade of energy through a broader range of frequencies. Finally, above the ion cyclotron frequency, the fluid description of the plasma becomes unsuitable since the phase velocity of the waves is close to the thermal velocity of the particles, thus allowing nonlinear instabilities to develop and energy to transfer between waves and particles. Linking the two regimes (fluid and kinetic) is thus fundamental to follow the energy cascade and to understand the role of the microphysics in the macrostructure of the solar wind (for extended reviews on turbulence in the solar wind, see Marsch, 1991b; Bruno and Carbone, 2005).

The magnetic power spectrum is, however, reliable only up to the ion-cyclotron frequency: above this frequency, the sensitivity of the magnetic field instruments is reduced (as compared to electric field measurements). The high frequency range of the spectrum (corresponding to the dissipative range) is thus better explored through electric field measurements. Intermittent fluctuations of the electric field well above the thermal noise level are indeed observed in the range $f_{ci} \ll f$. Part of these fluctuations are the counterparts of the coherent electrostatic structures observed with waveform analyzers (Lacombe et al., 2002). Linking magnetic and electric power spectrum is far from being a trivial task, since, for example, the contribution of electrostatic waves is not seen in the magnetic spectrum but may represent a large contribution in the higher frequency range.

This paper aims to review the present knowledge on several of the waves in the range $f_{ci} < f < f_{pe}$ from the observational point of view in the free (i.e., not magnetically connected to the Earth bow shock) solar wind. The information obtained from such observations set the fundamental constraints on the most basic physical processes leading to the permanent and large scale structure of the solar wind. This range of frequencies is dominated by electrostatic waves in the higher part (like ion acoustic and Langmuir waves), and includes also electromagnetic waves in the lower part (like whistler-modes and lower hybrid waves). Numerous papers describe these waves in the Earth magnetospheric environment and auroral region but much less exist in the free solar wind (Gurnett and Murdin, 2000).

The paper is organized as follows: after a rapid overview on the different space instruments that have been providing data of the solar wind since the 60's (Sect. 2), a review on the present knowledge on different coherent waves is given. It concerns in particular the Langmuir waves (Sect. 3.1), the ion acoustic waves (Sect. 3.2), the lower hybrid and whistler-mode waves (Sect. 3.3) and finally the multipolar isolated electrostatic structures (Sect. 3.4).

Table 1. List of the space missions that have been providing data on plasma waves in the solar wind. The horizontal line in the table splits up missions with spectrum analyzer (first part) from missions with waveform measurements on board. The peripasis and apoapsis of the orbit of the mission (fifth and sixth column) are given in astronomical units. (*): in December 1983, ISEE-3 was renamed ICE and its main scientific objectives were redefined. (**): missions which have provided waveform measurements during their journey in the solar wind while reaching their final destination (Galileo and Cassini) or during excursions outside the Earth magnetosphere (Cluster II).

Mission Name	Launch year	End Year	Orbit	Periapsis (AU)	Apoapsis (AU)
PIONEER 8	1967	1996	Heliocentric near ecliptic plane	0.992	1.088
PIONEER 9	1968	1983	Heliocentric near ecliptic plane	0.754	0.99
HELIOS 1	1974	1981	heliocentric near ecliptic plane	0.309	0.985
HELIOS 2	1976	1986	heliocentric near ecliptic plane	0.29	0.983
ISEE 1-2	1977	1987	Highly elliptical geocentric	1.	1.
ISEE 3	1978	1983(*)	Highly elliptical geocentric	1.	1.
VOYAGER 1/2	1977	2007	Interstellar mission	1	–
GALILEO(**)	1989	2003	Jupiter Orbiter	1	5
ULYSSES	1990	2008	Solar Polar	2.3	5.4
WIND	1994	–	Ecliptic plane		
CASSINI(**)	1997	–	Saturn Orbiter	1	10
CLUSTER II (**)	2000	–	Elliptical geocentric	1	1
STEREO	2006	–	Ecliptic plane	0.9 (sat A)	1 (sat B)

2 Space instrumentation

Immediately after the beginning of the space venture during the International Geophysical Year (1957), the exploration of the interplanetary medium started (see Table 1). The PIONEER missions provided the very first in situ measurements of the interplanetary environment albeit still in the Earth vicinity. HELIOS 1 and 2 explored regions down to a distance of 0.3 AU to the Sun (Gurnett and Anderson, 1977) while VOYAGER provided information from the heliosphere well beyond 1AU. This two dimensions view of the interplanetary space was afterwards completed with ULYSSES which probed the unknown regions perpendicular to the ecliptic plane (Wenzel et al., 1992; Marsden et al., 1996).

Low frequency (below the ion gyrofrequency) hydromagnetic instabilities were first studied. The higher frequency domain ($f \sim f_{pe}$) attracted more attention when spectrum analyzers and waveform receivers were implemented on board interplanetary missions. Spectrum analyzers give the intensity of the electric field in several frequency channels with narrow bandwidth. The intensity is usually averaged from a fraction of a second (typically 0.5 s) to a few seconds (36 s in case of HELIOS for example). Peak intensities are also measured. Such measurements provide continuous measurements over long time intervals(Fig. 3).

However, spectral analyzers lose an important information: the phase of the signal. Waveform analyzers have been implemented since the 90's[2]. Contrary to the spectrum analyzers, the records of waveforms at high frequency rate are often much shorter. WIND/WAVES (Bougeret et al., 1995), for example, provides waveforms of 15 msec or 230 msec each (see for example Fig. 7) and STEREO/WAVES (Bougeret et al., 2008) provides events 131 msec long. Due to telemetry constraints, one to two hundreds events can be recorded each day. An extremely small fraction of the day (a few seconds at most) is thus covered by the observations. Longer time coverage can, however, be achieved at the expense of the frequency rate (CASSINI/RPWS or CLUSTER/WBD).

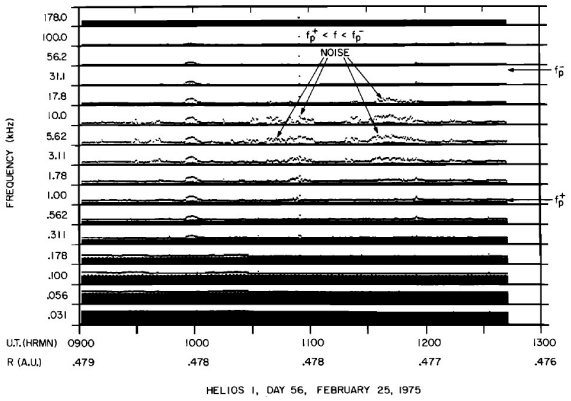

Fig. 3. Example of data obtain by the spectral analyzer on board of HELIOS 1. Black area shows the time average (over 50 ms) field strength while the upper curve gives the maximum intensity peak for the same time interval. From Gurnett and Anderson (1977).

[2]Note that Voyager had a waveform analyzer but the data were mainly used to generate high spectral resolution dynamical spectrum.

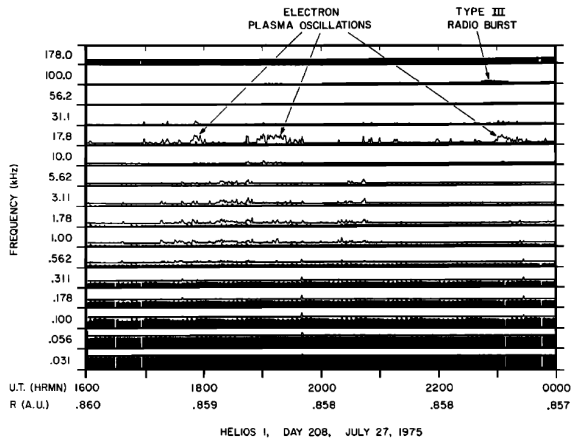

Fig. 4. HELIOS first measurements revealing the presence of Langmuir waves in the solar wind. From Gurnett and Anderson (1977).

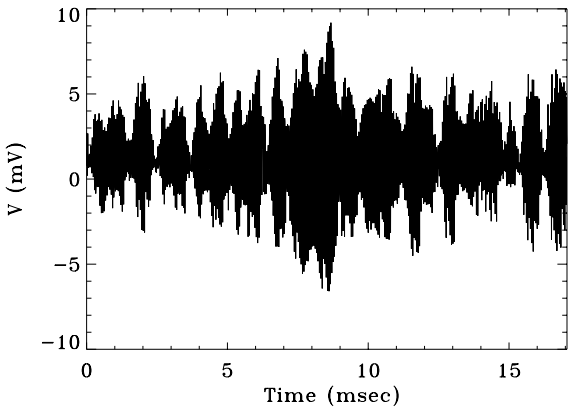

Fig. 5. Langmuir waveform as observed by WIND in the quiet solar wind (15/09/2007).

3 In situ measurement of waves in the free solar wind

3.1 Langmuir waves

Langmuir waves are commonly observed in the Earth environment (for example in the vicinity of the bow shock or the foreshock), and they are also a common feature of the solar wind spectrum (Fig. 4). They are observed associated with electron beams generated by flares, beam induced by shocks, or in the presence of magnetic depressions (also called magnetic holes). Langmuir waves are usually thought to result from bump-on-tail instabilities induced by beams propagating in the solar wind. Their dispersion relation is given by:

$$\omega^2 = \omega_p^2(1 + 3k^2\lambda_D^2) \quad (1)$$

$$\omega_p \propto n_e^{1/2} \quad (2)$$

where λ_D stands for the Debye length and n_e the electron density of the medium.

Since the pioneer work of Ginzburg and Zheleznyakov (1958), Langmuir waves have been intensively studied in relation with Type III radio emission. Indeed, these electromagnetic radio emissions at the plasma frequency, or twice of this frequency, are thought to result from wave coupling implying ion acoustic waves and Langmuir waves. From the observational point of view, numerous works have been devoted to test the validity of this model (Lin et al., 1981, 1986; Gurnett et al., 1993; Thejappa et al., 1993; Cairns, 1995; Thejappa et al., 2003). New evidence of such wave coupling processes have been recently provided from the analysis of waveform data from the STEREO/WAVES experiment (Henri et al., 2009). Since the phase of the waves are available from such measurements, it is possible to test the energy and momentum conservation laws induced by such coupling.

As can be expected from the $1/r^2$ variation of the electron density with heliocentric distance r, the Langmuir wave peak, observed in the context of Type III bursts, moves towards lower frequencies as the heliocentric distance increases (Fig. 15 of Gurnett and Anderson, 1977). Their amplitude is of a few mV/m. The development of waveform analyzers has provided more information about these waves. The analysis of waveforms from the WIND/TDS instrument first revealed their coherent nature (Fig. 5), and show that they often appear as highly modulated wavepackets (Kellogg et al., 1999; Mangeney et al., 1999). Recently, Malaspina et al. (2008) proposed a model based on waves trapping in density homogeneities to explain the envelop of Langmuir waves.

Langmuir waves also develop within magnetic holes (Lin et al., 1995; MacDowall et al., 1996). These structures consist of magnetic depressions lasting for a few tens of second up to half an hour. Figure 6 displays such an event as observed by Ulysses. At higher latitudes, the occurrence of Langmuir waves increases in close correlation with the increase of the number of magnetic holes (Fig. 3 of Winterhalter et al., 1994). The amplitude of the electric field decreases with the heliocentric distance to the sun, as in the case of Type III related Langmuir waves (MacDowall et al., 2003). As noted by Lin et al. (1996), the depression of the magnetic field where Langmuir waves occur does not need to be deep (10% of the ambient magnetic field is enough). More recently, MacDowall et al. (2003) pointed out that Langmuir waves, when not related to particles beams, are mostly encountered in magnetic holes throughout the heliosphere and preferentially in the fast solar wind. The mechanism at the origin of the Langmuir waves within magnetic depression is still unclear. The only model (waves generated by electron beams of thermal energies, formed by adiabatic focusing of the electrons) is indeed unable to also explain the presence of

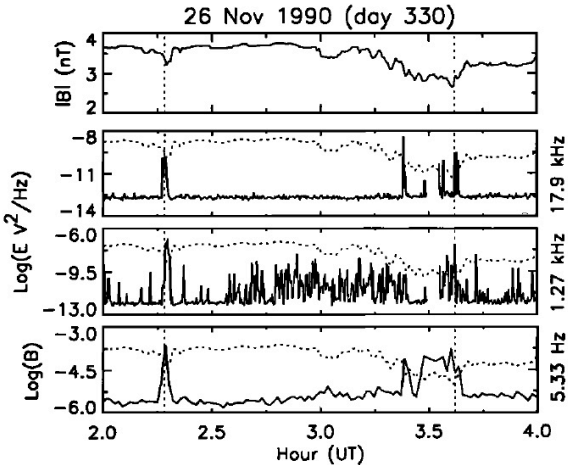

Fig. 6. Time serie of magnetic and electric field measurements from Ulysses. The plasma wave (17.9 kHz) occur in depression in magnetic field (upper panel). The 1.27 kHz electric signal is identified as whistler mode. Note the correlation in time between the occurrence of the two electric signals; From Lin et al. (1995).

other waves often observed simultaneously with the Langmuir waves (and other observational aspects not discussed here).

Finally, Thejappa et al. (2003) have reported Langmuir wave activity not related to either the presence of magnetic holes nor to interplanetary shocks or Type III beams. Such observations encourage statistical studies on Langmuir waves outside obvious periods of electron beam propagation or presence of magnetic holes to complete our knowledge about the formation of Langmuir waves in the solar wind.

3.2 Ion acoustic waves

The very first measurements obtained by spectrum analyzers revealed the presence of low frequency turbulence in the quiet solar wind. These emissions, called "$f_p^+ < f < f_p^-$ noise" by Gurnett and Anderson (1977, where f^+ and f^- stands for the local ion and electron plasma frequency respectively), appear as sporadic bursts with a duration from a few minutes to a few days. Figure 3 shows such emissions detected by HELIOS 1 at a distance of 0.47 AU in the quiet solar wind. The "$f_p^+ < f < f_p^-$ noise" is clearly visible between 1.78 and 17.8 kHz. The absence of magnetic field signature and the alignment with the interplanetary magnetic field reveal their electrostatic nature. From comparisons with events produced upstream of the Earth bow shock, which show similar characteristics, the waves were finally identified as Ion Acoustic Waves (thereafter IAW), Doppler shifted by advection in the solar wind (Gurnett and Anderson, 1977; Gurnett and Frank, 1978; Kurth et al., 1979).

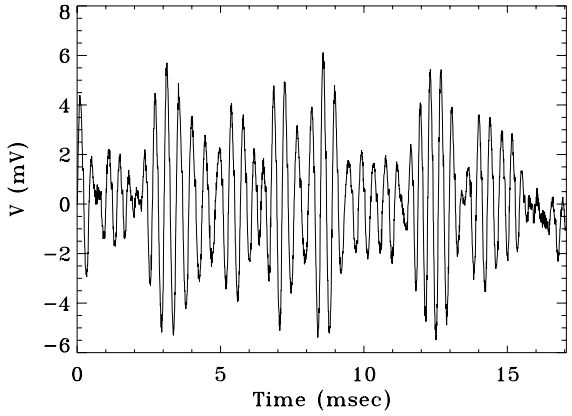

Fig. 7. Example of ion acoustic waveform as observed by the waveform analzer (TDS) on board of WIND.

The intensity of the waves varies between 1 to 10 μV/m in quiet period of solar activity but may reach a few tens of mV/m during more active periods. Combined observations from HELIOS I and VOYAGER showed that the intensity of the waves decreases and the frequency peak drifts towards lower frequencies with increasing heliocentric distance (see Fig. 1 of Gurnett et al., 1979). The measurements from ULYSSES also revealed that the IAW activity level depends on the latitude: at low latitude (mostly slow solar wind), the waves present a strong intensity and occur very often, while at higher latitudes (intermediate and fast solar wind) their occurrence and intensity decrease (Lin et al., 2001).

More recently, Mangeney et al. (1999), using the waveform analyzers on board of the WIND spacecraft, gave more details on the characteristics of the IAW. The coherent nature of these waves are obvious from their data (Fig. 7).

A polarization analysis and simultaneous magnetic field measurements confirmed the electrostatic nature of the waves. They estimated the wavelength from the Doppler shift and found $10 \leq \frac{\lambda}{\lambda_D} \leq 50$ (where λ_D stands for the Debye length). They also showed that the wave vector is always directed towards the Earth, independently of the sign of the radial component of the magnetic field. A more surprising result concerns the relationship between the occurrence of these emissions and the proton temperature.

Theoretical arguments, corroborated by numerous simulations, have shown that the ratio of the electron to proton temperature, T_e/T_p, is a fundamental parameter for the stability of the IAW. If $T_e/T_p \approx 1$, the phase velocity of the waves $\sqrt{\kappa(T_e+3T_p)/m_p}$ is very close to the thermal speed of the protons and they are strongly damped by Landau effect. Thus, a necessary condition for the ion acoustic wave to exist is that $T_e/T_p \gg 1$. Gurnett et al. (1979, their Figs. 7 and 8) indicated that the average peak intensity of the IAW increases with the temperature ratio T_e/T_p. However, according to

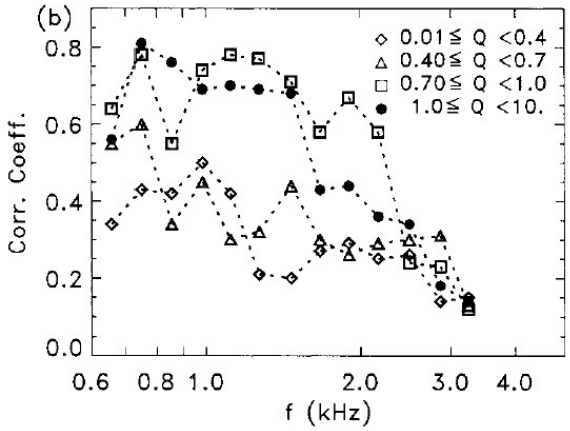

Fig. 8. Correlation of the electric field energy (normalized to temperature energy) in IAW and the ratio T_p/T_e vs. frequencies for several values of (normalized) electron heat flux. From Lin et al. (2001).

Mangeney et al. (1999) from WIND observations, (i) IAW are measured even when $T_e/T_p \leq 1$ and (ii) the presence of IA wave packets depends more strongly on T_p than on T_e/T_p, with a low value of T_p ($\leq 10eV$) favoring the waves. In fact, this apparent contradiction between observations results from the fact that in the solar wind, the temperature ratio variations are mainly controlled by the proton temperature, since electrons keep an almost constant temperature of $1-2\times10^5$ K.

Lin et al. (2001) analyzed the correlation between ion acoustic waves energy, electron heat flux and electron to proton temperature ratio from ULYSSES data. They concluded that heat flux and temperature ratio are not completely independent parameters (Fig. 8). The correlation with temperature ratio is higher when the electron heat flux is large (when normalized to the energy of the core electron velocity).

Ion Acoustic Waves are also often (but not always) reported in connection to interplanetary shocks (Kurth et al., 1979; Hess et al., 1998; Wilson et al., 2007). The IAW activity is strongly increased at the shock time passage but is also noticeable several hours upstream and downstream of a shock. However, the presence of a shock is not a sufficient condition to generate ion acoustic waves: in several cases, no increase of IAW activity has been noted in spite of the presence of a shock. The occurrence probability of IAW related to interplanetary shocks increases with decreasing latitude but no specific variation with heliocentric distance has been reported. As in the case of the quiet solar wind, temperature of the particles and shape of the distribution functions are the most critical parameters related to the increase of the IAW activity.

Two sources of free energy have been proposed to explain the generation of ion acoustic waves: (i) an electron heat flux (Forslund, 1970), (ii) an electrostatic double-ion beams instability (Gary, 1978). However, up to now, observations have not been able to disentangle between the two sources. Ion acoustic waves have been observed in regions where the ratio T_e/T_p would predict strong Landau damping and particle distribution function measurements lack of energy and time resolution to check the stability criterions. The identification of the mechanism(s) at the origin of the ion acoustic waves from direct hydrodynamical conditions of the solar wind is thus still an open question.

3.3 Lower hybrid and whistler-mode waves

Lower hybrid waves (also called lower "hybrid" whistlers) and whistler-mode waves are electromagnetic waves propagating parallel to the background magnetic field. At large angle from the magnetic field, the electromagnetic lower hybrid becomes electrostatic. The electromagnetic modes are typical modes found within the electron MHD (where the frequencies are sufficiently high for protons to be considered as fixed). Electromagnetic and electrostatic modes should be distinguished from each other by means of simultaneous measurements of magnetic and electric fields. However, such measurements at low frequencies are hardly available since the sensitivity of the instruments are not always compatible.

Low frequency ($f_{ci} < f < f_{ce}$) magnetic signals are a permanent feature of the solar wind, at least close enough to the sun - below 3 AU (Lengyel-Frey et al., 1996). This magnetic activity is enhanced in case of disturbances of the solar wind like near interplanetary shocks (Lin et al., 2003), high-speed streams (Coroniti et al., 1982; Lin et al., 1997; Lengyel-Frey et al., 1996) or magnetic clouds (Moullard et al., 2001). It does not exhibit any specific dependence with latitude (Lengyel-Frey et al., 1996). The spectral density shows a f^{α} power law, with a spectral index $\alpha = -0.65$ in quiet solar wind condition (Beinroth and Neubauer, 1981). From one day average values, Beinroth and Neubauer (1981) showed that the spectral density of the magnetic fluctuations correlate with the proton density and magnetic field strength. Since the correlations disappear in shorter time averages, the spectral density variations reflect the large scale behaviors of these parameters. Lin et al. (1997, 1998) also showed that the occurrence of these waves was associated with enhanced heat flux conditions. Moullard et al. (2001) observed whistler-mode waves in magnetic clouds. The electric *and* magnetic waveforms measurements analysis (Fig. 9) reveals that the waves are planar, (right-handed) circularly polarized. Contrary to the results of Coroniti et al. (1982) who found waves propagating at large angle to the magnetic field background, the observations of Moullard et al. (2001) seem to show a propagation aligned with the interplanetary magnetic field. This discrepancy can be explained by an incorrect identification of the waves in the former case. Marsch and Chang (1983) indeed suggested that the waves observed by Coroniti et al. (1982) are more likely lower hybrid waves.

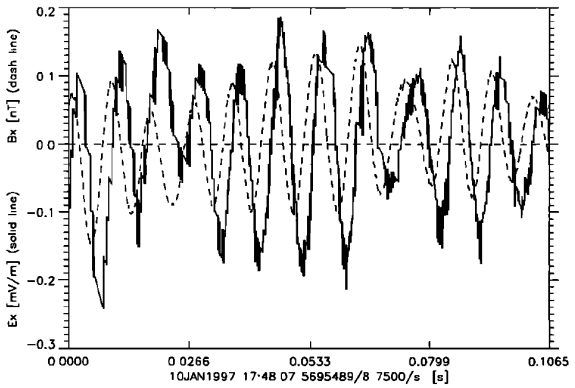

Fig. 9. Example of whistler waveform: Electric field component (solid line) magnetic field component (dashed line). Observed inside a magnetic cloud by the WIND/WAVES(TDS) instrument. From Moullard et al. (2001).

The long-lived background of whistler-mode (or lower hybrid) waves rises the question of the presence of a permanent source of free energy. Loss cone in the electron distribution function, heat flux and electron beams with $T_{\perp} \gg T_{\parallel}$ (and combination of these conditions) are thought to be some possible sources of such free energy. Lengyel-Frey et al. (1996) also suggested that a nonlinear cascade of low-frequency Alfvén waves merging to give higher frequency waves could be at the origin of the background whistler-mode activity. The analysis of the electron distribution function at the time of increased activity of whistler-modes show the presence of loss cone oriented either sunward or anti-sunward (Fig. 7 of Moullard et al., 2001). These observations favor the idea of a local generation of the waves; still a lot of observations and theoretical developments are required to explain the mechanisms leading to the formation of these very low frequency waves.

3.4 Multipolar electrostatic structures

We cannot close this review on plasma waves in the solar wind without saying a few words about the bipolar (sometimes tripolar) electrostatic structures (Fig. 10). From the observational point of view they are also referred to as electron, ion or electrostatic solitary waves. In the following, we will prefer the term "isolated bipolar electrostatic structures" (rather than solitary waves) since the mechanism at the origin of these structures is likely to be quite different from the one of solitons. When a net potential drop exists across the structure, they are called double layers.

The first detection of bipolar electrostatic structures and weak double layers was obtained in the auroral region (Temerin et al., 1982). Since then, they are commonly observed in auroral regions (Ergun et al., 1998; Cattell et al., 2001; Pickett et al., 2004) but also in several Earth magnetic environments (Matsumoto et al., 1994; Franz et al., 1998; Cattell et al., 2003; Pickett et al., 2003) and in the Earth bow shock (Bale et al., 1998; Behlke et al., 2004). Evidence for the presence of isolated bipolar electrostatic structures in the solar wind is more recent: Mangeney et al. (1999) first reported the observation of such structures in the free solar wind and Williams et al. (2006) showed some examples associated to an interplanetary shock. Finally, they were also observed in the vicinity of the magnetosphere of Europa (Kurth et al., 2001) and Saturn (Williams et al., 2006).

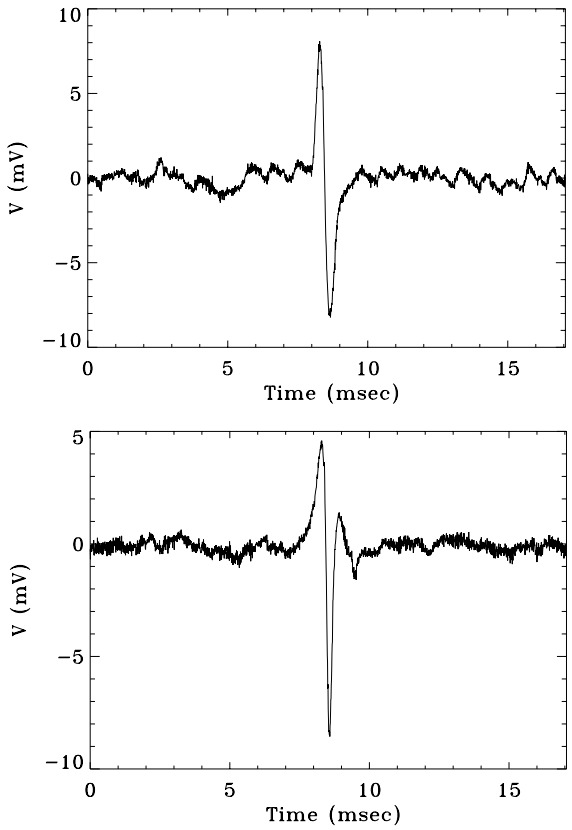

Fig. 10. Examples of isolated electrostatic structures as observed by WIND (15/09/2007): bipolar structures (top panel) and tripolar structures (bottom panel).

From observations with the WIND/WAVES waveform analyzer, Mangeney et al. (1999) deduced that the typical spatial width is about $25\lambda_D$. They also showed that the structures propagate along the magnetic field line at a velocity smaller than the solar wind velocity. Moreover, 29% of the observed isolated electrostatic structures consists in weak double layers, with a potential jump of a few mV[3]. The

[3] An error of calibration seems to be at the origin of the published tripolar shape. A new calibration of the data was performed and

low potential side is directed towards the Earth and a rough estimate of the total potential difference generated by the succession of such weak double layers from the solar corona to the Earth is consistent with exospheric models (Lacombe et al., 2002). Pickett et al. (2004) performed an extensive statistical analysis of the bipolar and tripolar electrostatic structures observed all along the Cluster II trajectory, which includes auroral zone, polar cusp, polar cap, magnetosheath, plasma sheet and solar wind. They first showed that the electric field amplitude (peak-to-peak) of such structures seem to slightly depend on the magnetic field strength. This could explain why the amplitude of the pulses observed in the solar wind are smaller compared to other magnetopheric environments. They also concluded that the duration of such structures is almost independent of the surrounding, except for the magnetosheath where they are much smaller.

Many questions are still unsolved that require more observations. For examples: what is the origin of these waves (ion/electron phase space holes or electron acoustic solitary waves)? what is the 3-D shape of these structures? 1-D simulations have shown that small structures are easily destroyed to form larger structures, but 2-D simulations demonstrate that, in a weakly magnetized plasma, fast and small amplitude structures are stable while large amplitude waves are unstable (Mottez et al., 1997; Muschietti et al., 1999; Mottez, 2001).

4 Conclusions

The waves above the ion cyclotron frequency play a critical role in the microphysics of space plasma. A better understanding of the generation, evolution and decay is required to understand not only the behavior of the plasma at small scale but also to explain the permanent or intermittent behavior of the large scale structures of the solar wind. These waves also play a fundamental role in many physical processes that fall out of the scope of this review (like magnetic reconnection, particles acceleration, Type III radio emissions, etc.). In situ measurements in the region 1–30 solar radii, where basic physical processes are expected to take place are necessary to solve the question of the solar wind heating and acceleration.

As already mentioned, the identification of the waves is often a difficult task for two main reasons. Firstly, contemporaneous measurements of magnetic and electric field are often missing. Secondly, the absence of phase information on the waves limits the studies on the polarization and coupling processes. Waveform analyzers for both electric and magnetic field are thus a requisite to progress any further. In particular, long time coverage events are necessary to study the low frequency range and try to follow the energy cascade from the MHD regime to the kinetic regime. In addition, high energy and temporal resolution of particles distribution functions are necessary to validate possible theories. As can be seen from Table 1 very few instruments will be available in the coming years. Efforts to maintain and develop new instrumentation are necessary to succeed in explaining the solar wind behavior and also Sun-Earth relation.

If more observations are required to impose new constraints on the theories or to validate (or invalidate) some of the already proposed ones, numerical simulations and laboratory experiments are required to understand the, often nonlinear, physics of the medium. The simulations with particles-in-cell, Vlasov-Poisson or hybrid codes have been intensively developed owing to the new capabilities of the computers. In particular, multi-dimensional codes allow now to simulate more realistic situations.

Acknowledgements. The author want to thank C. Salem for providing her a set of newly calibrated WIND/WAVES(TDS) data and for interesting discussions, A. Mangeney and J. L. Bougeret for the careful reading of the paper, and the two referees for their constructive remarks.

Edited by: R. Pottelette
Reviewed by: L. Muschietti and another anonymous Referee

The publication of this article is financed by CNRS-INSU.

References

Bale, S. D., Kellogg, P. J., Larson, D. E., Lin, R. P., Goetz, K., and Lepping, R. P.: Bipolar electrostatic structures in the shock transition region: Evidence of electron phase space holes, Geophys. Res. Lett., 25, 2929–2932, doi:10.1029/98GL02111, 1998.

Behlke, R., André, M., Bale, S. D., Pickett, J. S., Cattell, C. A., Lucek, E. A., and Balogh, A.: Solitary structures associated with short large-amplitude magnetic structures (SLAMS) upstream of the Earth's quasi-parallel bow shock, Geophys. Res. Lett., 31, 16805, doi:10.1029/2004GL019524, 2004.

Beinroth, H. J. and Neubauer, F. M.: Properties of whistler mode waves between 0.3 and 1.0 AU from HELIOS observations, J. Geophys. Res., 86, 7755–7760, 1981.

Bougeret, J.-L., Kaiser, M. L., Kellogg, P. J., Manning, R., Goetz, K., Monson, S. J., Monge, N., Friel, L., Meetre, C. A., Perche, C., Sitruk, L., and Hoang, S.: Waves: The Radio and Plasma Wave Investigation on the Wind Spacecraft, Space Sci. Rev., 71, 231–263, doi:10.1007/BF00751331, 1995.

Bougeret, J. L., Goetz, K., Kaiser, M. L., Bale, S. D., Kellogg, P. J., Maksimovic, M., Monge, N., Monson, S. J., Astier, P. L., Davy, S., Dekkali, M., Hinze, J. J., Manning, R. E., Aguilar-Rodriguez, E., Bonnin, X., Briand, C., Cairns, I. H., Cattell, C. A., Cecconi, B., Eastwood, J., Ergun, R. E., Fainberg, J., Hoang, S., Huttunen, K. E. J., Krucker, S., Lecacheux, A., MacDowall, R. J.,

the presence weak double layers was confirmed (Salem, personal communication).

Macher, W., Mangeney, A., Meetre, C. A., Moussas, X., Nguyen, Q. N., Oswald, T. H., Pulupa, M., Reiner, M. J., Robinson, P. A., Rucker, H., Salem, C., Santolik, O., Silvis, J. M., Ullrich, R., Zarka, P., and Zouganelis, I.: S/WAVES: The Radio and Plasma Wave Investigation on the STEREO Mission, Space Sci. Rev., 136(1–4), 487–528, doi:10.1007/s11214-007-9298-8, 2008.

Bruno, R. and Carbone, V.: The Solar Wind as a Turbulence Laboratory, Living Reviews in Solar Physics, 2, 1–186, 2005.

Cairns, I. H.: Detectability of Electrostatic Decay Products in ULYSSES and Galileo Observations of Type III Solar Radio Sources, Astrophys. J. Lett., 449, L95–L98, doi:10.1086/309621, 1995.

Cattell, C., Crumley, J., Dombeck, J., Lysak, R., Kletzing, C., Peterson, W. K., and Collin, H.: Polar observations of solitary waves at high and low altitudes and comparison to theory, Adv. Space Res., 28, 1631–1641, 2001.

Cattell, C., Neiman, C., Dombeck, J., Crumley, J., Wygant, J., Kletzing, C. A., Peterson, W. K., Mozer, F. S., and Andr, M.: Large amplitude solitary waves in and near the Earths magnetosphere, magnetopause and bow shock: Polar and Cluster observations, Nonlin. Processes Geophys., 10, 13–26, 2003, http://www.nonlin-processes-geophys.net/10/13/2003/.

Coroniti, F. V., Kennel, C. F., Scarf, F. L., and Smith, E. J.: Whistler mode turbulence in the disturbed solar wind, J. Geophys. Res., 87, 6029–6044, 1982.

Ergun, R. E., Carlson, C. W., McFadden, J. P., Mozer, F. S., Delory, G. T., Peria, W., Chaston, C. C., Temerin, M., Elphic, R., Strangeway, R., Pfaff, R., Cattell, C. A., Klumpar, D., Shelley, E., Peterson, W., Moebius, E., and Kistler, L.: FAST satellite observations of electric field structures in the auroral zone, Geophys. Res. Lett., 25, 2025–2028, doi:10.1029/98GL00635, 1998.

Forslund, D. W.: Instabilities associated with heat conduction in the solar wind and their consequences., J. Geophys. Res., 75, 17–28, 1970.

Franz, J. R., Kintner, P. M., and Pickett, J. S.: POLAR observations of coherent electric field structures, Geophys. Res. Lett., 25, 1277–1280, doi:10.1029/98GL50870, 1998.

Gary, S. P.: Ion-acoustic-like instabilities in the solar wind, J. Geophys. Res., 83, 2504–2510, 1978.

Ginzburg, V. L. and Zheleznyakov, V. V.: On the Possible Mechanisms of Sporadic Solar Radio Emission (Radiation in an Isotropic Plasma), Soviet Astronomy, 2, 653 p., 1958.

Gurnett, D. and Murdin, P.: Solar Wind Plasma Waves, 72805–72813, Encyclopedia of Astronomy and Astrophysics, doi:10.1888/0333750888/2305, 2000.

Gurnett, D. A. and Anderson, R. R.: Plasma wave electric fields in the solar wind – Initial results from HELIOS 1, J. Geophys. Res., 82, 632–650, 1977.

Gurnett, D. A. and Frank, L. A.: Ion acoustic waves in the solar wind, J. Geophys. Res., 83, 58–74, 1978.

Gurnett, D. A., Marsch, E., Pilipp, W., Schwenn, R., and Rosenbauer, H.: Ion acoustic waves and related plasma observations in the solar wind, J. Geophys. Res., 84, 2029–2038, 1979.

Gurnett, D. A., Hospodarsky, G. B., Kurth, W. S., Williams, D. J., and Bolton, S. J.: Fine structure of Langmuir waves produced by a solar electron event, J. Geophys. Res., 98, 5631–5637, 1993.

Henri, P., Briand, C., Mangeney, A., Bale, S. D., Califano, F., Goetz, K., and Kaiser, M.: Evidence for wave coupling in type III emissions, J. Geophys. Res. (Space Physics), 114, 3103, doi:10.1029/2008JA013738, 2009.

Hess, R. A., MacDowall, R. J., Goldstein, B., Neugebauer, M., and Forsyth, R. J.: Ion acoustic-like waves observed by ULYSSES near interplanetary shock waves in the three-dimensional heliosphere, J. Geophys. Res., 103, 6531, doi:10.1029/97JA03395, 1998.

Kellogg, P. J., Goetz, K., Monson, S. J., and Bale, S. D.: Langmuir waves in a fluctuating solar wind, J. Geophys. Res., 104, 17069–17078, doi:10.1029/1999JA900163, 1999.

Kurth, W. S., Gurnett, D. A., and Scarf, F. L.: High-resolution spectrograms of ion acoustic waves in the solar wind, J. Geophys. Res., 84, 3413–3419, 1979.

Kurth, W. S., Gurnett, D. A., Persoon, A. M., Roux, A., Bolton, S. J., and Alexander, C. J.: The plasma wave environment of Europa, Planet. Space Sci., 49, 345–363, 2001.

Lacombe, C., Salem, C., Mangeney, A., Hubert, D., Perche, C., Bougeret, J.-L., Kellogg, P. J., and Bosqued, J.-M.: Evidence for the interplanetary electric potential? WIND observations of electrostatic fluctuations, Ann. Geophys., 20, 609–618, 2002, http://www.ann-geophys.net/20/609/2002/.

Lemaire, J. and Scherer, M.: Kinetic models of the solar wind., J. Geophys. Res., 76, 7479–7490, doi:10.1029/JA076i031p07479, 1971.

Lengyel-Frey, D., Hess, R. A., MacDowall, R. J., Stone, R. G., Lin, N., Balogh, A., and Forsyth, R.: Ulysses observations of whistler waves at interplanetary shocks and in the solar wind, J. Geophys. Res., 101, 27555–27564, doi:10.1029/96JA00548, 1996.

Lin, N., Kellogg, P. J., MacDowall, R. J., Balogh, A., Forsyth, R. J., Phillips, J. L., Buttighoffer, A., and Pick, M.: Observations of plasma waves in magnetic holes, Geophys. Res. Lett., 22, 3417–3420, doi:10.1029/95GL03266, 1995.

Lin, N., Kellogg, P. J., MacDowall, R. J., Tsurutani, B. T., and Ho, C. M.: Langmuir waves associated with discontinuities in the solar wind: a statistical study., Astron. Astrophys., 316, 425–429, 1996.

Lin, N., Kellogg, P. J., MacDowall, R. J., Scime, E. E., Phillips, J. L., Balogh, A., and Forsyth, R. J.: Low frequency plasma waves in the solar wind: from ecliptic plane to the solar polar regions, Adv. Space Res., 19, 877–881, 1997.

Lin, N., Kellogg, P. J., MacDowall, R. J., Scime, E. E., Balogh, A., Forsyth, R. J., McComas, D. J., and Phillips, J. L.: Very low frequency waves in the heliosphere: Ulysses observations, J. Geophys. Res., 103, 12023–12036, doi:10.1029/98JA00764, 1998.

Lin, N., Kellogg, P. J., MacDowall, R. J., and Gary, S. P.: Ion Acoustic Waves in the Heliosphere, Space Sci. Rev., 97, 193–196, doi:10.1023/A:1011823505395, 2001.

Lin, N., Kellogg, P. J., MacDowall, R. J., McComas, D. J., and Balogh, A.: VLF wave activity in the solar wind and the photoelectron effect in electric field measurements: Ulysses observations, Geophys. Res. Lett., 30(19), 8029, doi:10.1029/2003GL017244, 2003.

Lin, R. P., Potter, D. W., Gurnett, D. A., and Scarf, F. L.: Energetic electrons and plasma waves associated with a solar type III radio burst, Astrophys. J., 251, 364–373, doi:10.1086/159471, 1981.

Lin, R. P., Levedahl, W. K., Lotko, W., Gurnett, D. A., and Scarf, F. L.: Evidence for nonlinear wave-wave interactions in solar type III radio bursts, Astrophys. J., 308, 954–965, doi:10.1086/164563, 1986.

MacDowall, R. J., Lin, N., Kellogg, P. J., Balogh, A., Forsyth, R. J., and Neugebauer, M.: Langmuir waves in magnetic holes: source mechanism and consequences., in: American Institute of Physics Conference Series, edited by: Winterhalter, D., Gosling, J. T., Habbal, S. R., Kurth, W. S., and Neugebauer, M., vol. 382 of American Institute of Physics Conference Series, 301–304, 1996.

MacDowall, R. J., Lin, N., and McComas, D. J.: Heliospheric Langmuir wave observations from the Ulysses spacecraft, Adv. Space Res., 32, 479–483, doi:10.1016/S0273-1177(03)00331-4, 2003.

Maksimovic, M., Pierrard, V., and Lemaire, J. F.: A kinetic model of the solar wind with Kappa distribution functions in the corona., Astron. & Astrophys., 324, 725–734, 1997.

Malaspina, D. M., Ergun, R. E., Cairns, I. H., Bougeret, J., Bale, S., Kellogg, P. J., and Kaiser, M. L.: Consequences of the Eigenmode Interpretation of Solar Wind Langmuir Waves, AGU Fall Meeting Abstracts, A1576, 2008.

Mangeney, A., Salem, C., Lacombe, C., Bougeret, J.-L., Perche, C., Manning, R., Kellogg, P. J., Goetz, K., Monson, S. J., and Bosqued, J.-M.: WIND observations of coherent electrostatic waves in the solar wind, Ann. Geophys., 17, 307–320, 1999, http://www.ann-geophys.net/17/307/1999/.

Mangeney, A., Salem, C., Veltri, P., and Cecconi, C.: Intermittency in the Solar Wind Turbulence and the Haar Wavelet Transform, in: Sheffield Space Plasma Meeting: Multipoint Measurements versus Theory, edited by: Warmbein, B., vol. 492 of ESA Special Publication, 53 pp., 2001.

Marsch, E.: Kinetic Physics of the Solar Wind Plasma, 45–133, Physics of the Inner Heliosphere II. Particles, Waves and Turbulence, XI, 352, 152 pp. figs. Springer-Verlag Berlin Heidelberg New York. Also Physics and Chemistry in Space, vol. 21; 2, 45–133, 1991a.

Marsch, E.: MHD Turbulence in the Solar Wind, 159–241, Physics of the Inner Heliosphere II. Particles, Waves and Turbulence, XI, 352, 152 pp. figs. Springer-Verlag Berlin Heidelberg New York. Also Physics and Chemistry in Space, vol. 21; 2, 159–241, 1991b.

Marsch, E. and Chang, T.: Electromagnetic lower hybrid waves in the solar wind, J. Geophys. Res., 88, 6869–6880, 1983.

Marsch, E., Rosenbauer, H., Schwenn, R., Muehlhaeuser, K.-H., and Denskat, K. U.: Pronounced proton core temperature anisotropy, ion differential speed, and simultaneous Alfven wave activity in slow solar wind at 0.3 AU, J. Geophys. Res., 86, 9199–9203, 1981.

Marsch, E., Schwenn, R., Rosenbauer, H., Muehlhaeuser, K.-H., Pilipp, W., and Neubauer, F. M.: Solar wind protons - Three-dimensional velocity distributions and derived plasma parameters measured between 0.3 and 1 AU, J. Geophys. Res., 87, 52–72, 1982.

Marsden, R. G., Smith, E. J., Cooper, J. F., and Tranquille, C.: ULYSSES at high heliographic latitudes: an introduction., Astron. & Astrophys., 316, 279–286, 1996.

Matsumoto, H., Kojima, H., Miyatake, T., Omura, Y., Okada, M., Nagano, I., and Tsutsui, M.: Electrotastic Solitary Waves (ESW) in the magnetotail: BEN wave forms observed by GEOTAIL, Geophys. Res. Lett., 21, 2915–2918, 1994.

Montgomery, M. D., Bame, S. J., and Hundhausen, A. J.: Solar Wind Electrons: Vela 4 Measurements, J. Geophys. Res., 73, 4999–5003, doi:10.1029/JA073i015p04999, 1968.

Mottez, F.: Instabilities and Formation of Coherent Structures, Astrophys. Space Sci., 277, 59–70, doi:10.1023/A:1012224820136, 2001.

Mottez, F., Perraut, S., Roux, A., and Louarn, P.: Coherent structures in the magnetotail triggered by counterstreaming electron beams, J. Geophys. Res., 102, 11399–11408, doi:10.1029/97JA00385, 1997.

Moullard, O., Burgess, D., Salem, C., Mangeney, A., Larson, D. E., and Bale, S. D.: Whistler waves, Langmuir waves and single loss cone electron distributions inside a magnetic cloud: Observations, J. Geophys. Res., 106, 8301–8314, doi:10.1029/2000JA900144, 2001.

Muschietti, L., Ergun, R. E., Roth, I., and Carlson, C. W.: Phase-space electron holes along magnetic field lines, Geophys. Res. Lett., 26, 1093–1096, doi:10.1029/1999GL900207, 1999.

Parker, E. N.: Suprathermal Particle Generation in the Solar Corona., Astrophys. J., 128, 677 pp., 1958.

Pickett, J., Chen, L., Kahler, S., Santolík, O., Gurnett, D., Tsurutani, B., and Balogh, A.: Isolated electrostatic structures observed throughout the Cluster orbit: relationship to magnetic field strength, Ann. Geophys., 22, 2515–2523, 2004, http://www.ann-geophys.net/22/2515/2004/.

Pickett, J. S., Menietti, J. D., Gurnett, D. A., Tsurutani, B., Kintner, P. M., Klatt, E., and Balogh, A.: Solitary potential structures observed in the magnetosheath by the Cluster spacecraft, Nonlin. Processes Geophys., 10, 3–11, 2003, http://www.nonlin-processes-geophys.net/10/3/2003/.

Pilipp, W. G., Muehlhaeuser, K.-H., Miggenrieder, H., Montgomery, M. D., and Rosenbauer, H.: Characteristics of electron velocity distribution functions in the solar wind derived from the HELIOS plasma experiment, J. Geophys. Res., 92, 1075–1092, 1987a.

Pilipp, W. G., Muehlhaeuser, K.-H., Miggenrieder, H., Montgomery, M. D., and Rosenbauer, H.: Unusual electron distribution functions in the solar wind derived from the HELIOS plasma experiment – Double-strahl distributions and distributions with an extremely anisotropic core, J. Geophys. Res., 92, 1093–1101, 1987b.

Temerin, M., Cerny, K., Lotko, W., and Mozer, F. S.: Observations of double layers and solitary waves in the auroral plasma, Phys. Rev. Lett., 48, 1175–1179, 1982.

Thejappa, G., Lengyel-Frey, D., Stone, R. G., and Goldstein, M. L.: Evaluation of Emission Mechanisms at omega P E Using ULYSSES Observations of Type III Bursts, Astrophys. J., 416, 831–844, doi:10.1086/173281, 1993.

Thejappa, G., MacDowall, R. J., Scime, E. E., and Littleton, J. E.: Evidence for electrostatic decay in the solar wind at 5.2 AU, J. Geophys. Res. (Space Physics), 108, 1139, doi:10.1029/2002JA009290, 2003.

Wenzel, K. P., Marsden, R. G., Page, D. E., and Smith, E. J.: The ULYSSES Mission, Astron. & Astrophys.s, 92, 207–219, 1992.

Williams, J. D., Chen, L.-J., Kurth, W. S., Gurnett, D. A., and Dougherty, M. K.: Electrostatic solitary structures observed at Saturn, Geophys. Res. Lett., 33, 6103, doi:10.1029/2005GL024532, 2006.

Wilson, III, L. B., Cattell, C., Kellogg, P. J., Goetz, K., Kersten, K., Hanson, L., MacGregor, R., and Kasper, J. C.: Waves in Interplanetary Shocks: A Wind/WAVES Study, Physical Review Letters, 99, 041101, doi:10.1103/PhysRevLett.99.041101, 2007.

Winterhalter, D., Neugebauer, M., Goldstein, B. E., Smith, E. J., Bame, S. J., and Balogh, A.: ULYSSES field and plasma observations of magnetic holes in the solar wind and their relation to mirror-mode structures, J. Geophys. Res., 99, 23371–23381, 1994.

Zouganelis, I., Maksimovic, M., Meyer-Vernet, N., Lamy, H., and Issautier, K.: A Transonic Collisionless Model of the Solar Wind, Astrophys. J., 606, 542–554, doi:10.1086/382866, 2004.

3.2.2 Génération d'ondes de Langmuir et d'ondes solitaires

Travail effectué en collaboration avec A. Mangeney (Astronome Emerite de l'Observatoire de Paris) et F. Califano de l'Université de Pise.
Articles de référence : Briand et al. (2007, 2008a)

Le but de cette étude est de comprendre comment un plasma non collisionnel répond à des perturbations temporelles et localisées de la fonction de distribution électronique. Pour cela, le code précédemment décrit (cf. Section 3.1.2) est utilisé dans la limite électrostatique, 1D-1V, en boite ouverte (non périodique). La perturbation est appliquée à l'entrée de la boite de simulation ($x = 0$). En $x = L$, les particules de vitesse positive sortent, tandis que des particules de vitesse négative rentrent selon une distribution Maxwellienne. Autrement dit, les électrons ne sont pas réfléchis sur les bords de la boite de simulation. Un traitement spécifique a été appliqué pour annuler le courant en $x = 0$ et $x = L$.
La perturbation est appliquée uniquement sur les électrons. La vitesse thermique des électrons est modifiée par un terme en cosinus dépendant du temps, tout en conservant le nombre de particules. Ceci est équivalent à un léger chauffage les électrons. Les protons sont considérés avec leur masse réelle ($m_p/m_e = 1836$) et représentent un fond quasi immobile de particules neutralisant le milieu.
Nous avons montré qu'une telle perturbation conduisait (a) au développement d'ondes de Langmuir modulées (générées par les particules non piégée – effet ballistique) (b) à l'apparition naturelle d'une zone de turbulence étendue. Nous avons par ailleurs introduit un gradient spatial de densité dans la boite, simulant ainsi les effets de la gravité. Celle-ci agissant sur les protons mais pas sur les électrons, un champ ambipolaire est induit dans le milieu, champ qui maintient la quasi-neutralité du plasma. Les conditions d'excitation du plasma reste par ailleurs semblable au cas homogène. On peut montrer que le champ de gravité $g^\star$ et le champ ambipolaire ϵ s'expriment simplement en unités normalisées par :

$$g^\star = \frac{1}{h}\left(\frac{T_p}{T_e}+1\right)\left(\frac{m_p}{m_e}+1\right)^{-1} \tag{3.6}$$

$$\epsilon = \frac{1}{h}\left(1-\frac{T_p}{T_e}\frac{m_e}{m_p}\right)\left(\frac{m_e}{m_p}+1\right)^{-1} \tag{3.7}$$

où h est la hauteur d'échelle du milieu, un paramètre libre de la simulation. On voit que ϵ s'exprime directement en fonction de h lorsque $m_p/m_e \gg 1$ et que $T_p/T_e = 1$. On a en effet alors $\epsilon = h^{-1}$.

La présence d'un gradient de densité électronique conduit à l'apparition de structures bipolaires électrostatiques semblables à celles qui sont observées dans la magnétosphère de la Terre et dans le vent solaire. Nous avons également montré qu'en présence d'espèces plus lourdes (telle que l'oxygène O^+ dans le cas de l'environnement terrestre), ces structures bipolaires voyaient leur trajectoire profondément modifiée : au lieu d'une propagation linéaire, elles reviennent vers les densités plus élevées (Fig. 9 du premier article). Ce point est important pour interpréter l'orientation des doubles couches par rapport à l'écoulement global du plasma.

JOURNAL OF GEOPHYSICAL RESEARCH, VOL. 113, A07219, doi:10.1029/2007JA012992, 2008

Coherent electric structures: Vlasov-Ampère simulations and observational consequences

C. Briand,[1] A. Mangeney,[1] and F. Califano[2]

Received 17 December 2007; revised 5 March 2008; accepted 15 April 2008; published 30 July 2008.

[1] Coherent electrostatic structures, like bipolar electric pulses (also called electrostatic solitary waves) or Langmuir waves, are frequently observed in many astrophysical plasma of the Earth environment (plasma sheet boundary layer, Earth bow shock, auroral regions etc.) or in the solar wind. They are thought to play a crucial role in the energy transfer from small to large scale and to reconnection processes. Numerous simulations have studied their emergence and evolution. Most of them are based on the development of two stream instabilities. Another mechanism is investigated here: the plasma is excited by a localized, time dependent modulation of the electron distribution function (heating of the electrons). The investigation is performed through a 1D Vlasov-Ampere code, in open boundary conditions. We explore the response of the plasma to several heating conditions, mass ratio and density gradient. We find that the heating leads to the development of an extended turbulent domain. We also show that the history of the electrostatic solitary waves (ESW) strongly depends on the presence of a density gradient and the mass ratio between species. If the positive charged neutralizing background is composed of heavy ions, the ESW turns back to the entrance domain when a density gradient is included. From the observational point of view, this means that the electric field shows a polarity reversal with time.

Citation: Briand, C., A. Mangeney, and F. Califano (2008), Coherent electric structures: Vlasov-Ampère simulations and observational consequences, *J. Geophys. Res.*, *113*, A07219, doi:10.1029/2007JA012992.

1. Introduction

[2] Space plasmas at kinetic length scales, let say the Debye length, are characterized by the presence of coherent structures superposed over a "sea" of high and low frequency oscillations often supported by a non-Maxwellian plasma, as for example observed in the solar wind. In this case, the non-Maxwellian character of the distribution function is, first of all, a signature of the weakness of collisional effects, but also of the continuous injection of energy resulting from a MHD wave cascade and of the presence of incoming supra thermal particles accelerated by complicated mechanisms, as for example reconnection in the solar corona or magnetosphere.

[3] High frequency Langmuir oscillations at nearly the plasma frequency f_p are often observed in the form of wave packets in the interplanetary space where also the harmonic at 2 f_p is detected. Typical values of the electric field associated to such wave packets are in the range $01 \leq E \leq 10$mV/m over typical length scales from 50 λ_D and 1000 λ_D corresponding to the so-called weak and intense wave packets. There is not an accepted model capable of explaining the mechanism underlying the generation of burtsy plasma wave packets [see *Nulsen et al.*, 2007, and references therein] although numerous suggestions have been made. For example, in a recent paper, *Ergun et al.* [2008] have shown that isolated Langmuir wave packets can be decomposed in low order eigenmodes of solitons formed in parabolic density depression in the solar wind.

[4] Coherent solitary structures are observed in space plasmas in the form of bipolar electric pulses mainly parallel to the ambient magnetic field. They have been first observed in strongly nonhomogeneous regions of the Earth's environment as for example the bow Shock [*Bale et al.*, 1998], the plasma sheet boundary [*Matsumoto et al.*, 1994], the auroral zone [*Temerin et al.*, 1982; *Ergun et al.*, 1998b] and have been then also detected in the solar wind [*Mangeney et al.*, 1999]. Today, they are routinely detected owing to spacecraft observations in all planetary environments. The electric field associated to such coherent structures spans over a wide range of value depending on the observed location: of the order or less than 0.1 mV/m in the solar wind and the plasma sheet boundary layer, it can reach 100 mV/m or more in the bow shock and the auroral regions.

[5] The standard theoretical argument used to explain the observed plasma oscillations as well as the coherent structures, relies on the development of two streams or bump-on-tail like instabilities which excite Langmuir waves. These waves then interact with plasma inhomogeneities or evolve nonlinearly giving rise to different phenomena, as for example Langmuir wave collapse, generation of ion acous-

[1] LESIA, Observatoire de Paris, CNRS, UPMC, Université Paris Diderot, Meudon, France.
[2] Dipartimento Fisica and CNISM, Università di Pisa, Pisa, Italy.

0148-0227/08/2007JA012992$09.00

Table 1. List of Some Typical Physical Values in the Quiet Solar Wind and Auroral Zone[a]

	n_e cm^{-3}	T_e 10^5 K	w_p kHz	λ_d m	E mV/m
S.W.	5	1.5	3	10	up to a few tens
Aurora	5	2–80	3	14–90	up to a few hundreds

[a]Electrical field values correspond to typical Langmuir waves.

tic modes, etc. [see, e.g., *Li et al.*, 2003, and references therein].

[6] However, even if all these studies were able to reproduce some of the observed features it appears to be quite difficult, in typical astrophysical conditions, to directly generate nearly monoenergetic beams except maybe in very peculiar cases. The maximum velocity of the observed beam shifts toward lower velocity values [*Lin et al.*, 1981] indicating that a broad range of velocities is involved in the interaction as time goes on, while the usual theoretical approach is based on a monoenergetic beam approach. In order to free the theoretical models from the necessity of initial monoenergetic beams, another mechanism for the generation of coherent electrostatic structures have been proposed by *Briand et al.* [2007]. The authors considered a plasma, initially at rest, perturbed from one boundary by localized, time dependent variations of the electron distribution function which corresponds to some local heating. The main result of this investigation was to show the possibility of generating electrostatic coherent structures of BGK type. In this former paper, the perturbation of the electron distribution function was continuous and the plasma was uniform. However, observations show that space plasmas are characterized by density gradients extending over a large range of scale heights (from thousands of Debye lengths in the solar wind to a few tens of Debye lengths in the Earth environment). The consequences of density gradient on the behavior of the electrostatic structure has also been recognized through PIC simulations [*Mandrake et al.*, 2000]. The present study thus extends our former investigation to the case of impulsive heating in a density stratified medium. The results also give some clue for observational tests in several environments.

2. Simulation Model

[7] The atmospheric model includes both electrons and protons and is limited to a 1D geometry since many observations show that most of the electric structures are field aligned [see e.g., *Ergun et al.*, 1998a]. It is density stratified following the Pannekoek-Rosseland [*Rosseland*, 1924] kinetic approach: the gravity $g^\star$ is balanced by a time independent electric field and dollar; and dollar; to maintain the charge neutrality. The two fields depend only on the species mass and temperature ratios and on the scale height h which are free parameters of the simulation. In absence of external forcing, the electric force compensates for the gravitational force and the atmosphere is in a state of stable equilibrium. Moreover, it can be shown that when $T_p/T_e = 1$ and $m_p \gg m_e$ and dollar; (which is the case of all the simulations presented here), the ambipolar electric field takes the simple relation $\varepsilon = 1/h$ and the gravity field can be expressed in terms of the ambipolar field and species mass ratio only ($g^\star = 2\ m_e/m_p$).

[8] The evolution of the distribution function of the particles is described by the Vlasov-Ampère system of equations, in a 1D geometry and with open boundary conditions. They are numerically solved following the scheme described by *Mangeney et al.* [2002]. The algorithm is based on the "splitting algorithm" which in practice reduces the numerical scheme to the solution of an advection equation obtained by the implementation of a third order accurate Van Leer scheme which conserves the total charge of the particles.

[9] The evolution of the self induced electric field E is determined through the Ampere's law. The Vlasov-Ampere system of equations, in dimensionless units, reads:

$$\frac{\partial f_\alpha}{\partial t} + v_\alpha \frac{\partial f_\alpha}{\partial x} + [\sigma_\alpha (E + \varepsilon) - g^\star] \frac{\partial f_\alpha}{\partial v_\alpha} = 0, \tag{1}$$

$$\frac{\partial E}{\partial t} = -J. \tag{2}$$

$$\int v_p f_p \, dv_p - \int v_e f_e \, dv_e = J. \tag{3}$$

where f is the distribution function, E the electric field, J the current density and the index α indicates the species (e for electrons and p for protons). In these equations we have taken the electron mass m_e, the electron thermal velocity v_{te}, the plasma frequency ω_e (taken at $x = 0$ and dollar;) as a characteristic mass, velocity and frequency. Then, the characteristic length, electric field and gravity, at $x = 0$ and $\lambda_D = v_{te}/\omega_e$ (Debye length), $\bar{E} = m_e v_{te} \omega_e / e$ and $\bar{g} = v_{te}\omega_e$. Finally, in our dimensionless unit $\sigma_e = -1$ and $\sigma_p = m_e/m_p$. Typical characteristic values for most of these parameters in different natural plasma contexts are summarized in Table 1.

[10] The distribution function of each species at time t = 0 is described by a normalized Maxwellian function:

$$f_e(x \neq 0, v_e, 0) = \exp\left(-\frac{x}{h}\right) \exp\left(-\frac{v_e^2}{2}\right), \tag{4}$$

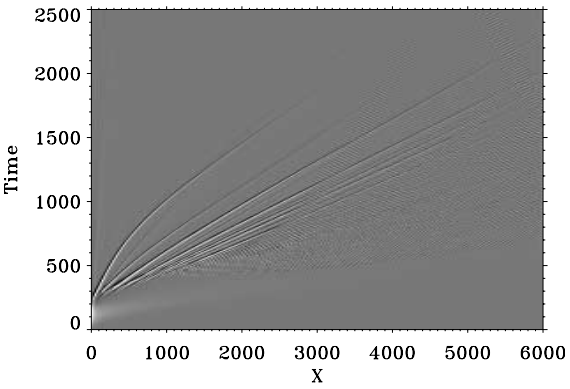

Figure 1. Typical example of electric field amplitude versus space and time in the case of homogeneous plasma.

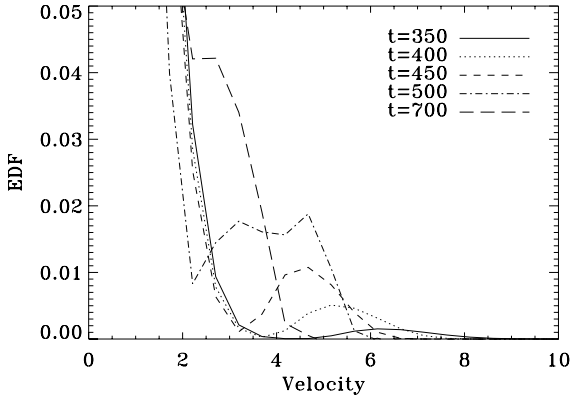

Figure 2. Electron Distribution Function versus velocity at position x = 1500 for several time (indicated on the graph).

$$f_p(x, v_p, 0) = \exp\left(-\frac{x}{h}\right)\exp\left(-\frac{v_p^2}{2}\frac{m_p}{m_e}\frac{T_e}{T_p}\right), \quad (5)$$

[11] Initially, the system is isothermal with the same temperature for both particle species (T_p/T_e = 1).

[12] In x = L (i.e., on the right side of the box), the particles with $v > 0$ are free to leave while those entering in the box ($v < 0$) are imposed by the following time independent boundary condition:

$$f_\alpha(x = L, v_\alpha < 0, t) = f_\alpha(x = L, v_\alpha, t = 0), \quad (6)$$

[13] For $t \geq 0$ the system is perturbed by the injection of heated electrons in x = 0 (left side). It is achieved by a time

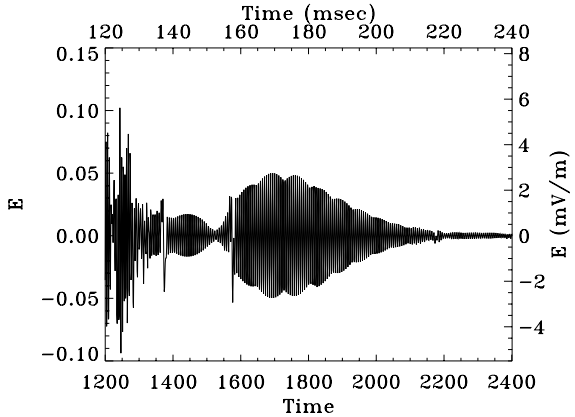

Figure 3. Electric field amplitude as a function of time for the position x = 2250 of Figure 1. The axis are expressed either in the dimensionless units of the code (left and bottom) or physical units (right and top).

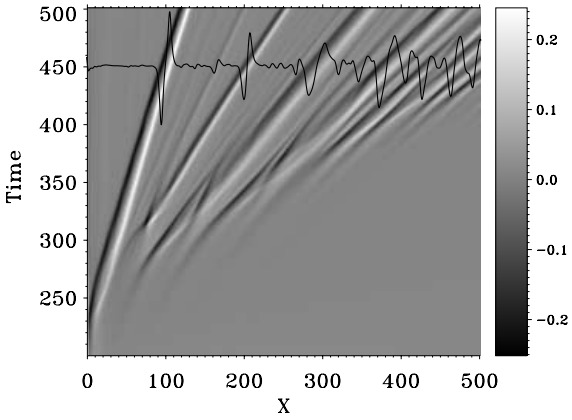

Figure 4. Electric field amplitude versus space and time together with the electric field profile at time t =450. Note its similarity with the observed profiles reported by *Matsumoto et al.* [1994].

dependent modulation of the electron Maxwellian distribution function:

$$f_e(x = 0, v_e, t) = \exp\left(-\frac{v_e^2}{2v_{\text{driver}}^2}\right), \quad (7)$$

$$v_{\text{driver}} = 1 + \alpha(t)\left[1 - \cos\left(\frac{2\pi t}{P}\right)\right]. \quad (8)$$

[14] The amplitude of the heating is thus set by and v_{driver} (equation (8)) which depends on time through the function and dollar; and dollar; and with a characteristic time equal to the period P. It is worth noting that this forcing mechanism conserves the charge density, thus charge neutrality.

[15] In the present work, L = 4000 λ_D, T_p/T_e = 1 P = 300, dt = 4.10^{-3} dx = 0.5 λ_D, dv_e = 0.15 and dv_p = 0.015. In the figures presented below, the parameters are expressed in normalized units, except when physical units are considered (in which case, they are made explicit).

3. Simulation

3.1. Wave Generation: General Overview

[16] In this section, the perturbation of the electron distribution function consists in a pulse of short duration. The parameter α of equation (8) follows the rule:

$$\alpha(t) \neq 0 \; for \; t \leq t_{\max} \quad (9)$$

$$\alpha(t) = 0 \; for \; t > t_{\max} \quad (10)$$

with $t_{\max}$ =300. For all runs of this part, $h = \infty$ (no density gradient), $\mu = m_p/m_e$ =1836. The consequences of the modification of these parameters on the plasma behavior are discussed in the next subsection. Several simulations were performed with $0.5 \leq \alpha \leq 2.5$. In the following examples,

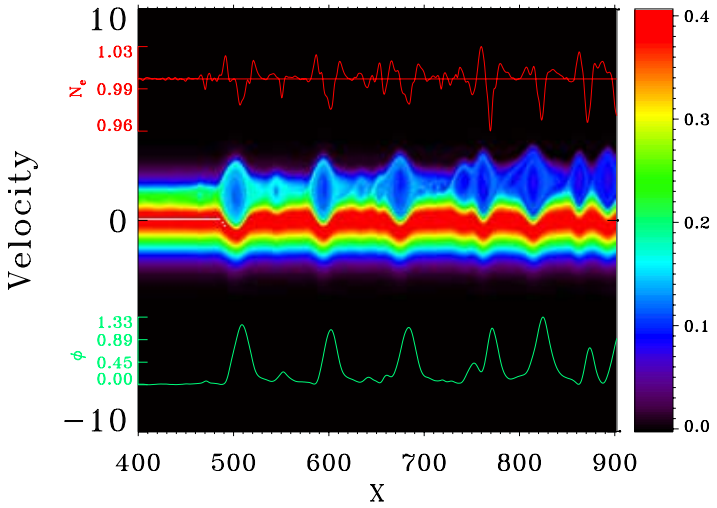

Figure 5. Electron distribution function as a function of space and velocity at time $t = 650$. Top graph (in red): Electron density; Bottom graph (in green): electric potential.

α = 0.75, which means a variation of 2.5 of the thermal velocity of the electrons. We must stress that another kind of forcing consisting in a series of pulses (similar to a sawtooth form) have also been tested. We have chosen not to detailed these simulations since they introduce another free parameter (the time between two successive pulses) and the results are qualitatively similar to those presented here.

[17] All runs lead to the development of several kinds of coherent waves, namely Langmuir and Electrostatic Solitary Waves (hereafter ESW [*Matsumoto et al.*, 1994]). They finally form a spatially and temporally extended turbulent domain. Figure 1 shows a typical example of the electric field as a function of space and time. ESW are clearly distinguished as large amplitude isolated structures while the turbulent domain appears below the limit formed by these ESW.

[18] Langmuir waves develop through a bump-on-tail instability. Indeed, most of the injected electrons freely travel across the simulation box following a ballistic trajectory leading to the generation of a bump on the tail of the electron distribution function. Coherent Langmuir waves grow and trap the resonant electrons, diffusing the bump to a flat distribution (Figure 2) which stops the wave growth. The graph also shows that, for a determined spatial position, the bump slowly moves toward lower velocities as time goes on. This shift of the central beam velocity results from the ballistic trajectory of the particles. Such behavior of the electron distribution function has also been observed in the solar wind [*Lin et al.*, 1981]. As a consequence, Langmuir waves with different phase velocity are excited, leading to a broad range of wave numbers and frequencies. It is worth noting that this broad spectrum naturally appears as a

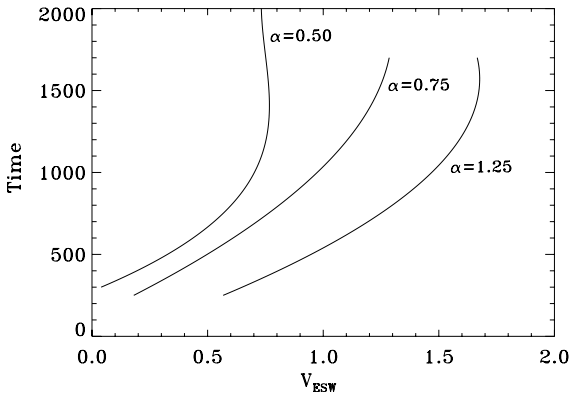

Figure 6. Velocity of one selected ESW as a function of time for three runs with different heating values (indicated on the plot through the α parameter): larger values of α indicate larger heating.

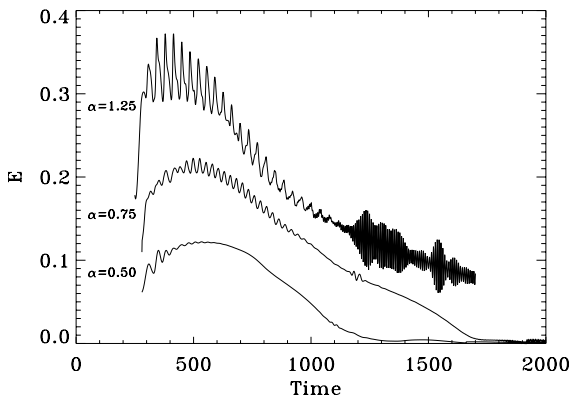

Figure 7. Electric field maximum amplitude along a selected ESW as a function of time for three runs with different heating values (indicated on the plot through the α parameter).

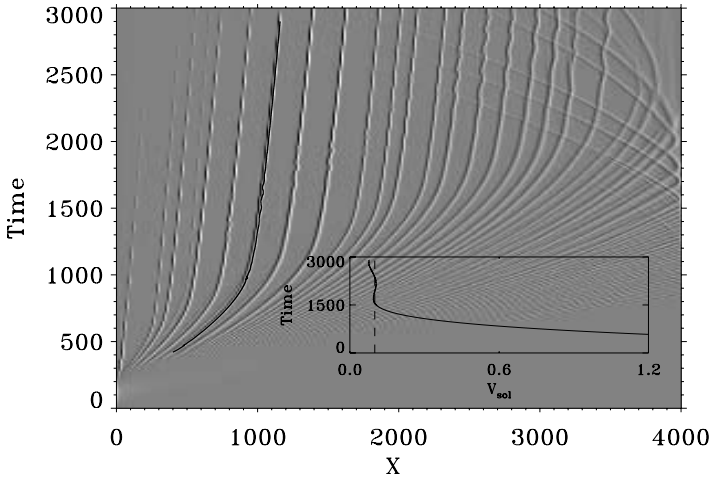

Figure 8. Electric field as a function of space and time (Run7). The inset shows the plot of the velocity as a function of time for the solitary structure underlined in black.

consequence of the time dependent injection of heated particles. The theories based on monoenergetic beams require nonlinear interactions and/or coupling with the inhomogeneous background medium in order to enlarge the wave vector spectrum of the excited waves, otherwise confined to a too narrow k interval (corresponding to the waves excited by the beam).

[19] The Langmuir waves generated in the simulation appear in the form of wave packets of limited sizes (Figure 3), as frequently observed in the solar wind. The analogy is not only qualitative, but also the amplitudes (using the parameters of Table 1) are comparable. To compare with observations, the time range of Figure 3 has been limited to a subset corresponding to records from the TDS/WAVES instrument [*Bougeret et al.*, 2008] on board of STEREO (examples are also given by *Ergun et al.* [2008]).

[20] Isolated Electrostatic Solitary Waves are one of the main feature observed in the simulations. These isolated waves form at the beginning of the simulations (Figure 4) as a consequence of the applied boundary conditions. Indeed, the applied heating preserves the total electron density but increases the density of high velocity particles. The plasma reacts to this current injection by generating a return current which shifts the core of the distribution function toward negative velocities. This implies a local charge separation that therefore generates an electric field. Low velocity electrons (i.e., $|v| < \sqrt{2\phi}$ in the particles frame) are trapped in the positive electric potential leading to the development of vortices in the phase space (Figure 5). The other ESW that develop well inside the simulation box result from a different mechanism, namely, the bump-on-tail instability. Because of the positive potential which repeals electrons, the vortices are associated with electron density cavities.

[21] These isolated bipolar electric fields cross the simulation box at a constant velocity spanning between 0.05 and $2v_{te}$. This velocity range depends on the applied heating: the stronger the heating, the larger the velocity (Figure 6). The electric structures are rapidly damped, and thus do not travel for long distances (Figure 7). However, the lifetime of an isolated structure is increased when a density gradient is present in the box (see below section 3.2).

[22] To understand the role of the dynamics of the positive charges, we have made simulations with a larger mass ratio: protons are replaced by oxygen ions (μ = 29,376). Qualitatively, the behavior of the plasma is similar to the previous section. So, for an initial *homogeneous* plasma, the protons or ions do not play a crucial role in the behavior of the plasma (at least, as long as real mass ratio are used, see *Califano et al.* [2007] for more comments when unrealistic mass ration are employed).

3.2. Density Gradient

[23] We now explore the consequences of the presence of a density gradient through the simulation box (see equations (4) and (5)). Similarly to the simulations of the previous section, several heating conditions were applied (through a variation of the α parameter). We present here results for α = 0.75.

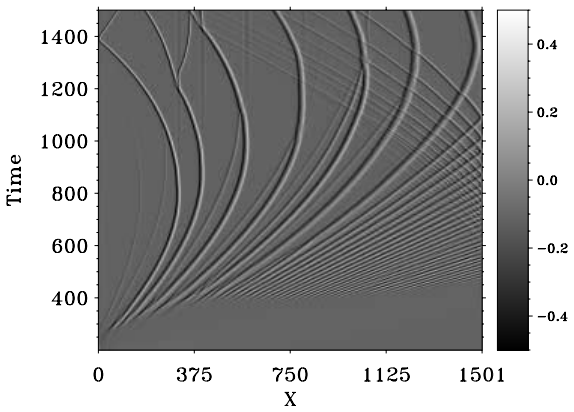

Figure 9. Electric field as a function of space and time (Run8).

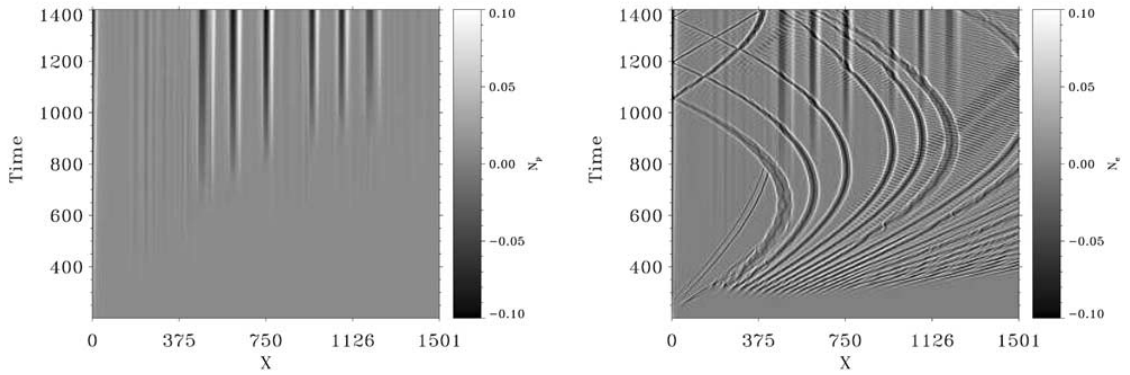

Figure 10. (left) Ion density and (right) electron density as a function of space and time (Run8). For sake of clarity, the density gradient has been removed.

[24] Two simulations are presented here to illustrate the behavior of the plasma. In both simulations, a gradient with a scale height $h = 3/4L$ is applied but with different mass ratio: in Run7 $\mu = 1836$ while in Run8 $\mu = 29{,}376$. This choice of scale height is not meant to represent any specific space environment but represents a compromise between real density gradient in different astrophysical contexts and computational resources. However, the simulations correspond to the real case of large scale density variations (homogeneous plasma) and approximate some cases of small scale inhomogeneities.

[25] Numerous ESW appear, now clearly isolated (Figures 8 and 9). Figure 8, shows the decrease of the ESW velocity from $1.2V_{te}$ when the structure is formed to a constant value of $0.1V_{te}$ around $t = 1000$. Note that this latest value is still much higher than the ion sound speed $v_i = \sqrt{\mu}\ 0.02v_{te}$. Conversely to the previous section, the lifetime of the ESW is increased: the waves survive the all duration of the simulation but they travel across limited distances (a few hundreds Debye length). In order to check spurious numerical effects driven by the presence of the right boundary, we have performed a number of simulations with different box size. The results were equivalent. This choice of box size was the best compromise to clearly distinguish the turbulent domain and the solitary structures.

[26] Run8 is the same as Run7 but with protons replaced by oxygen ions. This choice correspond to auroral regions where O^+ are the dominant ion species. Figure 9 shows the electric field resulting of Run8. Clear isolated ESW appear. After a more or less extended displacement in the box, each potential structure turns back toward the left boundary $x = 0$. Many other phenomena are also observed (like splitting of the vortex, waves trapping in the EWS etc): they will be detailed in a subsequent paper. As illustrated on Figure 10 at the direction reversal, a ion density cavity forms and decouples from the electrostatic structure. A decrease of electron density immediately develops to locally maintain the charge neutrality. These stationary density cavities are observable quantities: at the end of the simulation they reach about 10% of the initial density level. This decoupling from density cavities and electrostatic field was also observed by *Eliasson and Shukla* [2005, Figure 2, Figure 3] where, however, the density perturbation is applied on an already formed electron hole. The change of direction of the ESW has an interesting consequence from the observational point of view. Figure 11 displays an electric field profile for a given position, as would observe a space instrument. Because of the direction reversal of the electric structure, the ESW is detected twice but with opposite field polarity. *Omura et al.* [1999] show opposite polarity of the observed electric field and interpret it as a change of the flow direction of the electric potential. We show here that such phenomena can also be explained without invoking strong modification of the velocity flows: a reversal of the structure displacement due to the presence of a gradient in a heavy ion background can also be at the origin of such polarity inversion.

4. Conclusions

[27] A former paper *Briand et al.* [2007] presented the response of a plasma to a continuous periodic time modu-

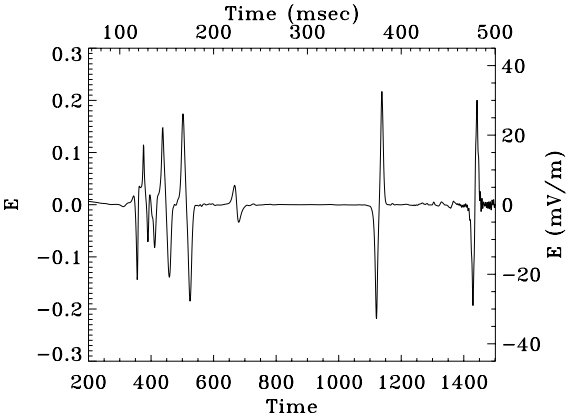

Figure 11. Electric field as a function of time for the spatial position $x = 200$ and dollar; (Run8 - see also Figure 9). The physical units are obtained taking a plasma frequency of 3 kHz given by *Omura et al.* [1999].

lation of the electron distribution function at the boundary of the simulation box (i.e., spatially localized). The present paper explores the response of a plasma to a different modulation mechanism (single pulse) varying the heating amplitude and discusses the role of mass ratio and density gradient. We first show that, even in absence of an initial extended, monoenergetic beam in the plasma, the applied heating lead to the formation of Langmuir and Electrostatic Solitary Waves. Indeed, the heated electrons travel through the simulation box following a ballistic trajectory. As they propagate, they generate bump-on-tail instabilities, at the origin of the waves. Once electrostatic waves are generated, low velocity particles are trapped in the electric potential but the majority of the particles follow their motion, giving rise to the development of the beam like instabilities further in the box. At each spatial position, the hump on the electron distribution function move toward lower velocities as a result of the ballistic effect of the slowest particles. The phase velocity of the resonant particles thus drifts toward smallest values, implying the excitation of a broad range of wave number and the development of a spatially extended turbulent domain.

[28] The presence of a density gradient strongly affects the behavior of the electron holes. First, it helps the stability of the ESW: compare to the situation in an homogeneous plasma, the presence of a density gradient increases their lifetime. However, their lower velocity (about $0.1v_{te}$ compare to about $1v_{te}$ in the homogeneous case) implies that they travel over smaller distances. So, ESW are not expected to be seen far from the generation site. This "local" characteristic may result from the 1D treatment. Indeed, as mentioned by *Oppenheim et al.* [2001], 3D increase the stabilization of the electron holes and allow them to travel over larger distances.

[29] It has been shown in several papers that when the dynamics of the positive particles is taken into account, the mass ratio play a crucial role in the stabilization of the electron holes. We underline here that it also affects their trajectory. In a density stratified atmosphere, ESW show a direction reversal in their displacement in the medium. The electric field presents a polarity reversal if observed at a given position. This is an important point since such observations have already been reported. At each direction reversal, a stationary, protons and electron cavity form. The amplitude of the cavities are strong enough to be observable by space instruments.

[30] **Acknowledgments.** F. Califano thanks the French INSU-CNRS, the Paris Observatory and the Université Pierre et Marie Curie for their financial support. The authors also thank the anonymous referees for their comments that helped to improve the manuscript.

[31] Amitava Bhattacharjee thanks Gregory Howes and S. Gary for their assistance in evaluating this paper.

References

Bale, S. D., P. J. Kellogg, D. E. Larsen, R. P. Lin, K. Goetz, and R. P. Lepping (1998), Bipolar electrostatic structures in the shock transition region: Evidence of electron phase space holes, *Geophys. Res. Lett.*, *25*, 2929–2932.

Bougeret, J. L., et al. (2008), S/WAVES: The radio and plasma wave investigation on the STEREO mission, *Space Sci. Rev.*, *136*(1–4), 487–528, doi:1007/s11214-007-9298-8.

Briand, C., A. Mangeney, and F. Califano (2007), Electrostatic coherent structures generation by local heating in a collisionless plasma, *Phys. Lett. A*, *368*, 82–86, doi:10.1016/j.physleta.2007.03.077.

Califano, F., L. Galeotti, and C. Briand (2007), Electrostatic coherent structures: The role of the ions dynamics, *Phys. Fluids*, *14*, 2306, doi:10.1063/1.2724807.

Eliasson, B., and P. K. Shukla (2005), The dynamics of electron and ion holes in a collisionless plasma, *Nonlinear Process. Geophys.*, *12*, 269–289.

Ergun, R. E., C. W. Carlson, J. P. McFadden, F. S. Mozer, L. Muschietti, I. Roth, and R. J. Strangeway (1998a), Debye-scale plasma structures associated with magnetic-field-aligned electric fields, *Phys. Rev. Lett.*, *81*, 826–829, doi:10.1103/PhysRevLett.81.826.

Ergun, R. E., et al. (1998b), FAST satellite observations of electric field structures in the auroral zone, *Geophys. Res. Lett.*, *25*, 2025–2028.

Ergun, R. E., D. M. Malaspina, S. Eriksson, and D. N. Newman (2008), Eigenmode structure in solar wind Langmuir waves, *Phys. Rev. Lett.*, in press.

Li, B., A. J. Willes, P. A. Robinson, and I. H. Cairns (2003), Dynamics of beam-driven Langmuir and ion-acoustic waves including electrostatic decay, *Phys. Fluids*, *10*, 2748–2762, doi:10.1063/1.1574515.

Lin, R. P., D. W. Potter, D. A. Gurnett, and F. L. Scarf (1981), Energetic electrons and plasma waves associated with a solar type III radio burst, *Astrophys. J.*, *251*, 364–373, doi:10.1086/159471.

Mandrake, L., P. L. Pritchett, and F. V. Coroniti (2000), Electron beam generated solitary structures in a nonuniform plasma system, *Geophys. Res. Lett.*, *27*, 2869–2872.

Mangeney, A., et al. (1999), WIND observations of coherent electrostatic waves in the solar wind, *Ann. Geophys.*, *17*, 307–320.

Mangeney, A., F. Califano, C. Cavazzoni, and P. Travnicek (2002), A numerical scheme for the integration of the Vlasov-Maxwell system of equations, *J. Comput. Phys.*, *179*, 495–538.

Matsumoto, H., H. Kojima, T. Miyatake, Y. Omura, M. Okada, I. Nagano, and M. Tsutsui (1994), Electrotastic Solitary Waves (ESW) in the magnetotail: BEN wave forms observed by GEOTAIL, *Geophys. Res. Lett.*, *21*, 2915–2918.

Nulsen, A. L., I. H. Cairns, and P. A. Robinson (2007), Field distributions and shapes of Langmuir wave packets observed by Ulysses in an interplanetary type III burst source region, *J. Geophys. Res.*, *112*, A05107, doi:10.1029/2006JA011873.

Omura, Y., H. Kojima, N. Miki, T. Mukai, H. Matsumoto, and R. Anderson (1999), Electrostatic solitary waves carried by diffused electron beams observed by the Geotail spacecraft, *J. Geophys. Res.*, *104*, 14,627–14,638, doi:10.1029/1999JA900103.

Oppenheim, M. M., G. Vetoulis, D. L. Newman, and M. V. Goldman (2001), Evolution of electron phase-space holes in 3D, *Geophys. Res. Lett.*, *28*, 1891–1894.

Rosseland, S. (1924), Electrical state of a star, *Mon. Not. R. Astron. Soc.*, *84*, 720–728.

Temerin, M., K. Cerny, W. Lotko, and F. S. Mozer (1982), Observations of double layers and solitary waves in the auroral plasma, *Phys. Rev. Lett.*, *48*, 1175–1179.

C. Briand and A. Mangeney, LESIA, Observatoire de Paris, CNRS, UPMC, Université Paris Diderot, 5 Place Jules Janssen, 92190 Meudon, France. (carine.briand@obspm.fr)

F. Califano, Dipartimento Fisica and CNISM, Università di Pisa, Largo Pontecorvo n.3, 56100 Pisa, Italy.

Available online at www.sciencedirect.com
ScienceDirect
Physics Letters A 368 (2007) 82–86
PHYSICS LETTERS A
www.elsevier.com/locate/pla

Electrostatic coherent structures generation by local heating in a collisionless plasma

C. Briand [a,*], A. Mangeney [a], F. Califano [b,a]

[a] *LESIA, Observatoire de Paris-Meudon, France*
[b] *Physics Department, University of Pisa, Pisa, Italy*

Received 30 January 2007; received in revised form 23 March 2007; accepted 26 March 2007

Available online 4 April 2007

Communicated by F. Porcelli

Abstract

We propose a new mechanism for the generation of electrostatic coherent structures and Langmuir fluctuations in a stratified plasma. The model is base on open boundary 1D Vlasov simulations where heated electrons are injected by applying a temporal continuous periodic modification of the width of the electron distribution function at one boundary of the simulation box. To our knowledge, that is the first time that a "localized heating" mechanism is studied as a driver for the development of bi(multi)polar electric field with their associated electron density holes and vortices in the phase space. After the development of many electrostatic coherent structures, the injected fast particles are free to move along their ballistic limit, while electrons moving at nearly, or less than, the thermal speed are diffused in phase space by the local fields.

PACS: 52.65.Ff; 52.65.-y; 52.35.Sb; 52.35.Fp; 94.05.Pt

1. Introduction

Electron holes and bipolar electric structures are frequently observed in the plasma sheet boundary layer of the magnetotail [1–3] near the bow shock [4–6], in the auroral ionosphere [7–11], in the solar wind [12,13] and also in the environment of the Jupiter's Satellite Europa [14]. Recently, it has been suggested that these structures could play an important role in magnetic field reconnection [3,15]. In the laboratory electron holes, also called BGK modes, have been generated experimentally in a Penning–Malberg trap by means of a nonlinear phase locking process (autoresonance) [16] and recently interpreted by means of Vlasov simulations and an analytic model [17]. The understanding of the physical processes responsible for the development of such structures is thus crucial.

Since almost identical electric structures and associated localized deviations from charge neutrality are observed in numerical simulations of the development of two stream or similar plasma instabilities [1,18–24], it is now commonly accepted that some sort of beam instability is responsible for the observed structures. This interpretation is strengthened by the frequent observations of bumps in the electron distribution functions in the regions where bipolar electric fields are observed.

Typically, these beams are considered to be a deformation of the distribution function in velocity space, sufficiently strong to excite "hydrodynamic" or Buneman type of instabilities. They are also spatially extended, so that any kind of flight effects occur only on time scales much larger than the typical growth time of the instability. Such beams are thought to be created by a dc electric field, as for example during magnetic field reconnection.

In the framework of a numerical approach, the term "beam" usually refers to a spatially, usually almost monoenergetic, long train of electrons or ions compensated by a second counter propagating electron/ion beam [25–27]. In situ solar wind observations of electron distribution functions during type III radiobursts also show the presence of a bump of high energy electrons [8,28]; this beam, however, moves towards smaller

* Corresponding author.
E-mail address: carine.briand@obspm.fr (C. Briand).

0375-9601/$ – see front matter
doi:10.1016/j.physleta.2007.03.077

velocities as time goes on, suggesting that time of flight effects are important. This is expected if the type III electrons are produced in some limited region, for example in the heated region where a nanoflare has occurred: the hot electrons escaping in the more tenuous higher corona forming a bump in the tail of the distribution function with a time varying mean velocity [29].

More generally, since the plasmas we are considering are collisionless, any perturbation of the distribution functions in a limited region is expected to affect by a combination of purely ballistic and wave particle interaction a much larger region. These processes replace the usual transport phenomena in a collisional fluid, where the distributions remain approximatively Maxwellian, while the macroscopic quantities evolve on hydrodynamic time scales. It is expected, in the collisionless case, to observe the ballistic formation of beam like features for suprathermal particles and something like thermalization for thermal ones.

The purpose of this Letter is to present some numerical simulations illustrating these processes and explore how *spatially localized time modulations* of the electron flux entering the numerical domain may produce, inside this domain, unstable deformations of the electron distribution function leading to the formation of electron holes. Finally, density gradients and density fluctuations are thought to play a critical role in the double layers development ([24] and references therein) and in the clumpy aspect of Langmuir waves in the solar wind [30]. A density stratified atmospheric model is thus considered.

2. Simulation conditions

We consider a density stratified atmospheric model, including both electrons and protons, with a time-independent gravity field $g^\star$ balanced by a self-consistent Pannekoek–Rosseland electric field ε (PR hereafter, [31]). The time evolution of the distribution functions is obtained by solving the Vlasov equation with open boundary conditions [32] in a 1D plasma box of length L. The numerical code is based on the "splitting algorithm" which in practice reduces the numerical scheme to the solution of an advection equation obtained by the implementation of a III order accurate Van Leer scheme which conserves the total charge of the particles [32]. The self induced electric field E is determined through the Ampere's law instead of solving the Poisson equation for which numerical errors introduced at the boundaries (in particular where heated electrons are injected, see Eq. (3)) immediately propagate inside the full box. The set of dimensionless equations is:

$$\frac{\partial f_\alpha}{\partial t} + v\frac{\partial f_\alpha}{\partial x} - \left[E + \varepsilon - g^\star\right]\frac{\partial f_\alpha}{\partial v} = 0, \tag{1}$$

$$\frac{\partial E}{\partial t} = -J, \quad J = \int v f_p \, dv - \int v f_e \, dv, \tag{2}$$

where f_α stands for the distribution function of each species (e for electrons and p for protons) and J is the electric current. Here length and time are normalized to the Debye length λ_D and the plasma period ω_{e0}^{-1} at the entrance of the simulation domain, $x = 0$ (corresponding to the density maximum), velocities v_α and masses m_α to the electron thermal velocity and electron mass, the electric field to $m_e v_e \omega_{e0}/e$ and the gravity to $(v_e\omega_{e0})^{-1}$. The distribution function of each species at time $t = 0$ is given by the following, normalized, Maxwellian function:

$$f_e(x, v_e, 0) = \frac{1}{\sqrt{2\pi}} \exp\left(-\frac{x}{h}\right) \exp\left(-\frac{v_e^2}{2}\right),$$

$$f_p(x, v_p, 0) = \frac{1}{\sqrt{2\pi}} \sqrt{\frac{m_e}{m_p}\frac{T_p}{T_e}} \exp\left(-\frac{x}{h}\right) \exp\left(-\frac{v_p^2}{2}\frac{m_p}{m_e}\frac{T_e}{T_p}\right),$$

h being the scale height of the atmosphere. Initially, the system is isothermal with the same temperature for both species. The scale height is a free parameter of the simulation which sets both the gravity and the PR electric field, which, when $T_p/T_e = 1$, takes the form $g^\star = 2/h = 2\varepsilon$. The atmosphere is in equilibrium: we observe no development of fluctuations in absence of external heating. In $x = L$ (corresponding to the density minimum), particles with $v > 0$ are free to leave while those with $v < 0$ maintain in time their initial distribution:

$$f_\alpha(x = L, v_\alpha < 0, t) = f_\alpha(x = L, v_\alpha < 0, t = 0).$$

The same boundary condition on the incoming particles, $v > 0$, is imposed on the protons at the left boundary $x = 0$ where, instead, heated electrons are injected by a modulation of their Maxwellian distribution function:

$$f_p(x = 0, v_p > 0, t) = f_p(x = 0, v_p > 0, t = 0),$$

$$f_e(x = 0, v_e > 0, t) = \frac{1}{\sqrt{2\pi}\, v_{\text{driv}}} \exp\left(-\frac{v_e^2}{2v_{\text{driv}}^2}\right),$$

$$v_{\text{driv}} = 1 + \alpha\left[1 - \cos\left(\frac{2\pi t}{T}\right)\right] \tag{3}$$

while outgoing particles, $v_e < 0$, are free to leave the domain. The width of the Maxwellian profile of the electron distribution function at $x = 0$ is thus controled by v_{driv} which is parameterized by the values of α and by the period T.

In the present work $T = 300$, $\alpha = 0.5$, $h = 3/4L$, $m_p/m_e = 1836$, $L = 2000\lambda_D$, $T_p/T_e = 1$, $-10 < v_e < 10$ and $-0.1 < v_p < 0.1$. The grid parameters were chosen to satisfy a compromise between a sufficient sampling of the phase space and a reasonable computational time: $\delta x = \lambda_{De}$, $\delta t = 0.01\omega_{pe}$. Other simulations with different values of T, α, L and h were performed. The results are qualitatively the same. Some specific comments on the role of the density gradient value are given in the next section. Those parameters do not to represent quantitatively a specific natural environment. They were chosen to allow long enough simulations (in space and time) with a reasonable computation time.

3. Results

Several profiles of the electron distribution function, at different time instants, close to the electrons injection boundary are displayed in Fig. 1. During the period $0 < t < 150$, heated electrons are introduced in the system. As a consequence, the width of the electron distribution function increases for the incoming particles. It also corresponds to the generation of a net

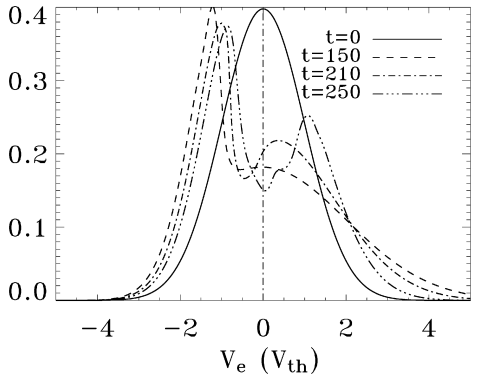

Fig. 1. Electron distribution function profiles in $x = 1$ for the times $t = 0$, 150, 210 and 250.

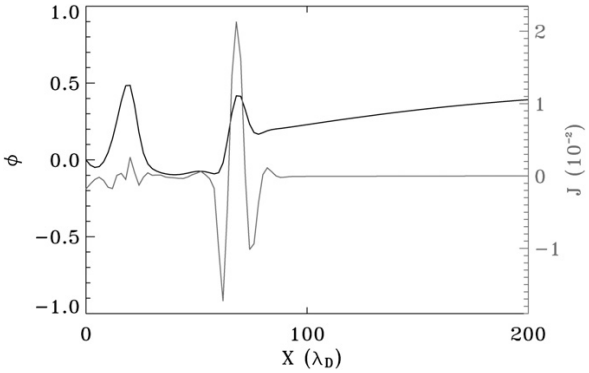

Fig. 2. Potential (black curve, left axis) and total current (gray curve, right axis) as a function of space for time $t = 330$.

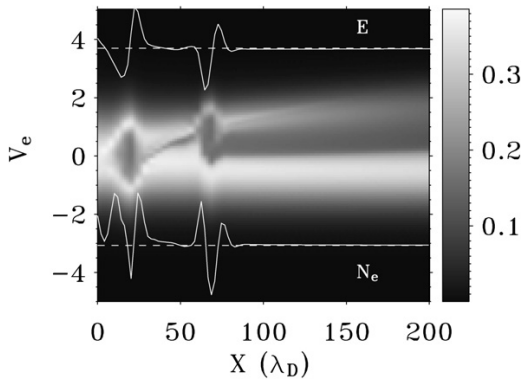

Fig. 3. Electron distribution function at time $t = 330$ for a reduced range of spatial points together with the electric field $E(x, t = 300)$ (top curve) and the electronic density curve $N_e(x, t = 300) - N_e(x, t = 0)$ (lower curve).

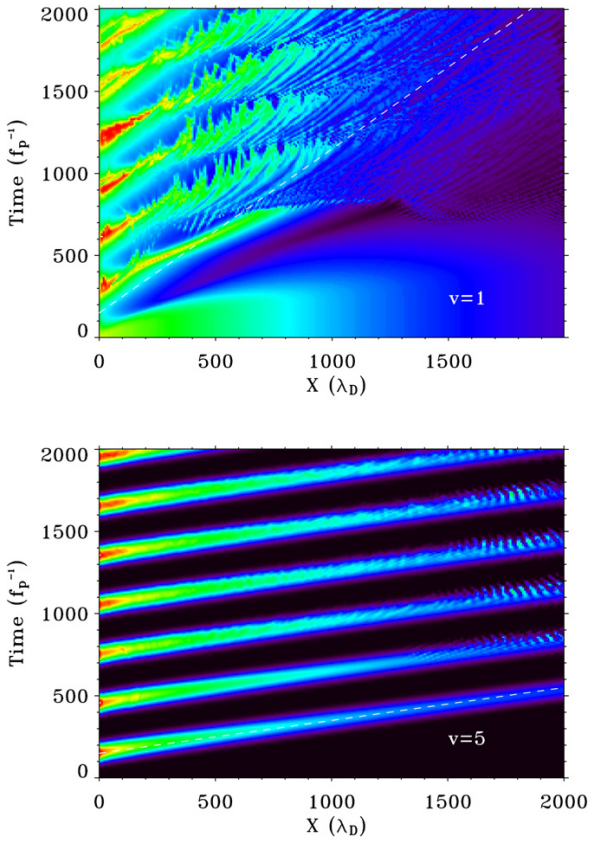

Fig. 4. Electron distribution function as a function of space and time for two velocities: $v = 1$ (upper) and $v = 5$ (lower). The white dashed line shows the ballistic limit for the given velocity.

current. The plasma immediately reacts by generating a return current in order to maintain quasi-neutrality. Consequently, the bulk of the electron distribution function is shifted towards negative velocity values. As a result, a positive valued electric field grows close to the boundary and pushes the electrons towards $x = 0$ creating an increase of the electron density and a decrease of the proton density, with some time delay due to their mass ratio. The opposite behavior happens during $150 < t < 300$, which corresponds to a decrease of the heating. Thus, even if the number of particles with positive velocities is maintained constant by the heating mechanism, the ($v_e > 0$) variations of the velocity distribution lead to a local charge separation: the number of particles travelling at a given velocity v is no longer compensated by the same number of particles travelling at the velocity $-v$. This charge separation induces the development of potential bumps (Fig. 2). These structures develop well inside the simulation domain (not shown here, see [33]). Vortices in phase space rapidly develop, associated with the electric structures previously described and with density holes (Fig. 3). They form along the electron ballistic limit, $x = v_e t$ and spread over a limited range of velocity ($v = \pm 2 v_{\text{th}}$). As a consequence, slow (less energetic) electrons are trapped by the electric potential. This electron trapping then implies velocity filtering: the fastest electrons move with an almost constant velocity while the slowest ones are confined in local potential wells. This is illustrated in Fig. 4 where the characteristics of the electron distribution function (i.e. the contour levels of $f_e(x, t)$ at constant velocity) are displayed for two selected velocity.

The displacement velocity of the vortices is of the order of the electron thermal speed, too fast to involve the protons in the

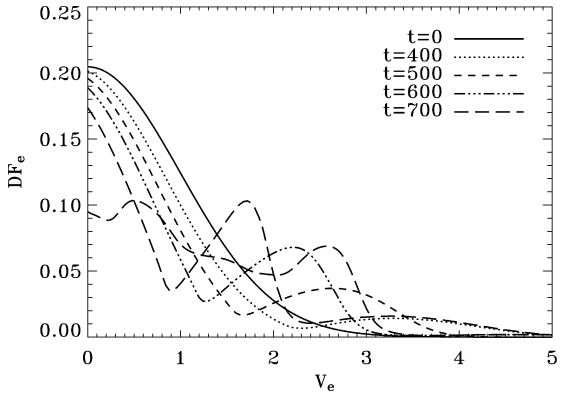

Fig. 5. Electron distribution function at position $x = 1000$ for the several times indicated on the figure. The bump results from the free streaming of the "high energy" (i.e. not trapped) electrons. Time $t = 700$ shows the perturbation of the distribution function when vortices appear.

dynamics; indeed, the ion distribution function does not show important modifications. A very important result is shown in Fig. 5 which displays the electron distribution function profiles for several times at a given position x. It shows how a bump in the distribution function moves from high to low velocities. This behavior of the distribution function hump is qualitatively similar to observations of electron distribution function associated with type III radio bursts in the solar wind [8,28].

Finally, there is a significant interaction between the electrostatic fluctuations produced by the repeated injection of heated electrons which induces the formation of a "turbulent" layer that progressively extends and fills the whole simulation box. This does not prevent the escape of the clouds of suprathermal electrons.

4. Conclusions

In this work we have shown that localized periodic temporal fluctuations of the electron distribution function width are able to reproduce the electric and density features observed in many natural plasma. The evolution of the resulting turbulent layer does not depend qualitatively of the details of the temporal variations at the boundary. Localized perturbations of the electron distribution function are probably easier to be generated than monoenergetic beams. We must also stress that the applied heating is relatively moderate (compare curve at $t = 0$ and $t = 150$ of Fig. 1): a factor 2 in the driver velocity. In subsequent papers (in preparation) we will present results for impulsive forcing and evolution of the turbulent layer at large scale and long time duration.

In the process of excitation we propose here, the values of parameters of the heating mechanism have been chosen such that the typical particles velocities remain limited to a few electron thermal velocities (depending on the initial heating). So, our results here cannot be directly applied to the problem of type III burst (which require velocities of about $0.1c$ i.e. $100v_{\text{th}}$) but may be considered as a possible explanation for other kinds of very fine radio signatures [34].

Furthermore, in the simulations presented here, no conditions were imposed on the total current at both boundaries of the simulation domain. However, other simulations (not discussed here) performed with $J = 0$ on each edge show that the structure development is qualitatively equivalent. The only relevant difference arise in the time delay for the structures to grow: in the case $J \neq 0$ the bi-polar electric field are generated more rapidly.

We finally note that in the present work the density gradient included in the model was mainly set for exploratory purposes (and comparison with already published works [23,24]) and was based on solar wind parameters [35]. On the other hand, for comparisons with ionospheric observations, a much longer scale length of the plasma should be used which, however, would require a much stronger computational effort. A detailed study on the influence of the density gradient on the hole dynamics and electrostatic fluctuations evolution is in preparation. Some preliminary tests suggest that any kind of temporal perturbation of any moment of the electron distribution function (temperature, heat flux, etc.) should lead to the development of a large turbulent domain filled by a large number of electron holes and to the velocity filtering mechanism.

References

[1] H. Matsumoto, et al., Geophys. Res. Lett. 21 (25) (1994) 2915.
[2] H. Kojima, H. Furuya, H. Usui, M. Matsumoto, Geophys. Res. Lett. 24 (23) (1997) 3049, doi:10.1029/97GL03043.
[3] C. Cattell, et al., J. Geophys. Res. 110 (A1) (2005) A01211, doi:10.1029/2004JA010519.
[4] H. Matsumoto, Adv. Space Res. 20 (4–5) (1997) 683.
[5] S. Bale, et al., Astrophys. J. 575 (2002) L25, doi:10.1086/342609.
[6] C. Cattell, et al., Nonlinear Process. Geophys. 10 (2003) 13.
[7] F.S. Mozer, et al., Phys. Rev. Lett. 79 (7) (1997) 1281, doi:10.1103/PhysRevLett.79.1281.
[8] R.E. Ergun, et al., Astrophys. J. 503 (1998) 435, doi:10.1086/305954.
[9] R.E. Ergun, et al., Geophys. Res. Lett. 28 (19) (2001) 3805, doi:10.1029/2001GL013024.
[10] B.T. Tsurutani, et al., J. Geophys. Res. 106 (A9) (2001) 19035.
[11] C. Cattell, et al., Adv. Space Res. 28 (11) (2001) 1631.
[12] A. Mangeney, et al., Ann. Geophys. 17 (1999) 307.
[13] C. Lacombe, et al., Ann. Geophys. 20 (2002) 609.
[14] W.S. Kurth, et al., Planetary Space Sci. 49 (3–4) (2001) 345.
[15] X.H. Deng, et al., Adv. Space Res. 37 (2006) 1373, doi:10.1016/j.asr.2005.05.129.
[16] L. Friedland, F. Peinetti, W. Bertsche, J. Fajans, J. Wurtele, Phys. Plasmas 11 (2004) 4305.
[17] L. Friedland, P. Khain, A.G. Shagalov, Phys. Rev. Lett. 96 (2006) 225001.
[18] Y. Omura, et al., J. Geophys. Res. 104 (A7) (1999) 14627.
[19] M.V. Goldman, M.M. Oppenheim, D.L. Newman, Geophys. Res. Lett. 26 (1999) 1821.
[20] D.L. Newman, M.V. Goldman, M. Spector, F. Perez, Phys. Rev. Lett. 86 (7) (2001) 1239, doi:10.1103/PhysRevLett.86.1239.
[21] D.L. Newman, M.V. Goldman, R.E. Ergun, A. Mangeney, Phys. Rev. Lett. 87 (25) (2001) 255001, doi:10.1103/PhysRevLett.87.255001.
[22] T. Umeda, Y. Omura, H. Matsumoto, H. Usui, J. Geophys. Res. 107 (A12) (2002) 1449, doi:10.1029/2001JA000286.
[23] N. Singh, Geophys. Res. Lett. 27 (7) (2000) 927, doi:10.1029/1999GL003709.
[24] N. Singh, Geophys. Res. Lett. 29 (17) (2002) 1833, doi:10.1029/2002GL015195.
[25] D.R. Nicholson, M.V. Goldman, P. Hoyng, J.C. Weatherall, Astrophys. J. 223 (1978) 605, doi:10.1086/156296.

[26] V.N. Mel'nik, E.P. Kontar, Phys. Scr. 58 (5) (1998) 510.
[27] V.N. Mel'nik, V. Lapshin, E. Kontar, Solar Phys. 184 (2) (1999) 353.
[28] R.P. Lin, D.W. Potter, D.A. Gurnett, F.L. Scarf, Astrophys. J. 251 (1981) 364, doi:10.1086/159471.
[29] A. Raoult, A. Mangeney, L. Vlahos, Solar Phys. 233 (1) (1990) 229.
[30] D.F. Smith, D. Sime, Astrophys. J. 233 (1979) 998.
[31] S. Rosseland, Mon. Not. R. Astron. Soc. 84 (1924) 720.
[32] A. Mangeney, F. Califano, C. Cavazzoni, P. Travnicek, J. Comput. Phys. 179 (2) (2002) 495.
[33] C. Briand, A. Mangeney, F. Califano, in: D. Danesy, S. Poedts, A. De Groof, J. Andries (Eds.), Proceedings of the 11th European Solar Physics Meeting "The Dynamic Sun: Challenges for Theory and Observations" (ESA SP-600), 11–16 September 2005, Leuven, Belgium, Published on CDROM., 2005, p. 81.1.
[34] C. Briand, A. Zaslavsky, A. Lecacheux, P. Zarka, M. Maksimovic, in: Proceedings of the 2nd Solar Orbiter Workshop, 16–20 October 2006, Athens, Greece, SP-641, December, 2006.
[35] P.A. Robinson, Solar Phys. 139 (1992) 147.

3.2.3 Chauffage localisé dans la couronne solaire ?

Articles de référence : Briand et al. (2008b)

Les observations du spectre dynamique solaire en radio montrent un très grand nombre de structures dérivantes dans le plan temps fréquences. Certaines sont bien connues (Type II, III etc) mais beaucoup d'autres sont plus difficiles à interpréter. Parmi ces structures récurrentes, des émissions de faible intensité dérivant soit vers les hautes soit vers les basses fréquences et de relativement courte durée (Figure 1 de l'article).

A partir de l'analyse statistique de plus de 1600 structures réparties sur près de 4 ans d'observation à Karkhov (Ukraine) et Nançay (France), nous avons déterminé leurs caractéristiques fondamentales. Notamment, en supposant que ces émissions étaient générées par des mécanismes équivalents à ceux donnant lieux aux émissions de Type III, nous avons montré que la pente des dérives conduit à des faisceaux d'électrons de quelques vitesses thermiques. Comment expliquer la présence de faisceaux de si faible vitesse dans la couronne solaire ?

La solution que nous proposons est basée sur les simulations exposées précédemment (voir Sect. 3.2.2) : ces émissions pourraient être la signature de faisceaux de particules se propageant le long du boucles fermées de champ magnétique dans la couronne solaire et ayant subi un chauffage localisé et variable avec le temps. Un tel chauffage même modéré peut en effet engendré des faisceaux de particules de faibles vitesses et la présence de structures dérivants vers les plus hautes fréquences traceraient les faisceaux retournant vers le soleil. Leur plus courte durée temporelle s'expliquerait d'ailleurs par une absorption du faisceau par les couches plus denses de l'atmosphère solaire.

A&A 490, 339–344 (2008)
DOI: 10.1051/0004-6361:200809842

Astronomy & Astrophysics

Faint solar radio structures from decametric observations

C. Briand[1], A. Zaslavsky[2], M. Maksimovic[1], P. Zarka[1], A. Lecacheux[1], H. O. Rucker[3], A. A. Konovalenko[4], E. P. Abranin[4], V. V. Dorovsky[4], A. A. Stanislavsky[4], and V. N. Melnik[4]

[1] LESIA, Observatoire de Paris, CNRS, UPMC, Université Paris Diderot, 5 Place Jules Janssen, 92190 Meudon, France
e-mail: carine.briand@obspm.fr
[2] Laboratoire de Physique et Technologie des Plasmas, Ecole Polytechnique, 91128 Palaiseau Cedex, France
[3] Space Research Institute, Austrian Academy of Sciences, Schmiedlstrasse 6 8042 Graz, Austria
[4] Institute of radio Astronomy, National Academy of Science of Ukraine, Ukraine

Received 25 March 2008 / Accepted 26 July 2008

ABSTRACT

Aims. Decameter radio observations of the solar corona reveal the presence of numerous faint frequency drifting emissions, similar to "solar S bursts" which are reported in the literature. We present a statistical analysis of the characteristics of these emissions and propose a mechanism to excite the Langmuir waves thought to be at the origin of these emissions.
Methods. The observations were performed between 1998 and 2002 with the Digital Spectro Polarimeter (DSP) receivers operated at the UTR-2 and Nançay decameter radio telescopes in the frequency range 15–30 MHz. Our theoretical explanation is based on Vlasov-Ampère simulations.
Results. Based on the frequency drift rate, three populations of structures can be identified. The largest population presents an average negative frequency drift of −0.9 MHz s^{-1} and a lifetime up to 11 s (median value of 2.72 s). A second population shows a very small frequency drift of −0.1 MHz s^{-1} and a short lifetime of about 1 s. The third population presents an average positive frequency drift of +0.95 MHz s^{-1} and a lifetime of up to 3 s. Also, the frequency drift as a function of frequency is consistent with the former results, which present results in higher frequency range.
No specific relationship was found between the occurrence of these emissions and the solar cycle or presence of flares.
Assuming that these emissions are produced by "electron clouds" propagating the solar corona, we deduce electron velocities of about 3–5 times the electron thermal velocity. As previously shown, a localized, time-dependent modulation of the electron distribution function (heating) leads to low velocity electron clouds (consistent with observations), which, in turn, can generate Langmuir waves and electromagnetic signals by nonlinear processes.

Key words. Sun: radio radiation – Sun: Corona – Sun: particle emission – methods: numerical

1. Introduction

Decameter radio observations of the solar corona reveal the presence of numerous types of emission among which the well studied type I, II, III, and IV bursts and storms. These intense emissions spread over a wide range of frequencies and usually exhibit fine structures (see Goldman 1983, for a review of type III emission; and Dulk 1985, for a general review of solar radio emission). Chains of stria of type III like bursts, named type IIIb (Ellis & McCulloch 1967; de La Noe & Boischot 1972) are frequently observed and appear to be precursors of type III emission. Emissions of short duration and limited frequency extent are also detected as isolated drift pairs (Roberts 1958; Warwick & Dulk 1969; de La Noe & Moller Pedersen 1971; Melnik et al. 2005), consisting of fundamental and harmonic radio emission, usually related to the presence of type III bursts.

High spectral and temporal resolution observations have revealed that the decameter range is also rich in faint intensity types of emission (Barrow et al. 1994). These structures can provide some indications of the physical processes taking place on small spatial scales. Single drift bursts of the same characteristics (occurrence, frequency drift) as the drift pairs were reported (de La Noe & Moller Pedersen 1971). Their emission is interpreted as the fundamental of the drift pairs. However, the isolated emission we are interested in is not related to the presence of drift pairs. The emission we study has characteristics similar to those of the "Fast Drift Bursts" (Ellis 1969), which were later referred as solar "S bursts" by McConnell (1980). A detailed analysis of these types of emission was presented by McConnell (1982) in the frequency range 40–80 MHz. Since then, this emission deserved little attention due to the difficulties in its observation.

The type II and III emission are explained in terms of electron beams propagating the interplanetary medium (Ginzburg & Zhelezniakov 1958). As they propagate, the electron beams excite electrostatic Langmuir waves, which couple each other to generate to electromagnetic waves at the fundamental of the local plasma frequency[1]. The drift in frequency with time is a consequence of the decrease in density (and the plasma frequency) with distance from the Sun. The electron acceleration mechanism differs however for type II and type III emissions. For type II emission, electrons are accelerated by shock propagating at thousands of km/s ahead of a Coronal Mass Ejection (CME). For type III emission, acceleration of electron beams is thought to be related to magnetic reconnection and energy release during flares. Both types of emission involve high velocity electron

[1] If this basic mechanism remains valid, a process should be proposed to limit the wave growth and retain the electron beams over long distances. This question is however outside the scope of this paper.

Table 1. Observation characteristics and instrumental configuration. First column: observing date; second column: radiotelescope used ("N" for Nançay and "K" for Kharkov) with the time resolution in parenthesis (in seconds); third column: start time of the observing run (in Universal Time); fourth colum: end time of the run (in UT); fifth column: frequency range of the observations; sixth column: number of drifting structures identified.

Date	Instr. (s)	Start time UT	End time UT	Frequency MHz	Structures #
May 2, 1998	N(0.05)	13:28:10	13:44:18	33–46	0
June 6, 1999	K(0.05)	08:33:50	08:59:54	15–28	0
June 26, 1999	K(0.20)	10:14:34	10:22:58	11–24	258
	K(0.10)	11:27:20	12:00:40	11–24	
June 27, 1999	K(0.10)	08:55:30	11:43:20	11–24	415
June 28, 1999	K(0.10)	09:04:20	10:08:20	11–24	9
July 1, 1999	K(0.02)	09:16:23	09:58:40	11–24	45
July 2, 1999	K(0.02)	09:51:52	10:08:45	11–24	53
July 3, 1999	K(0.02)	10:05:52	10:12:59	11–24	16
Aug. 3, 1999	N(0.10)	09:49:58	12:29:14	18–30	1(?)
Feb. 27, 2000	N(0.10)	09:17:02	11:49:40	33–46	0
July 12, 2002	K(0.05)	07:04:15	10:41:09	18–29	51
July 13, 2002	K(0.05)	06:23:37	11:16:52	18–29	808

beams (0.2 c to 0.6 c) and their occurrence is strongly correlated with solar activity (and therefore the solar cycle).

This paper presents a statistical analysis of faint, isolated, drifting solar emission in the range 15–30 MHz, extending the work of McConnell (1982) to the low frequencies of the decameter domain. Our set of observations covers an extended period of time around the last solar maximum (1998–2002). In Sect. 2, we present the instruments and data selection procedure used for the analysis. The results of the statistical analysis are described in Sect. 3. The characteristics of the emission suggest that electron beams propagating outwards (and inwards) through the solar corona could be the origin of the emission. The physical properties of these beams are determined in Sect. 4. Finally, Sect. 5 discusses the results and proposes a physical mechanism to explain the generation of Langmuir waves from low velocity electron beams.

2. Observations and selection procedure

2.1. Observations

The observations were performed at the UTR-2 Kharkov decameter array in Ukraine (Braude et al. 1978) and the Nançay decameter array in France (Boischot et al. 1980). The two radio telescopes were equipped with a Digital Spectro Polarimeter (DSP, Lecacheux et al. 1998) allow us to analyze the spectral range 15–33 MHz within 1024 channels. The main characteristic of the DSP is a temporal resolution of 50 milliseconds per spectrum. Combined with a dynamic range of 70 dB, the DSP is well adapted to observe the very faint and short structures of the solar corona. Polarization measurements are available from the Nançay array but this information is not used in the present study (because no faint structures was detected).

Several long series of observations are analyzed in the present work. Table 1 summarizes the characteristics of each observing run. They are distributed about the last solar maximum (between May 1998 and July 2002).

2.2. Structures selection

The analysis is based on time-frequency images (dynamic spectra). Each image covers a range of 50 s in time and 11 MHz in frequency. Figure 1 shows an example of these images.

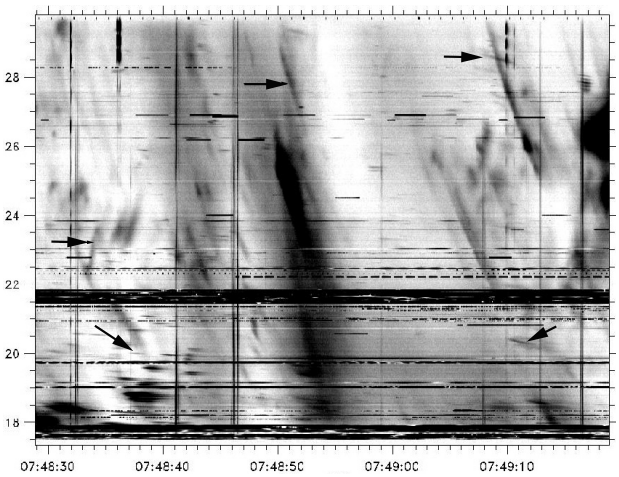

Fig. 1. Example of dynamic spectra from UTR-2 from the time series of July, 13 2002. Examples of the drifting structures studied here are indicated by arrows.

Due to the variety of their shapes (length, time profile, slope) and their low intensity level, each structure had to be identified by manual selection of several points along the crest line. The following selection criteria were used:

- continuity in time and frequency;
- start and end points clearly identified (the drifting structures starting or ending inside a strong emission were rejected);
- low intensity level.

This selection procedure introduces some biases. First, the starting and ending point locations depend strongly on the contrast in images. If the intensity is too low, these points may be undistinguishable from the background. Also, some structures start or end too close to parasitic emissions. These two errors lead to an underestimation of the actual time duration of the emission, which is difficult to quantify. Another error comes from the manual selection along the structure estimated to be 0.5 s in time and 0.1 MHz in frequency. To reduce the impact of these uncertainties on the frequency drift computation, each structure is fitted by a straight line. The result of the fitting determines the frequency drift.

Another bias in the selection procedure is the difficulty in distinguishing between one long structure with intensity variations and two distinct structures. This implies that there is an underestimation in the length of some structures. The number of such cases is however limited and in cases of doubt the emission was rejected.

Finally, emission with a positive drift was usually more difficult to identify due to its low intensity, leading to an underestimation of its population.

In spite of these limitations, some significant characteristics of the emission can be obtained (see below). When present, drift pairs were included in the statistics. As we see, their characteristics are similar to the faint structures that we are interested in.

The frequency associated with each structure is the starting point frequency, which provides information about the altitude of emission in the solar corona. The length in time and frequency is determined from the selected ending points.

Table 1 indicates the total number of structures identified in each observing run. In the following, the characteristics (time

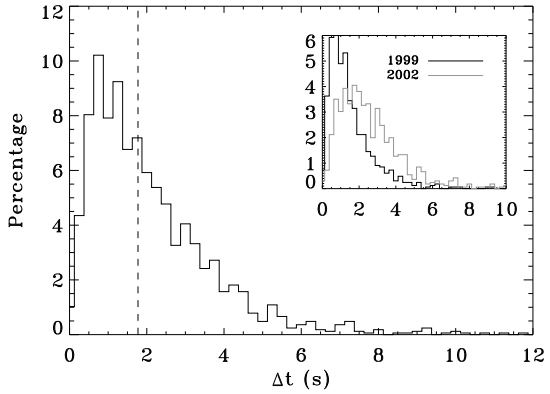

Fig. 2. Histogram of the time duration for the entire set of drifting structures. The vertical dashed line indicates the median value. The inset shows the same histogram, distinguishing between the observations of 1999 and 2002 (normalized to the total number of emissions).

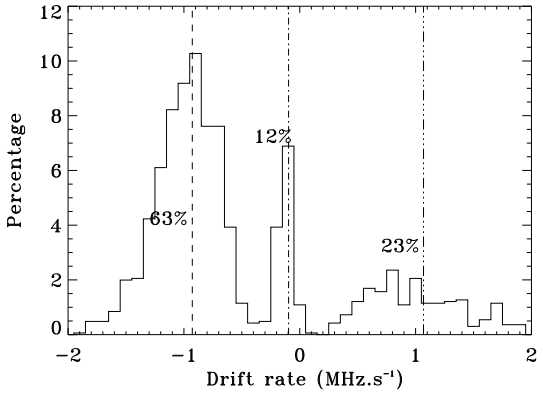

Fig. 4. Histogram of the frequency drift rate expressed as a percentage of the total number of structures. The median value of each population is indicated by the vertical lines. For sake of clarity, only structures between ±2 MHz s^{-1} are displayed.

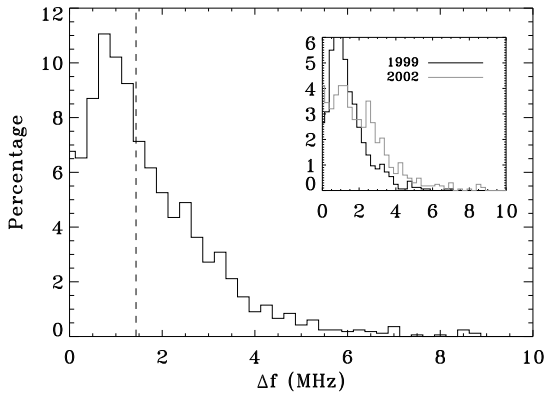

Fig. 3. Histogram of the frequency extent of drifting structures. The vertical dashed line indicates the median value. The inset shows the same histogram, but with the observations of 1999 and 2002 being displayed separately.

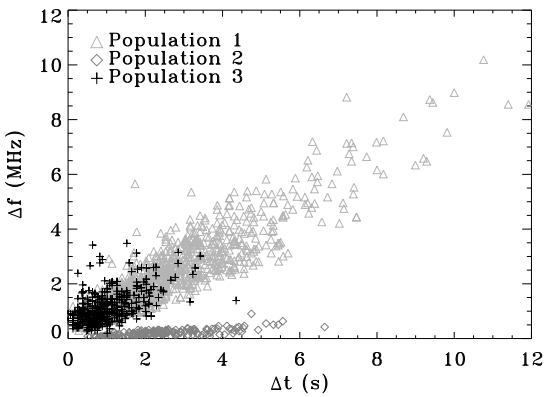

Fig. 5. Frequency extent as a function of the time duration of the structures. The three populations discussed in the text (see also Fig. 4) are distinguished by different symbols.

duration, frequency length, frequency drift) are deduced from a statistical analysis of the 1655 identified structures.

3. Characteristics of the emission

The histogram of the time duration of each emission is presented in Fig. 2. The median value is 1.75 s.

The histogram of the frequency extent is shown in Fig. 3. The median value is 1.4 MHz.

The emission is shorter in time and more narrow-banded than either type II to IV emission, but comparable to both drift pairs and S bursts, which justifies the inclusion of these last two types of emission in our study.

The histogram of frequency drifts (Fig. 4) reveals three distinct populations: the largest population (Population 1: 63% of the sample) has a median value of −0.9 MHz s^{-1}; a second one (Population 2: 12% of the sample) has a median value of −0.10 MHz s^{-1}; and a third (Population 3: 23% of the sample) has a median value of +1.1 MHz s^{-1}. The remaining 2% consists of structures with velocities scattered above +2 MHz s^{-1}. The presence of structures with reverse drift (towards higher frequencies) was also mentioned (for example by Ellis 1969; McConnell 1982) but not studied in detail, probably due to the lack of high sensitivity instruments. Also, the sporadic nature of this emission make it difficult to detect. The relationship between the frequency extent and the duration is shown in Fig. 5. A first group (crosses and triangles on the graph) presents a linear variation with a slope of 0.76 MHz s^{-1}, while a second group (diamond on the graph) shows a slope of 0.03 MHz s^{-1}. This latter represents only 9% of the entire sample.

The three populations discussed previously (and shown in Fig. 4) are separated well in Fig. 5: population 2 (small negative drift) corresponds to the almost horizontal structures, while populations 1 and 3 have the same steeper slope. Population 3 consists of structures with the shortest extent (both in time and frequency).

Frequency drifts are plotted as a function of frequency in Fig. 6 (left). We first note that the emission appears at all studied frequencies. Drift distributions within populations 1 and

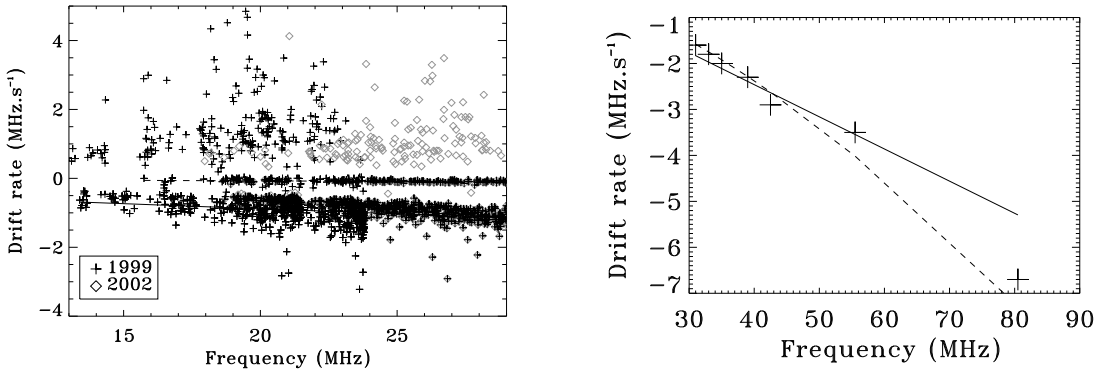

Fig. 6. Drift rate as a function of the frequency. *Left*: from our observation. Linear fits are indicated for populations 1 and 2. *Right*: from Table II of McConnell (1982). The straight line is the extent of the fit deduced from our data, the dashed line correspond to the fit of McConnell paper.

Table 2. Summary of the solar activity during the observing runs (in bold, flare starting after the end of our run). First column: observing date; second column: number of structures selected from the full observing run; third column: time (UT) of the maximum of Hα Flares with in parenthesis the duration (in minutes); fourth column: time of maximum (in UT) of X-ray Flares followed by the class and duration (in minutes); fifth: time of occurrence of type III radio emission. "NA" means "Not available" information while dashes mean "no activity" in the corresponding emission. Sources for flares: Solar Geophysical Data; source for the radio emission: our observations.

Date	Structures	Hα flare	X-rays flares	type III
	#	Time (duration)	Time (Class; duration)	Time
May 2, 1998	0	13:28(20)	13:31 (X1.1; 20)	13:38
June 6, 1999	0	08:55(3)	–	08:51
June 26, 1999	258	–	11:39(C3.1;NA)	11:49
June 27, 1999	415	09:07(60)	–	11:34
June 28, 1999	9	09:21(8), 09:21(7)	–	09:06, 09:08, 09:16
				09:19, 09:57, 10:07
July 1, 1999	45	–	–	09:23
July 2, 1999	53	10:15(20)	–	–
July 3, 1999	16	–	–	–
August 3, 1999	1(?)	09:47(8), 10:32(10)		09:53, 10:09, 10:30, 10:42
		–	11:40 (C4.6; 14), 12:25 (C3.1; 8)	11:20, 12:16, 12:24
Feb. 27, 2000	0	–	–	09:59
July 12, 2002	51	08:51(14)	06:59(C1.7; 28), 08:56(C1.6; 12), 10:35 (B8.4; 6)	08:00, 10:17
July 13, 2002	808	07:35(19), 07:53(4)	07:53(C1.6; 5), 08:15 (C2.2; 6)	06:29, 07:31
		08:15(9)		09:11, 09:13, 09:30

2 themselves drift at -0.07 MHz s^{-1}/MHz for population 1 and -5×10^{-3} MHz s^{-1}/MHz for population 2. The positive values do not exhibit any distinctive trend. The measurements presented by de La Noe & Moller Pedersen (1971, see their Fig. 2) agree with our own set of data, at least in the range of frequencies studied here. It seems, however, that their slope at negative values is larger (but their set of observation is limited). Figure 6 (right) shows the drift rate as a function of time from McConnell (1982), who explored the complementary domain 30–82 MHz. The fit of the current study is extrapolated towards the higher frequencies and superimposed on the fit proposed by McConnel ($\mathrm{d}f/\mathrm{d}t = -af^b$ with $a = 6.5 \times 10^{-3}$ and $b = 1.60$). The results of the two studies are consistent except for the last point at 80 MHz where a strong decrease in the drift rate appears that is not evident in our set of data.

3.1. Link with solar cycle and solar activity

Drift pairs appear to be precursors of type III bursts, which means that their occurrence is related to solar activity. It is therefore interesting to test if the isolated, faint emission, which shares common characteristics with drift pairs, is dependent on any kind of activity or solar cycle.

In Figs. 2 and 3, the duration and frequency extent of the emission is distinguished for the two years 1999 and 2002. A slight tendency towards longer duration is present in 2002. However, no difference in drift rate is apparent in Fig. 6. The coverage of the last solar maximum is too incomplete to be conclusive about the dependence on solar cycle. More investigation is required to draw any conclusion.

The relationship between emission occurrence and solar activity is analyzed in Table 2 which presents a summary of the solar activity recorded during each observing run. Flares in Hα, X-rays, and type III allow us to appreciate the activity in the chromosphere, the corona and the propagation of electron beams in the interplanetary medium. Of course, decameter radio emission are characteristics of the high altitude corona (see Sect. 4) but activity in the lower atmosphere of the Sun can generate instabilities that propagate into the higher solar layers and produce radio emission.

The strong X-ray flare of May 2, 1998 or the more moderate ones of August 3, 1999 apparently did not produce any faint

structure. However, only the Nançay instrument was observing at that time and it did not detect any structure, which may simply be due to a too high sensitivity threshold. On July 2 and 3, 1999, 69 structures were detected while no specific solar activity was present during the observing run. On July 12, 2002, 51 structures were detected while the activity was quite significant (3 X-ray flares, 1 Hα flare and 2 type III), while on the next day, 808 structures were observed while the solar activity was limited to the beginning of the observation run. It therefore appears that the faint, isolated, drifting emission is not related to any specific solar activity. However, our set of observations is limited. In particular, the data set for 2002 consists of only two days of observations.

4. Interpretation

Due to their similarity with other decameter radio bursts (type III, drift pairs), we assume that this type of radio emission is the signature of electron beams propagating in the solar corona. Assuming that the observed emission is at the fundamental of the plasma frequency and given an electron density model, the beam velocity can be deduced from the observations.

The plasma frequency f_p is given by:

$$f_p = A\sqrt{n(r)} \tag{1}$$

with $A \simeq 9$ for frequencies in kHz and density (as a function of the distance r to the sun) $n(r)$ in cm^{-3}. The frequency drift can thus be written:

$$\frac{df}{dt} = \frac{df}{dn}\frac{dn}{dr}\frac{dr}{dt} \tag{2}$$

which leads to the following expression, assuming a constant velocity V of the beam:

$$\frac{df}{dt} = \frac{A \cdot V}{2\sqrt{n(r)}}\frac{dn}{dr}. \tag{3}$$

The velocity V can be derived from an a priori known density model. Since the corona is highly structured, no unique density model can describe it. Among the many existing models that can be found in the literature, we have chosen to use three: the model of Leblanc et al. (1998) of the solar corona and interplanetary medium (deduced from coronographic observations and type III radio bursts), the model of Newkirk (1961) of solar quiet corona, and the model of Doyle et al. (1999) of a solar coronal hole. Alvarez & Haddock (1973) also derived electron densities from type III bursts, but their model is applicable mainly to large distances from the Sun. Mann et al. (1999) also proposed another density model which agrees to within 15% with the model of Newkirk in the range of altitude we are interested in. The density stratification corresponding to each model is shown in Fig. 7. The altitude range in the solar atmosphere covered by the frequency range of our observations (indicated by the horizontal grey lines) spans between 1.3 and 2.2 solar radii from solar mass center.

The three selected models provide similar results. Figure 8 displays the beam velocity as a function of the distance to the Sun, as obtained from the model of Leblanc et al. (1998).

We first check that the assumption allowing us to deduce Eq. (3) (constant beam velocity) is reasonable. The three models provide values below 0.1 c (0.1 $c \simeq 10 \times v_{te}$, v_{te} being the thermal velocity of the electrons at this range of altitudes). The median velocity deduced from the models is given in Table 3 for each

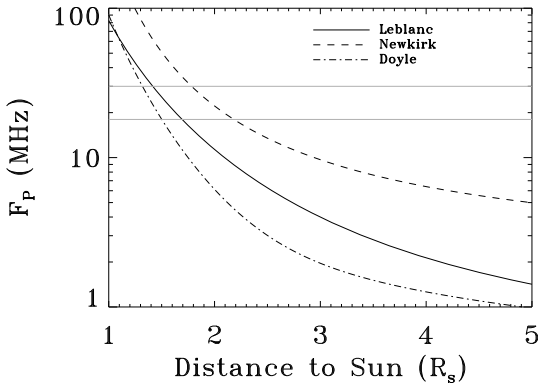

Fig. 7. Density stratification expressed in term of plasma frequency for the three models considered. The two grey horizontal lines delimitate the range of frequencies covered by our observations.

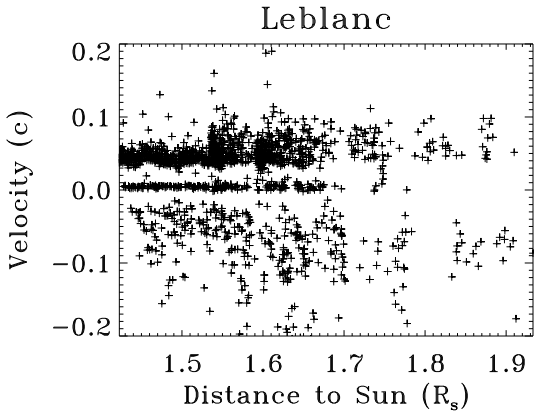

Fig. 8. Velocity of the observed structures (expressed in term of velocity of light) as a function of the distance to the Sun from the density model of Leblanc et al. (1998).

Table 3. Median value of the beam velocity deduced from each density model. Negative velocities are in the direction towards the Sun.

Model	Newkirk	Leblanc	Doyle
$V > 5 \times 10^{-3}$ (c)	+0.06	+0.04	+0.03
$V \approx 0$ (c)	$+6 \times 10^{-3}$	$+4 \times 10^{-3}$	$+3 \times 10^{-3}$
$V < -5 \times 10^{-3}$ (c)	−0.07	−0.05	−0.09

population. Finally, we recall that in an atmosphere of 10^6 K, the thermal velocity is about 0.01 c. This means that the beams that we are considering travel at a few times the thermal velocity.

5. Discussion

The characteristics of the decameter emission that we have studied show that they are produced at all ranges of altitudes in the solar corona corresponding to the range 18–30 MHz (from about 1 to 2 solar radii). Most emission presents a drift rate suggesting a propagation of the source outwards from the Sun. The extent in frequency and time of these structures can be quite large (up to 10 MHz and 11 s, respectively). Emission with positive velocity drift also suggests a propagation of the source towards

the Sun. However, in contrast to the previous group the extent in time and frequency is limited, which could indicate absorption in the denser layers of the solar atmosphere, close to the emission point.

In all cases, the frequency drift rate is far lower than those associated with type III radio bursts. If we admit that the same mechanism holds for the direct and reverse drift emissions, the electron beams generating the Langmuir waves at the origin of the radio emission must have velocities far smaller than the beams generating the type III emission. From standard coronal density models, we deduce velocities of a few times the electron thermal velocity. The electron beams at the origin of the type III radiobursts are thought to be generated by reconnection processes. This mechanism produces velocities at least 10 times higher than the velocity deduced from the present observations. We propose instead a *moderate, localized, time-dependent heating* to be at the origin of the Langmuir waves. As discussed in Briand et al. (2007), this mechanism yields electron clouds that can propagate, following a ballistic trajectory, at velocities of a few electron thermal velocity and generate Langmuir waves. If this interpretation is correct, this faint emission would be the signature of local plasma heating events in the corona. Population 2 emission processes must be different, since bump-in-tail instabilities (the basic instability that produces the Langmuir waves) are inefficient for beams of too low velocity. Processes similar to those implicated in the solar type IIIb are more likely to be at the origin of the isolated almost non drifting structures.

Since the mechanism that we propose does not require strong heating, the emission should correlated to neither solar activity nor solar cycle as actually observed. The present study appears to support this idea. However, more observations are required to be conclusive on this point.

Acknowledgements. This work was partly realized within the framework of the INTAS project N97-1964.

References

Alvarez, H., & Haddock, F. T. 1973, Sol. Phys., 29, 197
Barrow, C. H., Zarka, P., & Aubier, M. G. 1994, A&A, 286, 597
Boischot, A., Rosolen, C., Aubier, M. G., et al. 1980, Icarus, 43, 399
Braude, S. I., Men, A. V., & Sodin, L. G. 1978, Antenny, 26, 3
Briand, C., Mangeney, A., & Califano, F. 2007, Phys. Lett. A, 368, 82
de La Noe, J., & Moller Pedersen, B. 1971, A&A, 12, 371
de La Noe, J., & Boischot, A. 1972, A&A, 20, 55
Doyle, J. G., Teriaca, L., & Banerjee, D. 1999, A&A, 349, 956
Dulk, G. A. 1985, ARA&A, 23, 169
Ellis, G. R. A. 1969, Aust. J. Phys., 22, 177
Ellis, G. R. A., & McCulloch, P. M. 1967, Aust. J. Phys., 20, 583
Ginzburg, V. L., & Zhelezniakov, V. V. 1958, SvA, 2, 653
Goldman, M. V. 1983, Sol. Phys., 89, 403
Leblanc, Y., Dulk, G. A., & Bougeret, J.-L. 1998, Sol. Phys., 183, 165
Lecacheux, A., Rosolen, C., Clerc, V., et al. 1998, in Advanced Technology MMW, Radio, and Terahertz Telescopes, ed. T. G. Phillips, Proc. SPIE, 3357, 533
Mann, G., Jansen, F., MacDowall, R. J., Kaiser, M. L., & Stone, R. G. 1999, A&A, 348, 614
McConnell, D. 1980, Proc. Astron. Soc. Aust., 4, 64
McConnell, D. 1982, Sol. Phys., 78, 253
Melnik, V. N., Konovalenko, A. A., Dorovskyy, V. V., et al. 2005, Sol. Phys., 231, 143
Newkirk, G. J. 1961, ApJ, 133, 983
Roberts, J. A. 1958, Aust. J. Phys., 11, 215
Warwick, J. W., & Dulk, G. A. 1969, ApJ, 158, L123

3.2.4 Ondes de Langmuir et trous magnétiques

Articles de référence : Briand et al. (2010a,b); Soucek et al. (2009)

Les ondes de Langmuir se rencontrent également au sein de dépressions magnétiques qui apparaissent soit sous forme de trous isolés (appelés trous linéaires) ou associés à des discontinuités tangentielles ou rotationnelles de champ magnétique. Les trous linéaires sont de dimension modeste : quelques rayons de gyration protonique. La dynamique du plasma doit donc être gouvernée par des effets cinétiques.

Des ondes de Langmuir sont souvent observées dans les trous magnétiques (quelle que soit leur nature). La génération de ces ondes est encore en débat. Grâce aux formes d'onde électriques obtenues par STEREO/WAVES nous avons étudié les caractéristiques des ondes autour de f_{pe} à l'intérieur de ces structures. Jusqu'à présent ces ondes avaient été observées uniquement avec des analyseurs de spectres. On montre en particulier des fluctuations rapides (quelques dizaines de milliseconde) et importantes (jusqu'à 50°) de leur polarisation par rapport au champ magnétique . Elles peuvent s'interpréter soit en termes de variation de l'orientation **B** soit en termes de propagation des ondes selon le mode Z.

Par ailleurs, les mesures des fonctions de distribution (3D avec CLUSTER et en pitch angle avec STEREO) montrent une isotropisation des électrons à l'intérieur des trous (aussi observable à travers une augmentation de la température perpendiculaire et une décroissance de la composante parallèle). Enfin, les données CLUSTER montrent une corrélation entre présence d'un strahl et présence d'ondes dans les trous magnétiques. Ces observations nous ont permis de raffiner le modèle de génération des ondes de Langmuir dans ces structures.

JOURNAL OF GEOPHYSICAL RESEARCH, VOL. 115, A12113, doi:10.1029/2010JA015849, 2010

Waves at the electron plasma frequency associated with solar wind magnetic holes: STEREO/Cluster observations

C. Briand,[1] J. Soucek,[2] P. Henri,[1,3] and A. Mangeney[1]

Received 21 June 2010; revised 7 September 2010; accepted 15 September 2010; published 29 December 2010.

[1] Magnetic depressions are common structures of the interplanetary medium. These magnetic holes can be just isolated dips of the amplitude of the field or they can be associated with discontinuities in the field orientation (tangential or rotational). Electrostatic waves at the plasma frequency (Langmuir waves) are often observed in these magnetic structures. The aim of the present paper is to provide the main characteristics of these waves and to propose a mechanism to explain their formation. The study is based on a statistical analysis of observations performed by STEREO (between March 2007 and August 2009) and Cluster (between 2002 and 2005) when each mission was in the free solar wind. Complementary information is provided by the two missions through the different instrumental configurations. We first provide new characteristics of the waves (polarization, energy, spectrum, occurrence). We then show that the occurrence of Langmuir waves activity inside a hole is closely linked to the presence of a significant electron strahl outside the hole. Finally, we propose a scenario for the generation of the Langmuir waves inside the holes.

Citation: Briand, C., J. Soucek, P. Henri, and A. Mangeney (2010), Waves at the electron plasma frequency associated with solar wind magnetic holes: STEREO/Cluster observations, *J. Geophys. Res.*, *115*, A12113, doi:10.1029/2010JA015849.

1. Introduction

[2] Langmuir waves modes are electrostatic waves close to the plasma frequency. They have been intensively studied in relation with type III radio bursts and in the Earth bow shock environment to understand the interactions of solar wind with the magnetosphere. Langmuir waves (LWs) are also observed in magnetic holes. In this paper we report recent observations of Langmuir waves in magnetic holes, providing new constraints to the models of wave generation and to physical conditions inside magnetic holes.

[3] Magnetic holes are commonly observed in space environment since the early flight of Pioneer 6: in the solar wind [*Turner et al.*, 1977; *Winterhalter et al.*, 1994; *Lin et al.*, 1996], in the Earth's magnetosheath [*Cummings and Coleman*, 1968; *Luehr and Kloecker*, 1987; *Treumann et al.*, 1990], in the cometosheath [*Russell et al.*, 1987], in the plasma behind interplanetary shocks, and in the heliosheath [*Burlaga et al.*, 2007]. These magnetic depressions can be either isolated structures not related to any particular change in the *B*-field direction (they are then called *linear holes*) or associated with directional discontinuities (DD) of the magnetic field.

[4] *Burlaga et al.* [1969] distinguished several classes of magnetic holes according to their duration: meso-scale (from a few days to 1 h), micro-scale (from 1 h to 1 min), and kinetic scale (less than 1 min). They suggested that larger holes are governed by hydromagnetic processes, while kinetic theory must be considered to explain the very short magnetic depressions, the size of the structures being of the order of the proton gyroradius. Several studies, using different selection criteria of the magnetic holes, showed that the size of the holes follows a power law, eventually with a break at about 20–40 s [*Fränz et al.*, 2000; *Stevens and Kasper*, 2007]. This change of scaling suggests that different processes indeed govern large and small structures.

[5] In spite of numerous observations, the question of the origin of the magnetic holes is still puzzling: Are they generated near the Sun and then convected by the solar wind or are they formed locally in the interplanetary space? The presence of magnetic dropouts can affect the transport properties of the particles and the study of magnetic holes and discontinuities can therefore provide information on the large scale structure of the solar wind.

[6] *Burlaga and Lemaire* [1978] first showed that magnetic holes are pressure equilibrium structures, solution of the Maxwell-Vlasov equations. In situ plasma measurements have confirmed this statement [*Winterhalter et al.*, 1995; *Neugebauer et al.*, 2001; *Zurbuchen et al.*, 2001; *Stevens and Kasper*, 2007]. They also suggested that magnetic holes could result from an adiabatic pressure response (diamagnetic) of the plasma to a local enhancement of the kinetic pressure. More recently *Buti et al.* [2001] and *Tsurutani et al.*

[1]LESIA, Observatoire de Paris, CNRS, UPMC, Université Paris Diderot, Meudon, France.
[2]Department of Space Physics, Institute of Atmospheric Physics, ASCR, Prague, Czech Republic.
[3]Also at Dipartamento di Fisica, Università di Pisa, Pisa, Italy.

0148-0227/10/2010JA015849

[2002] proposed that diamagnetic effects could also result from an energization of protons.

[7] Langmuir waves are often excited within magnetic holes. Using data from the URAP instrument on board of ULYSSES, *Lin et al.* [1996] showed the correlation between the electric field power spectrum peaks and the presence of directional discontinuity in magnetic field. In their data set 9% of magnetic discontinuities displayed Langmuir waves activity, but this percentage increased to more than 30% when considering discontinuities associated with a large dip in field intensity. The waves were usually observed at the edges of the holes, that is, where the magnetic gradient is large. Thus, they concluded that the amplitude of magnetic field depression gradient, rather than the amplitude of the holes itself, is a key parameter for the development of Langmuir waves. They also showed that currents generated at magnetic field discontinuities play little role in the excitation of LWs. However, they could not give any details on the waveforms.

[8] Studying the dependence of the LW activity with the heliographic latitude, *MacDowall et al.* [1997, 2001, 2003] reached the following conclusions:

[9] 1. The intensity of the electric field is much higher outside a band of ±20° in latitude;

[10] 2. At high latitude, the wave activity is more likely observed in magnetic holes or other magnetic field discontinuities;

[11] 3. The probability of wave activity is higher outside the streamer belt than inside (magnetic holes are more common in the high-latitude solar wind); and

[12] 4. The electric field intensity is higher closer to the sun and shows a tendency to decrease with the distance to the Sun (but also a more surprising increase seems to occur at about 5AU).

[13] All the proposed mechanisms for the formation of magnetic holes are adiabatic, thus very slow. The presence of high-frequency electrostatic waves inside these magnetic dips is thus puzzling. Indeed, Langmuir waves usually require time-dependent fluctuations of the electron distribution function, hardly compatible with a slow formation of magnetic holes. In this study we present new observations of *E*-field waveforms and electron distribution functions providing clues to the understanding of the formation of these waves and reveal new properties of the magnetic holes themselves.

2. Instrumentation

[14] For the present study, we shall use two independent sets of magnetic hole observations, coming from two space missions: STEREO and Cluster.

[15] The STEREO observations are restricted to the ecliptic plane at a distance of about 1 AU from the Sun but cover a large longitudinal extension at large distances from the Earth. The data considered here span over the period 1 February 2007 to 31 August 2009. During this period of time, the Sun was very quiet. The two STEREO S/C were in the free solar wind (except for a short period in March 2007 when STEREO-B reached the flank of the magnetopause). The following data are used: (1) Three-component electric field waveforms of 130 ms duration from the Time Domain Sampler (TDS) mode of the WAVES instrument [*Bougeret et al.*, 2008]; (2) 8 Hz magnetic field (in spacecraft coordinates) measurements, pitch angle electron distribution, and electron temperature from IMPACT/SWEA [*Luhmann et al.*, 2008; *Sauvaud et al.*, 2008]; (3) 1 min average solar wind bulk velocity and proton temperature from PLASTIC [*Galvin et al.*, 2008].

[16] The plasma thermal noise ("plasma line") is hidden by the impact noise prohibiting the use of the thermal noise spectroscopy to deduce the electron density. The peak frequency of the Langmuir waves is used instead.

[17] The TDS instrument performs on-board selection of waveform snapshots that are transmitted to the ground if their amplitude is larger than a given threshold. The waveform data are therefore restricted to a limited number of the most intense wave events encountered by the spacecraft (typically less than 100 per day). Therefore, the absence of wave measurements in a magnetic hole does not necessarily mean that the waves were indeed absent. This is important to keep in mind when interpreting the STEREO data presented later in this article.

[18] Unlike STEREO, the Cluster spacecraft orbit the Earth and spend only a small part of their orbit in the unperturbed solar wind. Because we can only consider these intervals in our analysis, care had to be taken to ensure that the spacecraft were located sufficiently far from the foreshock region and the measurements were not perturbed by foreshock electrons and associated waves. The foreshock edge location was calculated from a model by *Cairns et al.* [1997] using local magnetic field and plasma data measured by the same Cluster spacecraft and only measurements further than 1 Earth radius from the model foreshock edge were considered. Furthermore, Cluster electric field spectrograms for the selected events were visually scanned for signatures of foreshock crossing, easily recognized by long continuous emission of intense narrowband waves. These intervals were excluded from the data set.

[19] In this study we used the following Cluster data: (1) Magnetic field vector sampled at 5 Hz from the fluxgate magnetometer (FGM) [*Balogh et al.*, 2001]; (2) high-frequency electric field from the Whisper instrument [*Décréau et al.*, 1997] (the spectra cover the frequency range from 2 to 80 kHz and are available approximately once in 2 s); (3) high-frequency electric field waveforms from the wideband (WBD) instrument [*Gurnett et al.*, 1997] sampled at 220 kHz and available in the form of 10 ms snapshots taken regularly every 80 ms; (4) pitch angle distributions provided by the PEACE electron instrument once or twice per satellite spin [*Johnstone et al.*, 1997].

[20] We used data from years 2002, 2004, and 2005. We restricted the search for suitable events to the periods when the Cluster apogee was on the day side of the Earth (December to May).

3. Data Selection and Classification of Magnetic Field Structures

[21] Due to instrumental constraints the selection of the events was performed differently for the STEREO and Cluster data set; each data set will be used to address different questions.

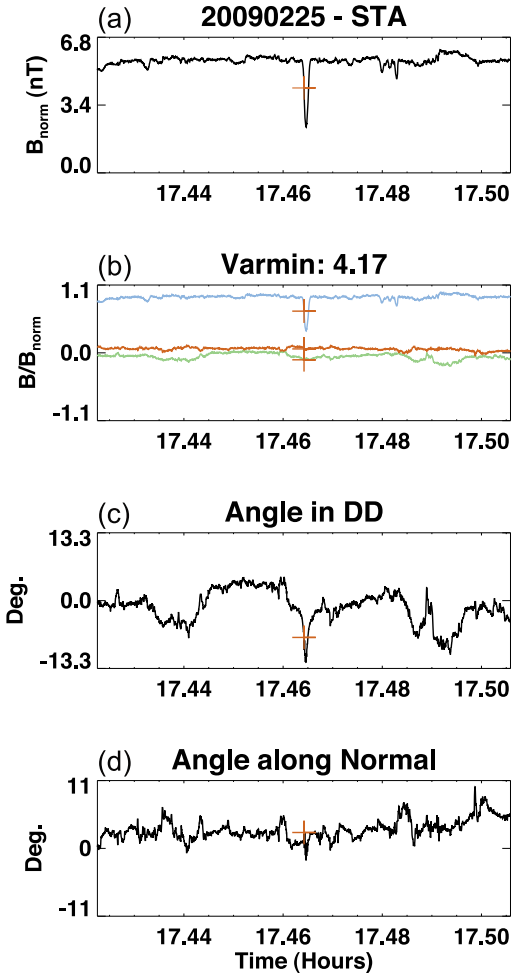

Figure 1. Example of linear magnetic hole. (a) Norm of the B field (in nanoteslas). (b) B field in the variance frame, normalized to the maximum value of the norm of B (in blue: the maximum variance, in red the minimum variance, in green the intermediate variance). "Varmin" indicates the ratio of the intermediate to maximum eigenvalue. (c) The rotation angle in the plane of the discontinuity. (d) The rotation angle perpendicular to the plane of the discontinuity (along the maximum variance axis). For Figures 1a–1d, the red crosses indicate the location of the wave activity.

3.1. STEREO Data Set

[22] Only a limited number of on-board selected TDS waveforms are transmitted by STEREO. Thus, we choose to select the magnetic configurations from the list of all TDS Langmuir wave observations in the analyzed period. So no criteria are applied on the selection of the magnetic configuration, except the presence of a significant E-field activity (i.e., a power spectrum at the Langmuir peak greater than 10 times the background level) above 5 kHz. Langmuir waves events associated with type II and type III emissions have been removed. The magnetic field configuration is plotted in a 5 min window for each interval of observed wave activity.

[23] The identification of the magnetic structures in terms of "Linear" or "Directional" holes is based on the following criteria: (1) linear hole: isolated depression of the norm of the magnetic field with a field rotation lower than about 10° (Figure 1); and (2) direction discontinuities: presence of a magnetic depression and together with a large rotation either on the plane of discontinuity (tangential) and/or in the plane perpendicular (rotational). In the following, we do not distinguish between the two types of DD (Figure 2).

[24] The instantaneous B-field rotation is defined as:

$$\sin(\theta) = |B(t)B(t+1)| \;/\; |B(t)| \times |B(t+1)| \qquad (1)$$

where B is the magnetic field vector at time t and $t+1$. This procedure allows to follow without ambiguity the rotation

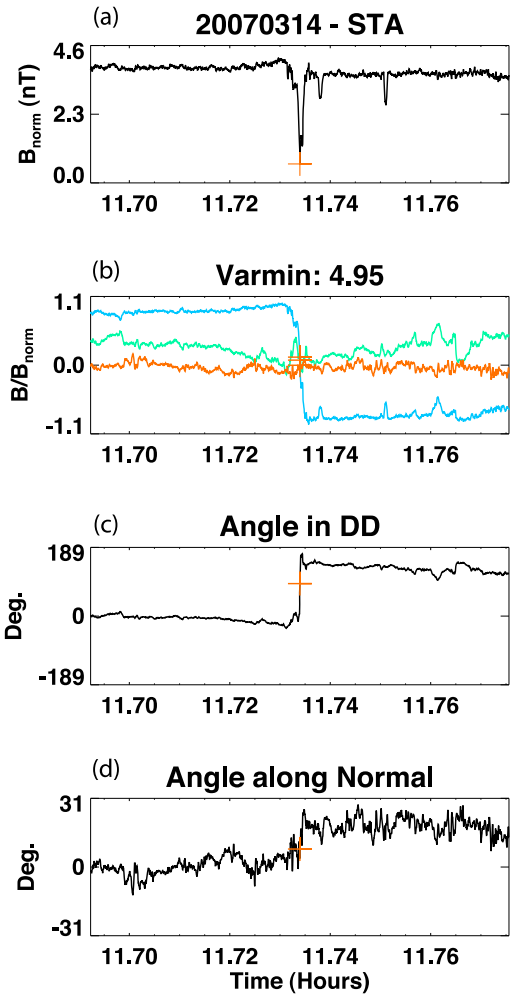

Figure 2. Same as in Figure 1 for a magnetic hole associated with directional discontinuities.

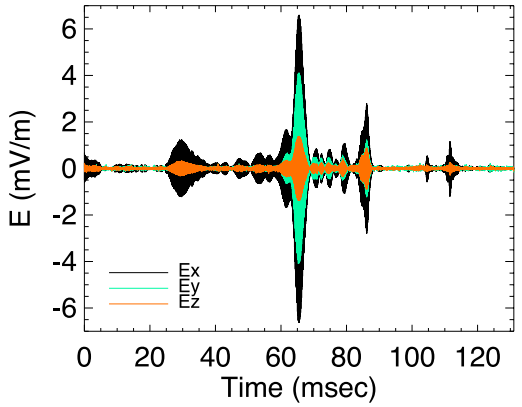

Figure 3. Example of electric waveforms inside a linear magnetic hole along three spatial directions (as defined by equation 2). Changes in the polarization can be appreciated by the variations of the relative amplitude along the three components inside short time wave packets. From S/WAVES.

of the field vector with time since the rotation remains small between two successive times. The magnetic field is expressed in minimum variance coordinates (maximum, intermediate, and minimum eigenvectors) to identify rotation in the plane of the discontinuity and perpendicular to it.

[25] We have chosen to identify visually the magnetic discontinuities since no exact criteria are valid: linear holes are usually associated with rotation angles smaller than 10° [*Winterhalter et al.*, 1994] to 15° [*Zhang et al.*, 2008], although no arguments are provided for the justification of these specific threshold values. Moreover, the Langmuir events are often located in dips embedded in a noisy magnetic background. The identification of the true nature of the hole with an automatic procedure is thus hazardous and would require a visual control anyway.

[26] From 1 February 2007 to 31 August 2009, 691 Langmuir events have been detected (311 from STEREO-A and 380 from STEREO-B) and are distributed among 358 distinct magnetic configurations. We restrict our study to the well-identified cases of linear holes and directional discontinuities that represent only 146 configurations. Linear holes represent 38% of the remaining samples and DD 62%. Note that a large majority of magnetic configuration has been rejected. They correspond to cases (i) where no magnetic depression was observed and (ii) where the edges of the magnetic depression were impossible to identify unambiguously because they are embedded in a rapidly varying background. The characterization of the waves in such peculiar environment will be the subject of another work.

3.2. Cluster Data Set

[27] Since the electric field data from the Whisper instrument are available almost continuously, the search for magnetic hole events in Cluster data was performed in a different way. An automatic algorithm was used to select free solar wind intervals in the Cluster data for the day-side seasons of 2002, 2004, and 2005, determined by visual inspection of the data and then manually searched for magnetic hole events. Magnetic holes were defined as localized decreases in magnetic field magnitude of at least 20% observed at timescales from few seconds to 5 min surrounded by intervals of nonfluctuating magnetic field. This semiautomatic procedure yielded a data set of 65 magnetic hole events.

[28] Although four spacecraft measurements are available for most events, data from only one spacecraft were included in the statistics for each hole. As the PEACE instrument is normally operated only on one spacecraft during solar wind passes, we usually selected the reference spacecraft based on PEACE data availability.

[29] The observed holes were included in the data set regardless of the presence of associated Langmuir waves; the data set therefore includes a significant fraction of holes without observed wave activity and can be used for statistical investigation of factors correlated with wave occurrence (section 4.1). The holes were classifield into "linear" and "directional" according to the same criteria described above for the STEREO data.

4. Properties of Observed Waves

[30] The waveforms reveal the very bursty nature of the electric field (Figure 3). The frequency peak of the different short time wave packets inside the TDS events vary by ±2 kHz, resulting in a broadening of the peak in the power spectrum around the primary wave frequency. The modulation can be a signature of (i) waves being generated by low-energy warm electron beams, (ii) the transient and fluctuating nature of the electron beam responsible for wave generation, (iii) inherent plasma density fluctuations, or (iv) electron trapping in the potential field of the waves [*Muschietti et al.*, 1994]. Thermal and Doppler shift broadening appear to be second order effects (about a few hundred hertz in the solar wind conditions and beam velocity of about 5 $v_{th,e}$).

[31] Owing to the 3-D waveform measurements, we can, for the first time, check the polarization of the waves with respect to the ambient magnetic field. To do so, B and E fields are first projected into the following frame:

$$e_x = B(t_0) \;/\; |B(t_0)| \tag{2}$$

$$e_y = e_x \times V_{sw} \;/\; |V_{sw}| \tag{3}$$

$$e_z = e_x \times e_y, \tag{4}$$

where $B(t_0)$ stands for the direction of the magnetic field at time t_0 of the beginning of the Langmuir event and V_{sw} the direction of the solar wind (assumed to be in the radial direction). By construction, the B field is along the e_x component.

[32] The tips of the E-field components in the $e_x - e_y$ and $e_x - e_z$ planes follow a curve that is fitted by an ellipse. The eccentricity of the ellipse in each plane serves to infer the type of polarization: A linear polarization implies an eccentricity is close to one in the two planes. The polarization angle $\alpha = \arccos(\cos\xi \cos\phi)$ defines the angle between the main axis of the E-field ellipsoid and the background magnetic field. Here ξ is the angle the projection of the E field in the plane $e_x - e_y$ and ϕ in the plane $e_x - e_z$. This angle α

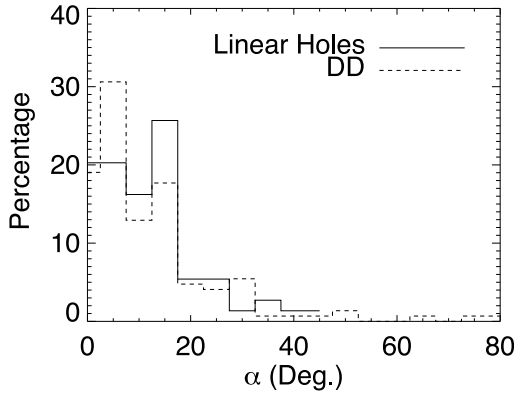

Figure 4. Histogram of the polarization angle α of the waves relative to the B field for linear holes (solid line) and DD (dashed line).

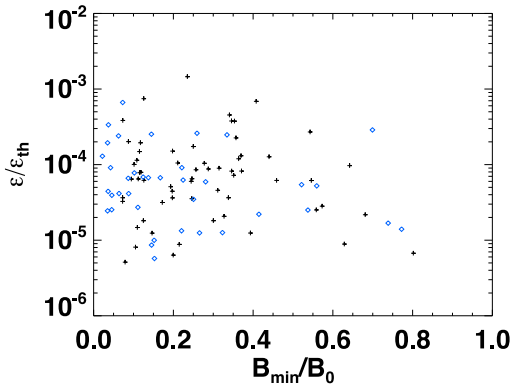

Figure 6. Electric energy of the waves versus hole depth. The energy is expressed in unit of thermal energy. Crosses, linear holes; diamonds, DD.

is zero for waves exactly polarized parallel to the magnetic field.

[33] Figure 4 displays the histogram of the angle α for waves inside the two types of holes. Although some of the waves exhibit a clear transverse component, a large majority of the observed waves is clustered in the region of small polarization angles and the polarization is linear (the eccentricity is close to 1). This confirms that the waves are linearly polarized mostly along the direction of the magnetic field. The median value of the polarization angle α is 11° for waves in linear holes and 13° for waves in DD. Thus, the type of B holes does not influence the polarization of the electrostatic waves.

[34] Now, individual wave packets inside a same TDS event of 130 ms often present multiple (still linear) polarization orientations: fluctuations up to 50° of the polarization angle are observed (Figure 5). Several interpretations are possible. If we assume that the waves are pure Langmuir waves (thus aligned with B), then the variations of polarization reveal very short time fluctuations of the magnetic field orientation. The second interpretation takes into account the weak magnetization of the plasma. In such a case, the Langmuir dispersion branch is continuously connected to the Z mode, which may lead to oblique propagation of waves close to the plasma frequency. The observed polarization would then be the signature of Z modes as the hole passes by the spacecraft.

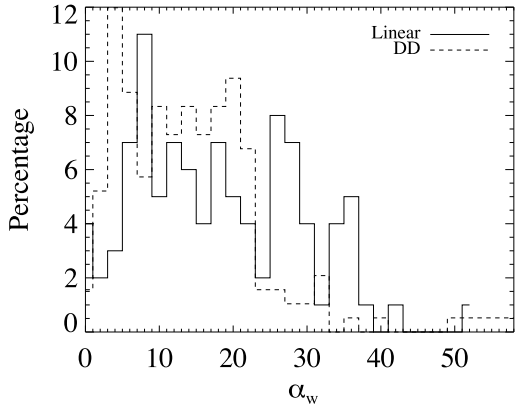

Figure 5. Histogram of the polarization angle α_w relative to B for individual wave packets chosen inside several TDS events.

[35] The maximum of the wave energy ϵ (normalized to the thermal energy) is shown as a function of the depth of the holes in Figure 6. The thermal energy is evaluated from the electron density deduced from the frequency peak of the Langmuir events and a constant electron temperature of 10^5 K. The energy in the waves is similar in linear and DD (median value of 5×10^{-5}): this is about one order of magnitude lower than the level of Langmuir waves associated to type III bursts [*Henri et al.*, 2009]. The observed energy is poorly correlated to the depth of the holes (Figure 6). The statistics are, however, biased by the small number of shallow holes.

[36] The Cluster data set allows us to characterize the probability of occurrence of Langmuir waves inside magnetic holes. Table 1 shows the number of holes containing Langmuir wave activity and holes without any wave activity for each type of magnetic holes. Despite the small size of the data set, it can be concluded that about half of all observed magnetic holes contain some indication of wave activity.

Table 1. Occurence of Langmuir Waves in Different Types of Magnetic Holes[a]

	All Holes	Linear Holes	Holes With DD
Cluster: Holes with waves	36 (55%)	26 (58%)	6 (50%)
Cluster: Holes with no waves	29 (45%)	19 (42%)	6 (50%)
STEREO: Holes with waves	146	55	91

[a]For the Cluster data set, eight holes fall in the unidentified category (neither linear nor directional). The last row shows the results for the STEREO data set. Note that for the STEREO data, events were identified based on the observation of Langmuir waves.

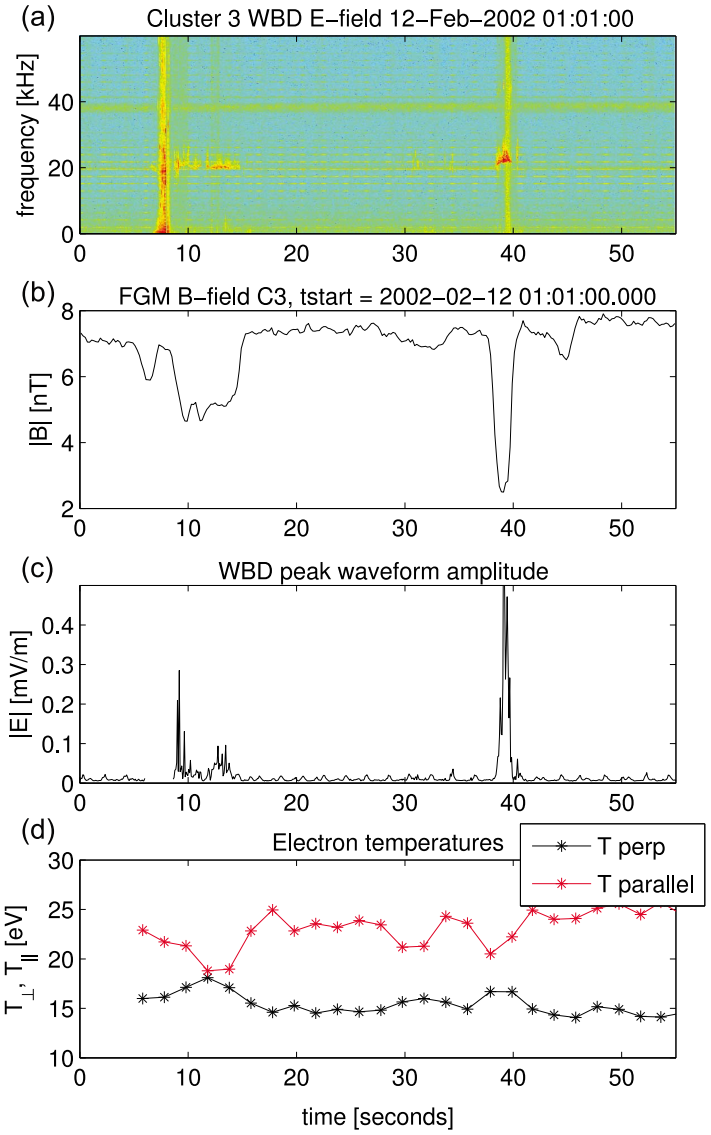

Figure 7. Detailed view of magnetic holes observed by Cluster. (a) Electric field spectrogram (WBD instrument). The strong broadband signature just before the first hole is an instrumental effect (a signature of Whisper resonance sounder sweep). (b) Magnetic field magnitude (FGM). (c) Peak electric field amplitude (WBD). (d) Parallel and perpendicular electron temperature.

This result is roughly consistent with the results of *Lin et al.* [1996].

[37] Also, among the 691 *E*-field events detected by STEREO, a large number of Langmuir events occur outside magnetic holes. Indeed, only 11% are located inside linear holes and 21% are located in DDs. Note that the larger number of waves inside DD can just result from the larger number of DD detected.

[38] Based on their analysis of Ulysses data, *Lin et al.* [1995] report that the waves are often observed at the edges of the holes. Our data partly confirm this statement. In several DD, waves occurs at the center of the hole. Moreover, in the case of narrower linear holes, Cluster data show that the waves typically fill the entire hole, although an increase in wave amplitude may be observed close to the hole boundary. An example is shown in Figure 7. The figure presents a rare event where a solar wind magnetic hole was observed on Cluster while high resolution electric field data from the WBD instrument were available. The two linear holes (8 and 3 s wide) are clearly associated with bursts of

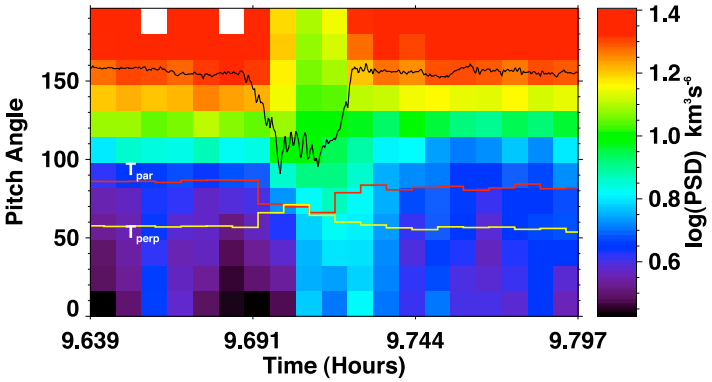

Figure 8. Pitch angle electrons at E = 257 eV (0° pitch angle means B-field-aligned particles) with superimposed the magnetic field strength (in black), the electron temperature T_{perp} (in yellow), and T_{par} (in red) for the same time interval. From STEREO.

wave activity at the plasma frequency over the full width of the holes.

5. Electron Distribution

5.1. Isotropization Inside the Holes

[39] The localized decrease in magnetic field modifies the properties of local electron distribution. Cluster and STEREO particle instruments allow us to investigate the change of the electron distribution function inside the magnetic holes. Figure 8 shows an example of electron pitch angle distribution measurements performed by the IMPACT/SWEA instrument of the STEREO spacecraft across a magnetic holes. The data come from a single energy channel of the instrument centered at an energy of 257 eV. At this suprathermal energy, the major contribution to the solar wind electron distribution comes from the field-aligned strahl component, as can be easily seen from the concentration of the distribution around antiparallel pitch angles.

[40] The figure indicates that there is a redistribution in pitch angle of the electrons, revealing an isotropization of the particle distribution inside the hole. The same effect is observed in other energy channels of the instrument and consistently in the data from the PEACE instrument of Cluster (not shown). This isotropization has an obvious effect on the electron temperatures measured by the spacecraft (temperature curves of Figure 8). As the parallel strahl intensity decreases, the parallel temperatures (derived from direct moment integration for electron energies above 45 eV.) strongly decrease and simultaneously the perpendicular temperature displays a moderate increase.

[41] Exactly the same effect is observed on Cluster, where higher time resolution of the measurements (2 or 4 s compared to 30 s on STEREO) allows us to demonstrate this effect even inside relatively narrow linear holes. Figure 7d shows the parallel and perpendicular temperatures estimated from the pitch angle distributions provided by the PEACE instrument (here data from the two sensors LEEA and HEEA were combined to obtain maximum time resolution of half the spin period). The isotropization described above shows up in this measurement as well. This increase (decrease) of the perpendicular (parallel) temperature inside the holes was already noticed for ions [*Fränz et al.*, 2000; *Neugebauer et al.*, 2001; *Tsurutani et al.*, 2002; *Stevens and Kasper*, 2007]. This is the first time it is also observed for electrons.

[42] The presence of a magnetic hole therefore leads to a scattering of the strahl and an isotropization of the electron distribution inside the hole. This effect was observed in a number of other events not shown in this article and appears to be relatively common in solar wind holes. A systematic statistical investigation of its occurrence is complicated by a number of instrumental effects associated with particle data and may be the subject of a future study. The measurements presented in the present paper were checked for instrumental effects and possible errors resulting from the rapid change in magnetic field direction during the measurement were ruled out in these cases. The fact that two instruments of different designs on different spacecraft observed the same effect also increases our confidence in the observation.

5.2. Relevance of Suprathermal "Strahl" Electrons

[43] The electron population of the solar wind plasma is known to present strong suprathermal non-Maxwellian features; it is traditionally decomposed into three populations: a bi-Maxwellian thermal "core," a non-Maxwellian but isotropic "halo," and a field-aligned "strahl" propagating usually in the anti-sunward direction [*Montgomery et al.*, 1968; *Feldman et al.*, 1975]. In this section we present observations of electron distribution functions associated with magnetic hole events potentially relevant to the mechanism of wave generation. We investigated a possible connection between the presence of the strahl and the occurrence of Langmuir waves inside magnetic holes by using the Cluster data set described in section 3.

[44] The presence of a strahl component was determined by evaluating the asymmetry of observed electron distribution in the solar wind surrounding the hole. A 20 s interval with minimum fluctuation of the magnetic field was chosen from a 2 min time range surrounding the hole. Four subsequent

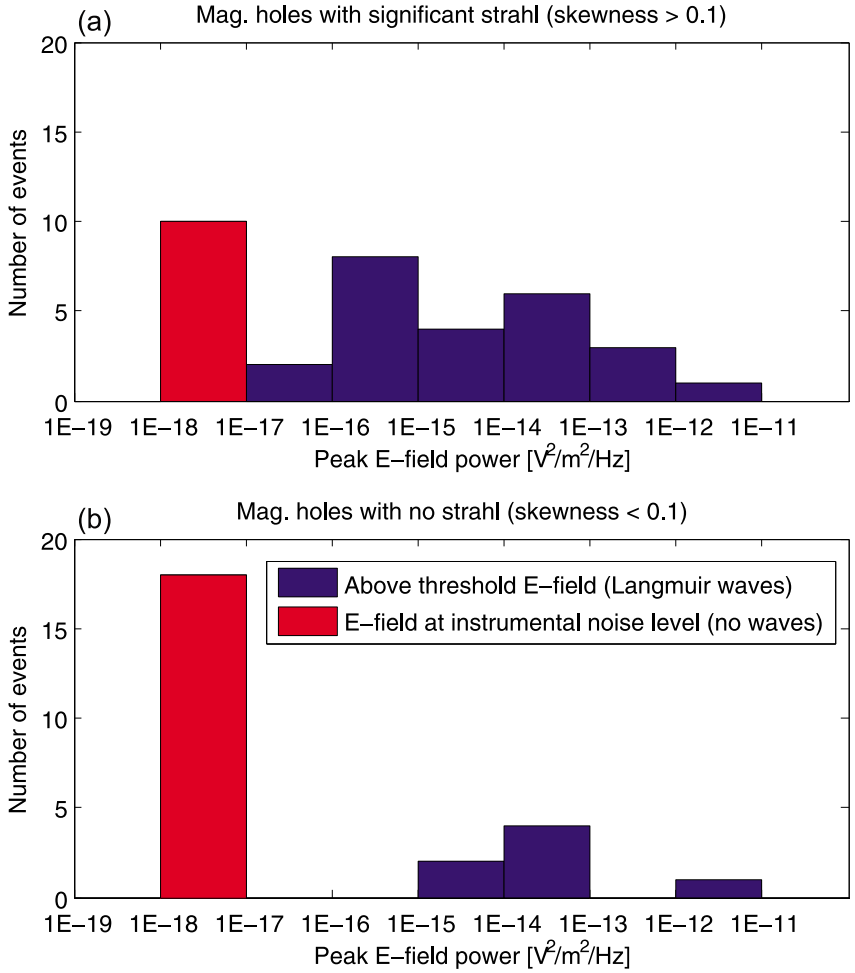

Figure 9. Histogram of the peak wave amplitudes for two groups of solar wind conditions: (a) events when a clear electron strahl is seen in the surrounding solar wind and (b) in absence of strahl in the local solar wind. The red column (power below 10^{-17} V^2 m^{-2} s^{-1} is the noise level of the Whisper instrument) corresponds to events with no Langmuir waves. The blue columns correspond to waves of experimentally significant measured amplitudes.

pitch angle distributions captured by the LEEA sensor of PEACE during this interval were averaged together to reduce the effect of relatively low particle counts. Next the averaged pitch angle distribution was integreated over perpendicular velocities yielding a reduced distribution $f(v_{\|})$.

[45] When a significant anti-sunward strahl component is present in the solar wind plasma, the reduced distribution will be strongly assymmetric with an enhancement in the anti-sunward half. The presence of a strahl can be therefore easily quantified by calculating the skewness of the reduced distribution:

$$S[f] = \int f(v_{\|}) v_{\|}^3 \, dv_{\|}. \tag{5}$$

[46] The PEACE instrument provided good electron measurements for 61 events of the 65 magnetic holes in our Cluster data set. These 61 events were divided into two categories according to the presence of strahl in the background solar wind at the time of their observation. After visual inspection of the distributions, the condition $S[f] > 0.1$ was chosen as a criterion for presence of a significant asymmetry in the distribution and hence significant strahl. From a total of 61 magnetic hole events 39 of them correspond to solar wind with significant strahl and 22 to solar wind with weak or no strahl.

[47] The occurrence of Langmuir waves inside the magnetic holes was investigated in these two groups of holes. The waves were identified by the maximum amplitude of the electric field inside the hole using the integrated electric field wave power data from the Whisper instrument of Cluster (available approximately five times per second). The results of the analysis are shown in Figure 9. The histograms show the distribution of peak wave power inside the holes

for the two groups. Blue columns indicate presence of Langmuir waves.

[48] Clearly, the occurrence of Langmuir waves inside magnetic holes was much higher during events where a strong strahl was present in the solar wind. In the case when no or a very weak strahl was observed in the solar wind plasma (Figure 9b) 17 holes show no wave activity and only 5 present some waves. In the category of events possessing a significant strahl (Figure 9a) the ratio is opposite: 11 holes with no waves and 28 holes with waves.

[49] This statistic shows that the occurrence of Langmuir wave activity inside solar wind magnetic holes is associated with the presence of a significant electron strahl population in the local solar wind. This observation suggests that the strahl likely plays a critical role in the generation of the waves, possibly supplying the suprathermal electrons responsible for the instability. Another possible interpretation that cannot be completely ruled out is that solar wind conditions corresponding to a diminished strahl are not favorable for the excitation of Langmuir waves inside magnetic holes.

6. Wave Generation Mechanism

[50] A likely candidate for the generation mechanism of longitudinally polarized electrostatic waves is the beam plasma instability ("bump on tail") responsible for similar waves in various environments (e.g., Earth foreshock and type II and type III bursts). Although a bump occurring at some nonzero pitch angle can generate Langmuir waves [*Yoon et al.*, 2000], we shall limit ourselves to the more robust instability criterion requiring a localized positive gradient $\partial \bar{f}(v_{\|})/\partial v_{\|} > 0$ in the reduced electron distribution function $\bar{f}$, easier to compare with the present low time resolution observations. It is not obvious to explain how such a positive slope in the electron distribution function may be formed in a magnetic hole, especially if one takes into account the fact that linear instability theory shows that "slow beams" (i.e., with velocity such that $v_b \approx v_{te}$) with a beam temperature similar to core electron temperature and density smaller (not necessarily much smaller) than the core plasma density are not sufficient to drive the plasma unstable [*Gary*, 1985].

[51] Consider the simplest case of a "linear hole" at rest in the solar wind (magnetic holes are generally believed to be nonpropagating structures convected by the solar wind flow [*Burlaga and Lemaire*, 1978; *Winterhalter et al.*, 1994]) and in pressure equilibrium with the surrounding plasma [cf. *Burlaga and Lemaire* 1978]. The electron population inside the hole may be affected in two ways: first, the adiabatic motion of the electrons (conservation of their magnetic momentum) passing through the hole along the magnetic field resulting in the filtering and focusing of the electrons and, second, time-of-flight effects associated with temporal variations in the properties of plasma entering the hole or nonstationarity of the hole itself. Because adiabatic focusing of thermal electrons by the hole will affect the electron temperature anisotropy, but hardly produce bimodal distributions or beamlike features, in a time stationary and symmetric situation (same electron distribution on both sides of the hole), some combination of both effects is required. Indeed, time-of-flight effects are well known to be responsible for reformation of electron beams in the foreshock [*Filbert and Kellogg*, 1979] or in type III solar bursts [*Papadopoulos et al.*, 1974]. Recent Vlasov simulations of generation of Langmuir waves by time-of-flight effects after a temporal change of electron distribution were performed by *Briand et al.* [2007].

[52] In the only published theoretical model for the formation of beams in magnetic holes proposed by *MacDowall et al.* [1996], the authors speculated that such a combination of adiabatic motion and time-of-flight effects acting on the thermal electron population could yield unstable distributions with the formation of two counterstreaming beams with velocities close to the electron thermal speed v_{te}. However these beams are not observed and would have hardly been unstable, as discussed above [*Gary*, 1985].

[53] The situation becomes significantly different if we take into account the suprathermal "strahl" component of the solar wind electron distribution, a field aligned population of electrons with speeds 3–10 times the electron thermal velocity and flowing along the field lines away from the Sun with a bulk speed larger than the solar wind velocity. The strahl electrons can thus penetrate the holes and provide a source population for the formation of electrons beams inside the magnetic holes.

[54] Indeed, we have shown in section 5.2, using Cluster data, that the occurrence of electrostatic waves inside magnetic holes is clearly associated with the presence of a significant strahl component in the ambient solar wind. We also show that the strahl inside the holes is weakened and dispersed in the holes. These observations suggest that the electrostatic waves are generated by electrons originating from the suprathermal strahl component. The formation of beams can be explained by a similar combination of adiabatic motion and time-of-flight effects as proposed by *MacDowall et al.* [1996] but applied to strahl electrons.

[55] As the strahl enters the hole due to its bulk flow velocity, its distribution is modified by two effects: (1) the adiabatic focusing described above and (2) particle drifts associated with magnetic field gradient and intrinsic electric field present inside the hole [*Burlaga and Lemaire*, 1978]. These two effects can drive the marginally stable distribution into an unstable state, resulting into wave excitation. This interpretation requires some level of fluctuations in the strahl component. The necessary electron beam can be formed from the fluctuating marginally stable strahl either directly by these effects (the strahl is also known to exhibit significant inhomogeneities and fluctuations on short timescales [*Louarn et al.*, 2009]) or by time-of-flight effects.

[56] This interpretation appears to be consistent with previous studies on the occurrence of high-frequency waves and strahl in the fast and slow solar wind. *Pilipp et al.* [1987], *Štverák et al.* [2009], and others showed that the strahl is on average more intense in the fast solar wind. *MacDowall et al.* [2003] concluded that the relative occurrence of Langmuir waves inside magnetic holes is higher in the fast solar wind comparing to slow solar wind. While this agreement may be a simple coincidence, it is consistent with our results.

7. Summary and Conclusion

[57] In this article we performed a comprehensive experimental study of electrostatic wave activity localized inside

solar wind magnetic holes using new data from Cluster and STEREO spacecraft. These new data allowed us to identify properties of these waves and of the solar wind electron distribution with direct relevance to the yet unexplained mechanism of their generation.

[58] Concerning the waves, we have shown that (1) the absence of waves outside the holes proves their local formation. (2) High-frequency waves inside magnetic holes are largely electrostatic. They can be interpreted either as Langmuir waves, beam-mode waves (eigenmodes of plasma perturbed by the presence of a beam) or *Z* mode. (3) Fluctuations of the plasma peak frequency are observed between different short time wave packets forming individual TDS events as well as rather large variations of the polarization angle between such successive wave packets. These two points suggest that some kind of small scale magnetic or/and density fluctuations are present inside the holes.

[59] We have also provided new information about the particle distribution inside (through pitch angle distribution) and outside (skewness) the magnetic holes. In particular we have shown (i) a strong correlation between the presence of a strahl outside the hole and the presence of high-frequency wave inside the hole and (ii) a scattering of the electrons occur inside the hole, leading to an isotropization of the distribution function [also seen as an increase (decrease) of the perpendicular (parallel) temperature of the electrons].

[60] Based on these observations, we have provided a model for the excitation of the waves at the electron plasma frequency. The new aspect of this model compared to previous ones is to point to the importance of the strahl electrons for the generation of a bump in the electron distribution function.

[61] **Acknowledgments.** We thank the IMPACT team, and in particular Peter Schroeder, for the support with the MAG/IMPACT files. STEREO PLASTIC investigation (A.B. Galvin PI) and NASA contract NAS5-00132. We also thank B. Lavraud for his help with the Pitch Angle measurements of IMPACT/STEREO. IMPACT and PLASTIC data can be access through the STEREO Web site (http://stereo-ssc.nascom.nasa.gov/data/ins_data/). Part of the data analysis was done with the AMDA science analysis system provided by the Centre de Donnes de la Physique des Plasmas (CESR, Universit Paul Sabatier, Toulouse) supported by the Centre National de la Recherche Scientifique and Centre National d'Études Spatiales. We thank the Cluster Active Archive and the instrument teams of the FGM, PEACE, Whisper, and WBD instruments of Cluster for the Cluster data used in this study. J.S. acknowledges the support of the grant 205/08/P129 of the Grant Agency of the Czech Republic.

[62] Philippa Browning thanks the reviewers for their assistance in evaluating this manuscript.

References

Balogh, A., C. M. Carr, M. H. Acuña, M. W. Dunlop, T. J. Beek, P. Brown, et al. (2001), The Cluster Magnetic Field Investigation: Overview of in-flight performance and initial results, *Ann. Geophys.*, *19*, 1207–1217.

Bougeret, J. L., et al. (2008), S/WAVES: The radio and plasma wave investigation on the STEREO Mission, *Space Sci. Rev.*, *136*, 487–528, doi:10.1007/s11214-007-9298-8.

Briand, C., A. Mangeney, and F. Califano (2007), Electrostatic coherent structures generation by local heating in a collisionless plasma, *Phys. Lett. A*, *368*, 82–86, doi:10.1016/j.physleta.2007.03.077.

Burlaga, L. F., and J. F. Lemaire (1978), Interplanetary magnetic holes: Theory, *J. Geophys. Res.*, *83*, 5157–5160, doi:10.1029/JA083iA11p05157.

Burlaga, L. F., K. W. Ogilvie, and D. H. Fairfield (1969), Microscale fluctuations in the interplanetary magnetic field, *Astrophys. J.*, *155*, L171, doi:10.1086/180329.

Burlaga, L. F., N. F. Ness, and M. H. Acuna (2007), Linear magnetic holes in a unipolar region of the heliosheath observed by Voyager 1, *J. Geophys. Res.*, *112*, A07106, doi:10.1029/2007JA012292.

Buti, B., B. T. Tsurutani, M. Neugebauer, and B. E. Goldstein (2001), Generation mechanism for magnetic holes in the solar wind, *Geophys. Res. Lett.*, *28*, 1355–1358, doi:10.1029/2000GL012592.

Cairns, I. H., P. A. Robinson, R. R. Anderson, and R. J. Strangeway (1997), Foreshock Langmuir waves for unusually constant solar wind conditions: Data and implications for foreshock structure, *J. Geophys. Res.*, *102*, 24,249–24,264, doi:10.1029/97JA02168.

Cummings, W. D., and P. J. Coleman Jr. (1968), Magnetic fields in the magnetopause and vicinity at synchronous altitude, *J. Geophys. Res.*, *73*, 5699–5718, doi:10.1029/JA073i017p05699.

Décréau, P., P. Fergau, V. Krasnoselskikh, et al. (1997), Whisper, a resonance sounder and wave analyser: Performances and perspectives for the Cluster mission, *Space Sci. Rev.*, *79*, 157–193.

Feldman, W. C., J. R. Asbridge, S. J. Bame, M. D. Montgomery, and S. P. Gary (1975), Solar wind electrons, *J. Geophys. Res.*, *80*, 4181–4196.

Filbert, P. C., and P. J. Kellogg (1979), Electrostatic noise at the plasma frequency beyond the earth's bow shock, *J. Geophys. Res.*, *84*, 1369–1381, doi:10.1029/JA084iA04p01369.

Fränz, M., D. Burgess, and T. S. Horbury (2000), Magnetic field depressions in the solar wind, *J. Geophys. Res.*, *105*, 12,725–12,732, doi:10.1029/2000JA900026.

Galvin, A. B., et al. (2008), The Plasma and Suprathermal Ion Composition (PLASTIC) Investigation on the STEREO observatories, *Space Sci. Rev.*, *136*, 437–486, doi:10.1007/s11214-007-9296-x.

Gary, S. P. (1985), Electrostatic instabilities in plasmas with two electron components, *J. Geophys. Res.*, *90*, 8213–8221.

Gurnett, D. A., R. L. Huff, and D. L. Kirchner (1997), The wide-band plasma wave investigation, *Space Sci. Rev.*, *79*, 195–208.

Henri, P., C. Briand, A. Mangeney, S. D. Bale, F. Califano, K. Goetz, and M. Kaiser (2009), Evidence for wave coupling in type III emissions, *J. Geophys. Res.*, *114*, A03103, doi:10.1029/2008JA013738.

Johnstone, A. D., et al. (1997), PEACE: A plasma electron and current experiment, *Space Sci. Rev.*, *79*, 351–398.

Lin, N., P. J. Kellogg, R. J. MacDowall, A. Balogh, R. J. Forsyth, J. L. Phillips, A. Buttighoffer, and M. Pick (1995), Observations of plasma waves in magnetic holes, *Geophys. Res. Lett.*, *22*, 3417–3420, doi:10.1029/95GL03266.

Lin, N., P. J. Kellogg, R. J. MacDowall, B. T. Tsurutani, and C. M. Ho (1996), Langmuir waves associated with discontinuities in the solar wind: A statistical study, *Astron. Astrophys.*, *316*, 425–429.

Louarn, P., et al. (2009), On the temporal variability of the "Strahl" and its relationship with solar wind characteristics: STEREO SWEA observations, *Sol. Phys.*, *259*, 311–321.

Luehr, H., and N. Kloecker (1987), AMPTE-IRM observations of magnetic cavities near the magnetopause, *Geophys. Res. Lett.*, *14*, 186–189, doi:10.1029/GL014i003p00186.

Luhmann, J. G., et al. (2008), STEREO IMPACT investigation goals, measurements, and data products overview, *Space Sci. Rev.*, *136*, 117–184, doi:10.1007/s11214-007-9170-x.

MacDowall, R. J., N. Lin, P. J. Kellogg, A. Balogh, R. J. Forsyth, and M. Neugebauer (1996), Langmuir waves in magnetic holes: Source mechanism and consequences, in *Solar Wind Eight: Proceedings of the Eighth International Solar Wind Conference*, edited by D. Winterhalter et al., *AIP Conf. Proc.*, *382*, 301–304.

MacDowall, R. J., R. A. Hess, N. Lin, and G. Thejappa (1997), Plasma wave observations from the ULYSSES spacecraft's fast heliographic latitude scan, *Adv. Space Res.*, *19*, 873–876, doi:10.1016/S0273-1177(97)00295-0.

MacDowall, R. J., N. Lin, and D. J. McComas (2001), Langmuir wave activity: Comparing the Ulysses solar minimum and solar maximum orbits, *Space Sci. Rev.*, *97*, 141–146, doi:10.1023/A:1011846700852.

MacDowall, R. J., N. Lin, and D. J. McComas (2003), Heliospheric Langmuir wave observations from the Ulysses spacecraft, *Adv. Space Res.*, *32*, 479–483, doi:10.1016/S0273-1177(03)00331-4.

Montgomery, M. D., S. J. Bame, and A. J. Hundhausen (1968), Solar wind electrons: Vela 4 measurements, *J. Geophys. Res.*, *73*, 4999–5003, doi:10.1029/JA073i015p04999.

Muschietti, L., I. Roth, and R. Ergun (1994), Interaction of Langmuir wave packets with streaming electrons: Phase-correlation aspects, *Phys. Plasmas*, *1*, 1008–1024, doi:10.1063/1.870781.

Neugebauer, M., B. E. Goldstein, D. Winterhalter, E. J. Smith, R. J. MacDowall, and S. P. Gary (2001), Ion distributions in large magnetic holes in the fast solar wind, *J. Geophys. Res.*, *106*, 5635–5648, doi:10.1029/2000JA000331.

Papadopoulos, K., M. L. Goldstein, and R. A. Smith (1974), Stabilization of electron streams in Type III solar radio bursts, *Astrophys. J.*, *190*, 175–186, doi:10.1086/152862.

Pilipp, W. G., K.-H. Muehlhaeuser, H. Miggenrieder, M. D. Montgomery, and H. Rosenbauer (1987), Characteristics of electron velocity distribu-

tion functions in the solar wind derived from the HELIOS plasma experiment, *J. Geophys. Res.*, *92*, 1075–1092.

Russell, C. T., W. Riedler, K. Schwingenschuh, and Y. Yeroshenko (1987), Mirror instability in the magnetosphere of Comet Halley, *Geophys. Res. Lett.*, *14*, 644–647, doi:10.1029/GL014i006p00644.

Sauvaud, J.-A., et al. (2008), The IMPACT Solar Wind Electron Analyzer (SWEA), *Space Sci. Rev.*, *136*, 227–239, doi:10.1007/s11214-007-9174-6.

Stevens, M. L., and J. C. Kasper (2007), A scale-free analysis of magnetic holes at 1 AU, *J. Geophys. Res.*, *112*, A05109, doi:10.1029/2006JA012116.

Štverák, Š., M. Maksimovic, P. M. Trávníček, E. Marsch, A. N. Fazakerley, and E. E. Scime (2009), Radial evolution of nonthermal electron populations in the low-latitude solar wind: Helios, Cluster, and Ulysses Observations, *J. Geophys. Res.*, *114*, A05104, doi:10.1029/2008JA013883.

Treumann, R. A., N. Sckopke, L. Brostrom, and J. Labelle (1990), The plasma wave signature of a 'magnetic hole' in the vicinity of the magnetopause, *J. Geophys. Res.*, *95*, 19,099–19,114, doi:10.1029/JA095iA11p19099.

Tsurutani, B. T., B. Dasgupta, C. Galvan, M. Neugebauer, G. S. Lakhina, J. K. Arballo, D. Winterhalter, B. E. Goldstein, and B. Buti (2002), Phase-steepened Alfvén waves, proton perpendicular energization and the creation of magnetic holes and magnetic decreases: The ponderomotive force, *Geophys. Res. Lett.*, *29*(24), 2233, doi:10.1029/2002GL015652.

Turner, J. M., L. F. Burlaga, N. F. Ness, and J. F. Lemaire (1977), Magnetic holes in the solar wind, *J. Geophys. Res.*, *82*, 1921–1924, doi:10.1029/JA082i013p01921.

Winterhalter, D., M. Neugebauer, B. E. Goldstein, E. J. Smith, S. J. Bame, and A. Balogh (1994), ULYSSES field and plasma observations of magnetic holes in the solar wind and their relation to mirror-mode structures, *J. Geophys. Res.*, *99*, 23,371–23,381.

Winterhalter, D., M. Neugebauer, B. E. Goldstein, E. J. Smith, B. T. Tsurutani, S. J. Bame, and A. Balogh (1995), Magnetic h in the solar wind and their relation to mirror mode structures, *Space Sci. Rev.*, *72*, 201–204, doi:10.1007/BF00768780.

Yoon, P. H., L. F. Ziebell, and C. S. Wu (2000), Excitation of Langmuir waves in interplanetary space, *J. Geophys. Res.*, *105*, 27,369–27,376, doi:10.1029/2000JA000230.

Zhang, T. L., et al. (2008), Characteristic size and shape of the mirror mode structures in the solar wind at 0.72 AU, *Geophys. Res. Lett.*, *35*, L10106, doi:10.1029/2008GL033793.

Zurbuchen, T. H., et al. (2001), On the origin of microscale magnetic holes in the solar wind, *J. Geophys. Res.*, *106*, 16,001–16,010, doi:10.1029/2000JA000119.

C. Briand, P. Henri, and A. Mangeney, LESIA, Observatoire de Paris, CNRS, UPMC, Université Paris Diderot, 5 place J. Janssen, F-92190 Meudon, France.

J. Soucek, Department of Space Physics, Institute of Atmospheric Physics, ASCR, CZ-14131 Prague, Czech Republic.

Waves at the plasma frequency inside magnetic holes: STEREO and Cluster observations

C. Briand*, J. Soucek†, A. Mangeney**, S.D. Bale‡ and K. Goetz§

*Observatoire de Paris - LESIA, CNRS, Université Pierre et Marie Curie, Université Paris-Diderot, France, email=carine.briand@obspm.fr
†Institute of Atmospheric Physics, Prague, Czech Republic
**Observatoire de Paris - LESIA, CNRS, Université Pierre et Marie Curie, Université Paris-Diderot, France
‡SSL and Dept. Of Physics, University of California, Berkeley, USA
§University of Minessota, School of Physics and Astronomy, USA

Abstract. Magnetic isolated large amplitude depressions in the interplanetary magnetic field are commonly observed in the solar wind. Some of these magnetic structures are accompanied by bursts of electrostatic waves close to electron plasma frequency. Combining STEREO/WAVES and IMPACT data we are able to accurately localize the waves emission. We show that they also appear inside kinetic holes, themselves situated inside larger holes. We provide, for the first time, the detailed waveform of the waves that reveal their very bursty nature. These results are complemented by CLUSTER data, which allow to resolve the electron distribution and obtain a better description of spatio-temporal variations in Langmuir wave activity. Such observations are confronted to different emission mechanisms.

PACS: 52.35.-g; 52.35.Qz; 96.50.Tf

INTRODUCTION

Magnetic discontinuities are commonly observed in space environment. Several kinds of discontinuities have been distinguished: (i) directional - mostly tangential but also rotational - discontinuities [1, 2, 3]; (ii) slow shocks; (iii) magnetic holes [4].
Following the classification of Burlaga et al. [3], the smallest magnetic holes are usually called "kinetic holes" since their width is of the order of a few proton gyroradii, implying that kinetic effects should play an important role. The largest ones are called "micro-scale holes" and they are thought to be governed by the MHD equations.
Magnetic holes are pressure balanced structures advected by the solar wind [5, 6, 7]: the magnetic depression is compensated by an increase of the density and/or the temperature. In small scale structures, the temperature seems to play the dominant role in establishing the pressure equilibrium. In larger depressions, the density increase seems to be the dominant factor.

In spite of numerous observations, the question of the origin of magnetic holes is still puzzling: are they generated near the Sun and then advected by the solar wind or are they formed locally in the interplanetary space?

Today, several models are still discussed to explain the formation of the kinetic magnetic holes: (i) diamagnetic response of the plasma to a local enhancement of the kinetic pressure [8, 9]; (ii) remnant of mirror-mode instability generated in the corona [10, 11]; (iii) Diamagnetic response of the plasma to the energization of the protons through the ponderomotive force generated by phase-steepened Alfvén waves [12]; (iv) signature of magnetic reconnection in the high corona [5].
Waves at a frequency close to the plasma frequency are often excited within magnetic holes [13, 14, 15, 16]. This Langmuir-like Wave Activity (hereafter LWA) is sometimes accompanied by low frequency waves (like ion acoustic or whistler-modes waves). Based on data from the URAP instrument on board of Ulysses, Lin et al. [17] studied the correlation between the electric field power spectrum peaks and the presence of Directional Discontinuities (DD) in the magnetic field. Only 9% of the DD's observed showed the presence of Langmuir waves. 75% of the DD's that have waves are associated with short duration magnetic field depressions, and the waves are seen at the edges of the holes (large gradient). Thus, they concluded that *the gradient* of the magnetic field intensity is a parameter favorable to the occurrence of LWA (not the amplitude of the holes itself).

The Langmuir-like waves inside the magnetic holes are likely to be generated by electron beams associated with the holes or the discontinuities. MacDowall et al. [18] proposed that these electron beams originate from the thermal electron population due to conservation of magnetic moment inside the holes. According to their interpretation these beams can either generate field-aligned

Langmuir waves or, if two very intense counterstreaming beams are present, they can excite obliquely propagating electrostatic beam modes in the range $1 < f/f_p < 2$. Observations of such waves give us new input for the study of the physical conditions inside magnetic holes.

The goal of the present study is to analyze the details of the waveforms of Langmuir waves and of the electron distribution function inside the magnetic holes when Langmuir-like waves are observed. This information is compared to the theoretical models proposed to explain the generation of such waves.

OBSERVATIONS

Only data from the quiet, free - not connected to the Earth bow shock - solar wind have been considered. None of the events presented here was associated with electron beams related to a specific solar eruptive event. The magnetic data were provided by the STEREO/IMPACT magnetometer (8Hz data[1]) and CLUSTER/FGM (averaged data at 5Hz resolution) instrument. Electric field spectra were obtained from CLUSTER/WHISPER and waveforms from STEREO/WAVES. Finally, electron distribution functions were provided by the PEACE instrument of CLUSTER.

The configuration of the magnetic field is studied in a reference frame derived by minimum variance analysis on a 5 minute window of IMPACT magnetic field data [19, 20]. In this reference frame, V_3 stands for the normal to the discontinuity, V_1 and V_2 are the components tangential to it. Only cases with a clear minimum variance orientation are considered (when the ratio of the intermediate to minimal eigenvalues is greater than 3). Figure 1 displays such an example with the localization of the LWA marked by color crosses.

Waves location, structures and polarization

The Langmuir-like wave activity appears to be located at the edges of the holes -i.e., in zones of large magnetic field intensity gradient- rather than inside. However, we show here that the electrostatic activity also appears to be located in a smaller magnetic depression (kinetic scale) inside a broader one (micro-scale). Figures 1 displays an example of a linear hole associated with LWA. It is characteristic of a linear magnetic hole: the magnetic field variation is mainly confined along the V_1 axis (this eigenvector happens to be mostly along the -Z direction in the spacecraft coordinate system, i.e. perpendicular to

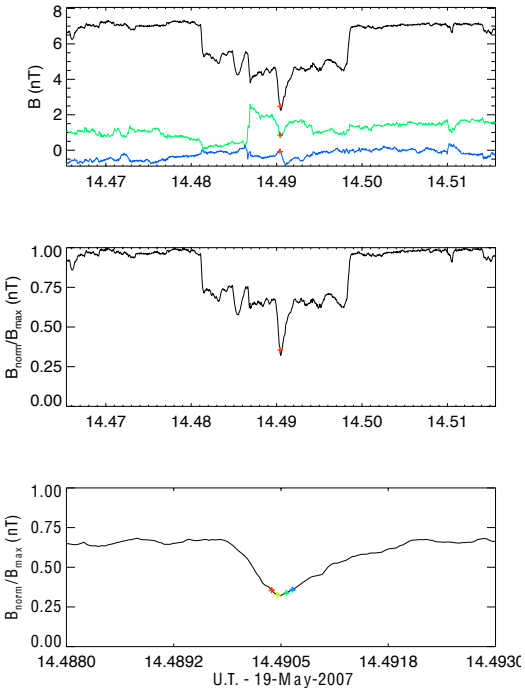

FIGURE 1. Linear magnetic hole and Langmuir wave activity - STEREO A, 2007/05/19. Top panel: the magnetic components (Black: V_1; green: V_2 and blue: V_3); Middle panel: the magnitude of the magnetic field relative to its maximum in the selected time interval. Bottom panel: an enlarged view around the period of Langmuir wave activity. The locations of the LWA are indicated by the colored crosses

the ecliptic). Two magnetic depressions are observed: a large hole (58 seconds wide) and a second depression (5 seconds wide) located inside the larger depression. The LWA occurs inside this second depression. Since the solar wind speed was 665 km.s^{-1} - and assuming that the magnetic holes are advected by the solar wind (have a negligible velocity in the plasma rest frame) the size of the two depressions is about 38500 and 4000 km respectively, roughly 50 and 5 ρ_p (ρ_p being the proton gyroradius).

A second case (STEREO A, 2008/05/06 12:01 UT - not shown) corresponds to a magnetic hole bounded by directional discontinuities with significant field rotation. The LWA is also located in a very small depression (1.1 sec wide) present during a rotation of the magnetic field. The solar wind speed was 375km.s^{-1}, thus the structure was about 410km large, that is of the order of ρ_p.

Similar electrostatic waves were observed by CLUSTER when spacecraft separation was smaller than the

[1] http : //stereo – ssc.nascom.nasa.gov/data/ins_data/impact

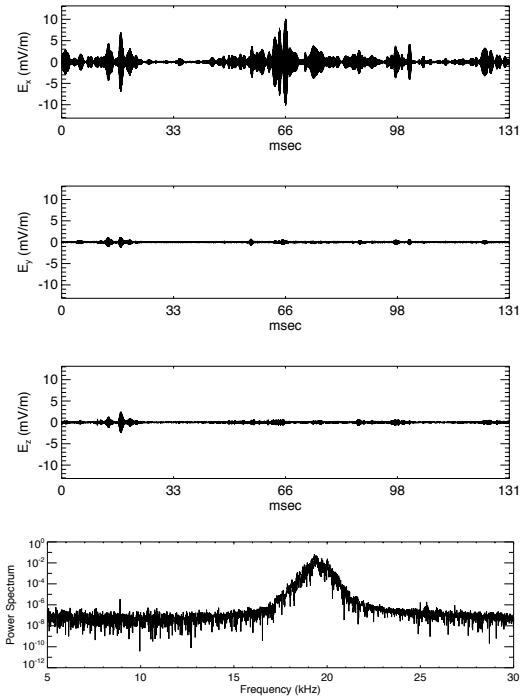

FIGURE 2. Example of electric waveforms components observed on May 19, 2007. The fourth panel displays the power spectrum of the X component, i.e. the field aligned component

typical scale of the hole (200 km). Combined magnetic field observations and electric field spectrograms from WHISPER show that the B-field profile was almost identical for all four spacecraft, but the electric field spectrograms are rather different on individual spacecraft. This suggests a bursty non-stationary nature of the wavepackets with a significant spatio-temporal structure.
This is confirmed with STEREO observations. Figure 2 displays the waveform corresponding to one period of Langmuir activity on May 19, 2007, in a magnetic field aligned reference frame. All the Langmuir wave events within this magnetic hole show the same characteristics:

- the waveforms are very bursty, leading to a broad spectrum around the plasma frequency;
- the Langmuir-like waves are mostly aligned with the magnetic field;
- in numerous cases non zero components perpendicular to the B-field are present. We will investigate more in details these interesting cases later on

The bursty nature of the waveforms suggests the presence of low energy electron beams. To test the presence of such beams, we used CLUSTER electron data.

Electron distribution functions

Figure 3 displays the magnetic field of a large magnetic hole together with a spectrogram showing enhancements of Langmuir-like wave activity. Reduced pitch angle electron distributions are available at times indicated by numbered red dots. The corresponding distributions are plotted in Figure 4. For points 2 and 3, associated

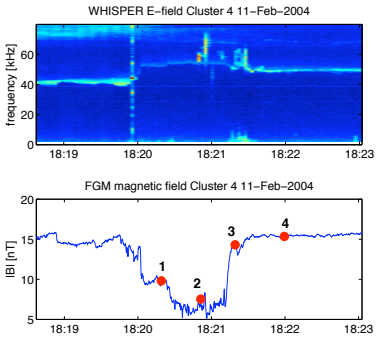

FIGURE 3. Top panel: spectrogram showing an enhancement of the LWA. Bottom panel: magnetic field intensity. The red dots with numbers display where the electron distribution was measured by the PEACE electron analyzer of Cluster (see Fig. 4)

with LWA, the electron distribution shows an enhancement in parallel electron flux consistent with electron beams at 30-50 eV (3-4 times the electron thermal velocity). Such a beam appears consistently in 3 subsequent independent PEACE measurements and it is therefore unlikely to be a result of instrumental effects. On the other hand, measurements at points 1 and 4 (no wave activity) exhibit an unperturbed isotropic Maxwellian distribution.

CONCLUSIONS

This study confirms that Langmuir waves are located at the edges of large magnetic depressions. Owing to the high time accuracy of the waveform measurements we show, for the first time, that they also appear on the deepest kinetic scale magnetic depressions present inside larger hole or rotational discontinuities. A statistical study is in progress to determine the proportion of LWA appearing inside such kinetic scale holes.

Low frequency electrostatic waves were not noticed in any of the electric field activity periods that we have studied. Moreover, the low to moderate solar wind speed could hardly lead to a strong Doppler-shift of ion acoustic waves. Thus, we are confident that the observed waves

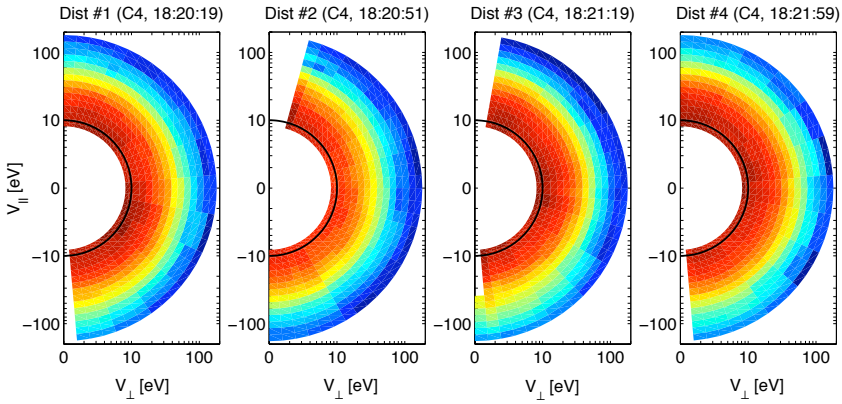

FIGURE 4. Electron Distribution functions corresponding to the observed point labeled 1 to 4 on Fig 3 (from PEACE/CLUSTER). In distributions 2 and 3 one can see an enhancement in parallel electron flux consistent with the presence of electron beams at several times the thermal velocity.

are indeed Langmuir-like electrostatic waves above electron plasma frequency.

Up to now, information about the Langmuir wave activity was obtained through power spectrum peaks. As shown in this article, waveforms reveal a very bursty nature of the wave-packets.

The Langmuir-like waves inside magnetic holes were shown to be mostly linearly polarized with a principal electric field component approximately aligned with the background magnetic field. Also, some waves deviate from strict linear polarization and include a transverse elliptically polarized component. The identification of this signal is still under study.

The generation mechanism of the beam is still unclear. However, the present data suggest that one of the models presented in [18] requiring two very intense electron beams at thermal energies can be rejected since the observed electron distributions are largely inconsistent with this hypothesis. Conversely, they are consistent with three other mechanisms: (i) Low velocity, counter-streaming beams of electrons resulting from conservation of magnetic moment [18]; (ii) Electric fields associated with the rapid change in magnetic field and resulting $E \times B$ drift; (iii) local heating of the electrons at the edge of the magnetic holes, leading to the generation of Langmuir waves as they propagate in the medium [21]. More observations of Langmuir waves and associated particles density are required to distinguish between these models.

ACKNOWLEDGMENTS

One of the authors (J.S.) wants to thank the Paris Observatory for the financial support provided for his stay during which part of this work was developed. We also thank the IMPACT team for providing us with the magnetic field data. We thank the Cluster FGM, WHISPER and PEACE instrument teams, as well as the Cluster Active Archive for the data used in this study.

REFERENCES

1. L. F. Burlaga, and N. F. Ness, *Sol. Phys.* **9**, 467–477 (1969).
2. L. F. Burlaga, *Sol. Phys.* **7**, 54–71 (1969).
3. L. F. Burlaga, K. W. Ogilvie, and D. H. Fairfield, *ApJ* **155**, L171+ (1969).
4. J. M. Turner, L. F. Burlaga, N. F. Ness, and J. F. Lemaire, *J. Geophys. Res.* **82**, 1921–1924 (1977).
5. T. H. Zurbuchen, S. Hefti, L. A. Fisk, G. Gloeckler, N. A. Schwadron, C. W. Smith, N. F. Ness, R. M. Skoug, D. J. McComas, and L. F. Burlaga, *J. Geophys. Res.* **106**, 16001–16010 (2001).
6. M. Fränz, D. Burgess, and T. S. Horbury, *J. Geophys. Res.* **105**, 12725–12732 (2000).
7. M. L. Stevens, and J. C. Kasper, *Journal of Geophysical Research (Space Physics)* **112**, 5109–+ (2007).
8. L. F. Burlaga, and J. F. Lemaire, *J. Geophys. Res.* **83**, 5157–5160 (1978).
9. R. J. Fitzenreiter, and L. F. Burlaga, *J. Geophys. Res.* **83**, 5579–5585 (1978).
10. D. Winterhalter, M. Neugebauer, B. E. Goldstein, E. J. Smith, S. J. Bame, and A. Balogh, *J. Geophys. Res.* **99**, 23371–23381 (1994).

11. D. Winterhalter, E. J. Smith, M. Neugebauer, B. E. Goldstein, and B. T. Tsurutani, *Geophys. Res. Lett.* **27**, 1615–1618 (2000).
12. B. T. Tsurutani, B. Dasgupta, C. Galvan, M. Neugebauer, G. S. Lakhina, J. K. Arballo, D. Winterhalter, B. E. Goldstein, and B. Buti, *Geophys. Res. Lett.* **29**, 240000–1 (2002).
13. N. Lin, P. J. Kellogg, R. J. MacDowall, A. Balogh, R. J. Forsyth, J. L. Phillips, A. Buttighoffer, and M. Pick, *Geophys. Res. Lett.* **22**, 3417–3420 (1995).
14. R. J. MacDowall, R. A. Hess, N. Lin, and G. Thejappa, *Adv. Space Res.* **19**, 873–876 (1997).
15. R. J. MacDowall, N. Lin, and D. J. McComas, *Space Science Reviews* **97**, 141–146 (2001).
16. R. J. MacDowall, N. Lin, and D. J. McComas, *Adv. Space Res.* **32**, 479–483 (2003).
17. N. Lin, P. J. Kellogg, R. J. MacDowall, B. T. Tsurutani, and C. M. Ho, *Astron. Astrophys.* **316**, 425–429 (1996).
18. R. J. MacDowall, N. Lin, P. J. Kellogg, A. Balogh, R. J. Forsyth, and M. Neugebauer, "Langmuir waves in magnetic holes: source mechanism and consequences.," in *American Institute of Physics Conference Series*, edited by D. Winterhalter, J. T. Gosling, S. R. Habbal, W. S. Kurth, and M. Neugebauer, 1996, vol. 382 of *American Institute of Physics Conference Series*, pp. 301–304.
19. B. U. O. Sonnerup, and L. J. Cahill, Jr., *J. Geophys. Res.* **72**, 171–183 (1967).
20. R. P. Lepping, and K. W. Behannon, *J. Geophys. Res.* **85**, 4695–4703 (1980).
21. C. Briand, A. Mangeney, and F. Califano, *Physics Lettters A* **368**, 82–86 (2007).

3.2.5 Couplage d'ondes : observations et simulations cinétiques

Travail de thèse de Pierre HENRI, en co-tutelle avec Francesco Califano (Université de Pise)
Articles de référence : Henri et al. (2009, 2010a)

Le processus de base à l'origine des ondes électromagnétiques des émissions de Type II et III a été proposé par Ginzburg and Zheleznyakov (1958). Des faisceaux d'électrons sont générés lors d'éruptions solaires ou en aval du choc des ICME. En se propageant dans le milieu interplanétaire, ils rencontrent un milieu dont la densité décroît. Ces faisceaux produisent localement une dérivée positive dans la fonction de distribution électronique et donc l'émission d'ondes de Langmuir. L'émission électromagnétique quant à elle résulterait de couplages non linéaires entre ces ondes et des ondes à plus basse fréquence (généralement des ondes acoustiques ioniques mais des modes whistlers ou des ondes hybrides basses sont parfois invoquées).

L'observation simultanée d'ondes acoustiques ioniques et d'ondes de Langmuir a été rapportée dans de nombreux cas. Toutes ces observations sont cependant basées sur des mesures spectrales. Mais la seule présence des ondes basses fréquences et des ondes de Langmuir ne suffit pas à garantir le couplage des ondes. Dans son travail de thèse, P. Henri a fourni des preuves observationnelles à l'existence d'un tel couplage en vérifiant les relations de conservation du moment et de l'énergie :

$$\omega_{L'} = \omega_L + \omega_{lf} \tag{3.8}$$

$$\kappa_{L'} = \kappa_L + \kappa_{lf} \tag{3.9}$$

ainsi que le couplage de phase, information disponible uniquement avec des mesures de formes d'ondes. Afin de tester le processus de couplage d'ondes (et donc la validité des équations 3.8 et 3.9), les données ont été soumises à trois tests indépendants : (a) l'égalité entre la séparation en fréquence des ondes de Langmuir et la fréquence du pic des ondes acoustiques ioniques ; (b) Analyse de bicohérence permettant de vérifier le couplage de phase sur l'ensemble du jeu de donnée. Une analyse en "wavelet" a de plus permis de déterminer la durée de couplage (et d'en déduire la taille de la zone de couplage)

Cette première étude observationnelle a été complétée par des simulations numériques de type Vlasov-Poisson. Ces simulations ont été menées avec des paramètres réalistes de vent solaire et d'onde de Langmuir (milieu isotherme et paquets d'ondes). Elles ont tout d'abord permis d'établir une nouvelle formulation analytique du seuil de déclenchement de l'instabilité paramétrique (les modèles théoriques présentés dans la littérature conduisaient à des seuils pour des ondes monochromatiques et des rapports de température non rencontrés dans le vent solaire). Par ailleurs, les simulations confirment qu'en dépit de l'énergie relativement faible (par rapport à l'énergie thermique) contenue dans les ondes observées, la décroissante paramétrique d'une onde de Langmuir est possible : l'amplitude des ondes dépasse les seuils nouvellement prédits.

Je présente à continuation les premières pages de ces articles mais j'invite le lecture à télécharger la thèse complète sur le site : http ://tel.archives-ouvertes.fr/tel-00532627/fr

JOURNAL OF GEOPHYSICAL RESEARCH, VOL. 114, A03103, doi:10.1029/2008JA013738, 2009

Evidence for wave coupling in type III emissions

P. Henri,[1,2] C. Briand,[1] A. Mangeney,[1] S. D. Bale,[3] F. Califano,[1,2] K. Goetz,[4] and M. Kaiser[5]

Received 8 September 2008; revised 5 December 2008; accepted 23 December 2008; published 5 March 2009.

[1] Using new capabilities of waveform analyses provided by the S/WAVES instruments onboard the two STEREO spacecraft, we present for the first time a complete set of direct evidence for three-wave coupling occurring during a type III emission and involving two Langmuir waves and an ion acoustic wave. Information on the Doppler-shifted frequencies and especially the phases of the waves are used in order to check first the conservation of momentum and energy, through Fourier analyses, and second the phase locking between the waves, through bicoherence analyses. Wavelet analyses allow us to resolve for the first time the coupling regions, in which spatial length is estimated to be 18 ± 5 km. The wave packets travel at comparable speed, and the characteristic available interaction time is about 1 s. Interpretations of the phase coupling and evaluation of the growth rate of the waves tend to favor the parametric decay, at least in the observational events considered in this work.

Citation: Henri, P., C. Briand, A. Mangeney, S. D. Bale, F. Califano, K. Goetz, and M. Kaiser (2009), Evidence for wave coupling in type III emissions, *J. Geophys. Res.*, *114*, A03103, doi:10.1029/2008JA013738.

1. Introduction

[2] Solar type III radio emissions are one of the most prominent features of the meter-decameter ranges of frequency. The emissions show a pronounced drift with time toward lower frequencies (an example is shown on Figure 2). Since the early work of *Wild* [1950] and *Ginzburg and Zheleznyakov* [1958], the generally accepted model for such emission is as summarized below. During a flare, high-energy electrons (1–100 keV) are expelled from the solar corona and travel along the interplanetary magnetic field lines. They produce a bump on the local electron distribution function generating Langmuir waves via the so-called "bump-on-tail instability." Then, nonlinear wave couplings generate electromagnetic waves at f_p^- (the local electron plasma frequency) or $2f_p^-$. The plasma frequency decreases with the heliocentric distance owing to the decrease of the electron density: this is the origin of the time frequency drift characteristic of the type III emissions.

[3] However, as noted by *Sturrock* [1964], such a mechanism should deplete all the energy of the beam on a very short time scale, which would not be able to travel long distances as observed. Since then, many studies have been devoted to validate the general model and to identify the processes able to remove the particles out of resonance with the waves and that stopping the growth of the waves and allowing the beam to survive long distances.

[4] Different lines of research were developed. The first one, within the frame of the quasi-linear theory, takes advantage of the turbulent state of the solar corona and solar wind: the fast particles are moved out of resonance with the waves through scattering of the unstable waves on density fluctuations covering a wide spectrum (from a few hundred of meters to several hundred of kilometers) [*Smith*, 1970; *Li et al.*, 2006]. However, *Lin et al.* [1981, 1986] provided observational evidence that quasi-linear relaxation alone cannot explained the evolution of the beam (at least for the events they studied). First, they showed that the electric field intensity computed from the theoretical growth rate, extrapolated using the observed positive slope of the electron distribution function, would be too large. The amplitude of the waves would grow out of the framework of quasi-linear theory. Second, quasi-linear models predicts a plateauing of the bump of the distribution function which is not observed.

[5] A second line of research takes into account inhomogeneities in the solar wind density [*Budden*, 1985] through linear mode conversion and scattering of Langmuir waves on density gradients. *Willes and Cairns* [2001] and *Willes et al.* [2002] explained how Langmuir waves propagating along the density gradients can be mode converted, which could remove the beam particles out of resonance with the waves. In the Stochastic Growth Theory framework [*Robinson*, 1993], the beam driven Langmuir growth rate is treated as a random variable that depends on random density inhomogeneities, thus allowing the beam to propagate long distances.

[6] Type III electromagnetic emissions are thought to be produced via two different nonlinear wave-wave couplings.

[1]LESIA, Observatoire de Paris, Université Paris Diderot, CNRS, UPMC, Meudon, France.
[2]Dipartimento di Fisica, Università di Pisa, Pisa, Italy.
[3]Physics Department and Space Sciences Laboratory, University of California, Berkeley, California, USA.
[4]School of Physics and Astronomy, University of Minnesota, Minneapolis, Minnesota, USA.
[5]NASA Goddard Space Flight Center, Code 674, Greenbelt, Maryland, USA.

0148-0227/09/2008JA013738$09.00

Through electromagnetic coupling, a pump Langmuir wave L decays into a low-frequency LF waves and a transverse electromagnetic wave T_{fp-} at the local plasma frequency, observed as type III fundamental emission:

$$L \rightarrow T_{f_p^-} + LF \tag{1}$$

Through electrostatic coupling, the pump Langmuir wave L decays into a low-frequency LF and a daughter Langmuir wave L', which can further couple with the pump wave to generate a transverse electromagnetic wave T_{2fp-} at twice the local plasma frequency, observed as type III harmonic emission:

$$L \rightarrow L' + LF \qquad L' + L \rightarrow T_{2f_p^-} \tag{2}$$

[7] This paper focuses on the electrostatic coupling. A number of authors have claimed that the spectral analyses of the electric field in the solar wind provides some support in favor of the electrostatic decay process [e.g., *Lin et al.*, 1986; *Kellogg et al.*, 1992; *Gurnett et al.*, 1993; *Thejappa et al.*, 1993, 1995, 2003; *Thejappa and MacDowall*, 1998]. They based their conclusions on some characteristics signatures like the simultaneous occurrence of Langmuir and low-frequency waves (like ion acoustic, whistlers or lower hybrid waves), or the comparison between theoretical thresholds and the observed energy in the waves. However, as already pointed out by *Kennel et al.* [1980] and *Thejappa et al.* [1995], the simultaneous occurrence of two waves in the spectrum doesn't necessarily mean wave coupling. Indeed, the waves can be generated by particles of different energy present in a same electron cloud; an efficient three-wave coupling requires the fundamental equations of energy and momentum conservation to be satisfied:

$$\omega_1 = \omega_2 + \omega_3 \tag{3}$$

$$\vec{k_1} = \vec{k_2} + \vec{k_3} \tag{4}$$

where ω and $\vec{k}$ refer to the pulsation and wave number of the waves. When observed onboard only one spacecraft, equations (3) and (4) reduce to a single relation for the Doppler-shifted frequencies $f^{Doppler} = \omega^{Doppler}/2\pi$:

$$\begin{aligned} f_1^{Doppler} &= f_1 + \frac{\vec{k}_1}{2\pi}.\vec{V}_{SW} \\ &= (f_2 + f_3) + \frac{(\vec{k}_2 + \vec{k}_3)}{2\pi}.\vec{V}_{SW} \end{aligned}$$

leading to the following equation for resonance:

$$f_1^{Doppler} = f_2^{Doppler} + f_3^{Doppler} \tag{5}$$

Equation (5) can be directly tested from in situ measurements which combine high spectral and temporal resolution, as well as phase information. Only waveforms measurements can provide the required information. Such observations are available with the S/WAVES investigation on the STEREO mission [*Bougeret et al.*, 2007].

[8] On the basis of data obtained on 14 January 2007 by the waveform analyzer of the S/WAVES instrument onboard STEREO, evidence for nonlinear coupling between Langmuir and ion acoustic waves (also known as ion sound waves in the literature), at $\approx$80–250 Hz, occurring during a type III event are presented. Three complementary methods are employed: (1) a spectral analyses that checks the frequency correlation, (2) a wavelet analyses that verifies the time occurrence of the waves, and (3) a bicoherence analyses that checks the phase correlation between the waves. The validity of equations (3) and (4) on observed data is thus directly tested (through equation (5)). The phase relation was already studied in the Earth bow shock [*Dudok de Wit and Krasnosel'Skikh*, 1995] and the foreshock [*Bale et al.*, 1996] environments, but, to our knowledge, it is the first time it is used on data related to type III event. This paper focuses on the parametric instability version of the electrostatic decay, through direct tests on the phase resonance, rather than its weak turbulence version [*Robinson et al.*, 1993]. This will be justified by the bicoherence analysis of the electric waveforms.

[9] Details on the instrument, the data and the solar wind conditions are presented in section 2. After identification of the low-frequency mode, three independent analyses for the three-wave coupling are presented in section 3. Section 4 discusses details on the coupling and describes it in the context of the type III.

2. Observations and Data

[10] S/WAVES is composed of three 6 m monopole antennas, orthogonal to each other, with an effective length of about 1 m [*Bougeret et al.*, 2007; *Bale et al.*, 2008]. Two modes of observation are available: remote sensing to follow the propagation of the radiosources in the solar wind with spectral radio receivers and *in situ* measurement of electric waveforms along the three antennas with the Time Domain Sampler mode (TDS).

[11] The TDS data reported in this paper are composed of N = 16384 samples with an acquisition rate of 125,000 samples per second (a time step of δt = 8 μs for a total duration of 130 ms per event). This long total duration allows us to capture entire Langmuir wave packets. In terms of frequencies, those electric field waveforms enable to cover a range from 10 Hz to 60 kHz. Thus, signatures from below the electron cyclotron frequency (typically 100 Hz in the solar wind) to above the plasma frequency (typically 10 to 20 kHz) are accessible. The frequency gain is flat in the frequency range of interest here (100 Hz to 20 kHz). Finally, the S/WAVES A/D converter is accurately linear. Thus spurious nonlinear artifacts are not introduced, so that studies of nonlinear wave interactions are possible.

[12] The voltage measured on the three antennas is then converted into an electric field, and projected in the spacecraft coordinates, using the set of parameters called w/base caps (Graz) by *Bale et al.* [2008, Table 13] in order to take into account the effective length and direction of the STEREO antennas.

[13] In its final orbit the spacecraft coordinates (X, Y, and Z) are defined as follows: the x component is sunward along the radial direction, the Z component is normal to the ecliptic plane, southward for STEREO A and northward

JOURNAL OF GEOPHYSICAL RESEARCH, VOL. 115, A06106, doi:10.1029/2009JA014969, 2010

Vlasov-Poisson simulations of electrostatic parametric instability for localized Langmuir wave packets in the solar wind

P. Henri,[1,2] F. Califano,[1,2] C. Briand,[3] and A. Mangeney[3]

Received 7 October 2009; revised 2 December 2009; accepted 12 January 2010; published 18 June 2010.

[1] Recent observation of large-amplitude Langmuir waveforms during a type III event in the solar wind has been interpreted as the signature of the electrostatic decay of beam-driven Langmuir waves. This mechanism is thought to be a first step to explain the generation of type III radio emission. The threshold for this parametric instability in the typical solar wind condition has been investigated through 1D-1V Vlasov-Poisson simulations. We show that the amplitude of the observed Langmuir beatlike waveforms is of the order of the effective threshold computed from the simulations. The expected levels of associated ion acoustic density fluctuations have also been computed for comparison with observations.

Citation: Henri, P., F. Califano, C. Briand, and A. Mangeney (2010), Vlasov-Poisson simulations of electrostatic parametric instability for localized Langmuir wave packets in the solar wind, *J. Geophys. Res.*, *115*, A06106, doi:10.1029/2009JA014969.

1. Introduction

[2] During a solar flare, high-energy electrons (1–100 keV) are expelled from the solar corona and travel along the interplanetary magnetic field lines, producing a bump on the local electron distribution function. Langmuir waves then grow via the so-called bump-on-tail instability. Langmuir waves are observed at amplitude large enough ($E^2/(8\pi nT) \simeq 10^{-3}$–$10^{-4}$) to further excite electromagnetic waves through nonlinear processes. These electromagnetic waves are the main signature of type III radio bursts. Wave-wave interaction through parametric instabilities have been shown to be the physical mechanism underlying the non linear evolution of large amplitude Langmuir waves.

[3] Langmuir electrostatic decay (LED), also called Langmuir decay instability (LDI) or parametric decay instability (PDI) in the literature, enables energy transfer from a finite amplitude Langmuir wave L toward a second Langmuir wave L' and an ion acoustic wave (IAW) S through a three-wave resonant interaction:

$$L \rightarrow L' + S.$$

This process is thought to be a first step toward the generation of solar wind type III radio emission at twice the plasma frequency ($T_{2f_{pe}}$), as a result of a coalescence of the two Langmuir waves [*Ginzburg and Zheleznyakov*, 1958]:

$$L + L' \rightarrow T_{2f_{pe}}.$$

[4] Spectral observations of high-frequency intense Langmuir waves and low-frequency ion acoustic waves during type III bursts have been interpreted as a signature of Langmuir electrostatic decay [*Lin et al.*, 1986a]. Furthermore, waveform observations during type III bursts of modulated Langmuir wave packets on one hand [*Cairns and Robinson*, 1992; *Hospodarsky and Gurnett*, 1995; *Bale et al.*, 1996; *Li et al.*, 2003] and of IAW frequency drift associated with type III electron beam velocity drift on the other hand [*Cairns and Robinson*, 1995] have both been interpreted by the Langmuir electrostatic decay.

[5] The LED is a resonant parametric instability. To be resonant, the three-wave coupling requires the fundamental equations of energy and momentum conservation to be satisfied:

$$\omega_L = \omega_{L'} + \omega_S \qquad \vec{k}_L = \vec{k}_{L'} + \vec{k}_S, \tag{1}$$

where ω and $\vec{k}$ are the frequency and wave number of the waves. Moreover, for the LED to develop, the electric field of the mother Langmuir wave has to reach a critical value. The analytical calculation of this threshold has been discussed by *Nishikawa* [1968], *Sagdeev and Galeev* [1969], *Dysthe and Franklin* [1970], *Bardwell and Goldman* [1976], and *Robinson et al.* [1993] by considering three monochromatic waves. The underlying idea is that for the instability to develop, the growth rate γ_{LED} of the two product waves must be higher than their own linear Landau damping rates $\gamma_{L'}$ and γ_S:

$$\gamma_{\mathrm{LED}} > \sqrt{\gamma_{L'}\gamma_S}.$$

[1]Dipartimento Fisica, Università di Pisa, Pisa, Italy.
[2]Also at Laboratoire d'Études Spatiales et d'Instrumentation en Astrophysique, Observatoire de Paris, Université Pierre et Marie Curie, Université Paris Diderot, CNRS, Meudon, France.
[3]Laboratoire d'Études Spatiales et d'Instrumentation en Astrophysique, Observatoire de Paris, Université Pierre et Marie Curie, Université Paris Diderot, CNRS, Meudon, France.

0148-0227/10/2009JA014969

The threshold for parametric decay of the mother Langmuir wave is thus evaluated in term of the electric to kinetic energy ratio [*Bardwell and Goldman*, 1976]:

$$\frac{\epsilon_0 E^2}{nk_B T} > 8\frac{\gamma_{L'}}{\omega_{L'}}\frac{\gamma_S}{\omega_S},$$

with $\omega_{L'}$, ω_S the angular frequency of the daughter waves. The threshold for electrostatic decay has been estimated for typical solar wind parameters to be $(\epsilon_0 E^2)/(nk_B T) \geq 2.5 \times 10^{-5}$ [*Lin et al.*, 1986b]. To our knowledge, only LED that couples three monochromatic waves have been considered analytically. Indeed, the analytical treatment of resonance becomes complicated when considering a finite frequency bandwidth, in which case a numerical treatment is necessary.

[6] Earlier related works on simulations of LED have been based on the Zakharov equations [*Sprague and Fejer*, 1995; *Gibson et al.*, 1995; *Soucek et al.*, 2003], considering the instability as a fluid mechanism. Recently, kinetic simulations using PIC codes [*Matsukiyo et al.*, 2004; *Huang and Huang*, 2008] and Vlasov codes [*Goldman et al.*, 1996; *Umeda and Ito*, 2008] have shown that the beam-plasma interaction can saturate through LED and have been able to reproduce the modulated shape of Langmuir waves.

[7] If the threshold for LED is commonly thought to be at moderate amplitude, a recent numerical work [*Umeda and Ito*, 2008] claims that no LED would occur until the electric energy is comparable to the plasma kinetic energy. As a result, it would be no more possible to consider the LED as a mechanism for the generation of type III radio emission.

[8] *Henri et al.* [2009] (hereinafter referred to as Paper I) recently reported direct observations of Langmuir waves decaying into secondary Langmuir waves and acoustic waves during a type III solar event, from STEREO/WAVES data. They found that the Doppler-shifted frequencies of the three observed waves satisfy the resonant relations of momentum and energy conservation expected for three-wave coupling. A bicoherence analysis confirmed the phase coherence of the three waves. In this former work, the LED threshold and the growth rate of IAW density fluctuations generated by LED were both evaluated from analytical solutions involving a purely monochromatic three-wave coupling [*Sagdeev and Galeev*, 1969]. However, observations show that (1) the large amplitude Langmuir waves are isolated wave packets with a packet width of the order of a few wavelengths and (2) ion and electron temperatures are close ($0.1 < T_e/T_i < 10$) so that ion acoustic waves associated with the LED should be Landau damped. Thus several questions remain open about the generation and the dynamics of the LED observed in the solar wind: (1) What are the threshold and the growth rate of the LED when electron and ion temperatures are close? What is the effective threshold of LED when the mother Langmuir wave is a localized wave packet? (2) What is the saturation level for IAW density fluctuations in these conditions? What is the expected level of IAW density fluctuations where saturation is not observed? The goal of this paper is to answer these questions by studying the dynamics of the LED through 1D-1V Vlasov-Poisson simulations.

[9] The paper is organized as follows. The Vlasov-Poisson simulation model is described in section 2. The numerical results are presented in section 3, first for a monochromatic mother Langmuir wave (section 3.1), then for a mother Langmuir wave packet (section 3.2). Growth rates, saturation levels for IAW density fluctuations and threshold for LED are studied. The simulation results are finally discussed in section 4 in the context of solar wind observations. Particular attention is paid to the case of equal temperature for electrons and ions, in which case the growth of IAW should be limited by its Landau damping.

2. Full Vlasov-Poisson Simulation Model

[10] In typical solar wind conditions, the ratio between electron and ion temperatures fluctuates around 1. The IAW produced during three-wave coupling should then be suppressed by Landau damping. This would limit the development of the IAW and thus the LED. However, the IAW Landau damping rate in such temperature condition cannot be solved analytically, so that it cannot be included in a fluid code. Kinetic effects due to wave-particle interactions are to be taken into account self-consistently as a possible limitation for the instability to grow. A Vlasov-Poisson approach has thus been used to study LED dynamics. It allows to consider self-consistently the decay of the Langmuir wave together with damping effect on the product waves. Since solar wind electrons are weakly magnetized ($\omega_{ce}/\omega_{pe} \simeq 10^{-2}$), magnetic effects are discarded.

[11] The Vlasov-Poisson system is solved for the electron and ion distribution function, $f_e(x, v, t)$ and $f_i(x, u, t)$, with the numerical scheme described by *Mangeney et al.* [2002], limiting our study to the 1D-1V case. The equations are normalized by using the following characteristic electron quantities: the charge e, the electron mass m_e, the electron density n_e, the plasma (angular) frequency $\omega_{pe} = \sqrt{4\pi n_e e^2/m_e}$, the Debye length $\lambda_D = \sqrt{T_e/4\pi n_e e^2}$, the electron thermal velocity $v_{\mathrm{th},e} = \lambda_D \omega_{pe} = \sqrt{T_e/m_e}$ and an electric field $\overline{E} = m_e v_{\mathrm{th},e}\omega_{pe}/e$. Then, the dimensionless equations for each species read:

$$\frac{\partial f_e}{\partial t} + v\frac{\partial f_e}{\partial x} - (E + E_{\mathrm{ext}}^{\mathrm{init}})\frac{\partial f_e}{\partial v} = 0, \tag{2}$$

$$\frac{\partial f_i}{\partial t} + u\frac{\partial f_i}{\partial x} + \frac{1}{\mu}(E + E_{\mathrm{ext}}^{\mathrm{noise}})\frac{\partial f_i}{\partial u} = 0, \tag{3}$$

$$\frac{\partial^2 \phi}{\partial x^2} = \int f_e dv - \int f_i du; \qquad E = -\frac{\partial \phi}{\partial x}, \tag{4}$$

where v (u, respectively) is the electron (ion, respectively) velocity normalized to the electron thermal velocity. Here $\mu = m_i/m_e = 1836$ is the ion-to-electron mass ratio. ϕ and E are the self-consistent electric potential and electric field generated by the plasma charge density fluctuations according to Poisson equation (4). $E_{\mathrm{ext}}^{\mathrm{init}}$ and $E_{\mathrm{ext}}^{\mathrm{noise}}$ are "external" drivers added to the Vlasov equation that can be switched on or off during the run. The electron (ion, respectively) distribution function is discretized in space for $0 \leq x < L_x$, with $L_x = 5000\ \lambda_D$ the total box length, with a resolution of $dx = \lambda_D$. The electron velocity grid ranges over $-5\ v_{\mathrm{th},e} \leq v \leq +5\ v_{\mathrm{th},e}$, with a resolution of $dv = 0.04\ v_{\mathrm{th},e}$. ($-5\ u_{\mathrm{th},i} \leq u \leq +5\ u_{\mathrm{th},i}$, respectively, with a reso-

3.2.6 Turbulence faible, turbulence forte

Travail de thèse de Pierre HENRI, en co-tutelle avec Francesco Califano (Université de Pise)
Articles de référence : Henri et al. (2010b)

Le développement des analyseurs de forme d'onde ont permis de révéler le caractère cohérent des ondes de Langmuir. Elles apparaissent soit sous la forme de paquets d'onde fortement modulés soit sous la forme de structures localisées intenses (ILS pour l'acronyme anglais, ou aussi appelé Soliton Langmuir wave packets – Thejappa et al. 1999). A partir de l'analyse de la distribution du champ électrique, Nulsen et al. (2007) ont montré qu'aucun des mécanismes classiques (processus non linéaires ou Stochastic Growth Theory) n'était capable d'expliquer ces ILS. Un nouveau modèle basé sur le piégeage d'onde dans des inhomogénéités de densité a récemment été proposé pour expliquer l'enveloppe des ondes de Langmuir (Malaspina et al. 2008).
Nous avons entrepris de reconsidérer le problème de la génération de ces ILS à partir de simulations Vlasov. Les premiers résultats montrent que, même en partant d'un niveau d'énergie modéré dans les ondes (domaine *a priori* de la turbulence faible), le soliton collapse peut s'envisager pour générer des ILS (figure caractéristique de la turbulence forte). Cette nouvelle approche des limites entre turbulence faible et forte motive une nouvelle relecture des observations.

3.3 Conclusions et perspectives

S'intéresser à la microphysique des plasmas héliosphériques, c'est tout d'abord s'intéresser à la question du transfert d'énergie dans un plasma non (ou très faiblement) collisionnel. C'est ensuite identifier les processus conduisant à la "dissipation" d'énergie. C'est aussi expliquer les mécanismes de génération et de saturation des instabilités cinétiques conduisant à l'émission d'ondes et de structures cohérentes. Dans les milieux comme le vent solaire, les magnétosphères des planètes et beaucoup d'autres environnements astrophysiques, les transferts et la dissipation d'énergie font appel à des mécanismes de microphysique où la dynamique de chaque espèce constituant le plasma et le développement d'ondes jouent un rôle déterminant. Ces processus sont fondamentalement multi-échelles et peuvent conduire à un comportement non linéaire du plasma. Les couplages onde-onde et onde-particules modifient la dynamique des particules et assurent le transfert d'énergie non seulement entre ondes mais également entre des espèces dont les échelles de temps caractéristiques restreignent normalement les échanges directs. La physique des plasmas héliophysiques couple les échelles électroniques, protoniques et fluides.
Si les processus cinétiques se développent aux échelles microscopiques (rayon de giration des particules, longueur de Debye), ils induisent néanmoins des perturbations irréversibles aux échelles macroscopiques. La reconnexion magnétique, par exemple, engendre une modification de la topologie du milieu permettant la propagation de plasma dans des espaces préalablement interdits. La présence d'une onde de choc dissipe l'énergie de l'écoulement le faisant passer de supersonique à sub-sonique. Ces deux processus participent également activement à la génération de particules de haute énergie (par exemple, les protons passent de quelques keV dans le vent solaire à quelques centaines de keV dans le foreshock de la terre).

Des progrès importants sur tous ces sujets sont réalisés grâce à un lien étroit entre observations *in situ* et simulations numériques cinétiques. L'héliosphère est pour les plasmiciens un laboratoire d'excellence dans lequel de nombreuses mesures dans des états de plasmas variés sont possibles. A noter qu'une approche astrophysique de la physique cinétique des plasmas est très complémentaire d'une approche de physique de laboratoire. L'environnement astrophysique fournit des conditions de plasma impossibles à reproduire dans une enceinte tandis que les expériences de laboratoires permettent un contrôle plus précis des paramètres environnementaux ainsi qu'un accès à une plus large gamme de paramètres. L'universalité des processus physiques conduit à travers des expériences en laboratoire et des mesures dans l'héliosphère à couvrir une large gamme de paramètres thermodynamiques (température, pression, densité, champ magnétique etc ...) et de fréquences. La confrontation des résultats obtenus dans ces différents milieux – tant du point de vue de la théorie, des simulations, des modélisations que des observations – est donc riche d'enseignement pour tous.

Le couplage étroit entre ondes (électrostatiques et électromagnétiques) et particules donne tout de suite la direction à suivre pour les développements instrumentaux des futures missions héliosphériques : **missions dédiées aux observations in-situ** associant des mesures des champs électriques et magnétiques ainsi que des fonctions de distribution 2D des particules. Les mesures radio et particules sont complémentaires du fait même des processus d'émission des ondes. Les missions passées ont aussi montré que les mesures radio pouvaient compenser certaines limitations des instruments particules aux hautes fréquences : spectroscopie du bruit thermique (Meyer-Vernet and Perche 1989), mesures des fluctuations de densité (traceurs des ondes acoustiques ioniques) via les variations du potentiel flottant du satellite (Henri et al. 2010c), aide à la calibration des instruments particules (Opitz et al. 2010). Par ailleurs, les instruments radio (télédétection) permettent le suivi de la propagation des particules sur de

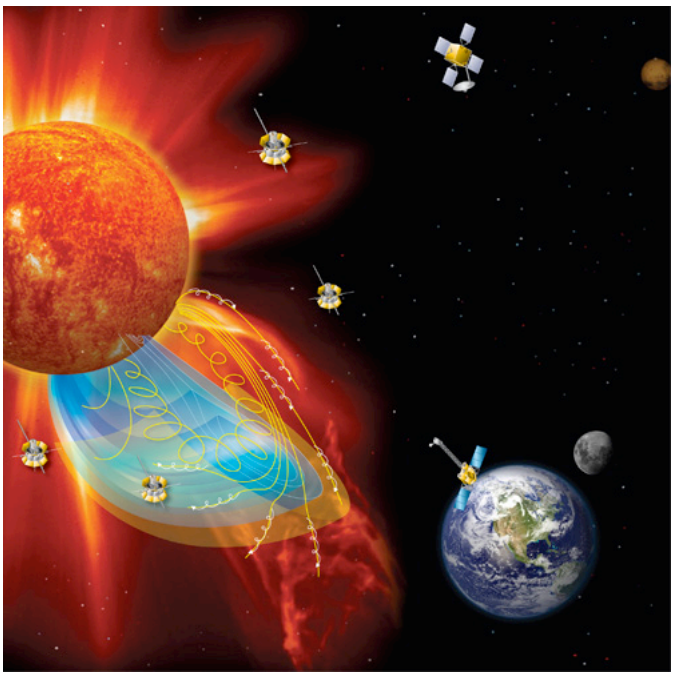

FIGURE 3.4 – Page de couverture du" Solar Sentinels : Report of the science and technology definition team"

grandes distances ainsi que la localisation des sources (voir les récents travaux dans l'environnement de Saturne par Cecconi et al. 2008, 2009). Nous avons montré (Section 3.2.5) la puissance des mesures de formes d'onde pour tester certains principes de base de physique des plasmas et pour interpréter les observations. L'accroissement de la télémétrie sur ces données est absolument nécessaire (notamment dans le milieu interplanétaire) : l' échantillonnage ne représente actuellement que quelques secondes ($\ll$ 10s) par jour, et est limité aux ondes les plus intenses !

Par ailleurs, les mesures ponctuelles avec un satellite ne permettent pas d'appréhender les différentes échelles des milieux observés (ni d'ailleurs de discriminer entre une évolution temporelle et spatiale d'une structure advectée – par le vent solaire ou un courant magnétosphérique). CLUSTER a démontré qu'une vision multi-satellites permet de lever – au moins en partie – ces ambiguïtés et donc de comprendre beaucoup mieux la dynamique des milieux observés. Les missions magnétosphériques proposées depuis lors sont toutes multi-satellites (5 satellites pour THEMIS lancée en 2007 par la NASA, 4 satellites pour la mission MMS – Magnetosphere Multiscale Mission de la NASA dont le lancement est prévu en 2014 –, et Cross-Scale – une proposition non retenue par l'ESA dans le programme Cosmic Vision – qui était composée initialement de 12 satellites pour appréhender simultanément toutes les échelles de la dynamique des plasmas – en prenant comme objet de test la magnétosphère terrestre). Du point de vue des plasmas interplanétaires et de la couronne solaire, seule la mission SENTINELS est multi-satellites [4]. Espérons que la phase actuelle de ce projet ne soit qu'une phase sommeil (et non un arrêt définitif).

Comme nous l'avons montré lors des récents travaux, l'interprétation de nombreuses observations s'appuie sur des simulations numériques cinétiques. Nous nous sommes restreints pour l'instant à des simulations 1D-1V. Cette approximation est valable tant que l'on considère des

4. Du point de vue des mesures *in situ* STEREO offre deux points de mesure mais ne constitue pas en soit une mission multi-satellitaire, la distance entre les deux sondes étant trop grande

milieux fortement ou non magnétisés, que les processus se déroulent sur des temps courts, ou quand les vitesses des particules sont petites devant la vitesse de la lumière. Mais l'aspect multi-dimensionnel des plasmas doit aussi être considéré par les simulations numériques et les modélisations. La stabilité des structures envisagées en 1D peut être complètement bouleversée dès que l'on passe à d'autres dimensions. De plus, dès qu'il s'agit de simuler l'interaction plasma-satellite ou du vent solaire avec un obstacle (une magnétosphère par exemple), l'approche cinétique seule devient impossible à gérer. Il faut plutôt chercher à considérer le plasma comme un fluide pour une partie du problème et de façon cinétique dans des zones restreintes pour les processus à petites échelles. Cette approche ne consiste pas uniquement à interconnecter deux codes différents. C'est toute l'approche du problème qui doit être revue. Pour que cela soit réalisable, il faut tout d'abord augmenter les puissances de calcul (multiplication des processeurs) et développer des codes parallèles. Mais l'augmentation de la puissance de calcul ne permettra cependant pas à elle seule de résoudre tous les problèmes. L'atout majeur sera surtout d'aborder la question du couplage entre codes cinétiques (pour les processus à petites échelles) et fluides (pour aborder les problèmes incluant les échelles macroscopiques).

Ces simulations bénéficieront non seulement à la compréhension des mécanismes de base se déroulant dans les milieux non collisionnels mais permettront également des avancées dans le cadre de la météorologie de l'espace. Dans ce cadre, mes études vont s'orienter vers deux sujets principaux : les structures bipolaires électrostatiques et la reconnexion magnétique.

Des pulses bipolaires électrostatiques, parallèles au champ magnétique ambiant ont été observés dans différents environnements héliosphériques (vent solaire, différentes régions de la magnétosphère terrestre ainsi que dans les zones aurorales terrestres). De telles structures sont interprétées comme (a) des sauts de potentiel électrostatique (autrement appelés doubles couches), (b) des trous d'ions (aussi appelés ondes solitaires ioniques), ou (c) des trous d'électrons dans l'espace des phases. Ces structures cohérentes pourraient jouer un rôle important dans le transport d'énergie, seraient source d'accélération de particules et offriraient un support pour expliquer la résistivité anormale nécessaire pour les processus de reconnexion magnétique.
Des structures similaires ont été observées sur STEREO, mais leurs caractéristiques sont très différentes de celles observées il y a quelques années par WIND dans le vent solaire calme (environ dix fois plus larges et présentant des polarisations différentes sur les trois dimensions d'espace). Une étude comparative entre les données de ces deux sondes est nécessaire afin de caractériser et d'identifier ces structures cohérentes électrostatiques dans le vent solaire. En parallèle, des travaux sont actuellement réalisés par des équipes américaines sur des signatures équivalentes dans la magnétosphère de la Terre. La possibilité d'utiliser des données de forme d'onde électrique de l'environnement d'autres planètes (Jupiter ou Saturne par exemple via les mesures de Cassini) sera explorée.
En parallèle, des simulations numériques cinétiques seront aussi menées afin de comprendre leurs mécanismes de génération. Des études ont déjà été développées dans une approche 1D-1V, en milieu non homogène (présence d'un gradient de densité dans le milieu), en conditions de "boite ouverte". Ces simulations ont montré que la dynamique des structures bipolaires était fortement modifiée par la présence d'un tel gradient mais également par la présence d'ions lourds (O^+ caractéristique de l'environnement ionosphérique terrestre). Il est nécessaire de raffiner ces études dans deux directions : (a) vérifier la dynamique de ces structures en présence d'un champ magnétique (plus ou moins fort selon le milieu), (b) étudier leur stabilité en 2 voire 3D, (c) déstabiliser le plasma par d'autres types de perturbation des moments de la fonction de distribution (flux de chaleur par exemple).

La reconnexion magnétique est le processus physique le plus invoqué pour expliquer des chan-

gements de topologie magnétique conduisant à la propagation de particules dans des lieux préalablement interdits, et s'accompagnant d'accélération de particules et d'émission de rayonnements énergétiques. De telles reconfigurations magnétiques ont été observées dans de nombreux environnements héliosphériques : le milieu interplanétaire, en amont de la magnétophère des planètes, dans la queue de la magnétosphère de la Terre. Elles joueraient également un rôle majeur dans le déclenchement des éruptions solaires.
Dans une approche MHD, la condition de champ gelé doit être levée pour initier la reconnexion magnétique. Pour étudier l'évolution à grande échelle du plasma lors d'une reconnexion, les simulations MHD introduisent une résistivité anormale. Mais ce sont des processus à petites échelles qui permettent de découpler les électrons et le champ magnétique. L'approche cinétique est donc indispensable pour une bonne compréhension des mécanismes à l'origine de la reconnexion magnétique.
Les données magnétiques de IMPACT sur STEREO montrent la présence de discontinuités tangentielles qui peuvent être la signature de reconnexion magnétique ou de couches de courant dans le milieu interplanétaire. Les observations de STEREO/WAVES montrent la présence d'ondes autour de la fréquence plasma au minimum de l'intensité du champ magnétique, indiquant que des instabilités plasma ont eu lieu à cet endroit. Quelle que soit l'origine de cette discontinuité, nous avons une occasion unique d'étudier du point de vue observationnel les conditions du plasma. Les changements de polarité du champ magnétique se produisant sur quelques secondes, seules les observations radio permettront une caractérisation sur des temps aussi courts (les instruments particules, au moins dans le vent solaire, ont des temps d'intégration plus longs).
Une nouvelle branche d'étude sera de me pencher sur des simulations numériques de la reconnexion magnétique. Au sein du LESIA, la reconnexion est étudiée sous l'approche MHD. Il s'agira ainsi d'apporter un complément via l'approche cinétique.

Enfin, du point de vue des objets astrophysiques mêmes, il sera très attrayant de suivre les missions apportant des éléments nouveaux tels que Bepi-Colombo (environnement de Mercure dont un des défis est de comprendre les conditions de fermeture des courants électriques dans la magnétosphère de la planète en absence d'une ionosphère constituée), Solar Orbiter (environnement solaire à 0.3 UA pour la compréhension des mécanismes d'accélération du vent solaire), les missions d'exploration de la Lune (notamment l'environnement plasma dans les premiers mètres au-dessus de la surface) ainsi que les missions multi-satellites pour étudier la magnétosphère de la Terre (queue magnétosphérique notamment pour étudier les conditions de déclenchement des sous orages magnétiques).

Bibliographie

Adam, J. C., Laval, G., and Pesme, D. : Reconsideration of Quasilinear Theory, Physical Review Letters, 43, 1671–1675, doi :10.1103/PhysRevLett.43.1671, 1979.

Arnaud, J., Briand, C., and Rayrole, J. : THEMIS : Télescope Héliographique pour l'Étude du Magnétisme et des Instabilités Solaires., Journal des Astronomes Francais, 53, 5–9, 1996.

Besse, N. and Sonnendrücker, E. : Semi-Lagrangian schemes for the Vlasov equation on an unstructured mesh of phase space, Journal of Computational Physics, 191, 341–376, doi : 10.1016/S0021-9991(03)00318-8, 2003.

Briand, C. : Solar activity I : aspects of magnetic activity, Astronomische Nachrichten, 324, 357–361, 2003a.

Briand, C. : Solar magnetic field at photospheric level, vol. 1, pp. 337–358, Research signpost, Trivandrum, India – Monographie, 2003b.

Briand, C. and Aboudarham, J. : Multi-line spectro-polarimetry on active region NOAA 9125, Nuovo Cimento C Geophysics Space Physics C, 25, 741–+, 2002.

Briand, C. and Ceppatelli, G. : THEMIS : instrumentation, results and perspectives, in : SOLMAG 2002. Proceedings of the Magnetic Coupling of the Solar Atmosphere Euroconference, edited by Sawaya-Lacoste, H., vol. 505 of *ESA Special Publication*, pp. 11–15, 2002.

Briand, C. and Martínez Pillet, V. : ASP Observations - First Analysis of Mgb_2 Stokes Parameters, in : Advanced Solar Polarimetry – Theory, Observation, and Instrumentation, edited by Sigwarth, M., vol. 236 of *Astronomical Society of the Pacific Conference Series*, pp. 565–+, 2001.

Briand, C. and Solanki, S. K. : Velocity fields below the magnetic canopy of solar flux tubes : evidence for high-speed downflows ?, Astron. & Astrophys., 330, 1160–1168, 1998.

Briand, C. and Vecchio, A. : Chromospheric polarity reversal on sunspots : New insight from spectro-polarimetric measurements, Astron. & Astrophys., 403, L33–L36, doi :10.1051/0004-6361 :20030553, 2003.

Briand, C., Collados, M., and Sütterlin, P. : THEMIS and DOT joint observations on NOAA 9716, in : SOLMAG 2002. Proceedings of the Magnetic Coupling of the Solar Atmosphere Euroconference, edited by Sawaya-Lacoste, H., vol. 505 of *ESA Special Publication*, pp. 361–364, 2002.

Briand, C., Mattig, W., Ceppatelli, G., and Mainella, G. : Mercury Transit for Stray Light Evaluation : IPM-THEMIS Case, Solar Phys., 234, 187–201, doi :10.1007/s11207-006-0033-5, 2006.

Briand, C., Mangeney, A., and Califano, F. : Electrostatic coherent structures generation by local heating in a collisionless plasma, Physics Lettters A, 368, 82–86, doi : 10.1016/j.physleta.2007.03.077, 2007.

Briand, C., Mangeney, A., and Califano, F. : Coherent electric structures : Vlasov-Ampère simulations and observational consequences, Journal of Geophysical Research (Space Physics), 113, 7219–+, doi :10.1029/2007JA012992, 2008a.

Briand, C., Zaslavsky, A., Maksimovic, M., Zarka, P., Lecacheux, A., Rucker, H., Konovalenko, A., Abranin, E., Dorovsky, V., Stanislasky, A., and Melnik, V. : Faint solar structures from decametric observations, Astron. & Astrophys., 490, 339–344, doi :10.1051/0004-6361 :200809842, 2008b.

Briand, C., Soucek, J., Henri, P., and Mangeney : Waves at the plasma frequency inside magnetic holes : STEREO and CLUSTER observations, J. Geophys. Research, 115, A12 113, doi :10.1029/2010JA015849, 2010a.

Briand, C., Soucek, J., Mangeney, A., Bale, S. D., and Goetz, K. : Waves at the plasma frequency inside magnetic holes : STEREO and Cluster observations, in : Twelfth International Solar Wind Conference, vol. 1216 of *AIP Publication*, pp. 271–274, doi :10.1063/1.3395853, 2010b.

Califano, F., Galeotti, L., and Briand, C. : Electrostatic coherent structures : The role of the ions dynamics, Physics of Plasmas, 14, 2306–+, doi :10.1063/1.2724807, 2007.

Cecconi, B., Bonnin, X., Hoang, S., Maksimovic, M., Bale, S. D., Bougeret, J., Goetz, K., Lecacheux, A., Reiner, M. J., Rucker, H. O., and Zarka, P. : STEREO/Waves Goniopolarimetry, Space Science Reviews, 136, 549–563, doi :10.1007/s11214-007-9255-6, 2008.

Cecconi, B., Lamy, L., Zarka, P., Prangé, R., Kurth, W. S., and Louarn, P. : Goniopolarimetric study of the revolution 29 perikrone using the Cassini Radio and Plasma Wave Science instrument high-frequency radio receiver, Journal of Geophysical Research (Space Physics), 114, 3215–+, doi :10.1029/2008JA013830, 2009.

Ceppatelli, G. and Briand, C. : Last news from THEMIS, Memorie della Societa Astronomica Italiana, 72, 558–564, 2001.

Ceppatelli, G. and Briand, C. : THEMIS : Status and Perspectives, in : SF2A-2002 : Semaine de l'Astrophysique Francaise, edited by Combes, F. and Barret, D., pp. 95–+, 2002.

Ceppatelli, G. and Briand, C. : THEMIS : Status and perspectives, Memorie della Societa Astronomica Italiana, 74, 790–+, 2003.

Chamberlain, J. W. : Interplanetary Gas.II. Expansion of a Model Solar Corona., Astrophys. J., 131, 47–+, doi :10.1086/146805, 1960.

Collett, E. : Polarized Light : fundamental and applications, CRC Press, 1992.

Crouseilles, N., Degond, P., and Lemou, M. : A hybrid kinetic fluid model for solving the Vlasov BGK equation, Journal of Computational Physics, 203, 572–601, doi : 10.1016/j.jcp.2004.09.006, 2005.

Del Moro, D., Criscuoli, S., Bonet, J. A., Márquez, I., Lemen, C., and Briand, C. : Phase diversity at THEMIS : first implementation, Memorie della Societa Astronomica Italiana, 74, 811–+, 2003a.

Del Moro, D., Lemen, C., Bonet, J. A., Márquez, I., Criscuoli, S., and Briand, C. : Phase diversity at THEMIS : first implementation, Astronomische Nachrichten, 324, 299–+, 2003b.

Dorch, S. B. F., Archontis, V., and Nordlund, Å. : 3D simulations of twisted magnetic flux ropes, Astron. & Astrophys., 352, L79–L82, 1999.

Eliasson, B. : Numerical modelling of the two-dimensional Fourier transformed Vlasov-Maxwell system, Journal of Computational Physics, 190, 501–522, doi :10.1016/S0021-9991(03)00295-X, 2003.

Eliasson, B. : Outflow boundary conditions for the Fourier transformed three-dimensional Vlasov Maxwell system, Journal of Computational Physics, 225, 1508–1532, doi : 10.1016/j.jcp.2007.02.005, 2007.

Elmore, D. F., Lites, B. W., Tomczyk, S., Skumanich, A. P., Dunn, R. B., Schuenke, J. A., Streander, K. V., Leach, T. W., Chambellan, C. W., and Hull, H. K. : The Advanced Stokes Polarimeter - A new instrument for solar magnetic field research, in : Society of Photo-Optical Instrumentation Engineers (SPIE) Conference Series, edited by Goldstein, D. H. and Chipman, R. A., vol. 1746 of *Society of Photo-Optical Instrumentation Engineers (SPIE) Conference Series*, pp. 22–33, 1992.

Emonet, T. and Moreno-Insertis, F. : The Physics of Twisted Magnetic Tubes Rising in a Stratified Medium : Two-dimensional Results, Astrophys. J., 492, 804–+, doi :10.1086/305074, 1998.

Fijalkow, E. : Numerical solution to the Vlasov equation : the 2D code, Computer Physics Communications, 116, 336–344, doi :10.1016/S0010-4655(98)00148-9, 1999.

Forslund, D. W. : Instabilities associated with heat conduction in the solar wind and their consequences., J. Geophys. Research, 75, 17–28, 1970.

Galeotti, L. and Califano, F. : Asymptotic Evolution of Weakly Collisional Vlasov-Poisson Plasmas, Physical Review Letters, 95, 015 002–+, doi :10.1103/PhysRevLett.95.015002, 2005.

Gary, S. P. : Ion-acoustic-like instabilities in the solar wind, J. Geophys. Research, 83, 2504–2510, 1978.

Ginzburg, V. L. and Zheleznyakov, V. V. : On the Possible Mechanisms of Sporadic Solar Radio Emission (Radiation in an Isotropic Plasma), Soviet Astronomy, 2, 653, 1958.

Gutnic, M., Haefele, M., Paun, I., and Sonnendrücker, E. : Vlasov simulations on an adaptive phase-space grid, Computer Physics Communications, 164, 214–219, doi : 10.1016/j.cpc.2004.06.073, 2004.

Henri, P., Briand, C., Mangeney, A., Bale, S. D., Califano, F., Goetz, K., and Kaiser, M. : Evidence for wave coupling in type III emissions, Journal of Geophysical Research (Space Physics), 114, 3103–+, doi :10.1029/2008JA013738, 2009.

Henri, P., Califano, F., Briand, C., and Mangeney, A. : Vlasov-Poisson simulations of electrostatic parametric instability for localized Langmuir wave packets in the solar wind, Journal of Geophysical Research (Space Physics), 115, 106–119, doi :10.1029/2009JA014969, 2010a.

Henri, P., Califano, F., Briand, C., and Mangeney, A. : Low energy Langmuir cavitons : asymptotic limit of weak turbulence, European Physical Letter – Submitted, 2010b.

Henri, P., Meyer, N., Briand, C., and Donato, S. : Fluctuation of spacecraft floating potential : using the STEREO spacecraft as a density probe, PoP – Submitted, 2010c.

Laval, G. and Pesme, D. : Inconsistency of quasilinear theory, Physics of Fluids, 26, 66–68, doi :10.1063/1.863985, 1983a.

Laval, G. and Pesme, D. : Breakdown of quasilinear theory for incoherent 1-D Langmuir waves, Physics of Fluids, 26, 52–65, doi :10.1063/1.863984, 1983b.

Laval, G. and Pesme, D. : Controversies about quasi-linear theory, Plasma Physics and Controlled Fusion, 41, A239–A246, 1999.

Lee, J., Chae, J., Yun, H. S., and Zirin, H. : The Effect of Seeing on Solar Magnetic Flux Measurements, Solar Phys., 171, 35–48, 1997.

Lemaire, J. and Pierrard, V. : Kinetic Models of Solar and Polar Winds, Astrophys. J. Supp. Series, 277, 169–180, doi :10.1023/A :1012245909542, 2001.

Lemaire, J. and Scherer, M. : Kinetic models of the solar wind., J. Geophys. Research, 76, 7479–7490, doi :10.1029/JA076i031p07479, 1971.

Li, W., Ai, G., and Zhang, H. : Reversed-polarity structures of chromospheric magnetic field, Solar Phys., 151, 1–14, doi :10.1007/BF00654077, 1994.

Lin, N., Kellogg, P. J., MacDowall, R. J., and Gary, S. P. : Ion Acoustic Waves in the Heliosphere, Space Science Reviews, 97, 193–196, doi :10.1023/A :1011823505395, 2001.

Mainella, G. and Briand, C. : Telescope guide and pointing precision at THEMIS, Nuovo Cimento C Geophysics Space Physics C, 25, 709–+, 2002.

Mainella, G., Briand, C., Maréchal, L., and Le Men, C. : Pointing and tracking analysis of alt-azimuthal multi-focus telescopes : the THEMIS case, Astronomische Nachrichten, 324, 309–312, 2003.

Malaspina, D. M., Ergun, R. E., Cairns, I. H., Bougeret, J., Bale, S., Kellogg, P. J., and Kaiser, M. L. : Consequences of the Eigenmode Interpretation of Solar Wind Langmuir Waves, AGU Fall Meeting Abstracts, p. A1576, 2008.

Mangeney, A., Salem, C., Lacombe, C., Bougeret, J.-L., Perche, C., Manning, R., Kellogg, P. J., Goetz, K., Monson, S. J., and Bosqued, J.-M. : WIND observations of coherent electrostatic waves in the solar wind, Annales Geophysicae, 17, 307–320, 1999.

Mangeney, A., Califano, F., Cavazzoni, C., and Travnicek, P. : A Numerical Scheme for the Integration of the Vlasov-Maxwell System of Equations, Journal of Computational Physics, 179, 495–538, 2002.

Marsch, E., Schwenn, R., Rosenbauer, H., Muehlhaeuser, K.-H., Pilipp, W., and Neubauer, F. M. : Solar wind protons - Three-dimensional velocity distributions and derived plasma parameters measured between 0.3 and 1 AU, J. Geophys. Research, 87, 52–72, 1982.

Martinez Pillet, V., Lites, B. W., Skumanich, A., and Degenhardt, D. : Evidence for supersonic downflows in the photosphere of a delta sunspot, Astrophys. J. Letter, 425, L113–L115, doi :10.1086/187323, 1994.

Mein, P., Briand, C., Heinzel, P., and Mein, N. : Solar arch filaments observed with THEMIS, Astron. & Astrophys., 355, 1146–1151, 2000.

Meyer-Vernet, N. and Perche, C. : Tool kit for antennae and thermal noise near the plasma frequency, J. Geophys. Research, 94, 2405–2415, doi :10.1029/JA094iA03p02405, 1989.

Mikhailovskii, A. : Theory of plasma instabilities, Consultants Bureau – New York London, 1974.

Moreno-Insertis, F., Caligari, P., and Schuessler, M. : Active region asymmetry as a result of the rise of magnetic flux tubes, Solar Phys., 153, 449–452, doi :10.1007/BF00712518, 1994.

Nulsen, A. L., Cairns, I. H., and Robinson, P. A. : Field distributions and shapes of Langmuir wave packets observed by Ulysses in an interplanetary type III burst source region, Journal of Geophysical Research (Space Physics), 112, 510, doi :10.1029/2006JA011873, 2007.

Opitz, A., Sauvaud, J.-A., Fedorov, A., Wurz, P., Luhmann, J. G., Lavraud, B., Russell, C. T., Kellogg, P., Briand, C., Henri, P., Malaspina, D. M., Louarn, P., Curtis, D. W., Penou, E., Karrer, R., Galvin, A. B., Larson, D. E., Dandouras, I., and Schroeder, P. : Temporal evolution of the solar wind electron core density at solar minimum by correlating the STEREO A and B SWEA measurements, Solar Phys., 266, 369, doi :10.1007/s11207-010-9613-5, 2010.

Parker, E. N. : Suprathermal Particle Generation in the Solar Corona., Astrophys. J., 128, 677–+, 1958.

Ruiz Cobo, B. : SIR : an Inversion Technique of Spectral Lines, Astrophys. J. Supp. Series, 263, 331–334, doi :10.1023/A :1002191418914, 1998.

Sanchez Almeida, J. : Chromospheric polarity reversals on sunspots. Are they consistent with weak line emission ?, Astron. & Astrophys., 324, 763–769, 1997.

Sigwarth, M. : Properties and Origin of Asymmetric and Unusual Stokes V Profiles Observed in Solar Magnetic Fields, Astrophys. J., 563, 1031–1044, doi :10.1086/323963, 2001.

Simon, S., Motschmann, U., Kleindienst, G., Saur, J., Bertucci, C. L., Dougherty, M. K., Arridge, C. S., and Coates, A. J. : Titan's plasma environment during a magnetosheath excursion : Real-time scenarios for Cassini's T32 flyby from a hybrid simulation, Annales Geophysicae, 27, 669–685, 2009.

Skumanich, A., Lites, B. W., Martinez Pillet, V., and Seagraves, P. : The Calibration of the Advanced Stokes Polarimeter, Astrophys. J. Supp. Series, 110, 357–+, doi :10.1086/313004, 1997.

Solanki, S. K. : Sunspots : An overview, Astron. & Astrophys., 11, 153–286, doi :10.1007/s00159-003-0018-4, 2003.

Sonnendrücker, E., Filbet, F., Friedman, A., Oudet, E., and Vay, J. : Vlasov simulations of beams with a moving grid, Computer Physics Communications, 164, 390–395, doi : 10.1016/j.cpc.2004.06.077, 2004.

Soucek, J., Briand, C., Mangeney, A., Bale, S., Goetz, K., and Pickett, J. : Micro-scale properties of Langmuir waves observed by STEREO and CLUSTER inside solar wind magnetic holes, AGU Fall Meeting Abstracts, p. A1527, 2009.

Thejappa, G., Goldstein, M. L., MacDowall, R. J., Papadopoulos, K., and Stone, R. G. : Evidence for Langmuir envelope solitons in solar type III burst source regions, J. Geophys. Research, 104, 28 279–+, doi :10.1029/1999JA900363, 1999.

Uitenbroek, H. and Briand, C. : The MgI λ285.21 Nanometer Line : an Example of Non-LTE Line Formation, Astrophys. J., 447, 453–+, doi :10.1086/175889, 1995.

Valentini, F., Veltri, P., and Mangeney, A. : A numerical scheme for the integration of the Vlasov Poisson system of equations, in the magnetized case, Journal of Computational Physics, 210, 730–751, doi :10.1016/j.jcp.2005.05.014, 2005.

Valentini, F., Trávníček, P., Califano, F., Hellinger, P., and Mangeney, A. : A hybrid-Vlasov model based on the current advance method for the simulation of collisionless magnetized plasma, Journal of Computational Physics, 225, 753–770, doi :10.1016/j.jcp.2007.01.001, 2007.

Vedenov, A. A. : Quasi-linear plasma theory (theory of a weakly turbulent plasma), Journal of Nuclear Energy, 5, 169–186, doi :10.1088/0368-3281/5/3/305, 1963.

Wang, J. and Shi, Z. : Flare-associated magnetic changes in an active region. I - Localized chromospheric polarity reversal, Solar Phys., 140, 67–84, 1992.

Wedemeyer-Böhm, S., Lagg, A., and Nordlund, Å. : Coupling from the Photosphere to the Chromosphere and the Corona, Space Science Reviews, 144, 317–350, doi :10.1007/s11214-008-9447-8, 2009.

Weiss, N. O. and Thompson, M. J. : The Solar Dynamo, Space Science Reviews, 144, 53–66, doi :10.1007/s11214-008-9435-z, 2009.

Yoon, P. H., Ziebell, L. F., and Wu, C. S. : Excitation of Langmuir waves in interplanetary space, J. Geophys. Research, 105, 27 369–27 376, doi :10.1029/2000JA000230, 2000.

Zouganelis, I., Maksimovic, M., Meyer-Vernet, N., Lamy, H., and Issautier, K. : A Transonic Collisionless Model of the Solar Wind, Astrophys. J., 606, 542–554, doi :10.1086/382866, 2004.